University of Alberta

A Comprehensive Approach to Constructing Human Long Bone Models: From CT to FE

by

Anthony Garky Au

A thesis submitted to the Faculty of Graduate Studies and Research in partial fulfillment of the requirements for the degree of

Doctor of Philosophy

Department of Mechanical Engineering

Edmonton, Alberta
Fall 2008

Your file Votre référence
ISBN: 978-0-494-46276-8
Our file Notre référence
ISBN: 978-0-494-46276-8

Abstract

Generic finite element (FE) bone models are valid for answering many general biomechanics questions, but additional research and clinical benefits can be obtained by models tailored to specific individuals. This thesis introduced a single comprehensive technique encompassing *in vivo* geometry and material properties with physiological loading conditions.

A semi-automated subject-specific (SASS) modeling technique was introduced for constructing *in vivo* knee bone geometry from computed tomography (CT) images. It improved upon current techniques to better capture the smooth natural curves and the thin cortex of the knee bones. The SASS method rapidly constructed the complex 3-D surface geometries with accuracy within 2 image pixel lengths. The geometry was complemented with personalized bone tissue properties that were both orthotropic and heterogeneous. The method uniquely modeled heterogeneity with bone groups based on similar density and location within the knee. The modeling of heterogeneity was optimized to produce accurate stress predictions with minimal computational time.

The technique also ensured that the model incorporated loading conditions representative of daily physical activities. Particular emphasis was placed on the inclusion of muscle and ligament forces, which was necessary to predict a more physiologically representative stress condition. A preliminary experimental

verification was performed and showed promising results regarding the ability of the FE models to mimic the real bone.

Subject-specific models created using the SASS technique are an alternative to generic models as a research and clinical tool. The technique sets the stage for future use of subject-specific models in cross-sectional studies of knee prosthesis and fixation device design.

Acknowledgements

I would like to extend my greatest thanks to my advisor, Dr. Alidad Amirfazli, and co-advisor, James Raso, for their guidance, patience, inspiration, and constant support during the completion of my thesis, and for all the opportunities they have given me over the years.

I would especially like to thank my mother for her wisdom, inspiration, and encouragement, particularly during the difficult times. The completion of my thesis would not have been possible without her.

I would like to extend a special thank you to Dr. Jason Carey for his invaluable support and advice during our frequent meetings. Thanks also to Dr. Adrian Liggins for his thoughtful advice and often original suggestions.

Also, my sincerest appreciation is given to my family, friends and colleagues, who were very much a part in my completion of this work; to all the front office staff (especially Gail Anderson and Linda Paulic), IT staff (especially Jonathan Clark), and machine shop technicians (especially Bernie Faulkner) at the University of Alberta, for performing small miracles; and to Darren Palathinkal, Justin Pullukatt, and Jena Dressler for their help with my research.

A special thanks to Dr. Walied Moussa, who has provided me with invaluable technical support in the FE modeling part of my thesis. Thank you also Dr. Robert Lambert, Ms. Shirley Palmer, and Mr. Dave Gauvreau from the University of Alberta Hospital's Department of Diagnostic Imaging for their assistance in obtaining the CT images used throughout this work. I also wish to thank the Alberta CIHR Training Program and in Bone and Joint Health and the Natural Science and Engineering Research Council (NSERC) for their financial support.

Table of Contents

Chapter 1: Introduction..... 1

1.1 The need for a comprehensive subject-specific finite element modeling technique..... 1

1.2 Modeling the physiological anatomy..... 2

1.3 Modeling bone tissue properties..... 5

1.4 Modeling physiologically representative loading conditions..... 9

1.5 Meshing subject-specific finite element models..... 11

1.6 Validating subject-specific finite element models..... 12

1.7 Objective of Thesis..... 13

1.8 Scope of Thesis..... 14

1.9 Outline of Thesis Chapters..... 16

References 18

Chapter 2: A NURBS-based technique for subject-specific construction of knee bone geometry 26

2.1 Introduction 26

2.2 Methods..... 29

2.2.1 Edge Extraction..... 30

2.2.2 Periosteum and Endosteum Construction..... 32

2.2.3 Validation..... 33

2.2.3.1 Periosteal Surface Validation..... 33

2.2.3.2 Endosteal Surface Validation..... 34

2.2.4 Slice separation sensitivity..... 35

2.3 Results..... 35

2.3.1 Construction Accuracy..... 35

2.3.1.1 SASS technique for composite bones..... 35

2.3.1.2 Voxel mesh technique for composite bones... 35

2.3.1.3 Laser scan technique for composite bones..... 36

2.3.1.4 SASS technique for bovine bones..... 36

2.3.1.5 Voxel mesh technique for bovine bones..... 37

2.3.1.6 Laser scan technique for bovine bones..... 37
2.3.2 In vivo construction..... 37
2.4 Discussion..... 39
2.4.1 Construction Accuracy..... 39
2.4.1.1 Periosteum identification (SASS technique)... 39
2.4.1.2 Periosteum identification (voxel mesh technique)..... 41
2.4.1.3 Periosteum identification (laser scan technique)..... 42
2.4.1.4 Endosteum identification..... 43
2.4.2 Computational Efficiency and Slice Separation Sensitivity..... 46
2.4.3 Sources of Error..... 48
2.4.3.1 Measuring Cortical Bone Thickness..... 48
2.4.3.2 Field of View..... 50
2.5 Summary and Conclusions..... 51
References..... 66

Chapter 3: Representation of heterogeneity in subject-specific finite element knee bone models 71
3.1 Introduction..... 71
3.2 Methods and Materials..... 74
3.2.1 CT Images..... 74
3.2.2 Grouping Technique..... 78
3.2.3 Determining Material Properties..... 78
3.2.4 Finite Element Model..... 78
3.2.5 Validation..... 80
3.3 Results..... 81
3.3.1 Material Properties Distribution..... 81
3.3.2 Computation time..... 81
3.3.3 Convergence..... 82

3.3.3.1 Von Mises Stress..... 82
3.3.3.2 Strain Energy Density..... 83
3.3.3.3 Nodal Displacement..... 83
3.3.3.4 Homogeneous and Isotropic Models..... 83
3.3.4 Verification of Grouping Results..... 84
3.4 Discussion..... 85
3.4.1 Verification of Grouping Results..... 87
3.4.2 Convergence Tolerance..... 89
3.4.3 Homogeneous Bone Properties..... 90
3.4.4 Computational Effort..... 92
3.4.5 Mapping Strategy..... 93
3.5 Summary and Conclusions..... 93
References..... 112

Chapter 4: A numerical stress analysis of the distal femur: the effect of soft tissue loading 116
4.1 Introduction..... 116
4.2 Materials and Methods..... 118
4.2.1 Applied Loads and Boundary Conditions..... 118
4.2.1.1 Tibiofemoral Compression..... 119
4.2.1.2 Patellofemoral Compression..... 120
4.2.1.3 Soft Tissue Representation..... 120
4.2.1.4 Soft Tissue Insertion Sites..... 121
4.2.1.5 Soft Tissue Lines of Action..... 122
4.2.2 Methodology to Study the Effect of Loading Conditions..... 123
4.2.3 Cortical Stress from Button-Type Fixation..... 124
4.3. Results..... 124
4.3.1 Insertion Sites..... 124
4.3.2 Influence of Soft Tissue Loading on Stress Distribution 125
4.3.3 Point Loading Versus Closed Area Loading..... 126

4.3.4 Cortical Bone Stress from the Button Device..... 126
4.4 Discussion..... 127
4.4.1 Insertion Sites..... 127
4.4.2 Point Loading versus Closed Area Loading..... 128
4.4.3 Influence of Soft Tissue Loading on Stress Distribution 129
4.4.4 Stress Distribution in ACL-reconstructed femur..... 130
4.5 Summary and Conclusions..... 132
References..... 147

Chapter 5: Experimental validation of finite element models of a composite femur and tibia 154
5.1 Introduction..... 154
5.2 Materials and Methods..... 155
5.2.1 Experiments..... 156
5.2.2 Finite Element Analyses..... 157
5.2.3 Sensitivity Analysis..... 159
5.3 Results..... 161
5.3.1 Experiments..... 161
5.3.2 Experiment and FE Model Comparison..... 162
5.3.2.1 Composite Tibia..... 162
5.3.2.2 Composite Femur..... 162
5.3.2.3 Bovine Tibia..... 163
5.3.3 Sensitivity Analysis of Material Properties..... 163
5.3.4 Sensitivity Analysis of Loading Conditions..... 164
5.3.5 Variability of Predicted Strains in Gauge Region..... 165
5.4 Discussion..... 165
5.4.1 Goodness of Prediction of FE Models..... 165
5.4.2 Sensitivity Analysis..... 167
5.4.2.1 Sensitivity of Strains to Material Properties.... 167
5.4.2.2 Sensitivity of Strains to Load Placement..... 168
5.4.2.3 Sensitivity of Strains to Load Direction and

Misalignment..... 169
5.4.2.4 Sensitivity of Strains to Point Contact Assumption..... 170
5.4.3 Replication of Experimental Loading Conditions..... 171
5.4.4 Improving Finite Element Strain Representation..... 172
5.4.5 Improving Principal Strain Comparison..... 173
5.5 Summary and Conclusions..... 174
References..... 197

Chapter 6: Contribution of loading conditions and material properties to stress shielding near the tibial component of total knee replacements 201
6.1 Introduction..... 201
6.2 Materials and Methods..... 202
6.2.1 Loading Conditions..... 202
6.2.2 Tibial Knee Prosthesis Model..... 203
6.3 Results and Discussion..... 204
6.3.1 Material property influence on stress distribution..... 205
6.3.2 Loading condition influence on stress distribution..... 205
References..... 215

Chapter 7: Summary, Conclusions, and Future Directions 219
7.1 Future Directions..... 223

Appendix A: Geometry Construction Details..... 225
Appendix B: Empirical Relationships for Modeling Cortical and Cancellous Bone..... 230
References..... 233

List of Figures

Figure		Page
2.1	Typical attenuation histogram from a transverse CT image of the distal human femur	57
2.2	Gradient-operated transverse image of the human distal femur after thresholding	58
2.3	Typical profile of attenuation and gradient values along intersection of endosteal interface	59
2.4	Transverse sets of smooth periosteal interface contours used to construct the 3-D surface of the composite femur	60
2.5	Human distal femur constructed using SASS and voxel mesh techniques	61
2.6	Comparison of construction results for Bovine Femur 1	62
2.7	Comparison of construction results for human distal femur	63
2.8	Composite femur constructed using SASS and commercial software techniques with 0.6 mm and 3.0 mm slice separations	65
3.1	Example of splitting procedure	100
3.2	Example of sub-region merging procedure	101
3.3	Example of enhanced merging procedure	102
3.4	Segments of femur cortex with control segment identified	103
3.5	Distribution of attenuation values for cortical and cancellous bone grouped using three different tolerance levels	104
3.6	Comparison of maximum von Mises stress, strain energy density and nodal displacements with tolerance level for FE femur model	105
3.7	Comparison of mean von Mises stresses with tolerance level for FE femur and tibia models	106
3.8	Comparison of mean strain energy density with tolerance level for FE femur model	107
3.9	Comparison of mean nodal displacement with tolerance level for FE femur model	107
3.10	Comparison of first computed region with thresholded CT image for femur slice	108
3.11	Comparison of second computed region with thresholded CT image for femur slice	108

3.12 Comparison of computed region with thresholded CT image for tibia slice..... 109

3.13 Comparison of computed regions using new method and conventional method..... 110

3.14 Comparison of von Mises stress accuracy and computational time with tolerance level for FE femur model..... 111

4.1 Schematic of muscle attachments in FE distal femur model..... 136

4.2 Schematic diagram of fixation button..... 137

4.3 Von Mises stress contour plots of femur with and without muscle and ligament loading..... 138

4.4 Von Mises stress paths traced across femur sections with and without soft tissue loading..... 142

4.5 Von Mises stress contour plots of femur with point loading and area loading..... 143

4.6 Von Mises stress paths traced across transverse sections of femur with point loading and area loading..... 145

4.7 Von Mises stress contour plots of cortical bone stress at tunnel aperture caused by button compression..... 146

4.8 Relationship of maximum cortical stress at tunnel aperture to ACL force over stance phase of gait cycle..... 146

5.1 Schematic of strain gauge rosette placement in composite tibia, composite femur, and bovine tibia..... 185

5.2 Schematic of mechanical testing apparatus and loading jig..... 186

5.3 FE models of composite femur, composite tibia, and bovine tibia..... 187

5.4 Comparison of measured and predicted strains in composite tibia..... 190

5.5 Comparison of measured and predicted strains in composite femur..... 193

5.6 Comparison of measured and predicted strains in bovine tibia..... 196

6.1 Schematic of FE models used in tibia TKR investigation..... 209

6.2 Schematic of 12 stress path locations viewed through transverse section of tibia..... 210

6.3 Comparison of normalized von Mises bone stresses resulting from changes in material properties and loading conditions of implant..... 212

6.4 Comparison of normalized von Mises bone stresses resulting from changes in loading conditions of implant..... 213

6.5 Comparison of normalized von Mises bone stresses resulting from

changes in load patterns of implant..... 214

A.1 Series of 16 interconnected splines defining periosteal contour..... 229

A.2 Transverse CT image of human distal femur showing endosteal interface points extracted using Path Analysis..... 229

List of Tables

Table		Page
2.1	CT image specifications for composite, bovine, and human bones	53
2.2	Error comparison of CMM coordinates with model surface coordinates	54
2.3	Error comparison in composite femur surfaces constructed with various transverse slice separations	55
2.4	Effect of smoothing on accuracy of composite femur surfaces	56
3.1	Specifications of CT images obtained for 37-year-old human female	95
3.2	Number of groups generated from grouping operation	95
3.3	Computational times needed to group bone into similar regions	95
3.4	Mean and standard deviation of von Mises stress in elements of control segment at various tolerance levels	96
3.5	Mean and standard deviation of strain energy density in elements of control segment at various tolerance levels	96
3.6	Mean and standard deviation of nodal displacements in control region at various tolerance levels	97
3.7	Means and standard deviations of von Mises stress, strain energy density, and displacement in control segment with homogeneous and isotropic bone	98
3.8	Comparison of number of groups generated using two different mapping strategies	99
3.9	Comparison of von Mises stresses in FE models with elements mapped using two strategies	99
4.1	Summary of tibiofemoral, patellofemoral, muscle and ligament loading forces at each interval of gait cycle	133
4.2	Difference in soft tissue attachment point locations for distal femur	134
4.3	Comparison of line of action angles with experimental values	134
4.4	Summary of maximum von Mises stress from button compression on tunnel aperture	135
5.1	Mean and standard deviation of five sets of load cell readings for composite tibia, composite femur, and bovine tibia	176
5.2	Mean and standard deviation of five sets of von Mises strains for composite tibia, composite femur, and bovine tibia	176
5.3	Measured and predicted von Mises strains with corresponding error for composite tibia	177

5.4 Measured and predicted von Mises strains with corresponding error for composite femur..... 178

5.5 Measured and predicted von Mises strains with corresponding error for bovine tibia..... 179

5.6 Von Mises strains observed in FE composite femur and tibia models with different Young's moduli..... 180

5.7 Regression analysis results of sensitivity analysis..... 181

5.8 Von Mises strains predicted in FE composite femur and tibia models implementing different load configurations..... 182

5.9 Variability of von Mises strains caused by 5 degree valgus rotation in FE composite femur and tibia models..... 183

5.10 Variability of von Mises strains inside each strain gauge region in FE composite femur and tibia models..... 184

6.1 Summary of loads placed on FE tibia model..... 208

6.2 Comparison of line of action angles with experimental data..... 208

A.1 Comparison of curve smoothness by varying curve origin..... 226

B.1 Elastic constants applied in homogeneous FE femur model..... 233

Chapter 1: Introduction

1.1 The need for a comprehensive subject-specific finite element modeling technique

Knowledge of mechanical stresses in human bones generated from physiological activities is necessary in both clinical practice and research. Unfortunately, these stresses cannot be measured in bones *in vivo* without the use of invasive surgical procedures, which is not ethically permissible (Taddei et al., 2006). Moreover, even invasive instruments have difficulty measuring stresses inside the bone. In 1972, a finite element (FE) model was introduced to non-invasively estimate stresses in human bones (Brekelmans et al., 1972). Since then, FE models have been used so frequently, it has become a recognized tool in orthopaedic biomechanics. FE models have been used to understand the complex movements of human joints such as the shoulder, hip and knee. One of its strongest attributes is its ability to perform parametric analyses, which has naturally led to its use as a tool for designing and improving prostheses for these joints. However, the majority of FE models are used as research tools because they are oversimplified and do not adequately replicate a particular physiological situation.

Most FE studies have evaluated the natural or pathological stresses induced in bones for a general biomechanical situation by employing models based on geometries and material properties of an average individual. The conclusions drawn from such models are therefore applicable only for the average population. Significant inter-subject variability in human beings, which can be caused by aging and anatomical deformities, does not allow conclusions drawn from generic FE models to be applied directly to a specific person (Noble et al., 1988, 1995; Hicks et al., 1995; Sugano et al., 1998).

While generic FE models are perfectly acceptable for understanding general biomechanics and design concepts, there is an increasing interest in using the FE method as a clinical tool. One application is to evaluate the risk of femoral fracture (Testi et al., 1999; Keyak and Rossi, 2000). With proper development,

these models can help in pre-operative planning (Kopperdahl et al., 1999) as well as post-operative rehabilitation after limb-salvage procedures (Taddei et al., 2003) and skeletal surgery (Sutherland et al., 1999; Taddei et al., 2002).

Subject-specific FE models can also be excellent research tools by complementing the use of generic FE models to improve design of prostheses. In particular, substantial insight can be gained by generating separate FE models for each member of a population to observe inter-subject differences for a particular design characteristic. The creation of subject-specific models is not a simple extension of techniques that have been used to construct generic models. In many of the major modeling areas, concepts must be improved and refined. Specifically, there are three main modeling aspects that need to be covered to ensure that a subject-specific FE model mimics the physiological situation: geometry, material properties, and loading conditions. Over the past decade, techniques have slowly evolved and the modeling of these aspects has become increasingly representative of the physiological situation. However, current models often oversimplify at least one aspect. There is currently no technique which comprehensively covers all the aspects needed to create a sufficiently sophisticated subject-specific FE model that is truly representative of the physiological situation. In this thesis, an interlinked framework is used to model the physiological situation of each of the three aspects. The aspects are all connected through the construction of subject-specific models of the knee bones. Each of these aspects is discussed below.

1.2 Modeling the physiological anatomy

The 3-D geometry of bones is so complex that it requires an intensive approach to adequately capture it. The geometry is not simple enough that a regular 3-D shape can be used to represent it. The outline of the shape is often extracted from images obtained using diagnostic techniques such as computed tomography (CT), magnetic resonance imaging (MRI), or ultrasound. Currently, ultrasound images cannot be used to accurately construct bone surface models because ultrasound

waves are strongly reflected by bone (Douglas et al., 2002; Pena et al., 2005). MRI has been used to create surface geometries (Li et al., 1999; Suggs et al., 2003) but they have not been used to create a full subject-specific FE model because bone density cannot be interpreted from MRI image data, which hinders its effectiveness for stress studies. At present, CT images represent the best source of information for interpretation of both *in vivo* bone morphology and mechanical properties. Surfaces created from CT images have been shown to be accurate (Viceconti et al., 1999).

Outer bone surfaces can be constructed from CT images using either voxel meshing (Keyak et al., 1990; Lengsfeld et al., 1998) or non-uniform rational B-spline (NURBS) surfaces (Viceconti et al., 1998). Voxel meshing takes a series of thresholded 2-D slices and stacks them to create a 3-D bone volume. Because it is a fairly simple and user-friendly technique, it has been adapted in commercial software. The software is used extensively in clinical communities for rapid construction of surface geometries from CT images. However, jagged surfaces are often associated with areas of high curvature in voxel meshed bone models and can compromise the accuracy of the predicted stresses during FE analysis (Keyak et al., 1990; Marks and Gardner, 1993; Viceconti et al., 1998).

Alternatively, geometries can be constructed by fitting smooth 3-D NURBS surfaces to a stack of 2-D contours extracted from CT images. NURBS surfaces can be constructed through a complicated process of reverse engineering from tiled surfaces (Taddei et al., 2006) or through "skinning", which is basically draping a form-fitting surface over the contours. Skinning is more user-friendly and is available in commercial CAD packages, but its major drawback is it cannot adequately handle bifurcating bone structures, such as the human femur (Viceconti et al., 1998).

The accuracy of the 3-D subject-specific bone surface is contingent upon the 2-D contours extracted from the CT images. Two contours need to be extracted in

each CT image: a periosteal contour, which outlines the border between the cortex and the surrounding muscle tissue, and an endosteal contour, which outlines the border between the cortical shell and the inner marrow-filled cancellous bone. This can be done manually using visual inspection. However, this is an extremely time consuming and subjective technique, which is not suitable for subject-specific modeling (Taddei et al., 2006).

Automated techniques, such as binary image thresholding (Coleman et al., 2000; Miyoshi et al., 2002), local pixel intensity analysis (Testi et al., 2001), and conjugated gradient algorithms (Viceconti et al., 1998), do not adequately capture the endosteum. Thresholding defines the bone contour by selecting pixels in a CT image within an intensity window. It is ineffective for identifying endosteal contours because cortical and cancellous bone sometimes have similar intensities, particularly in epiphyseal bone. This property similarly hampers local pixel intensity analysis, which is also thresholding-based. Voxel mesh techniques are based on thresholded images and therefore the models often do not have defined endosteal interfaces. The similar intensity between cortical and cancellous bone results in weak gradients at the endosteal interface. Consequently, gradient-based tracing algorithms may not be entirely effective. The inadequacy of current techniques for detecting endosteal edges has resulted in nearly all subject-specific femur and tibia FE models unable to capture the endosteal interface.

The current challenge in constructing subject-specific knee bone geometries is to accurately define the endosteum in poorly contrasted bone near the articulation, where the cortex is thin and less distinguishable from the cancellous bone. This requires the development of a more sophisticated interpretation of image data than the current techniques provide. This thesis introduces a semi-automated technique which accurately constructs 3-D surfaces of both periosteal and endosteal interfaces (Chapter 2).

1.3 Modeling bone tissue properties

The hard outer cortical bone of the knee consists of lamellar bone and provides structural stability for the joint (Carter and Spengler, 1978). Cancellous bone is structurally different from cortical bone, consisting of trabeculae, and is much softer and more porous (Gibson, 1985). Consequently, the cortical and cancellous bones defined in the geometry process require different definitions of material properties. In defining the material properties of these bones, it is necessary to characterize them as isotropic or anisotropic, homogeneous or heterogeneous, and linearly elastic or viscoelastic. The conditions being simulated in FE models generally have low strain rates and therefore it is reasonable to model the bone as linearly elastic (Ashman et al., 1984).

The nature of cancellous bone can be described by both material and structural properties. Structural properties are defined at the macroscopic level and contain the extrinsic properties of both trabeculae and pores, whereas material properties are defined at the microstructural level, containing the intrinsic properties of the trabecular struts only (Rho, 1992). The size of the typical trabeculae is small (approximately 0.3 mm diameter and 2 mm length) and specimens must span at least five intertrabecular lengths in order to relate local strains in trabecular bone to those on the apparent level (Harrigan et al., 1998). This thesis focuses on the bone as a whole and therefore models the macrostructure of cancellous bone rather than the microstructure.

To capture the unique nature of each individual's bone in FE models, the stiffness of the bone must be interpreted from the attenuation data of the CT image. This is done by using a series of empirical equations. The complicated nature of bone makes it difficult to measure bone properties experimentally. As a result, numerous different empirical relationships have been observed. Most have found that axial stiffness is related to density either by a linear or power relationship (Rho et al., 1995; Keyak et al., 1994; Keller, 1994; Carter and Hayes, 1977);

transverse stiffness has also been found to be similarly related (Rho et al., 1995; Keyak et al., 1994).

While it is clear that cortical and cancellous bones are physiologically different, their mechanical properties are often not modeled differently in subject-specific FE models. This may be due to the absence of an endosteal interface. Subsequently, stiffness is often interpreted using equations assumed to be applicable for both cortical and cancellous bone (Carter and Hayes, 1977; Keller, 1994). However, such equations were derived under the assumption that cortical bone was simply dense cancellous bone, an assumption which has been shown to be incorrect (Rice et al., 1988). As further evidence, Rho et al. (1995) have found that while cancellous bone stiffness can be determined from density, cortical bone is weakly related to density, and have emphasized use of the appropriate relationship during material properties modeling. Thus, the importance of first distinguishing cortical from cancellous bone prior to material property assignment is even more important as it has been suggested this can affect the material properties assignment (Taddei et al., 2004). The subject-specific FE models in this thesis have separate cortical and cancellous bone geometries and therefore different relationships were used to define the elastic constants for the two bone types.

Reilly and Burstein (1975) have characterized cortical bone as having transversely isotropic mechanical properties, being stronger and stiffer in the longitudinal direction (parallel to the long axis of the bone) than in the transverse direction. However, evidence suggests that this may not be sufficiently descriptive and cortical bone in the femur and tibia should be considered orthotropic (Rho, 1992). In contrast, cancellous bone has clearly been shown to be orthotropic, with axial stiffness also much higher than the transverse stiffness (Ashman et al., 1989; Rho, 1992).

Despite what has been observed experimentally, many FE models represent cortical and cancellous bone as isotropic to simplify the computational problem. Huiskes et al. (1981) have stated, based on a theoretical analysis, that when the cortical bone is assumed to be completely isotropic, a good theoretical prediction of the most significant stresses in bending and axial loading should be possible. However, even better predictions can be provided by using transversely isotropic cortical bone (Huiskes et al., 1981). This has been confirmed by a recent analysis showing orthotropic bone provides slightly more accurate results compared with isotropic bone (Peng et al., 2006). The slight difference between isotropic and anisotropic results becomes much more exaggerated in tibia TKR models, mainly because of the shear forces that are created by a prosthesis (Askew and Lewis, 1981).

It appears the appropriateness of incorporating isotropic or anisotropic bone depends on the associated loading condition. Isotropic bone should only be used in conjunction with axial or bending loading; anisotropic bone is needed for more complex loading such as torsion (Huiskes et al., 1981). In models where loading conditions are not known *a priori*, anisotropic bone should therefore be used. Employing anisotropic bone will produce more accurate results regardless of the loading conditions, and is more appropriate when FE models are used in clinical situations where the accuracy may become a concern.

Just as important as characterizing the anisotropy of bone is characterizing its heterogeneity. Numerous studies have shown that the stiffness of cancellous bone varies significantly within the femur and tibia (Ashman et al., 1989; Goldstein et al., 1983; Ciarelli et al., 1991), sometimes by as much as 800% (Rho, 1992). Cortical bone, on the other hand, is less heterogeneous. Small changes in stiffness of about 10 to 20% have been observed in differing regions of the cortex (Van Buskirk and Ashman, 1989). However, no significant difference in stiffness has been detected in the cortical bone along the length of the femur and tibia (Ashman et al., 1984; Rho, 1992). Around the circumference of the femur, axial stiffness in

the posterior cortex has been observed to be significantly higher than the rest of the bone (Ashman et al., 1984), but this has not been consistently seen (Rho, 1992).

Cancellous bone must be carefully modeled because it transfers loads to the cortex (Askew and Lewis, 1981) and improperly modeling it can affect stress accuracy not only in the cancellous bone itself but also in the surrounding cortex (Taddei et al., 2006). FE models requiring high levels of accuracy must properly represent the non-uniformly distributed nature of the bone stiffness. In subject-specific modeling, this heterogeneity is generally interpreted from the CT image data.

The heterogeneity of cortical and cancellous bones has been considered in nearly all subject-specific FE models of the lower limb. However, the degree to which heterogeneity has been represented has varied vastly, from 82 different sets of bone properties (Keyak et al., 1993) to over 1,000 different sets (Taddei et al., 2004). Modeling the vast number of material properties can be computationally expensive (Taddei et al., 2006). Therefore, models are often simplified by grouping bone of similar attenuation together to reduce the number of material properties, thereby reducing the computational time needed to calculate a solution (Peng et al., 2006; Lengsfeld et al., 1998; Keyak et al., 1993). Fully heterogeneous models, i.e. those with no grouping, can accurately predict strains and stresses (Taddei et al., 2006, 2007). However, a moderate amount of grouping should not change the solution (Peng et al., 2006) and therefore FE models with a slightly lower degree of heterogeneity can still be fairly accurate (Keyak et al., 1993). Thus, while it is obvious that heterogeneity needs to be represented in FE models, there is no consensus regarding the degree to which this is necessary (i.e. the size and number of groups required) in order to generate accurate solutions. It appears to date that the selection of the degree of heterogeneity is a subjective matter. In Chapter 3 of this thesis, a method of interpreting mechanical bone properties from CT data that captures the

physiological heterogeneity in a subject's bone is presented. In addition, the optimal level of heterogeneity required to minimize computational effort and generate an accurate solution was determined using an objective criteria.

1.4 Modeling physiologically representative loading conditions

Correctly modeling physiologically representative loads in the knee joint is time consuming because of the numerous forces that must be represented. The majority of FE bone models have simplified load representations of daily activities to reduce the computational problem and ease interpretation of the results; the resulting strain values were considerably larger than those measured *in vivo* in humans (Polgar et al., 2003). Muscle forces are nearly always neglected in subject-specific FE models and may reduce the clinical impact of such models since realistic modeling of muscle forces is essential to predict physiological strains (Duda et al., 1997).

A physiological representation of loading conditions in the knee joint requires incorporation of tibiofemoral joint compression, patellofemoral compression, and muscle and ligament forces. All three of these components have been either simplified or neglected in FE models because they are difficult to incorporate. There are several reasons for this. First, the exact physiological forces produced during daily activities are not known with certainty (Polgar et al., 2003). Obtaining such data *in vivo* in humans can be quite invasive and therefore most of the information is estimated from musculoskeletal models. These mathematical models, containing pre-defined muscle and ligament attachments, have been used to predict joint compression and muscle and ligament forces produced during gait (Brand et al., 1986; Anderson and Pandy, 2003).

The second problem is, even with the knowledge of joint and muscle forces, it is not known with certainty where to place these forces in the FE model. Subject-specific models do not come with pre-defined muscle attachments, therefore the

exact placement location of these forces within the joint is uncertain. Joint and soft tissue forces generally do not originate at bony landmarks and, therefore, the anatomical geometry itself does not provide enough information to place the forces. Attachment sites of muscles and ligaments can be estimated using data from literature and anatomical texts (Duda et al., 1996; Brand et al., 1986; Kepple et al., 1998; Delp, 1990; Netter, 2002; Gray's Anatomy, 1973), but it is rather time-intensive to map these data to a model and therefore soft tissue forces are often neglected. Personalized muscle and ligament insertions are even more difficult to model since the CT data from which most models are constructed cannot be used to define soft tissue attachments.

A third problem is an uncertainty in representing the three components of physiological loading. Point loading is often used to simplify tibiofemoral and patellofemoral loading in FE models. However, experimental evidence has shown that tibiofemoral and patellofemoral compression produce non-uniform pressure distributions on the joint surface (Fukubayashi and Kurosawa, 1980; Ahmed et al., 1983). St. Venant's principle suggests that the effect of point loading may not affect stresses far enough away from the origin of loading. However, the femoral condyles are often a region of interest and its stress levels can be artificially increased from stress concentrations due to its proximity to the tibiofemoral point loads. This may have consequences in bone remodeling simulations where an overestimation of stress may lead to sites of potential bone resorption being overlooked. Soft tissues physiologically insert into the bones as bands and therefore their forces should be distributed over their insertion area. However, nearly all models have assumed soft tissue point loading. Aside from the method of insertion, the lines of action for soft tissue forces must also be defined. This requires knowledge of the insertion location of the opposite end of the soft tissues. This is equally difficult to define because such data is scarce in literature.

The complexity involved in representing physiological load conditions for any daily activity can be daunting and therefore such conditions are often neglected in favour of ease of modeling and computation. It is often assumed that such simplification will not greatly affect the conclusions that are drawn by such models (Duda et al., 1997). Whereas this may be acceptable for parametric analyses, such an approach is not suitable for clinical or subject-specific studies, where the accuracy of stress results is important in drawing conclusions. A technique to obtain personalized sets of loading conditions complementing the subject-specific geometry and material properties has not yet been achieved. This is representative of the difficulty involved in characterizing physiological loading. In Chapter 4 of this thesis, an adequate alternative for estimating loading conditions is provided by synthesizing experimental data from a variety of sources.

1.5 Meshing subject-specific finite element models

Although the meshing of subject-specific FE models is not influenced by physiological conditions, it is important to the internal consistency of the FE model and therefore is discussed briefly here. Subject-specific FE models should employ automated meshing because of the potentially numerous models that may be employed in cross-sectional studies. It is also necessary when the FE method is to be compatible with the times of clinical practice (Taddei et al., 2006). The geometric complexity of knee bones may lend itself to ill-conditioned meshes that may potentially compromise stress predictions (Viceconti et al., 2004). Therefore, the adequacy of the mesh in each FE model should be confirmed using a convergence analysis. This is particularly important for subject-specific FE models since confidence is needed in stress predictions when models are used to generate results for use in diagnostic or treatment decisions.

Adequate parameters for meshing geometries of the femur and tibia have been previously established (Au et al., 2005). FE models of the femur and tibia can provide converged solutions when meshed with 10-node tetrahedral elements that

are at least 2 mm in size. Consequently, all models used in this thesis have been meshed using these elements via an automatic mesh generator.

1.6 Validating subject-specific finite element models

Validation is necessary for all FE models to gauge how well a simulation predicts reality. This is sometimes neglected in FE studies and therefore the conclusions drawn in such studies become severely restricted, even in cases where generic models are used for parametric analyses. For subject-specific modeling, it is obviously extremely important to develop a model that can properly mimic the physiological situation when drawing conclusions for clinical applications. Constructing a subject-specific FE model involves approximating the geometry, material properties and loading conditions in the knee joint of a particular individual. Whereas assumptions are necessary due to the inherent complexities of the physiological situation, the ultimate determination of their appropriateness comes from comparison of the FE model with experimental data. However, validating a subject-specific FE model using *in vivo* experimental data is nearly impossible. Therefore, *in vitro* experimental data are often used as a substitute. If the model compares well with the *in vitro* data, it is assumed that it can be used to predict *in vivo* situations under similar circumstances. Subject-specific FE models of the proximal femur can accurately predict stresses in human bones under simple load cases (Taddei et al., 2006). It is reasonable to assume such a method can be extended to the distal femur and proximal tibia, however no subject-specific FE models of the distal femur or proximal tibia have currently been reported.

Validation of femur and tibia FE models is most often accomplished by simulating a physiological situation using a materials testing machine. However, the physiological situation is frequently simplified to purely axial compression, bending, or torsion under load levels observed clinically. Displacements and strains of the bones are measured and compared with predictions generated from the FE model under similar loading. The FE models are constructed from CT

images of the bones obtained prior to testing. Cadaveric bones are the most relevant system to be used for experimentation but they are difficult to obtain and often composite or animal bones are used as surrogate models (Gray et al., 2007).

While the validation procedure seems quite straightforward, replicating the experiment in the FE simulation can be quite difficult, due to the complex geometry of the bones. In Chapter 5 of this thesis, a preliminary validation of the subject-specific technique was conducted using composite bone models. Confounding factors that may cause discrepancy between experimental results and the numerical predictions were examined in detail.

1.7 Objectives of Thesis

The overall objective of the thesis was to create a comprehensive framework that could be used to generate subject-specific finite element models of the femur and tibia from CT images. The framework needed to encompass four interlinked aspects of FE model creation: generation of 3-D geometry, application of bone tissue properties, incorporation of physiological loading conditions, and validation.

A method was needed to rapidly and accurately construct subject-specific geometry from CT scans of composite, animal and human bones. The technique needed enough flexibility to model the irregular geometry of the tibia and, in particular, the bifurcating region of the femur. It also needed to accurately represent the cortical thickness. The algorithms involved were required to interface with the material properties algorithm and the CAD software.

A technique was needed to interpret both mechanical properties and density distribution from CT images. Orthotropic tissue properties were to be calculated directly from the attenuation values of the CT images. The distribution of bone density needed to be captured in a manner which was computationally efficient. A specific requirement was to consider cortical and cancellous bones as separate

entities throughout the modeling procedure. The procedure must not require more than 1 day of user time and the material properties must be properly modeled to generate accurate stresses (< 5% error). The algorithms involved needed to interface with FE software.

A technique was also needed to map physiological attachment areas of muscles and ligaments to the FE models. Muscle and ligament lines of action associated with functional activities such as gait needed to be determined. The technique required interaction with CAD software. An algorithm was needed to apply the soft tissue force vectors and complementary non-uniform tibiofemoral and patellofemoral forces to the FE models, therefore it needed to interface with FE software.

Several stages of validation were needed to ensure that the resulting models were representative of reality. Geometry needed to be validated using experimentally obtained surface data. Surface strains in the FE models also needed to be similar to those generated in mechanically loaded specimens.

1.8 Scope of Thesis

The modeling framework presented in this thesis was developed for subject-specific modeling of the femur and tibia. Although the approach could possibly apply to other bones, none of these possibilities was investigated in this study. The framework was comprehensive in that it considered geometry, material properties and loading conditions together during model construction. However, each aspect was modeled using separate and distinct algorithms. The surface geometries were rapidly constructed using this technique, but the construction process was not automated and substantial user input was needed during CAD surface generation. A limited number of human subjects were used for demonstration purposes and composite bones were used to obtain a sense of findings for generic systems.

Analysis of bone heterogeneity was performed using the region split and merge image processing technique. While there may be other image processing techniques that may be equally applicable for material property analysis, the region split and merge was deemed suitable for the objective. Other image processing techniques were not investigated and are outside the scope of this thesis. Only one implementation of the region split and merge technique was used to analyze bone heterogeneity. This thesis focused on a *methodology* of creating a subject-specific FE models and therefore technical efficiencies (e.g. computational efficiencies, adaptive meshing) of the image processing and FE methods were not the main focus in the development of this tool.

The loading conditions applied to the subject-specific FE model were obtained entirely from outside sources, although a personal interpretation of that data was applied to our FE models.

The validation of the subject-specific technique is only preliminary in nature. Cadaveric bones were not used for validation because the thesis was mainly focused on the intensive task of developing a comprehensive framework. The preliminary validation employed a comparison of measured and predicted data for composite bones based on an order of magnitude analysis. Strictly speaking, this process of testing whether the model is representative of physical reality is better described as "verification" rather than "validation". Validity of a model is the precision by which the entity of mathematical descriptions of structural aspects (loading, geometry, material properties, boundary and interface conditions) mimics the real structure. The validity must be assessed by experimental verification (Huiskes and Chao, 1983). However, in finite element modeling literature, validation is frequently is used interchangeably with verification and is also done so in this thesis for ease of communication. To further clarify another term commonly used in the FE method: "accuracy" is the precision by which the FE mesh can approximate the exact solution for the model and is checked with a convergency test (Huiskes and Chao, 1983).

The suitability of the technique was frequently evaluated using von Mises stresses. Von Mises stress is a nominal stress magnitude that represents only the applied stresses that cause distortion. Strictly speaking, the scalar von Mises stress may not be the most suitable measure of mechanical stress for situations in which knowledge of stress direction is of particular importance. In such cases, a combination of principal, von Mises, and normal stresses can provide a more complete sense of the stress state. The FE models constructed in this thesis were not used to examine any situations where stress direction was crucially important. Therefore, a scalar measure such as von Mises stresses was used to provide a simple comparison of stress states across the different FE models, with the overall purpose of establishing a general sense of the acceptability of each technique.

A variety of techniques were introduced in this thesis to provide a more sophisticated modeling of geometry, material properties and loading conditions, but the resulting models were not meant to address a particular clinical or research question. Depending on the question that the FE model is being used to answer, it may not be necessary to implement all levels of sophistication into a particular model. Although the techniques were presented under a framework umbrella, most of the techniques can be used in isolation to improve a particular aspect of a FE model. The goal of this thesis was to provide a road map and related methodology to tackle any problems desired using a subject-specific FE model.

1.9 Outline of Thesis Chapters

This thesis presented in 'Mixed-Paper' format. Two of the body chapters have been published; the other three body chapters have been written as papers and will be submitted for publication in peer reviewed journals. Each of the chapters discusses an aspect that is needed to generate a comprehensive subject-specific finite element model. In Chapter 2, a method of constructing three-dimensional subject-specific knee bone geometry from computed tomography (CT) images is presented. In Chapter 3, the interpretation of mechanical properties of knee bone

tissue from CT images is discussed. A method to capture and represent regions of similar bone density in the knee is presented. In Chapter 4, a method of representing the complex physiological loading generated by ligaments and muscles surrounding the knee is presented. The method shows how synthesizing data from various sources can result in a comprehensive representation of physiological gait in FE knee models. In Chapter 5, the subject-specific modeling technique is validated with experimental data. In Chapter 6, a potential application of FE knee bone models is shown. A tibia FE model is used to show how slight alterations in the design of current total knee replacement implants can potentially improve bone health in the tibia.

References

Ahmed, A. M., Burke, D. L., Yu, A., 1983. In-vitro measurement of static pressure distribution in synovial joints – Part II: Retropatellar surface. Transactions of the ASME: Journal of Biomechanical Engineering 105, 226-236.

Anderson, F. C., Pandy, M. G., 2003. Individual muscle contributions to support in normal walking. Gait and Posture 17, 159-169.

Ashman, R. B., Rho, J. Y., Turner, C. H., 1989. Anatomical variation of orthotropic elastic moduli of the proximal human tibia. Journal of Biomechanics 22, 895-900.

Askew, M. J., Lewis, J. L., 1981. Analysis of model variables and fixation post length effects on stresses around a prosthesis in the proximal tibia. Transactions of ASME, Journal of Biomechanical Engineering 103, 239-245.

Au, A. G., Liggins, A. B., Raso, V. J., Amirfazli, A., 2005. A parametric analysis of fixation post shape in tibial knee prostheses. Medical Engineering and Physics 27, 123-34.

Brand, R. A., Pedersen, D. R., Friederich, J. A., 1986. The sensitivity of muscle force predictions to changes in physiologic cross-sectional area. Journal of Biomechanics 19, 589-596.

Brekelmans, W. A. M., Poort, H. W., Slooff, T. J. J. H., 1972. A new method to analyse the mechanical behaviour of skeletal parts. Acta Orthopaedica Scandinavica 43, 301-317.

Carter, D. R., Hayes, W. C., 1977. The compressive behavior of bone as a two-phase porous structure. Journal of Bone and Joint Surgery [Am] 59-A, 954-962.

Carter, D. R., Spengler, D. M., 1978. Mechanical properties and composition of cortical bone. Clinical Orthopaedics and Related Research 135, 192-217.

Ciarelli, M.J., Goldstein, S.A., Kuhn, J.L., Cody, D.D., Brown, M.B., 1991. Evaluation of orthogonal mechanical properties and density of human trabecular bone from the major metaphyseal regions with materials testing and computed tomography. Journal of Orthopaedic Research 9, 674-682.

Coleman, J. C., Roberts, M. D., Maender, C. M., Hart, R. T., 2000. Solid Model Creation from CT Image Data, Technical Report TU-BONE-2000-03, Tulane University.

Delp, S. L., 1990. A computer-graphics system to analyze and design musculoskeletal reconstructions of the lower limb. Ph.D. thesis, Stanford University, Stanford, CA, USA.

Douglas, T., Solomonidis, S., Sandham, W., Spence W., 2002. Ultrasound imaging in lower limb prosthetics. IEEE Transactions on Neural Systems and Rehabilitation Engineering 10, 11-21.

Duda, G. N., Brand, D., Freitag, S., Lierse, W., Schneider, E., 1996. Variability of femoral muscle attachments. Journal of Biomechanics 29, 1185-1190.

Duda, G. N., Schneider, E., Chao, E. Y. S., 1997. Internal forces and moments in the femur during walking. Journal of Biomechanics 30, 933-941.

Fukubayashi, T., Kurosawa, H., 1980. The contact area and pressure distribution pattern of the knee. Acta Orthopaedica Scandinavica 51, 871-879.

Gibson, L. J., 1985. The mechanical behaviour of cancellous bone. Journal of Biomechanics 18, 317-328.

Goldstein, S. A., Wilson, D. L., Sonstegard, D. A., Matthews, L. S., 1983. The mechanical properties of human tibial trabecular bone as a function of metaphyseal location. Journal of Biomechanics 16, 965-969.

Gray's Anatomy, 1973, 29th American ed., edited by Goss, C.M. Lea and Febiger, Philadelphia, PA.

Gray, H. A., Zavatsky, A. B., Taddei, F., Cristofolini, L., Gill, H. S., 2007. Experimental validation of a finite element model of a composite tibia. Proceedings of the Institution of Mechanical Engineers (Part H) 221, 315-324.

Harrigan, T. P., Jasty, M., Mann, R. W., Harris, W. H., 1988. Limitations of the continuum assumption in cancellous bone. Journal of Biomechanics 21, 269-275.

Hicks, C. A., Noble, P., Tullos, H., 1995. The anatomy of the tibial intramedullary canal. Clinical Orthopaedics 321, 111-116.

Huiskes, R., Janssen, J. D., Slooff, T. J., 1981. A detailed comparison of experimental and theoretical stress-analyses of a human femur. Proceedings of the joint ASME-ASCE applied mechanics, fluids engineering and bioengineering conference AMD, 211-234.

Huiskes, R., Chao, E. Y. S., 1983. A survey of finite element analysis in orthopaedic biomechanics: the first decade. Journal of Biomechanics 16, 385-409.

Keller, T. S., 1994. Predicting the compressive mechanical behavior of bone. Journal of Biomechanics 27, 1159-1168.

Kepple, T. M., Sommer, H. J., Lohmann Siegel, K., Stanhope, S. J., 1998. A three-dimensional musculoskeletal database for the lower extremities. Journal of Biomechanics 31, 77-80.

Keyak, J., Meagher, J., Skinner, H., Mote, C., 1990. Automated three-dimensional finite element modelling of bone: a new method. Journal of Biomedical Engineering 12, 389-397.

Keyak, J.H., Fourkas, M.G., Meagher, J.M., Skinner, H.B., 1993. Validation of an automated method of three-dimensional finite element modelling of bone. Journal of Biomedical Engineering 15, 505-509.

Keyak, J. H., Lee, I. Y., Skinner, H. B., 1994. Correlations between orthogonal mechanical properties and density of trabecular bone: Use of different densitometric measures. Journal of Biomedical Materials Research 28, 1329-1336.

Keyak, J. H., Rossi, S. A., 2000. Prediction of femoral fracture load using finite element models: an examination of stress- and strain-based failure theories. Journal of Biomechanics 33, 209-214.

Kopperdahl, D. L., Roberts, A. D., Keaveny, T. M., 1999. Localized damage in vertebral bone is most detrimental in regions of high strain energy density. Journal of Biomechanics 121, 622-628.

Lengsfeld, M., Schmitt, J., Alter, P., Kaminsky, J., Leppek, R., 1998. Comparison of geometry-based and CT voxel-based finite element modelling and experimental validation. Medical Engineering and Physics 20, 512-522.

Li, G., Gil, J., Kanamori, A., Woo, S., 1999. A validated three-dimensional computational model of a human knee joint. Transactions of the ASME: Journal of Biomechanical Engineering 121, 657-662.

Marks, L. W., Gardner, T. N., 1993. The use of strain energy as a convergence criterion in the finite element modelling of bone and the effect of model geometry on stress convergence, Journal of Biomedical Engineering 15 , 474-476.

Miyoshi, S., Takahashi, T., Ohtani, M., Yamamoto, H., Kameyama, K., 2002. Analysis of the shape of the tibial tray in total knee arthroplasty using a three dimension finite element model. Clinical Biomechanics 17, 521-525.

Netter, F. H., 2002. Atlas of Human Anatomy, 3rd ed., ICON Learning Systems, Teterboro, NJ.

Noble, P. C., Alexander, J. W., Lindahl, L. J., Yew, D. T., Granberry, W. M., Tullos, H. S., 1988. The anatomic basis of femoral component design. Clinical Orthopaedics 235, 148-165.

Noble, P. C., Box, G. G., Kamaric, E., Fink, M. J., Alexander, J. W., Tullos, H. S., 1995. The effect of aging on the shape of the proximal femur. Clinical Orthopaedics 316, 31-44.

Pena, E., Calvo, B., Martínez, M. A., Palanca, D., Doblare, M., 2005. Finite element analysis of the effect of meniscal tears and meniscectomies on human knee biomechanics. Clinical Biomechanics 20, 498-507.

Peng, L., Bai, J., Zeng, X., Zhou, Y., 2006. Comparison of isotropic and orthotropic material property assignments on femoral finite element models under two loading conditions. Medical Engineering and Physics 28, 227-233.

Polgar, K., Gill, H. S., Viceconti, M., Murray, D. W., O'Connor, J. J., 2003. Development and numerical validation of a finite element model of the muscle standardized femur. Proceedings of the Institution of Mechanical Engineers (Part H) 217, 165-172.

Reilly, D. T., Burstein, A. H., 1975. The elastic and ultimate properties of compact bone tissue. Journal of Biomechanics 8, 393-405.

Rho, J. Y., 1992. Mechanical properties of cortical and cancellous bone. Ph.D. thesis, University of Texas Southwestern Medical Center, Dallas, TX, USA.

Rho, J.Y., Hobatho, M.C., Ashman, R.B., 1995. Relations of mechanical properties to density and CT numbers in human bone. Medical Engineering and Physics 17, 347-355.

Rice, J. C., Cowin, S. C., Bowman, J. A., 1988. On the dependence of the elasticity and strength of cancellous bone on apparent density. Journal of Biomechanics 21, 155-168.

Sugano, N., Noble, P. C., Kamaric, E., Salama, J. K., Ochi, T., Tullos, H. S., 1998. The morphology of the femur in developmental dysplasia of the hip. Journal of Bone and Joint Surgery [Br] 80, 711-719.

Suggs, J., Wang, C., Li, G., 2003. The effect of graft stiffness on knee joint biomechanics after ACL reconstruction - a 3D computational simulation. Clinical Biomechanics 18, 35-43.

Sutherland, A. G., D'Arcy, S., Smart, D., Ashcroft, G. P., 1999. Abductor weakness and stresses around acetabular components of total hip arthroplasty: a finite element analysis. International Orthopaedics 25, 275-278.

Taddei, F., Viceconti, M.., Manfrini, M., Toni, A., 2002. Growth and remodelling of the autologous bone transplant used in a pediatric femoral reconstruction. Proceedings of the Institute of Mechanical Engineers (Part H) 216, 95-104.

Taddei, F., Viceconti, M., Manfrini, M., Toni, A., 2003. Mechanical strength of paediatric oncology: a finite element study. Proceedings of the Institution of Mechanical Engineers (Part H) 217, 111-119.

Taddei, F., Pancanti, A., Viceconti, M., 2004. An improved method for the automatic mapping of computed tomography numbers onto finite element models. Medical Engineering and Physics 26, 61-69.

Taddei, F., Cristofolini, L., Martelli, S., Gill, H.S., Viceconti, M., 2006. Subject-specific finite element models of long bones: an in vitro evaluation of the overall accuracy, Journal of Biomechanics 39, 2457-2467.

Taddei, F., Schileo, E., Helgason, B., Cristofolini, L., Viceconti, M., 2007. The material mapping strategy influences the accuracy of CT-based finite element models of bones: An evaluation against experimental measurements. Medical Engineering and Physics 29, 973-979.

Testi, D., Baruffaldi, F. V. M., Cappello, A., 1999. Risk of fracture in elderly patients: a new predictive index based on bone mineral density and finite element analysis. Computer Methods and Programs in Biomedicine 60, 23-33.

Testi, D., Zannoni, C., Cappello, A., Viceconti, M., 2001. Border-tracing algorithm implementation for the femoral geometry reconstruction, Computer Methods and Programs in Biomedicine 65, 175-182.

Van Buskirk, W. C., Ashman, R. B., 1981. The elastic moduli of bone. Proceedings of the joint ASME-ASCE applied mechanics, fluids engineering and bioengineering conference AMD, 211-234.

Viceconti, M., Zannoni, C., Pierotti, L., 1998. TRI2SOLID: an application of reverse engineering methods to the creation of CAD models of bone segments. Computer Methods and Programs in Biomedicine 56, 211-220.

Viceconti, M., Zannoni, C., Testi, D., Cappello, A., 1999. CT data sets surface extraction for biomechanical modeling of long bones. Computer Methods and Programs in Biomedicine 59, 159-166.

Viceconti, M., Davinelli, M., Taddei, F., Cappello, A., 2004. Automatic generation of accurate subject-specific bone finite element models to be used in clinical studies. Journal of Biomechanics 37, 1597-1605.

Chapter 2: A NURBS-based technique for subject-specific construction of knee bone geometry*

2.1 Introduction

Advances in our understanding of knee pathologies come from a combination of physical experimentation, clinical observation, and computer modeling. One particularly effective application of computer modeling is finite element (FE) analysis of total knee replacements (TKR), where they have highlighted the importance of stress shielding in aseptic implant loosening (Dawson and Bartel, 1992; Rakotomanana et al., 1992; Tissakht et al., 1996; Taylor et al., 1998; Van Loon et al., 1999). FE TKR implant design studies have frequently employed generic knee models (Eibeck et al., 1979; Beaupre et al., 1986; Lewis et al., 1998; Iesaka et al., 2002). Although this approach is valid for answering general biomechanics questions, it can be envisaged that additional clinical and research benefits can be obtained by models tailored to specific individuals. Such subject-specific models offer the possibility of customized TKR implants for individuals presenting a higher risk for implant failure due to ageing, illness or anatomical deformities. They can also be used to provide support for interpretation of clinical results in follow-up studies of populations with large inter-subject variability (Taddei et al., 2006). Advances in subject-specific modeling have mostly been directed toward the proximal femur (Taddei et al., 2006; Lengsfeld et al., 1998) thus additional efforts are needed for modeling of the distal femur and proximal tibia.

Subject-specific bone geometries have been created using data from magnetic resonance imaging (MRI) (Li et al., 1999) and ultrasound (Douglas et al., 2002), but at present computed tomography (CT) represents the best source from which to create these models (Taddei et al., 2006). Subject-specific modeling requires that geometries be constructed both accurately and rapidly. Models need to be

* A version of this chapter has been published in Au et al., 2008. Computer Methods and Programs in Biomedicine 92, 20-34.

reconstructed rapidly to be compatible with clinical practice times and for cases where analyses are conducted on a large population (Taddei et al., 2006).

Periosteal surfaces can generally be constructed from CT images using either voxel meshing or non-uniform rational B-splines (NURBS). By requiring minimal user intervention, the voxel mesh technique has been adapted by commercially available software for rapid construction of surface geometries. However, jagged surfaces often associated with voxel meshed bone models are known to compromise the accuracy of the predicted stresses during FE analysis (Keyak et al., 1990; Marks and Gardner, 1993; Viceconti et al., 1998b). Alternatively, geometries can be constructed by fitting NURBS surfaces to contours extracted from CT images using border tracing algorithms. NURBS surfaces can be constructed via computationally intensive processes such as creating tiled surfaces using a Delaunay triangulation algorithm and subsequently reverse-engineering the NURBS surface (Taddei et al., 2006). A more rapid operation is "skinning" but it cannot adequately handle the bifurcation of human femoral condyles, making construction of the distal femur challenging and time-consuming (Viceconti et al., 1998a).

Another challenge for current subject-specific construction techniques is representing the geometrical distinction between cortical and cancellous bone (Taddei et al., 2006; Lengsfeld et al., 1998). A major reason is poorly contrasted CT images frequently obtained from hip and knee replacement candidates (Taddei et al., 2006). Poor contrast at the endosteal interface may result from extremely thin cortical bone inadequately captured due to poor image resolution (Prevhral et al., 1999). In such cases, voxel mesh techniques cannot distinguish between cortical and cancellous bone due to their reliance on a single threshold attenuation value (Lengsfeld et al., 1998). Generic NURBS-based femur models have frequently identified the endosteum manually (Tissakht et al., 1996; Taylor et al., 1998; Askew and Lewis, 1981). However, when measuring from intensity-based CT images, this is an inaccurate technique (Testi et al., 2001), particularly for

extremely thin cortical bone (Prevhral et al., 1999; Anderson et al., 2005), and is too cumbersome for use in subject-specific modeling.

Automated border extraction techniques employing binary image thresholding (Coleman et al., 2000; Miyoshi et al., 2002), local pixel intensity analysis (Testi et al., 2001), and conjugated gradient algorithms (Viceconti et al., 1998a) have been proposed. Binary thresholding techniques are ineffective for contour extraction from poorly contrasted images due to their reliance on entire image contrast (Testi et al., 2001), a problem similarly faced by voxel mesh techniques. In the epiphysis, the large variability in bone densities creates numerous gradients, which obscures the endosteum. Consequently, current conjugate gradient-based tracing algorithms may not be entirely effective. Local pixel intensity analysis varies in accuracy and repeatability (Testi et al., 2001), possibly because in poorly contrasted images, contour attenuations and gradients may be difficult to identify. Thus, a current challenge in constructing subject-specific knee bone models is developing a more sophisticated interpretation of image data than the current techniques provide, particularly to identify the endosteum in poorly contrasted bone near the articulation, where the cortex is thin and less distinguishable from the cancellous bone.

This study focused on the development of subject-specific knee bone models from a geometry construction perspective. A technique for constructing the knee bones from CT images was introduced, with specific focus on edge detection strategies for periosteal and endosteal bone surfaces. A NURBS technique of surface construction using a CAD package was described, with a proposed solution to the femoral condyle bifurcation problem. A novel technique was introduced to accurately construct endosteal surfaces. Models were constructed for bovine, composite, and *in vivo* human bones, with validation of this technique using the former two bones. This new NURBS-based technique was compared with a voxel mesh-based technique.

2.2 Methods

Two human, 4 bovine and 2 composite knee bones were used to provide different levels of assessment for the techniques described herein. *In vivo* CT scans of the left knee of a 47-year-old male were used to replicate a clinical situation. The male subject had a normal asymptomatic knee and was not a prospective TKA patient; both the femur and tibia of this subject were examined in this study. The SOMSO-plast composite bones were similar to product #5158 from Sawbones (Pacific Research Labs, Vashon Island, WA). The bovine and composite human bones were used to verify the proposed construction technique as obviously access to various physical dimensions (i.e. cortical bone thickness, periosteum, etc.) of the *in vivo* human subject was not possible. Bovine bones were used because they contained soft tissue and presented a bone density variation similar to humans (Hodgskinson and Currey, 1992). The endosteal surface was validated using these bones since their endosteal interfaces better represented the clinical situation than the composite bones. Validity of the periosteal surface construction technique was primarily verified using composite bones, which closely matched human anatomy.

A GE Lightspeed 16 CT scanner (General Electric, Fairfield, CT) was used to scan the human subject. CT scans of the SOMSO-plast composite and the bovine bones were obtained from a second scanner (Somatom Sensation 64, Siemens AG, Munich, Germany) as the first CT machine was no longer available; using a second CT machine also provided information about sensitivities of the proposed technique to various machines. Image specifications can be found in Table 2.1. For composite and bovine bones, a slice of thickness of 0.6 mm could not be obtained with the CT scanner therefore 1 mm thick slices were overlapped at 0.4 mm to obtain CT information 0.6 mm apart; slice overlap was applied to CT images of the human subject for similar reasons.

Voxel mesh models were constructed using a commercial software package (ScanIP, Simpleware, Exeter, UK). A sequence of non-smoothed transverse-

plane CT images was imported into the program and the cortical bone in each image was identified by manually defining a range of grayscale values based on visual inspection. Each CT slice was individually edited to remove extraneous voxels not associated with the bone. The resulting series of 2-D masks was used to automatically generate a 3-D voxel-based mesh with an exterior tetrahedral surface through Simpleware's proprietary technique. Voxel sizes for each model are summarized in Table 2.1.

A second set of models was constructed using a semi-automatic subject-specific (SASS) technique, which combined semi-automated edge extraction with surface generation. Edge extraction operations, described below, were performed by modules written in MATLAB 6.1 (Mathworks, Natick, MA). Each operation was performed automatically with minimal user intervention where described.

2.2.1 Edge Extraction

Sharp attenuation differences at the interface of the cortical and cancellous bones can be highlighted by calculating attenuation gradients. A Sobel gradient operator was used to perform a 2-D spatial gradient measurement on the attenuation-based CT images to emphasize the regions of high spatial gradient inherent in edges. Gradient-based images were obtained by applying a pair of 3x3 pixel masks to the native CT images, resulting in areas of strong gradient appearing in white. Noise can greatly affect the results of gradient-based edge detection by introducing artificial gradients and therefore needs to be removed from the image beforehand (Parker, 1997). Each CT image was smoothed using a Gaussian operator (σ=2.0) to reduce image noise. Smoothed data was only used with the SASS technique and not the voxel mesh technique since the voxel mesh technique relied on intensity-based images. Prior to tracing bone contours, a thresholding process was used to improve extraction of the periosteal interface. The threshold value was selected from an attenuation histogram of the CT image, which contained a characteristic peak resulting from the high frequency of cancellous bone pixels

(Fig 2.1). Thresholding above this attenuation value removed soft tissue from the image and isolated the bone.

The periosteal interface was defined by tracing the outer ring of the bone in the resulting image (Fig 2.2). Within the context of the gradient-operated image, the term "gradient value" refers to its pixel value/intensity. The trace began with the gradient-tracing algorithm locating the strongest gradient value within a localized region of the outer ring selected by the user. Starting from this initial pixel, the algorithm automatically searched for the pixel with the strongest gradient value in the counter-clockwise direction. Pixels were tracked until the starting point was reached again. The output was an array containing an ordered sequence of pixel coordinates defining the closed periosteum contour. The initial pixel location does not significantly affect the result of the contour trace as found through a sensitivity analysis.

The inner ring in epiphyseal bone was often not clearly defined since the attenuation change between cortical and cancellous bone was more subtle (Fig 2.2), therefore, the above tracing operation was not used to extract the endosteum. A more effective method was to analyze a line of pixels intersecting the endosteal interface region to identify certain features. The line (i.e. PATH, see Fig 2.2) originated from a periosteal interface pixel and was oriented in the principal gradient direction. A typical profile of the attenuations and gradients along PATH can be seen in Fig 2.3. The attenuation peak was first identified to locate the mid-cortex and then the gradient peak to its right was used to locate the endosteal interface point. A single endosteal point was defined for each originating periosteal point, producing an unchained ring of points.

The pixel coordinates obtained from the above procedure were only an intermediate step to fully defining the periosteal and endosteal contours. For each slice, the periosteal interface points were fitted by a series of interconnected cubic least-square splines to produce a single smooth curve (see Appendix A). The

original points were abandoned once the smooth curve was generated. One smooth endosteal curve was generated per CT slice by applying the same process to each set of endosteal interface points. Application of this technique to all CT slices produces two sets of smooth curves for periosteal and endosteal surfaces (Fig 2.4).

All edge extraction operations were performed automatically using MATLAB algorithms developed in-house. Manual inputs necessary for each edge extraction operation (e.g. initial pixel region) were defined in a shell module at the beginning of the analysis. The shell module called each of the edge extraction operation functions (from smoothing to spline-fitting) in successive order.

2.2.2 Periosteum and Endosteum Construction

The entire sets of smooth periosteal and endosteal curves were exported to a CAD package (Pro/Engineer, PTC, Needham, MA) for construction of 3-D surfaces. A single surface bounded the entire set of periosteal curves under a boundary blend (skinning) operation. Construction of a surface solely from transverse plane curves had two drawbacks. First, the highly curved surface of the femoral condyles was not sufficiently captured. Second, the bifurcation of the femoral condyles could not be constructed without creating an artificial connecting curve to join the condyles to the shaft (Viceconti et al., 1998a). A more effective method of capturing the condyles was to generate a second surface based on curves extracted from sagittal CT images and combining it with the transverse surface using a transition surface (Fig 2.5a). Sagittal images were processed in an identical manner to the transverse images; registration using Digital Imaging and Communications in Medicine (DICOM) header information allowed the sagittal curves to properly overlap with the transverse curves. The process was repeated with endosteal curves to generate an endosteal surface. The completed model resulted in a periosteal surface fully enclosing an endosteal one. Composite and bovine bone surfaces were constructed from transverse and sagittal curves spaced 2.4 mm and 3.0 mm apart, respectively. Human bone surfaces were constructed

from transverse and sagittal curves spaced 3.0 mm and 1.0 mm apart, respectively.

2.2.3 Validation

2.2.3.1 Periosteal Surface Validation

Periosteal surfaces of the composite and bovine bones were compared with data obtained experimentally, using a coordinate measuring machine (CMM; Microval, Brown and Sharpe, North Kingstown, RI), and digitally, using 2 laser scanners. The CMM was used to measure discrete surface coordinates on the composite and bovine bones along their diaphyses, metaphyses, and epiphyses. Using Pro/Engineer, each CMM point was digitized and overlapped with the surfaces constructed by the commercial and SASS techniques. A built-in function in Pro/Engineer was used to measure the normal distance between a CMM point and the closest point on the constructed surface, henceforth defined as error. The CMM data were assumed to be the gold standard for comparison.

The constructed surfaces of the bovine and composite bones were also compared with laser scan data. Bovine bones were scanned using a FARO digitizing arm (Creaform Inc., Levis, QC) with a precision of 15 microns. For access reasons, a second laser scanner (ShapeGrabber SG-100, ShapeGrabber, Ottawa, ON) with a precision of 70 microns was used for the composite bones. Similar to the above procedure, Pro/Engineer was used to overlap CMM points with the laser scanned surfaces for error analysis.

Ball bearings embedded in the bones were used as points of commonality between the physical and digital models to assist in aligning their two coordinate systems. The ball bearings were inserted into the animal and composite bones before CT scanning and their coordinates were subsequently measured using CMM. Alignment was performed by transforming the CMM coordinate system to the CAD coordinate system using the locations of 3 ball bearings. However, the construction process inherently produced a misalignment between the physical

and digital ball bearing locations, resulting in a mean alignment error of 0.388 mm (less than half the thickness of each CT slice). Alignment errors for each model can be found in Table 2.2.

2.2.3.2 Endosteal Surface Validation

To investigate the accuracy of the endosteum construction, physical slices of Bovine Femur 1 and Bovine Tibia 1 were compared with corresponding slices of the digital models. To allow comparison with their CT images, the bones were physically rotated and measured using CMM until their 3 ball bearing coordinates matched their corresponding CT location. Once correctly rotated, the orientation was fixed by encasing the bone in a wooden box using plaster and subsequently sliced. The femur and tibia were sliced transversely and sagittally, respectively, with a band saw (Diemaster 2, Lenox, East Longmeadow, MA). Each slice was photographed with a digital camera (D-70, Nikon, Tokyo, Japan) attached to a copy stand, which placed the focal plane of the camera parallel to that of the slice. An AF-Micro Nikkor 105 mm lens (Nikon, Tokyo, Japan) was used to reduce fish eye distortion in the image.

Cortical thickness measurements were estimated directly from these high-resolution (3008 x 2000 pixels) digital photos using ImageJ software (NIH, Bethesda, MD); these measurements were considered the baseline cortical thicknesses. The digital SASS and voxel mesh Bovine Femur 1 and Bovine Tibia 1 models were cut at the same locations as the bandsaw cuts and images of each slice were captured. Previously-obtained transverse and sagittal CT slices corresponding to the bandsaw cut locations were also used for comparison. For each slice, the 4 images (photo, SASS image, voxel mesh image, CT slice) were overlapped, rotated, and scaled for proper matching. Overlapping the 4 slices allowed the thickness to be measured at the same locations on the images. In each picture, the cortical thickness was measured at several locations (Fig 2.6a) and compared with corresponding measurements taken from CT, SASS model, and voxel mesh model slices.

2.2.4 Slice separation sensitivity

Using fewer 2D contours (see Fig 2.4) would reduce time and cost in constructing bone models. To determine whether the accuracy of a constructed surface was sensitive to the distance between slices (i.e. slice separation), the composite femur model was constructed using 5 different distances between each transverse curve (i.e. 0.6, 1.2, 1.8, 2.4, and 3.0 mm) and each sagittal curve (i.e. 1.0, 2.0, and 3.0 mm). Slice separation sensitivity in the Simpleware composite femur models was analyzed at 0.6 and 3.0 mm separations. Each model was compared with CMM data using the procedure described in Section 2.2.3. A two-tailed, unequal variance t-test was used to determine if there was any significant difference between the models; $p < 0.05$ was considered significant. It should be emphasized that slice separation, while related to slice thickness, was investigated as a separate parameter from thickness in this study.

2.3 Results

2.3.1 Construction Accuracy

The results of the comparison between the constructed surfaces and the CMM data are summarized in Table 2.2 and elaborated upon below. The standard of comparison was taken as the physical measurements obtained by CMM.

2.3.1.1 SASS technique for composite bones

The periosteal surfaces of the composite bones were constructed with a mean error of 0.369 mm over 213 observed locations (Table 2.2). The error was of the same order of magnitude as the pixel resolution (0.3125 mm/pixel) and an order of magnitude lower than the slice separation (2.4 mm). The largest errors in the composite femur model occurred at the epicondyles and intercondylar notch.

2.3.1.2 Voxel mesh technique for composite bones

The voxel mesh models of the composite bones displayed a mean error of 0.281 mm based on 218 locations. The mean error was of the same order of magnitude

as the pixel resolution (0.3125 mm/pixel) and slice separation (0.6 mm). The largest errors were observed at the posterior femoral condyles.

2.3.1.3 Laser scan technique for composite bones

The laser scanned composite bones had a mean error of 0.235 mm based on 215 surface points. The error was on the same order of magnitude as those observed from the other two techniques. The largest errors were in the femoral condyles.

2.3.1.4 SASS technique for bovine bones

Periosteal surface

The periosteal surfaces of the 4 constructed bovine bones had a mean error of 0.757 mm based on 417 observed locations. The mean error was on the same order of magnitude as the pixel resolutions and an order of magnitude lower than slice separation. The largest errors were observed at the patellar groove for all samples.

Endosteal surface (cortical thickness)

Bovine Femur 1 and Bovine Tibia 1 had a large range of thicknesses. To represent the thicker bone, 15 regions in the diaphyseal bone were measured (with thickness ranging from 5.6 mm to 37.8 mm as measured from the high-resolution digital photos). To represent the thinner bone, 34 locations in the metaphyseal and epiphyseal bone were measured (with thickness ranging from 0.8 mm to 6.3 mm as measured from the digital photos).

For the SASS models, the 15 measured diaphyseal bone locations were constructed with a mean error of 0.6 mm. The 34 metaphyseal/epiphyseal bone locations were constructed with a mean error of 1.2 mm. Spatial resolution is critical in the SASS construction technique as the technique operates in the gradient domain (see Section 2.4.3.1). The thicker cortical bone in the diaphyses was constructed from transverse CT images that had spatial resolutions of approximately 0.4 x 0.4 mm (Table 2.1). Therefore, the 0.6 mm average error

translates into approximately a 2 pixel error. The thinner cortical bone in the metaphyseal/epiphyseal regions of Bovine Femur and Tibia 1 was constructed from sagittal CT images, where the image resolutions were 0.8242 x 0.8242 mm (Table 2.1). Although the physical error was larger in the metaphyseal/epiphyseal region (i.e. 1.2 mm), it translated into approximately a 2 pixel error. The large sagittal plane pixels limited the ability to extract the cortex with greater accuracy.

When considering all 49 measurement locations together, the endosteal surfaces were constructed with a mean error of 1.0 mm. The largest errors were observed in the epiphyseal bone where the cortex was particularly thin.

2.3.1.5 Voxel mesh technique for bovine bones

Periosteal surface

The periosteal surfaces of the 4 voxel mesh bovine models were constructed with a mean error of 0.557 mm based on 461 locations, with the largest errors occurring at the patellar groove. The mean error was on the same order of magnitude as slice separation distance (0.6 mm) and pixel resolutions.

Endosteal surface (cortical thickness)

For the voxel mesh model, the 15 measured diaphyseal bone locations were constructed with an average error of 0.7 mm, which is approximately a 2 pixel length error. The thin cortical bone of the metaphyseal/epiphyseal regions could not be distinctly identified and therefore could not be constructed. As such, measurements at the remaining 34 endosteum observation points failed due to limitations of the commercial voxel mesh technique.

2.3.1.6 Laser scan technique for bovine bones

The 4 laser scanned bovine bones had a mean error of 0.668 mm based on 462 periosteal interface points. The mean error was on the same order of magnitude as those observed from the other two techniques and, in similar fashion, the

largest errors occurred at the patellar groove. Obviously, the laser scan technique could not be used for endosteal surface construction.

2.3.2 In vivo construction

The accuracy of the *in vivo* human knee construction could not be quantified directly since access to physical structures such as the periosteum and endosteum were not possible. The edge extraction and surface generation procedures for constructing the human knee were identical to those used in the composite and bovine bone constructions. Thus, validating the procedure using composite and bovine bones indirectly gauged the accuracy and validated the human knee construction.

In the SASS technique, the thresholding values used to remove the soft tissue from the human knee images were similar to those used for bovine bones, as expected. The inner ring was less evident than the outer ring, but using the proposed Path Analysis method was effective in identifying the endosteal interface. Several areas of thin cortical bone were evident where the profiles showed no gradient. For such locations, the interface was interpolated based on the cortical thickness of the surrounding bone (see Appendix A). For the voxel mesh models, the thin cortical bone required use of a lower grayscale threshold in defining the periosteal surface. Consequently, the endosteal surface could not be properly represented and the cortical thickness was grossly overestimated in some locations such as the epiphyseal bone (Fig 2.7c).

The constructed geometry of the *in vivo* knee appeared very similar to the composite knee and was much less complex than the bovine knees. The SASS surfaces were much smoother and more realistic than their commercial voxel mesh counterparts (Fig 2.5). Using CT images from different scanners did not require any of the construction techniques to be adjusted.

2.4 Discussion

The backbone of subject-specific modeling is the automated, accurate and rapid generation of models. Subject-specific modeling of the distal femur and proximal tibia, while of great interest and clinical relevance, has not been accurately performed due to the complex nature of the bones (Taddei et al., 2006). A particular complexity is the identification of the endosteal interface, a challenge further compounded where the cortex is very thin. However, accurate periosteal and endosteal surface construction is particularly important for bone property assignment in FE stress analysis.

This study focuses on the geometry construction of subject-specific knee bone models using NURBS- and voxel mesh-based techniques. These geometry models are the first step to FE-based stress analyses of the bones. While the FE modeling aspect of the models employed here is beyond the scope of this study, voxel-based FE analyses were briefly and necessarily mentioned due to the intricate link between voxel mesh geometry and voxel-based FE analysis. However, it should be noted that many FE analyses of the knee are not voxel-based, rather voxel-based FE approaches are only a subset of FE modeling. In fact, the SASS geometries are not intended for voxel-based FE analyses.

2.4.1 Construction Accuracy

The ultimate application of the SASS technique introduced in this study is for subject-specific modeling of human subjects in clinical and research settings. The *in vivo* model did not allow for direct validation and necessarily required that it be first validated indirectly with composite and bovine models. If the technique was found to be accurate for these two models, it could then reasonably be applied to human subjects with some confidence.

2.4.1.1 Periosteum identification (SASS technique)

Despite the complex 3-D curvatures existing in the composite and bovine bones, the SASS technique constructed the geometries of their periosteal surfaces to an

accuracy matching the order of magnitude of the in-plane CT image resolution. The observed errors compared well with acceptable errors found in other surface representations of composite femora (Testi et al., 2001; Viceconti et al., 1999).

The bovine bone surface constructions contained a larger amount of error compared to the composite bones (0.757 mm versus 0.372 mm). One explanation is that the bovine bones had considerably more complex geometry than the composite human bones, particularly in the patellar groove and articulating surface where the largest errors were observed. A second component to the overall larger error was that soft tissue was not completely removed from the bovine bones, therefore the CMM measurement may have been affected by a thin soft tissue layer remaining on the surface. The SASS technique ignored the soft tissue and constructed the bone surface directly.

Subject-specific modeling of the distal femur is challenging and has largely been ignored in current literature. The bifurcation of human femoral condyles makes the distal femur particularly challenging to construct with a skinning technique (Viceconti et al., 1998a) but this challenge can be overcome by constructing the bifurcating region using sagittal CT slices as in this study. Accuracy is not compromised using such a technique; the error in the composite femur periosteal surface constructed from sagittal curves was 0.364 mm, the same order of magnitude as the image resolution. However, using a purely sagittal-based surface to model the distal femur is not recommended as it is not as accurate as a transverse-based surface. For the composite femur, the metaphyseal and diaphyseal periosteum constructed from sagittal CT slices had twice the error of that constructed from transverse slices for identical locations (0.763 mm versus 0.339 mm, respectively). Combining transverse- and sagittal-based surfaces most accurately models the interface while overcoming the bifurcation problem (see Fig 2.5a).

The largest errors occurring in SASS constructed surfaces originated at locations with large surface curvatures, such as the patellar groove and articulating surfaces of the bovine femur. In constructing human anatomy, the intercondylar notch and epicondyles contained the largest errors (1.862 and 1.516 mm, respectively). These maximum errors are comparable to those seen in other studies (Testi et al., 2001). The errors may have origins in stair-step artifacts of the CT images, which are unique to helical CT, since it requires planar interpolation of helical projection data (Fleischmann et al., 2000). Artifacts associated with objects inclined relative to the table translation direction can occur because of aliasing and rotation effects of the scanning procedure (Wang et al., 1994). Curves in the frontal and sagittal planes would therefore be rendered as piece-wise steps. Such artifacts can be reduced by decreasing slice thickness, overlapping slices, and decreasing table increment (Wang et al., 1994), essentially making the piece-wise steps smaller and allowing improved modeling of highly curved surfaces.

2.4.1.2 Periosteum identification (voxel mesh technique)

Constructing the distal femur and proximal tibia adequately using a skinning operation is time-consuming (Viceconti et al., 1998a) and a voxel mesh technique can be a helpful alternative. Despite the jagged surfaces observed on the periosteal surfaces of the composite and bovine bones, often stated as a weakness of the voxel mesh technique when used with FE analysis (Keyak et al., 1990; Marks and Gardner, 1993; Viceconti et al., 1998b), the models were still geometrically accurate, with errors on the order of magnitude of the CT image resolution. It should be noted that the voxel elements (0.3125 x 0.3125 x 0.6 mm) used to create the models were more than 5 times smaller than those typically seen in other models (Lengsfeld et al., 1998; Keyak et al., 1990). As such, the results presented here may overestimate the accuracy that practical models may possess. Additionally, application of very fine voxels may be computationally costly when FE analyses are to be performed.

One of the disadvantages of the commercial technique is its reliance on CT slices from a single plane of view. Transverse plane data were used to construct the voxel mesh models as they had the best resolution and adequately captured the midshaft. Representation of the femoral condyles could be improved if they were segmented using independent data from sagittal plane images (rather than sagittal data reconstructed from the existing transverse plane data). The sagittal plane-based condyles could then be coupled with the transverse plane-based midshaft to form a superior voxel mesh model. This was not possible since the commercial software could not simultaneously import the sagittal plane data while transverse plane data were in session. The condyles of the voxel mesh model of the composite femur were therefore less accurate than the SASS model, with mean errors of the condyles being 0.570 mm and 0.390 mm, respectively. This was a statistically significant difference based on a two-tailed, unequal variance *t-test* with $p < 0.05$ considered significant. The larger error is partly due to construction exclusively from transverse CT slices, whose plane of view does not fully capture the large condylar curvature. The SASS technique segmented the shaft using transverse plane CT images and coupled it with segmentations of the condyles captured using independent sagittal plane CT images. Thus, SASS provides a unique capability of combining 2 different data sets to create a single more comprehensive geometric model.

2.4.1.3 Periosteum identification (laser scan technique)

Laser scanned models were employed in this study to present a non-diagnostic imaging point of comparison for the SASS and commercial software construction techniques. The mean errors of the laser scanned models were within one pixel length of the SASS and voxel mesh errors. Data are not available in literature comparing laser scanned long bones with experimentally obtained surface data, but errors between NURBS-based and laser scan composite femora models (Ploeg et al., 2004) are similar to those observed here.

The results of this study show that a variety of techniques can be used to construct the periosteal surface of the knee bones accurately but with varied effort levels. Construction using high precision instruments like laser scanners require extensive manual effort compared to CT- and MRI-based techniques. MRI has been used to construct periosteal surface models of the knee (Li et al., 1999; Pena et al., 2005) but the process does not appear to be automated and likely requires more effort compared to more automated techniques such as SASS and voxel meshing. Ultrasound, although a common clinical imaging technique, cannot be used to accurately construct bone surface models because it is strongly reflected by bone (Douglas et al., 2002; Pena et al., 2005).

2.4.1.4 Endosteum identification

Cortical bone provides support and stiffness to the overall bone structure and appropriate representation of its thickness and material properties is needed to generate representative internal stress distributions (Askew and Lewis, 1981). The cortex carries most of the load in a bone structure (Anderson et al., 2005) and its characterization in FE models can have substantial effects on stress magnitudes and distributions (Askew and Lewis, 1981; Au et al., 2005); its absence altogether in such models can result in underprediction of internal stresses in the cancellous bone since the structural stiffening provided by the cortex promotes load transfer (Askew and Lewis, 1981). Thus, proper modeling of the cortex is crucial in the design of TKR implants and for FE studies of internal stresses for bones in general (Au et al., 2005). For simplified cases where dense cortical bone can be easily distinguished from the surrounding cancellous bone, such as in the diaphysis, a variety of methods are available to effectively perform this task (Keyak et al., 1990; Viceconti et al., 1998a; Testi et al., 2001; Coleman et al., 2000; Miyoshi et al., 2002). Indeed, in this study, the endosteal surfaces of the diaphyses of Bovine Femur 1 and Bovine Tibia 1 were constructed using the SASS and voxel mesh techniques to within 2 pixel lengths. Notably, the commercial software could successfully apply a single global grayscale window to distinguish the cortical from cancellous bone.

A source of error in measuring cortical bone thickness was the inability to clearly distinguish the endosteal interface during visual inspection of the baseline photos. Cortical thickness was measured visually and some measurement error resulted from the blurred bony edges in the images. The poor contrast at the endosteum in some regions of the bone also contributed error.

However, the simple case of bovine bones is limited for clinical applications where frequent bone pathologies would degrade image contrast and the effectiveness of the above methods. Poorly contrasting CT images are not unexpected *in vivo* (Testi et al., 2001); even in the 47-year-old subject used in this study, several areas of poor contrast were present in the epiphyseal bone. The endosteal interface in such areas has traditionally been difficult to model, resulting in poor representation or omission of the surface (Lengsfeld et al., 1998; Keyak et al., 1990; Testi et al., 2001). This study is the first comprehensive examination of these difficult cases and a novel method is proposed to overcome the associated challenges.

Thresholding techniques for entire images do not allow for precise definition of the endosteal interface in the metaphyseal and epiphyseal regions because the large variation in cancellous bone attenuations overlap with those of cortical bone, thus no single attenuation value clearly distinguishes the two bone types. In applying a single grayscale value to identify cortical bone, the commercial software produced voxel mesh models which severely overestimated cortical thickness in areas like the condyles (Figs 2.6 and 2.7).

This problem can be partly addressed by analyzing image properties locally rather than globally. A more localized thresholding process for the voxel mesh method can be obtained by applying different grayscale windows at various transverse distances along the bone. Additionally, thresholding can be applied using sagittal and frontal view planes (reconstructed from the transverse plane) to further isolate

the cortex. However, the appropriateness of a particular threshold range is based on visual inspection; multiple thresholding applications lead to a very cumbersome construction process and the simplicity of the voxel mesh technique becomes lost, and model construction becomes subjective.

Locally analyzing attenuations alone may not be entirely effective due to the large local attenuation variations in epiphyseal cancellous bone. The SASS technique overcomes this limitation by applying a gradient operator to identify all the attenuation changes in each image. The Path Analysis provides the localized method needed to correctly identify the endosteum gradient among the myriad of other gradients resulting from the large bone density variability. Such an approach is effective: endosteum construction at the metaphyses and epiphyses produced considerably better results for the SASS than the voxel mesh technique (see Section 2.3.1.5). The SASS bovine models captured these regions with a mean error of 1.124 mm, an order of magnitude larger than the pixel resolution, and comparable to errors from endosteal surfaces constructed elsewhere (Testi et al., 2001).

The largest errors of the SASS models occurred at the epiphyseal bone, where the gradients were extremely weak. In such conditions, detection methods in literature and in this study may be ineffective. The SASS technique overcomes this problem by estimating the cortical thickness from the surrounding cortex, where detection was successful, and interpolating the endosteal interface (see Appendix A). This is a necessary step since a clearly defined endosteal curve is needed for surface generation.

Path Analysis offers a more sophisticated method of interpreting CT image data via local analyses of attenuation and gradient profiles. It accurately identified endosteal interfaces of both composite and bovine bones and can reasonably be assumed to do so for *in vivo* human subjects as well. In our human subject, endosteal interfaces detected by Path Analysis were qualitatively compared with

their corresponding CT images; interface points were observed in the expected location based on visual inspection. As Path Analysis is done in an automated environment, it offers to bring subject-specific FE knee models a step closer to clinical applications.

2.4.2 Computational Efficiency and Slice Separation Sensitivity

Subject-specific geometries, in addition to being accurate, must also be produced in a reasonable time frame. The times reported below were the total times required to construct the geometry, which combined the user times and computational times. One of the advantages of using a voxel mesh is the speed with which models can be created (Lengsfeld et al., 1998). A voxel mesh (0.3125 x 0.3125 x 0.6 mm) of the human femur required 4 hours to construct with the commercial software. Visual inspection was needed to determine the appropriate threshold range to represent the cortex, particularly the endosteum; ultimately, two threshold ranges were needed for proper segmentation. Approximately 3.5 hours of user time were necessary to eliminate extraneous pixels which did not belong to the model but were selected due to the threshold ranges. This required visual inspection for all 58 slices used to construct the human femur voxel mesh model. The voxel mesh model required a large amount of computer memory (~ 70 Mb) and larger voxels may be necessary to produce more clinically practical models for voxel-based FE modeling. In voxel meshed composite femur models, increasing the voxel height from 0.6 mm to a more typical 3.0 mm (Lengsfeld et al., 1998; Keyak et al., 1990) reduced construction time by 80%. The geometrical accuracy significantly decreased but remained at the same order of magnitude (Table 2.3). Particularly concerning is the increased jaggedness in the epiphyseal region from the larger voxels (Fig 2.8), which studies have contended may result in lack of stress convergence during finite element analysis (Marks and Gardner, 1993; Viceconti et al., 1998b). A smoothing algorithm supplied with the commercial software was applied to improve the surface (Camacho et al., 1997). However, this did not significantly improve the geometric accuracy nor the jaggedness for the composite femur constructed with 0.6 or 3.0 mm voxels (Fig

2.8 and Table 2.4). Thus, a smaller voxel size is recommended to avoid jagged surfaces, but will produce cumbersome models.

The SASS model of the human femur constructed using 0.6 mm transverse and 1 mm sagittal slice separations would require approximately 20 hours and 5 Mb of memory. The vast majority of the time was spent on the manual aspects of the construction as only 200 minutes (or approximately 2.5 minutes/slice) were needed for the automated edge detection and spline-fitting. Increasing slice separation to 3.0 mm would reduce overall user time to under 4 hours (with 50 minutes of computational time for edge detection) without compromising the accuracy of the construction. A recent study reported that geometric accuracy of an ovine femur construction decreased with increasing slice spacing but did not report statistical significance (Schmutz et al., 2007). This study similarly observed that accuracy of diaphyseal and epiphyseal composite femur surfaces decreased with increased slice spacing. But statistical analysis showed that the mean error did not increase significantly (Table 2.3). Similarly, no significant differences in accuracy were found among the surfaces constructed using sagittal slice separations of 1, 2, or 3 mm. By extension, one can therefore reasonably assume that geometrically accurate human models can be generated using the SASS technique using slice spacings of up to 3 mm. This may also benefit the patient by reducing their exposure to harmful radiation under both single- and multi-detector CT scanners are used (see Appendix A).

A smooth surface, as presented in this study, is defined to be one in which artificial irregularities are not introduced in the reconstructed surface. Aesthetically, the SASS surface constructed using a 3.0 mm separation reduced the rippling observed when using a 0.6 mm separation (Fig 2.8), which originated from the slight variations in closely spaced curves; such rippling has also been observed in other CAD-based femoral surfaces (Greer, 1999). Smoothing in the SASS method was also aided by the application of spline fitting, which allowed increased flexibility in defining periosteal and endosteal curves, and prevented

artificial irregularities such as jagged edges from forming on the constructed surface. At the condyles, where the voxel meshed model was particularly jagged, a much smoother surface was generated by using a NURBS based surface, avoiding potentially compromising artificial stress concentrations during finite element analysis.

In the study, the SASS and commercial techniques are applied to healthy bones. Under such a case, a 3 mm slice separation will produce a smooth NURBS surface and a jagged voxel mesh surface. The smoother SASS surface is more representative of the physiology of the healthy bone. However, there are cases where bony irregularities may need to be captured (e.g. osteophytes). Adequately capturing these physiological irregularities will likely require a smaller slice separation than 3 mm. The SASS technique can use the thinner slices to capture natural irregularities while still generating a representative surface free of artificial irregularities (i.e. a "smooth" surface).

2.4.3 Sources of Error

2.4.3.1 Measuring Cortical Bone Thickness

The spatial resolution of a CT system can be characterized by the full width half maximum (FWHM) of its two-dimensional point spread function (PSF) (Prevhral et al., 1999). Based on observations made using intensity-based CT images scanned from a typical CT machine, it has been suggested that the thinnest cortical bone that could be measured with < 10% error is 0.7 mm (Prevhral et al., 1999; Anderson et al., 2005), a value close to FWHM. However, it is also possible to measure cortical bone thickness from gradient-operated images. By operating in the gradient domain rather than the intensity domain, the accuracy with which cortical thickness can be measured may not be limited by FWHM.

In Prevhral et al. (1999), a phantom was CT scanned and its edges were characterized with a PSF from an intensity-based CT image. The PSF had a Gaussian shaped curve, which we can assume is characteristic of the intensity

profile across the thickness of the cortex in humans. Indeed, a near-Gaussian curve was seen in this study (Fig 2.3). A step function would most realistically represent the boundary between the phantom and its surroundings but due to sampling and noise, a ramp/curve function results at the edges of the phantom. The lack of sharp edges in Gaussian PSF curves makes the exact boundaries of the cortex difficult to measure (Prevhral et al., 1999) and is characterized by blurring at the edges of an object in an image. Blurred edges make it especially difficult to locate edges manually and result in low repeatability as seen in the findings of Testi et al. (2001). Edge detection using an intensity-based image would be even more difficult in regions of osteopenic/osteoporotic bone where PSF profiles across the cortex would be nearly flat at the endosteal interface. Edges detected from these intensity-based CT images, at best, would have an accuracy of approximately 0.7 mm.

A more common way of locating edges (especially in machine vision literature) is using a gradient (or derivative) operator, which is based on rates of change in the intensity of the image (Parker, 1997). A 3x3 Sobel operator, for example, examines the intensity changes of the 8 pixels adjacent to a central pixel of interest (POI) and returns a gradient value for the POI that would be large near an edge and small in constant areas (Parker, 1997). Ramps indicating edges on the Gaussian PSF would show up as spikes on the gradient profile (Fig 2.3); even subtle changes in intensity, which may not be visually detected due to poor contrast, would be amplified and detected using gradient images.

Since phantom studies employing gradient-operated images could not be located, it is not known if the lower limit of measurement accuracy would be less than 0.7 mm. However, methods using Sobel operators have been shown to have subpixel accuracy in capturing circular edges (Kim et al., 1999) and near-perfect accuracy in capturing straight edges (Parker, 1997; Kittler, 1983). Gradient-based methods more sophisticated than the Sobel technique are available which provide even better accuracy (Parker, 1997; Kim et al., 1999). With current image processing

techniques, the ability to measure cortical thickness may not be necessarily limited by the FWHM of the scanner in the way intensity-based measurements are.

The limiting factor in measuring accuracy from Sobel-operated images lies in the spatial resolution of the image since pixel size determines the interval from which the gradients are calculated. Thus, in the gradient domain, pixel/voxel resolution is a critical factor in reconstructing and measuring the cortical thickness. While a greater spatial resolution does not appear to improve measurement of cortices thinner than 0.7 mm from intensity-based images (Prevhral et al., 1999; Anderson et al., 2005), it may provide a finer distinction of the edges in a gradient-based domain. Since detector size places a maximum limit on spatial resolution (Curry et al., 1990), this may be what limits the accuracy of the gradient technique, hence the reporting of accuracy per pixel for techniques using gradient-operated images to find cortical thickness.

Edge detection within the SASS technique is completely based in the gradient domain and therefore the CT image resolution is linked to the accuracy with which cortical thickness can be constructed. Thus, results were reported with respect to image resolution in addition to absolute accuracy. Voxel mesh models are constructed from intensity-based CT images and therefore FWHM may be a limiting factor for measuring/constructing cortical thickness for such models. Nonetheless, its accuracy was reported using similar criteria to SASS models to provide a balanced comparison.

2.4.3.2 Field of View

A varying field of view (FOV) was used while maintaining a constant 512x512 in-plane pixel resolution to maximize the physical resolution of the composite and bovine bones in the CT images. An improved physical resolution is necessary because the SASS technique is based in the gradient domain and therefore a smaller physical size for pixels will help construct more accurate surfaces. Thus,

the FOV is smaller for the composite bones and larger for the bovine bones. CT scans of the human knee were not obtained exclusively for this study but its FOV was selected for maximum physical resolution of the knee bones.

2.5 Summary and Conclusions

A new NURBS-based technique was introduced (i.e. SASS) for constructing *in vivo* subject-specific knee bone geometry from CT scans and was validated using composite and bovine bones. The SASS method introduced new techniques for improved edge detection of endosteal interfaces and CAD surface generation. This method was compared with a voxel mesh-based technique alternatively used for subject-specific modeling.

The two methods were examined for periosteal and endosteal accuracy. Both methods constructed the periosteal surfaces to an accuracy better than 2 pixel lengths, matching the order of magnitude of image resolution. However, the voxel mesh technique could not construct endosteal surfaces with reasonable accuracy near the joint articulation due to the poor distinction between cortical and cancellous bones, a common problem with whole image thresholding methods. The SASS method constructed entire endosteal surfaces by applying a novel Path Analysis technique, which examined local attenuation and gradient trends. Cortical thickness was captured with an average error of 1 mm.

The SASS method is unique in that it combined transverse and sagittal plane CT data to construct models, overcoming bifurcation problems previously limiting skinning techniques. In contrast, the commercial software limited construction to images from a single plane of view, resulting in jagged voxel mesh models. The SASS method applied carefully selected splines to smooth jagged contours, with further smoothing enabled by increasing slice spacing.

The proposed technique considers the global nature of the image as well as local attenuation changes to arrive at accurate descriptions of cortical bone thickness and, consequently, periosteal and endosteal surface geometries.

Using the SASS technique, geometries can be accurately constructed from CT slices up to 3 mm apart, reducing radiation exposure to the patient. This semi-automated technique allows for rapid and accurate model generation for *in vivo* situations, and can be applied to deal with thin cortical bone in other locations such as the proximal femur.

Table 2.1: CT image specifications for composite, bovine, and human bones. Specifications are provided for both transverse (T) and sagittal (S) plane slices. Element sizes used to construct voxel mesh models were based directly on image resolution and provided for each subject.

Subject	Field of View (mm)	Slice Thickness (mm)	Slice separation (mm)	Slice overlap (mm)	Pixel Resolution (mm/pixel)	Voxel Size (LxWxH mm)
47-year-old male	160 (T) 160 (S)	1.25 (T) 1.0 (S)	1.0 (T) 1.0 (S)	0.25 (T) 0 (S)	0.3125 (T) 0.3125 (S)	0.3125x0.3125x1.0
Composite Femur & Tibia	160 (T) 422 (S)	1.0 (T) 1.0 (S)	0.6 (T) 1.0 (S)	0.4 (T) 0 (S)	0.3125 (T) 0.8242 (S)	0.3125x0.3125x0.6
Bovine Femur 1	230(T) 422 (S)	1.0 (T) 1.0 (S)	0.6 (T) 1.0 (S)	0.4 (T) 0 (S)	0.4492 (T) 0.8242 (S)	0.4492x0.4492x0.6
Bovine Femur 2	227 (T) 422 (S)	1.0 (T) 1.0 (S)	0.6 (T) 1.0 (S)	0.4 (T) 0 (S)	0.4434 (T) 0.8242 (S)	0.4434x0.4434x0.6
Bovine Femur 3	260 (T) 422 (S)	1.0 (T) 1.0 (S)	0.6 (T) 1.0 (S)	0.4 (T) 0 (S)	0.5878 (T) 0.8242 (S)	0.5878x0.5878x0.6
Bovine Tibia 1	220 (T) 422 (S)	1.0 (T) 1.0 (S)	0.6 (T) 1.0 (S)	0.4 (T) 0 (S)	0.4297 (T) 0.8242 (S)	0.4297x0.4297x0.6

Table 2.2: Error comparison of CMM surface coordinates with coordinates from surfaces constructed using SASS technique, laser scan, and voxel meshing with commercial software. All errors are reported as absolute values.

		SASS	Laser Scan	Voxel
Composite Femur	Mean Ball Bearing Alignment Error (mm)	0.400	0.521	0.522
	Sample Points	151	152	155
	Mean Error ± Standard Deviation (mm)	0.359±0.305	0.233±0.232	0.304±0.259
	Maximum Error (mm)	1.862	1.175	1.554
	Minimum Error (mm)	0.000	0.001	0.001
Composite Tibia	Mean Ball Bearing Alignment Error (mm)	0.291	0.661	0.235
	Sample Points	62	63	63
	Mean Error ± Standard Deviation (mm)	0.394±0.236	0.248±0.286	0.223±0.141
	Maximum Error (mm)	1.057	1.083	0.507
	Minimum Error (mm)	0.003	0.001	0.000
Bovine Femur 1	Mean Ball Bearing Alignment Error (mm)	0.378	0.306	0.317
	Sample Points	100	107	107
	Mean Error ± Standard Deviation (mm)	0.800±0.646	0.758±0.498	0.588±0.622
	Maximum Error (mm)	3.895	2.047	3.600
	Minimum Error (mm)	0.035	0.000	0.010
Bovine Femur 2	Mean Ball Bearing Alignment Error (mm)	0.305	0.465	0.280
	Sample Points	116	125	124
	Mean Error ± Standard Deviation (mm)	0.820±0.984	0.612±0.645	0.661±0.859
	Maximum Error (mm)	6.517	4.884	6.316
	Minimum Error (mm)	0.001	0.000	0.000
Bovine Femur 3	Mean Ball Bearing Alignment Error (mm)	0.448	0.330	0.323
	Sample Points	88	99	99
	Mean Error ± Standard Deviation (mm)	0.609±0.641	0.566±0.656	0.682±0.799
	Maximum Error (mm)	2.645	2.760	3.646
	Minimum Error (mm)	0.007	0.001	0.006
Bovine Tibia 1	Mean Ball Bearing Alignment Error (mm)	0.635	0.362	0.175
	Sample Points	111	131	131
	Mean Error ± Standard Deviation (mm)	0.725±0.425	0.706±0.475	0.326±0.254
	Maximum Error (mm)	1.935	2.178	1.769
	Minimum Error (mm)	0.017	0.001	0.012

Table 2.3: Comparison of error in composite femur surfaces constructed with various transverse slice separations using SASS and voxel meshing techniques. Errors were measured with respect to CMM data and are reported as absolute values. P value was used to determine statistical significance (i.e. P<0.05) in the difference of mean error relative to a 0.6 mm separation.

Technique	SASS					Voxel	
Separation Distance (mm)	0.6 mm	1.2 mm	1.8 mm	2.4 mm	3.0 mm	0.6 mm	3.0 mm
Sample points	135	135	135	135	135	155	155
Mean Error ± Standard Deviation (mm)	0.360±0.295	0.343±0.284	0.345±0.286	0.341±0.288	0.350±0.284	0.304±0.259	0.432±0.386
Maximum error (mm)	1.862	1.862	1.862	1.862	1.862	1.554	2.598
Minimum error (mm)	0.000	0.000	0.000	0.000	0.000	0.001	0.005
P value	--	0.62	0.66	0.59	0.76	--	< 0.05

Table 2.4: The effect of smoothing on accuracy of composite femur surfaces constructed using commercial software technique. Errors were measured with respect to CMM data and are reported as absolute values. P value was used to determine statistical significance (i.e. $P<0.05$) in the difference of mean error relative to a non-smoothed surface.

Surface	Non-smooth	Smooth	Non-smooth	Smooth
Separation Distance (mm)	0.6 mm	0.6 mm	3.0 mm	3.0 mm
Sample points	155	155	155	155
Mean Error ± Standard Deviation (mm)	0.304±0.259	0.327±0.265	0.432±0.386	0.412±0.399
Maximum error (mm)	1.554	1.466	2.598	2.654
Minimum error (mm)	0.001	0.001	0.005	0.000
P value	--	0.434	--	0.667

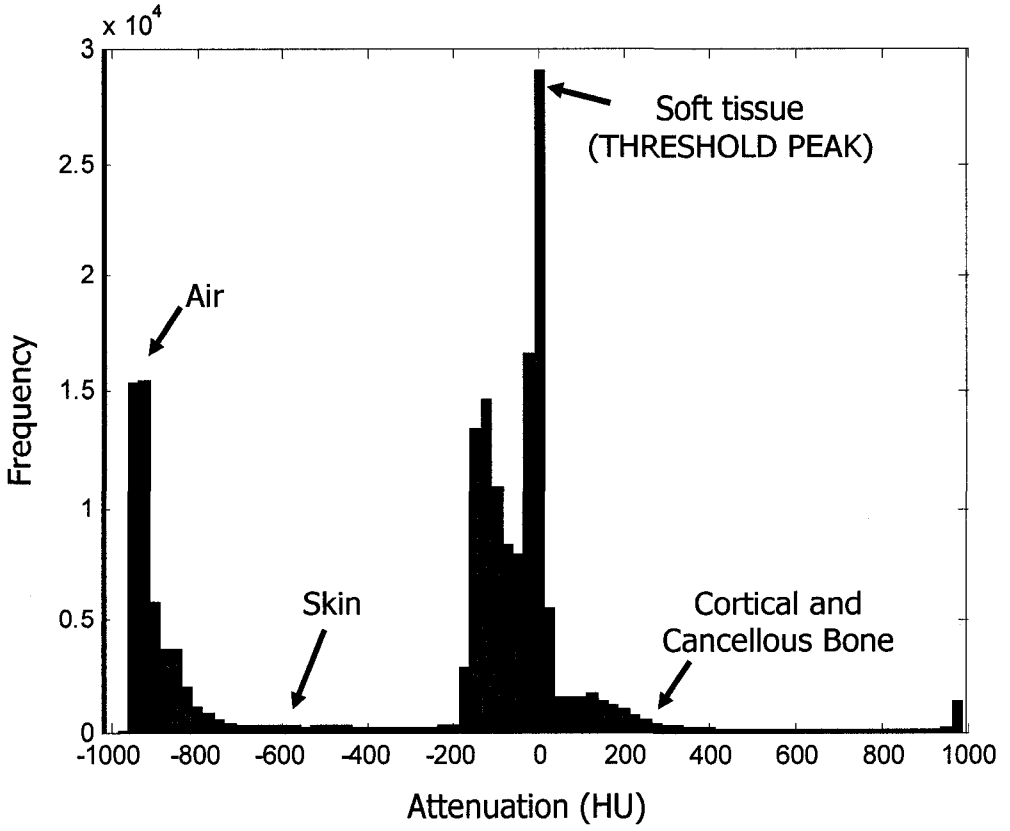

Figure 2.1: A typical attenuation histogram from a transverse CT image of the distal human femur, located 54 mm proximal to the joint line. All attenuations are in Hounsfield Units (HU). The attenuation associated with the soft tissue peak was used to threshold the CT image to eliminate soft tissue. Regions in the histogram associated with air, skin and bone are also identified.

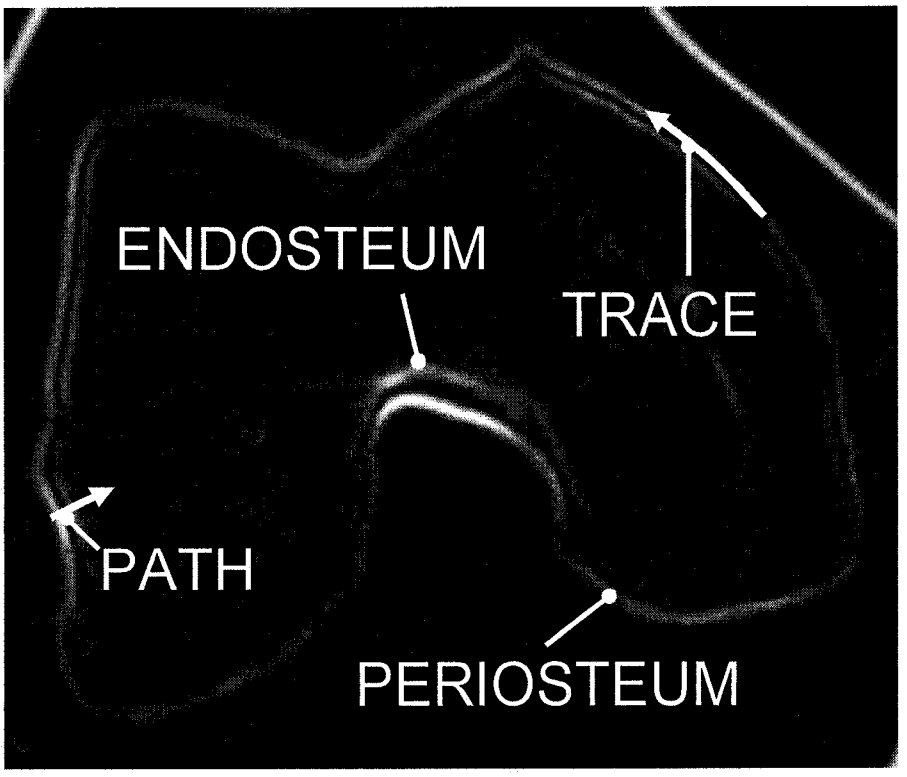

Figure 2.2: Gradient-operated transverse image of the human distal femur after thresholding, located 12 mm from the joint line. A partial trace of the outer ring, representing the periosteal interface, is shown (TRACE). The endosteal interface is represented by the inner ring. PATH illustrates a line of pixels intersecting the endosteum for generation of attenuation and gradient profiles to identify the location of the endosteal interface (see Fig 2.3).

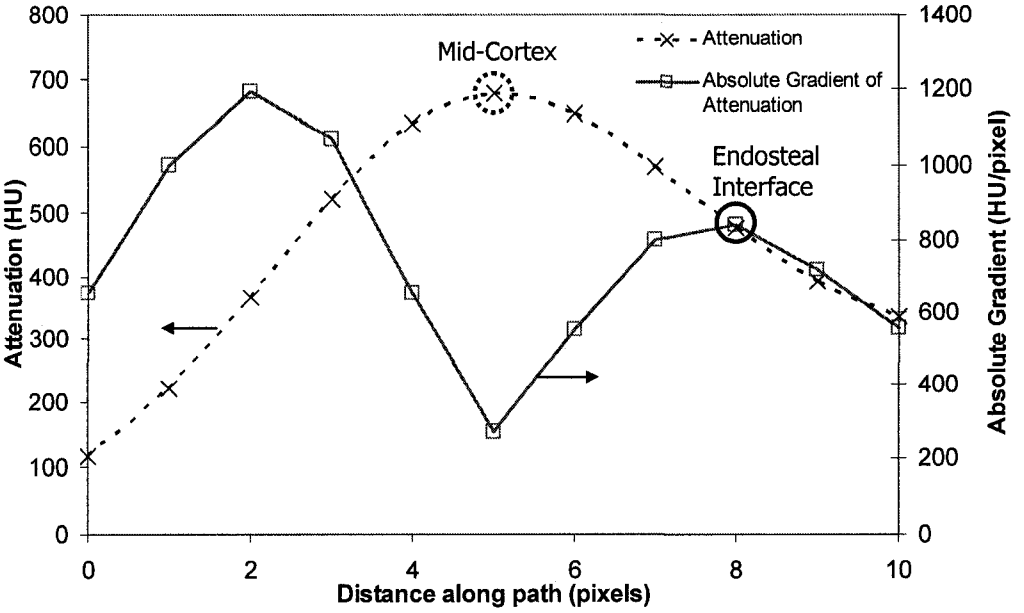

Figure 2.3: Typical profile of attenuation and gradient values along "PATH" (see Fig 2.2) intersecting an endosteal interface. The dotted circle identifies the attenuation peak used to locate the mid-cortex; the solid circle shows the gradient peak used to determine endosteal interface location. Solid and dotted lines are included to guide the eye.

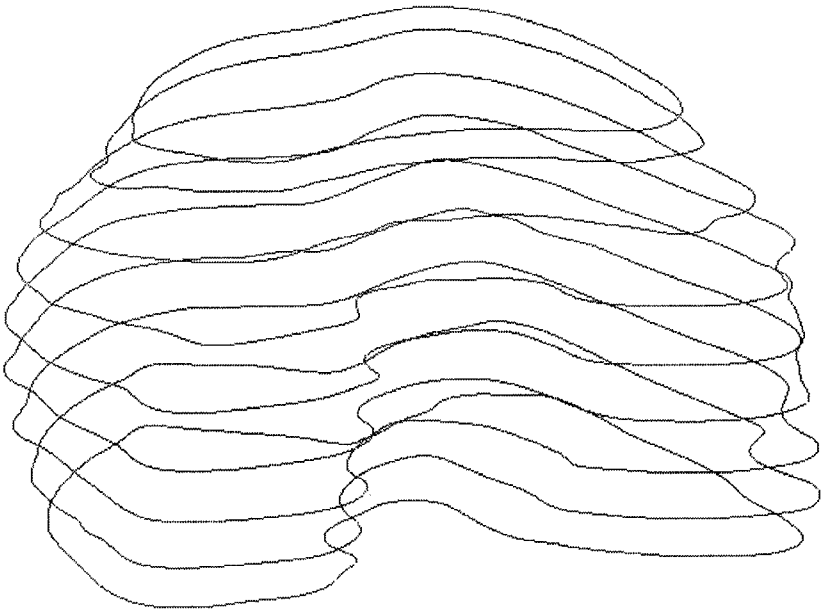

Figure 2.4: The transverse sets of smooth periosteal interface contours used to construct the 3-D surface of the composite femur. The transverse contours were defined using transverse plane CT slices.

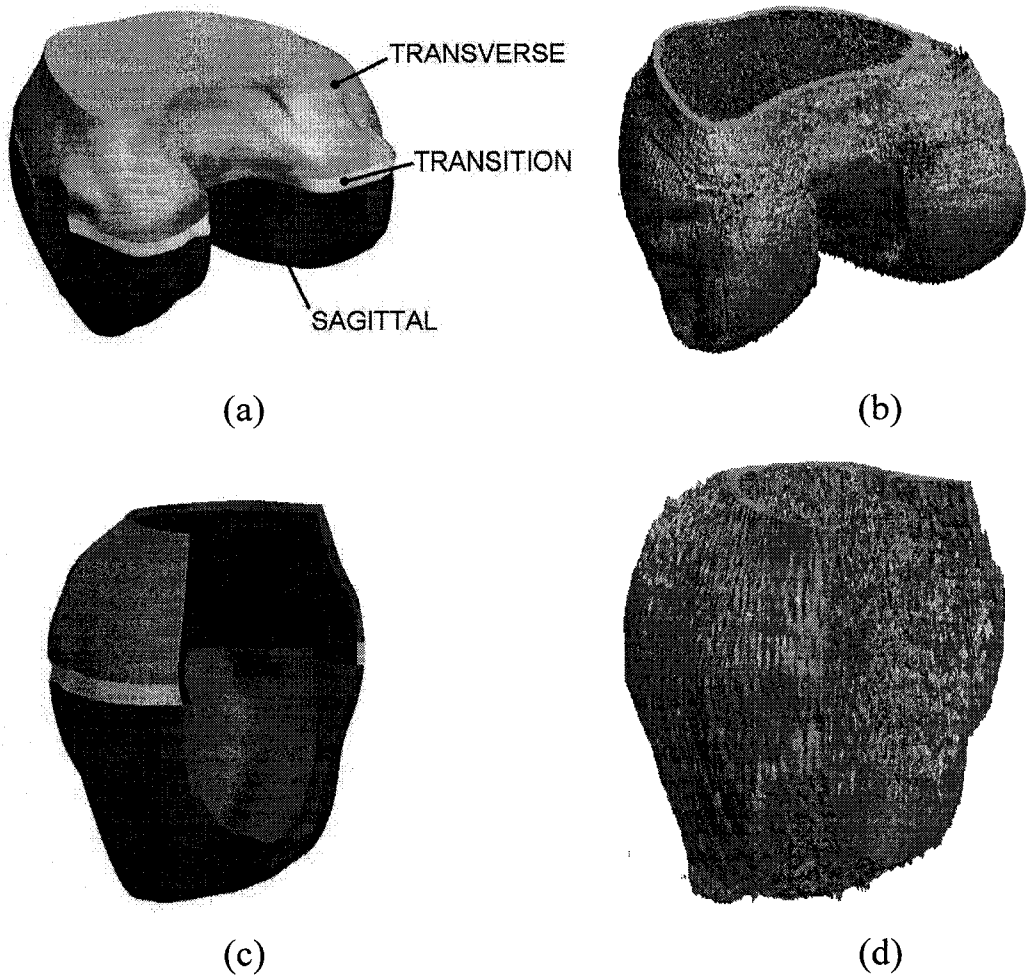

Figure 2.5: (a) Human distal femur constructed using SASS technique where a surface generated using transverse curves (TRANSVERSE) was combined with a surface generated using sagittal curves (SAGITTAL) using a transition surface (TRANSITION); (b) the same bone constructed from transverse slices using voxel mesh technique. (c) A cutaway view shows the endosteal surface of the SASS model, which is not well represented in the voxel mesh model (d).

(a) (b)

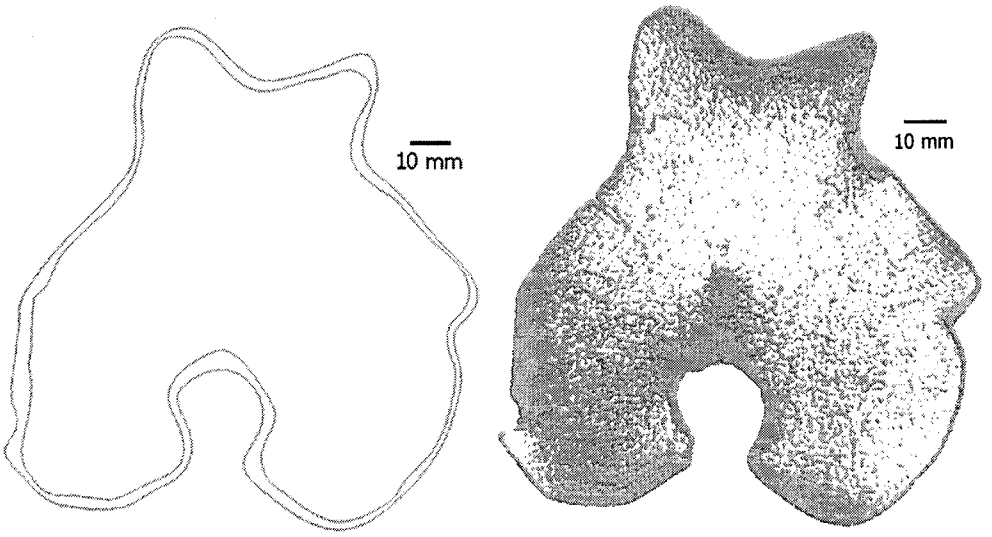

(c) (d)

Figure 2.6: A comparison of construction results for Bovine Femur 1. The transverse slices are located approximately 36 mm proximally from the distal-most point of the bone (inset in (a)). (a) A transverse slice of the bone is shown alongside (b) its CT slice, (c) its constructed form using the SASS technique, and (d) commercial software. The circles in (a) show the 5 locations used to measure cortical thickness. For clarity, (c) shows only the periosteal and endosteal outlines of the SASS model. In constructing the geometry using the commercial software, thresholding the entire image using a single attenuation range leads to overestimation of cortex thickness (gray area) in the femoral condyles.

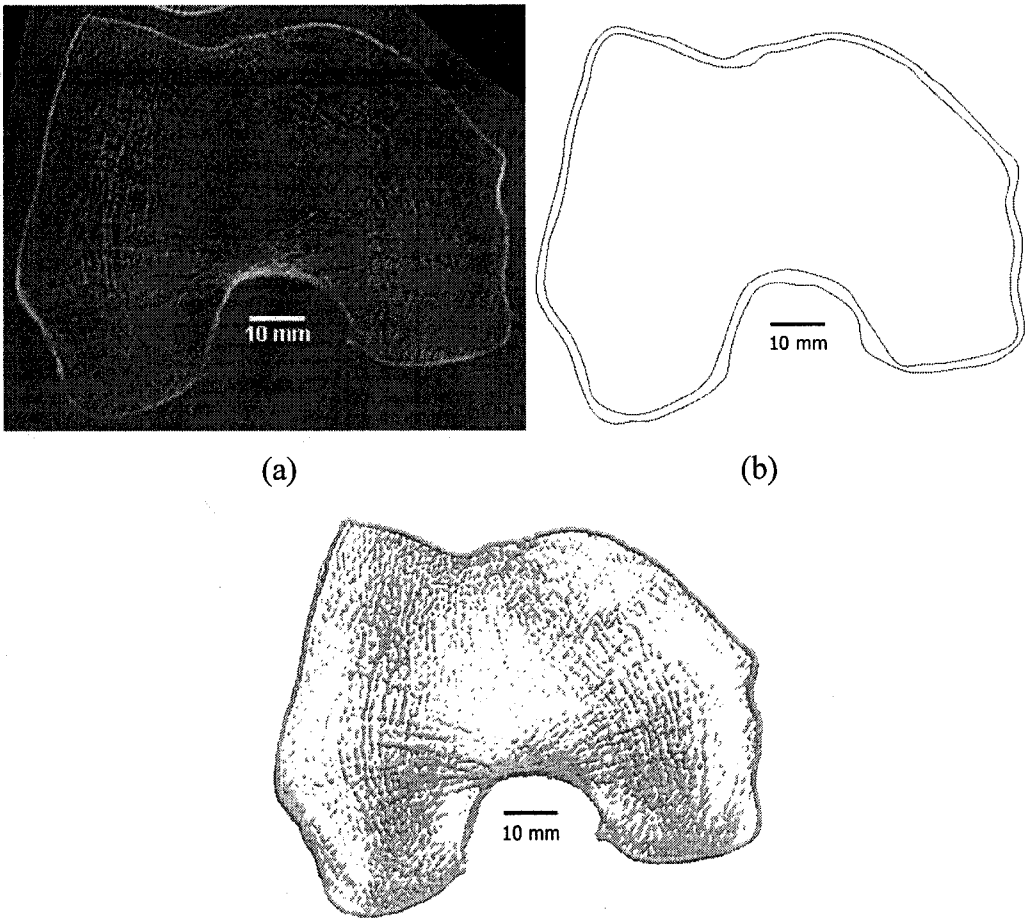

(a) (b)

(c)

Figure 2.7: A comparison of construction results for the human distal femur. The transverse slices are located approximately 28 mm from the distal-most point of the bone. (a) A transverse CT slice of the bone is shown alongside (b) its constructed model using the SASS technique and (c) voxel mesh technique. For clarity, (b) shows only the periosteal and endosteal outlines from the SASS model. In constructing the geometry using the commercial software, thresholding the entire image using a single attenuation range leads to overestimation of cortex thickness in the femoral condyles (all grey areas in (c) are considered as cortical bone and white background is considered cancellous bone).

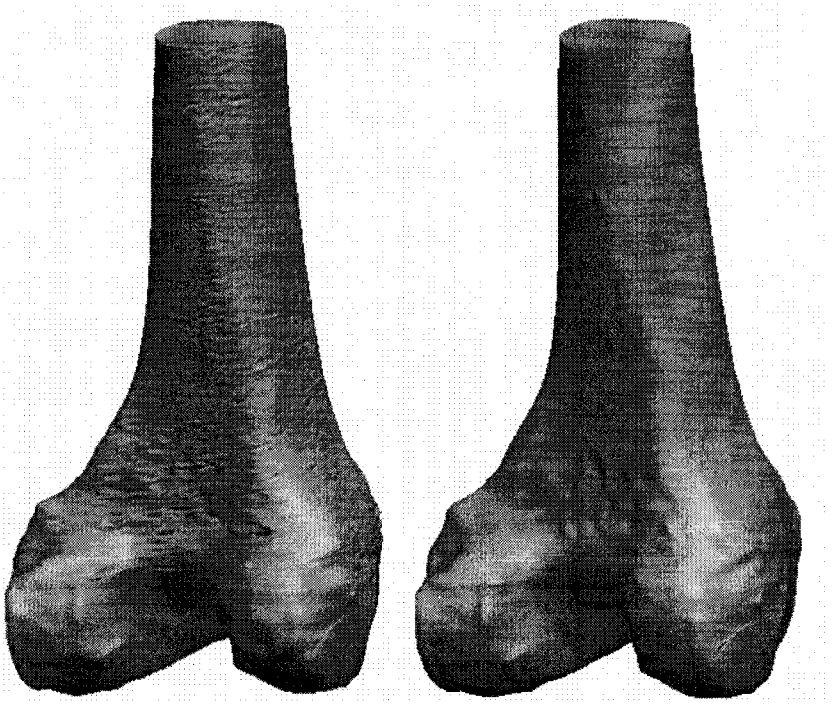

(a) (b)

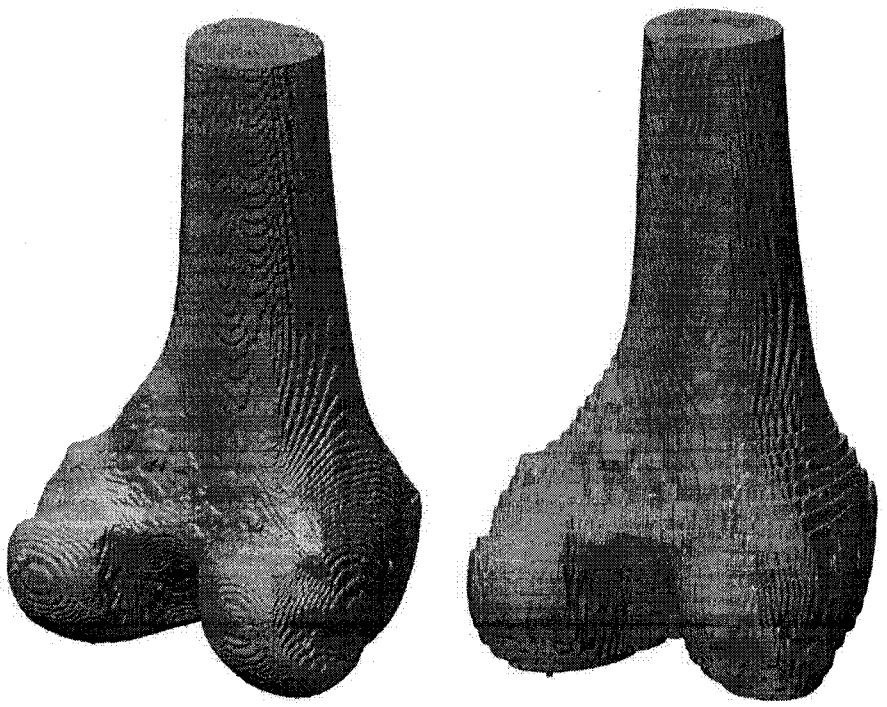

(c) (d)

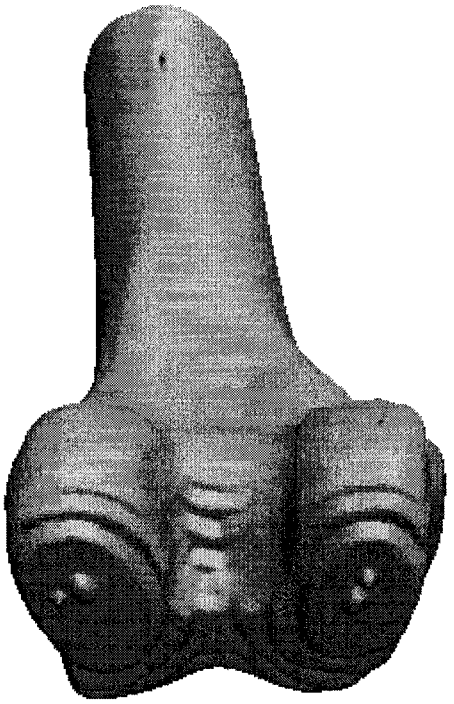

(e)

Figure 2.8: Composite femur constructed using SASS and commercial software techniques with 0.6 mm and 3.0 mm slice separations. With the SASS technique, the composite femur surface constructed using (a) a 0.6 mm separation became smoother when using (b) a 3.0 mm separation, but accuracy was not significantly different. The surface constructed using commercial software was noticeably more jagged when (d) a 3.0 mm separation versus (c) a 0.6 mm separation was used, and also significantly less accurate. (e) Applying a smoothing algorithm to (d) did not completely eliminate jaggedness from the model.

References

Anderson, A. E., Peters, C. L., Tuttle, B.D., Weiss, J.A., 2005. Subject-specific finite element model of the pelvis: development, validation and sensitivity studies. Transactions of the ASME: Journal of Biomechanical Engineering 127, 364-373.

Askew, M. J., Lewis, J. L., 1981. Analysis of model variables and fixation post length effects on stresses around a prosthesis in the proximal tibia. Transactions of the ASME: Journal of Biomechanical Engineering 103, 239-245.

Au, A. G., Liggins, A. B., Raso, V. J., Amirfazli, A., 2005. A parametric analysis of fixation post shape in tibial knee prostheses. Medical Engineering and Physics 27, 123-34.

Au, A. G., Palathinkal, D., Liggins, A. B., Raso, V. J., Carey, J., Lambert, R. G., Amirfazli, A., 2008. A NURBS-based technique for subject-specific construction of knee bone geometry. Computer Methods and Programs in Biomedicine 92, 20-34.

Beaupre, G. S., Vasu, R., Carter, D. R., Schurman, D. J., 1986. Epiphyseal-based designs for tibial plateau components - II. Stress analysis in the sagittal plane. Journal of Biomechanics 19, 663-673.

Camacho, D. L. A., Hopper, R. H., Lin, G. M., Myers, B. S., 1997. An improved method for finite element mesh generation of geometrically complex structures with application to the skullbase. Journal of Biomechanics 30, 1067-1070.

Coleman, J. C., Roberts, M. D., Maender, C. M., Hart, R. T., 2000. Solid Model Creation from CT Image Data, Technical Report TU-BONE-2000-03, Tulane University.

Curry, T. S., Dowdey, J. E., Murry, R. C., 1990. Christensen's Physics of Diagnostic Radiology, 4th ed. (Lea and Febiger, Philadelphia PA).

Dawson, J. M., Bartel, D. L., 1992. Consequences of an interference fit on the fixation of porous-coated tibial components in total knee replacement. Journal of Bone and Joint Surgery [Am] 74-A, 233-238.

Douglas, T., Solomonidis, S., Sandham, W., Spence W., 2002. Ultrasound imaging in lower limb prosthetics. IEEE Transactions on Neural Systems and Rehabilitation Engineering 10, 11-21.

Eibeck, P. A., Swenson, L. W., Schurman, D. J., Piziali, R. L., 1979. Finite element stress analysis of hinged tibial component total joint replacements. Transactions of the 25th ORS, 298.

Fleischmann, D., Rubin, G. D., Paik, D. S., Yen, S. Y., Hilfiker, P. R., Beaulieu, C. F., Napel, S., 2000. Stair-step artifacts with single versus multiple detector-row helical CT. Radiology 216, 185-196.

Greer, B.B., 1999. Finite element modeling and analysis of the proximal femur [thesis], University of Nevada, Reno.

Hodgskinson, R., Currey, J. D., 1992. Young's modulus, density and material properties in cancellous bone over a large density range. Journal of Materials Science: Materials in Medicine 3, 377-381.

Iesaka, K., Tsumura, H., Sonoda, H., Sawatari, T., Takasita, M., Torisu, T., 2002. The effects of tibial component inclination on bone stress after unicompartmental knee arthroplasty. Journal of Biomechanics 35, 969-974.

Keyak, J., Meagher, J., Skinner, H., Mote, C., 1990. Automated three-dimensional finite element modelling of bone: a new method. Journal of Biomedical Engineering 12, 389-397.

Kim, T. H., Moon, Y. S., Han, C. S., 1999. An efficient method of estimating edge locations with subpixel accuracy in noisy images. Proceedings of the 1999 IEEE TENCON, 589-592.

Kittler, J., 1983. On the accuracy of the Sobel edge detector. Image and Vision Computing 1, 37-42.

Lewis, G., Jonathan, V., Kambhampati, S., 1998. Effect of material property representation on stresses in endoprostheses, Bio-Medical Materials and Engineering 8, 11-23.

Lengsfeld, M., Schmitt, J., Alter, P., Kaminsky, J., Leppek, R., 1998. Comparison of geometry-based and CT voxel-based finite element modelling and experimental validation. Medical Engineering and Physics 20, 512-522.

Li, G., Gil, J., Kanamori, A., Woo, S., 1999. A validated three-dimensional computational model of a human knee joint. Transactions of the ASME: Journal of Biomechanical Engineering 121, 657-662.

Marks, L. W., Gardner, T. N., 1993. The use of strain energy as a convergence criterion in the finite element modelling of bone and the effect of model geometry on stress convergence, Journal of Biomedical Engineering 15 , 474-476.

Mehta, B. V., Rajani, S., Sinha, G., 1997. Comparison of image processing techniques (magnetic resonance imaging, computed tomography scan and ultrasound) for 3D modeling and analysis of the human bones. Journal of Digital Imaging 10 (Suppl 1), 203-206.

Miyoshi, S., Takahashi, T., Ohtani, M., Yamamoto, H., Kameyama, K., 2002. Analysis of the shape of the tibial tray in total knee arthroplasty using a three dimension finite element model. Clinical Biomechanics 17, 521-525.

Parker, J. R., 1997. Algorithms for Image Processing and Computer Vision (Wiley Computer Publishing, New York NY).

Pena, E., Calvo, B., Martínez, M. A., Palanca, D., Doblare, M., 2005. Finite element analysis of the effect of meniscal tears and meniscectomies on human knee biomechanics. Clinical Biomechanics 20, 498-507.

Ploeg, H., Ploeg, L., Byrne, N., Garcia, S., Kersh, M., Nair, D., 2004. How accurate are solid models made from CT scan data?, 13th Biennial Conference, Canadian Society for Biomechanics (CSB), Halifax, NS.

Prevrhal, S., Engelke, K., Kalender, W.A., 1999. Accuracy limits for the determination of cortical width and density: the influence of object size and CT imaging parameters. Physics in Medicine and Biology 44, 751-764.

Rakotomanana, R. L., Levyraz, P. F., Curnier, A., Heegaard, J. H., Rubin, P. J., 1992. A finite element model for evaluation of tibial prosthesis-bone interface in total knee replacement. Journal of Biomechanics 25, 1413-1424.

Schmutz, B., Wullschleger, M. E.., Schuetz, M. A., 2007. The effect of CT slice spacing on the geometry of 3D models, 6th Australasian Biomechanics Conference, Auckland, New Zealand.

Taddei, F., Cristofolini, L., Martelli, S., Gill, H. S., Viceconti, M., 2006. Subject-specific finite element models of long bones: an in vitro evaluation of the overall accuracy. Journal of Biomechanics 39, 2457-2467.

Taylor, M., Tanner, K. E., Freeman, M. A. R., 1998. Finite element analysis of the implanted proximal tibia: a relationship between the initial cancellous bone stresses and implant migration. Journal of Biomechanics 31, 303-310.

Testi, D., Zannoni, C., Cappello, A., Viceconti, M., 2001. Border-tracing algorithm implementation for the femoral geometry reconstruction, Computer Methods and Programs in Biomedicine 65, 175-182.

Tissakht, M., Ahmed, A. M., Chan, K. C., 1996. Calculated stress-shielding in the distal femur after total knee replacement corresponds to the reported location of bone loss. Journal of Orthopaedic Research 14, 778-785.

Van Loon, C. J. M., De Waal Malefijt, M. C., Buma, P., Verdonschot, N., Veth, R. P. H., 1999. Femoral bone loss in total knee arthroplasty: a review. Acta Orthopaedica Belgica 65, 154-161.

Viceconti, M., Zannoni, C., Pierotti, L., 1998a. TRI2SOLID: an application of reverse engineering methods to the creation of CAD models of bone segments. Computer Methods and Programs in Biomedicine 56, 211-220.

Viceconti, M., Bellingeri, L., Cristofolini, L., Toni, A., 1998b. A comparative study on different methods of automatic mesh generation of human femurs. Medical Engineering and Physics 20, 1-10.

Viceconti, M., Zannoni, C., Testi, D., Cappello, A., 1999. CT data sets surface extraction for biomechanical modeling of long bones. Computer Methods and Programs in Biomedicine 59, 159-166.

Wang, G., Vannier, M. W., 1994. Stair-step artifacts in three-dimensional helical CT: an experimental study. Medical Physics 191, 79-83.

Chapter 3: Representation of heterogeneity in subject-specific finite element knee bone models

3.1 Introduction

Subject-specific finite element (FE) bone models are being used with increasing frequency to advance understanding of a broad range of topics regarding the knee, such as pathologies, surgical techniques, and implant design. Accurate creation of subject-specific FE knee bone models requires construction of a surface geometry representative of a particular individual. In Chapter 2, a method was introduced to accurately construct subject-specific bone geometries that distinguished cortical and cancellous bone in the knee using computed tomography (CT) images. A key aspect of subject-specific FE bone models also includes capturing the unique distribution of bone density within the cortical and cancellous bone of an individual. An accurate characterization of the stiffness in the overall bone structure is critical to successfully predicting internal stresses of the bone. This can be done using CT image data, which have been successfully used to interpret mechanical properties of the bone in the past (Taddei et al., 2006).

Numerous studies have shown that bone density in the knee varies significantly within each person (Rho, 1992; Ashman et al., 1989; Ciarelli et al., 1991). Modeling such heterogeneity can be computationally expensive (Taddei et al., 2006) and is often simplified. In the proximal femur, it appears the representation of heterogeneity can be quite simplified while still producing relatively accurate results. Fully heterogeneous models, i.e. those not employing grouping strategies, can accurately predict strains and stresses for a wide range of range of activities (Taddei et al., 2006, 2007). Models with a moderate degree of heterogeneity (Keyak et al., 1993) and even no heterogeneity (Lengsfeld et al., 1998) predicted relatively acceptable strains under a range of loading conditions. Parametric analyses have also supported this by showing slight improvement in accuracy with greater degrees of heterogeneity (Taddei et al., 2006; Peng et al., 2006). In the proximal tibia, however, such simplifications produced qualitatively different

stress levels (Au et al., 2005). It would be of interest to quantitatively determine if such simplification is acceptable in models of the distal femur and proximal tibia. However, it is emphasized that the acceptable level of simplification, i.e. the required level of accuracy, is case-specific.

The predominant method in the literature for modeling heterogeneity is to group bone of similar attenuation together and then define each group by an effective attenuation (Keyak et al., 1993; Taddei et al., 2004; Peng et al., 2006). An explanation of this technique has been provided in Taddei et al. (2004). The intent of such grouping is to reduce the number of material properties used in the FE model thereby reducing the computational time needed to calculate a solution. The number of groups that are employed by any particular model is controlled by the user (Taddei et al., 2004) and therefore the level of heterogeneity represented is completely subjective. The degree of heterogeneity employed in the models is varied and is ostensibly linked to the level of accuracy needed to address the objectives of each study. However, a general sense of an appropriate level of heterogeneity cannot be gained because this conventional grouping technique does not rely on any objective parameter. A different technique which characterizes the level of heterogeneity with an objective metric is needed to allow better comparison across various models to gain a general sense of how much heterogeneity needs to be modeled.

It is not known how much computational effort is reduced by using grouped models (Keyak et al., 1993; Taddei et al., 2004) compared to non-grouped models (Taddei et al., 2006, 2007). Peng et al. (2006) employed models with varying degrees of heterogeneity but did not report the computational time required by each model to generate a solution. Generally, the more accurate models contained a greater number of elements and sets of material properties. Ideally, a balance between computational time and solution accuracy should be employed by FE models. Currently, no studies have been conducted directly comparing computational savings with the degree of heterogeneity.

In the models employed in current literature, bone groups have been designated purely on a mathematical basis by collecting elements into attenuation bins. This method groups bone independently of the anatomical structure (Peng et al., 2006), and is similar to the global thresholding approach used to segment cortical bone in voxel models (Lengsfeld et al., 1998). However, the current subject-specific models rely upon this material properties modeling technique to distinguish between cortical and cancellous bone (Taddei et al., 2004). Thus, in epiphyseal regions of the bone, physiologically cortical and cancellous bones are sometimes grouped together, resulting in an unrealistic and overly thick representation of the cortex. A model with an overly thick cortex may underestimate stress levels in the bone (Au et al., 2008), and can influence the mapping and distribution of bone properties in FE models (Taddei et al., 2004). It is necessary to distinguish cortical from cancellous bone types because the mechanical properties of each bone type should be interpreted differently from the CT data (Rho et al., 1995). Many models have not done so and interpreted the mechanical properties of the entire bone with a single relationship, thereby assuming that cortical bone is simply dense cancellous bone, an assumption which has been shown to be incorrect (Rice et al., 1988).

The mechanical properties of bone tissue in the knee are widely recognized as being anisotropic rather than isotropic (Rho et al., 1995; Ciarelli et al., 1991). However, many studies have found it acceptable to assume isotropic mechanical properties in the proximal femur when axial loading is simulated (Huiskes et al., 1981; Keyak et al., 1993; Taddei et al., 2006). Peng et al. (2006) found that this simplification had little difference on maximum von Mises stresses and displacements in the proximal femur. In the proximal tibia, however, Au et al. (2005) have seen qualitatively different stress results with the assumption of isotropic bone. Quantifying the effects of isotropic bone properties in the distal femur and proximal tibia can be helpful in ensuring bone tissue properties of the subject-specific FE models of these bones are not oversimplified.

This study focused on the development of subject-specific knee bone models from a material property construction perspective. A novel application of an image processing technique in the context of bone modeling was introduced to characterize the heterogeneity of bone density using CT image data. Both the spatial and attenuation properties were considered during modeling. The technique was used to estimate an optimal level of heterogeneity required to minimize computational effort while maintaining solution convergence. It can be envisioned that the ability of this technique to detect both local and global density patterns in CT images can be helpful in certain radiological applications. For example, it can be used to monitor density changes in the bone of an osteoporotic patient who has recently received a total knee replacement.

3.2 Methods and Materials

3.2.1 CT Images

In vivo CT scans of the left knee of a 37-year-old female were used to demonstrate the applicability of the proposed methodology. The female subject did not have osteoarthritis and was not a prospective total knee replacement patient; both the femur and tibia of the subject were examined in this study. A GE Lightspeed 16 CT scanner (General Electric, Fairfield, CT) was used to scan the human subject. The image specifications can be found in Table 3.1.

3.2.2 Grouping Technique

In this study, grouping was performed separately on the cortical and cancellous bones. The cortex was segmented from the cancellous bone using the CT gradient-based edge detection procedure described in Chapter 2. The grouping operation described below was performed directly on the image data using a custom routine written in MATLAB (version 7.0.0.19920 (R14), Mathworks, Natick, MA).

The heterogeneity within the cortical or cancellous bone was characterized by forming groups that were physiologically representative through a novel application of a region split and merge technique (Gonzalez and Woods, 2008). Region splitting involved taking a region of bone (e.g. cortical or cancellous bone) and dividing it into smaller sub-regions based on a split criterion. The process begins by evaluating whether the attenuation of each pixel in the entire bone met the split criterion:

$$(\mu_{mean} - \alpha\mu_{mean}) \leq \mu_{pixel} \leq (\mu_{mean} + \alpha\mu_{mean}) \quad (1)$$

where μ_{pixel} is the attenuation of a pixel in the region, μ_{mean} is the mean attenuation of the region, and α is a tolerance factor.

If all pixels satisfied equation (1), the entire bone remained intact; otherwise, it was divided into quarters and each of the 4 sub-regions were evaluated using the same criterion (Fig 3.1). The process continued until all sub-regions met the split criterion. The splitting process may result in new adjacent regions being identical (Gonzalez and Woods, 2008). This drawback was remedied by applying a merge process, which grouped similar regions together while satisfying a merge criterion:

$$\left(\mu_{\min}^{R1} < \mu_{\min}^{R2}\right) \& \left(\mu_{\max}^{R1} > \mu_{\max}^{R2}\right) \quad (2)$$

where R1 and R2 are two adjacent sub-regions; $\mu_{\min}^{R1}$ and $\mu_{\min}^{R2}$ are the minimum attenuations of regions R1 and R2, respectively; $\mu_{\max}^{R1}$ and $\mu_{\max}^{R2}$ are the maximum attenuations of regions R1 and R2, respectively.

The merge process had the advantage of reducing the number of sub-regions created in the split process. Merging was conducted by taking a sub-region (e.g. one of the 7 regions in Fig 3.1c) and testing if it met the merge criterion with a touching neighbour; if the merge criterion was met, they combined, otherwise they remained split. This process continued until no further merging was possible.

The following is an example illustrating the merge procedure (after completion of the splitting step) using two sub-regions taken from the tibial cancellous bone (Fig 3.2). Merging begins with the sub-region containing the largest attenuation spread (i.e. R1) and comparing it with an adjacent sub-region (i.e. R2) (Fig 3.2a). If all the attenuations contained within R2 are within the attenuation spread of R1 (i.e. satisfying the merge criterion), then the sub-regions are merged into a meso-region (Fig 3.2b). This process is continued by comparing the spread of the merged sub-region (which remains that of R1) with all regions touching it. R1 grows until it can no longer merge with any other sub-region. Merging then begins anew with a non-merged sub-region containing the largest spread. This sub-region is compared with all the regions touching it and grows until it cannot merge with any other sub-region. The merge process subsequently cycles through all non-merged sub-regions and ends when merging is no longer possible.

The above merging process produces meso-regions with straight borders, which may generate internal stress gradients depending on the magnitude of the attenuation difference between neighbouring meso-regions. This can be improved by enhancing the merge process to include partial sub-regions rather than entire sub-regions. For example, if not all attenuations within R2 are within the spread of R1, the previous merge process would leave the two sub-regions unmerged (Fig 3.3a). With the enhanced merge process, the pixels in R2 within the spread of R1 would be merged with R1 (Fig 3.3b), resulting in a border between R1 and R2 that is more curved and natural.

For smaller α values (e.g. 0.1), many sub-regions contained a small number of pixels. Some of these sub-regions may not have merged with surrounding regions due to noise artifacts in the CT image. Forcing these small sub-regions to merge with their neighbours did not change the stress results of the subsequent FE analysis.

Ideally, merging should be performed with the split criterion (equation (1)) so the merging process does not undo the results of the splitting. However, merging with the split criterion biased the results towards the order in which the meso-regions were merged. Bias was prevented by merging with a criterion based on the spread (i.e. equation (2)) rather than the mean of the attenuations (i.e. equation (1)). This process does not undo the split results (and therefore does not bias) if the spread of a merged meso-region maintains the spread of the original meso-region. It should be noted that, in this study, the term "grouping" is meant to describe the combination of the splitting and merging procedures. The amount of grouping, i.e. the level of heterogeneity represented in the model, is essentially controlled at the splitting stage by the tolerance parameter (α); the results of the merge procedure are not individually adjusted and are completely a consequence of results of the splitting procedure.

The degree of heterogeneity in the bone was adjusted using the tolerance factor, α, in the split criterion (equation (1)). The CPU time was observed for various levels of heterogeneity by adjusting α between 0 and 0.5. Thus, when α=0.5, all attenuations within a region or sub-region are within 50% of the mean attenuation. Fifteen tolerance levels were examined in total (0, 3, 6, 10, 13, 16, 20, 23, 26, 30, 33, 36, 40, 43, 46, and 50%), but particular emphasis was placed on tolerances of 0% (no grouping), 10%, 20%, 30%, 40%, and 50% to observe the general trend. The CPU time needed to group the bone using tolerances of 10%, 20%, 30%, 40%, and 50% was analyzed. The appropriateness of a particular grouping can also be characterized by comparing von Mises stresses, strain energy densities and nodal displacements in a FE model. The development of the FE model is described in detail in Section 3.2.4. All operations were performed on an Intel Pentium D (3 GHz, 1 Gb RAM) personal computer.

A baseline model with no grouping (i.e. one material property is assigned to one element) was used as a benchmark in this study, and was assumed to be the most accurate in terms of stress level. However, the baseline model should not be

interpreted as being the optimal model since it did not provide the best compromise between computational expense and solution accuracy (see below).

3.2.3 Determining Material Properties

Once merging was completed, the mean attenuation of each meso-region was calculated. The elastic constants were calculated using the mean attenuation, which was generally different than the pre-merge mean. The mean attenuation was converted into elastic constants using empirical relationships. The following power relationship was used to determine the apparent density from the CT attenuation, HU (Hounsfield Units), for both cortical and cancellous bones (Snyder and Schneider, 1991):

$$\rho = 10.488 HU^{0.689655} \tag{2}$$

This relationship yields the apparent density ρ in kg/m^3. Separate relationships were used to calculate Young's and shear moduli for the cortical and cancellous bones. The relationships used to calculate the elastic constants for the femur and tibia are provided in Appendix B. To investigate the effects of homogeneity, a single set of elastic constants for each of the cortical and cancellous bones in the distal femur was calculated from their average CT attenuations (see Table B.1 in Appendix B). To investigate the effects of isotropy, the distal femur baseline model was modified by retaining only the axial Young's modulus and assigning a Poisson's ratio of 0.3 (Au et al., 2005) to each material property group.

3.2.4 Finite Element Model

FE models of the subject's femur and tibia bones were created to demonstrate the appropriateness of the grouping strategy via a convergence analysis. Three convergence indicators typically used in convergence analyses were employed in this study to compare the appropriateness of a particular grouping result, i.e. von Mises stress, strain energy density and nodal displacement (Zannoni et al., 1998; Viceconti et al., 1998; Peng et al., 2006). In FE modeling, accuracy is used as a measure of convergence, while validity indicates how faithfully the physical problem is simulated (Polgar et al., 2003). Thus, the convergence results can only

be used as a measure of internal accuracy, and are not necessarily indicative of true stress levels. A model was assumed to be accurate when all three indicators varied by less than 5% from baseline levels.

Geometries of the femur and tibia were generated from a CAD model created using the technique described in Chapter 2. The geometries were exported to ANSYS (Swanson Inc., Houston, PA) and meshed with 2 mm 10-node tetrahedral elements using HyperMesh (Altair Inc., Troy, MI) (Fig 3.4). The resulting femur model consisted of 107,498 elements (25,328 cortical and 82,170 cancellous) and 152,779 nodes. The tibia FE model consisted of 106,175 elements (24,680 cortical and 81,495 cancellous) and 149,997 nodes.

The grouping operation was performed exclusively in MATLAB, in isolation from the FE model. Once the grouping was completed, each bone meso-region was mapped to the FE mesh. To assign material properties to an element, the attenuation values of all voxels from the CT domain that intersected a particular element volume were averaged and assigned to the element in the FE domain. This average attenuation was then used to find Young's and shear moduli according to the technique described in Appendix B. Separate models were created for the 5 tolerance levels, as well as a baseline model with no grouping. In each of the 12 models (6 for the femur and 6 for the tibia), two point loads of 1000 N compression were placed on the condyles while the base of the shaft was fixed in all directions. The CPU time needed to generate a solution was observed for each model.

The cortex of each FE model was divided into 16 segments for a more detailed examination (Fig 3.4). A control segment was selected in the lateral cortex of the femur where the largest stresses and strain energy densities were observed (aside from the boundary conditions) (Fig 3.4); in the tibia, the control segment was in the posterior cortex. A *Student's t-test* was used to compare the stresses at each tolerance level with the baseline stresses. The appropriateness of the groupings at

each tolerance were examined with a two-tailed, unequal variance *t-test*, with significance assumed when $P<0.05$. These control segments were positioned sufficiently far from the boundary conditions to prevent influence from stress concentrations.

The remaining 15 segments in both bones were also observed, and showed trends similar to those observed in the control segment. Hence, the results from the control segment were used to demonstrate the general trends of the model.

3.2.5 Verification of grouping results

It is difficult to experimentally verify if the groups formed by the region split and merge technique have similar density because bone with similar density cannot easily be identified through bench-top or *in vivo* examination. However, bone density is strongly correlated with attenuation levels in CT images. Thresholding using an attenuation window is one way to highlight bone of similar density in a CT image. The pattern displayed by the highlighted bone in the thresholded image will change with adjustment of the attenuation window. A basic verification was performed by visually comparing thresholded CT slices of the subject's femur and tibia with their computed counterparts. In each slice, the split and merge procedure was applied with a tolerance level of 20%. This tolerance level was selected as it provided large groups of bone that were easily distinguishable in the CT image and, as will be shown below, resulted in the most accurate and computationally efficient model. After merging, the attenuation range of the largest meso-region was observed. The range was used to specify adjust the attenuation window for the corresponding thresholded CT slice. The attenuation window was applied as a binary threshold to the CT image, with pixels in black falling within the window. The shape of the region highlighted in the CT image was compared with the shape of the computed counterpart.

3.3 Results

3.3.1 Material Properties Distribution

Grouping the bone into meso-regions of similar attenuation substantially reduced the number of material property sets. Without any grouping, the femur FE model contained 47,159 different material properties (cortical and cancellous bone combined). Grouping with a 50% tolerance (i.e. reducing the degree of heterogeneity) reduced the number of material property sets to 1,210. A similar trend was seen with the FE tibia model (Table 3.2).

To gain a sense of the effect of the merging process, attenuation values before and after merging were observed for all levels of tolerance. A distribution of the attenuations showed a shift toward the median values of the baseline model's distribution. In the femur, the larger groups had attenuations of approximately 500 to 600 HU (Fig 3.5). In general, at higher tolerances, groups containing mid-level HU tended to be more frequent. Because several non-linear relationships were used to translate the HU to stiffness (see Appendix B), the frequency distribution of Young's moduli was slightly different from the HU distribution. However, because the merging operation is performed on the attenuation field, analysis of the results of the merging technique was focused on HU.

3.3.2 Computation time

The computational effort in this study was observed at two different intervals. The CPU time was measured during the grouping operation and then again during the FE operation. The finite element analysis time was differentiated into the time needed to assign material properties to the elements and the solution generation time. The time required to perform each operation is shown in Table 3.3. Operating at 10% tolerance required the greatest computational effort because time was needed to both group and calculate a solution. Implementing grouping at 50% tolerance required 97% less CPU time compared to no grouping.

3.3.3 Convergence

Solution convergence was studied by observing von Mises stresses, strain energy densities, and displacements in the control region. For each indicator, the convergence of three metrics was separately examined to determine the tolerance level at which convergence was reached. Note that the convergence was assessed with regards to the benchmark described earlier. Once the convergence was observed, an objective criterion for the level of heterogeneity was essentially established.

3.3.3.1 Von Mises Stress

For the von Mises stress indicator, the first metric observed was the maximum stress level of the control segment. Maximum stress converged toward the baseline value when a tolerance of less than 23% was applied (Fig 3.6a). A more detailed analysis was employed by observing the second metric, i.e. the stress levels of each element in the control segment. The stress levels of the elements (averaged together) generally decreased with increasing tolerance and diverged from the baseline stress when a tolerance of greater than 20% was used (Fig 3.7). The difference became significantly different with tolerances greater than 40% (Table 3.4). The third metric presented another method of measuring stress change, calculating the percentage change in stress level from its baseline level ($\Delta\sigma_e^{VM}$), i.e.

$$\Delta\sigma_e^{VM} = \left(\sigma_{tol}^{VM} - \sigma_{baseline}^{VM}\right) / \sigma_{baseline}^{VM}\Big|_i \qquad (3)$$

where σ_{tol}^{VM} is the von Mises stress at a selected tolerance level, $\sigma_{baseline}^{VM}$ is the stress at the baseline level, and i is the element index. This indicator measured the impact (in the context of stress change) of altering the Young's modulus of an individual element (a consequence of the grouping) from its "natural" non-grouped modulus. Once $\Delta\sigma_e^{VM}$ was determined for each element in the control segment, its mean value was calculated; this value is not the same as the percentage difference calculated from the mean stresses in Table 3.4. The mean

$\Delta\sigma_e^{VM}$ became greater than 5% when a tolerance of greater than 23% was applied (Fig 3.7a), with the difference becoming statistically significant when the tolerance was larger than 40% (Table 3.4). Considering the three different metrics, a tolerance of less than 20% must be applied to obtain accurate stresses for the case studied here. The convergence results of the FE tibia model showed a similar trend to the femur model, with stress accuracy achieved at approximately 20% tolerance (Fig 3.7b).

3.3.3.2 Strain Energy Density

The strain energy density was analyzed in the exact same manner as von Mises stress. Maximum strain energy density (SED) in the control segment converged toward the baseline value with tolerances below 23% (Fig 3.6a). The average SED in the elements of the control segment generally increased with larger tolerances and diverged away from baseline SED with tolerances greater than 23% (Fig 3.8). The difference became statistically significant with tolerances greater than 30% (Table 3.5). The percentage change of SED in each element relative to its baseline level (ΔSED_e) was calculated in the same manner as $\Delta\sigma_e^{VM}$. The mean ΔSED_e was greater than 5% with tolerance levels greater than 26% (Fig 3.8). This became significantly different when the tolerance was greater than 30% (Table 3.5). When considering SED, grouping using a tolerance of less than 23% will generate accurate solutions for the case studied here. In the tibia, SED convergence to baseline model values occurred at approximately 16% for all three metrics. These results were not displayed as they were similar to those of the femur model.

3.3.3.3 Nodal Displacement

Three metrics were also examined for the displacement, except displacements in the control segment were observed at nodes since element displacements were not available. Maximum nodal displacements converged toward baseline values with tolerances less than 16% (Fig 3.6b). Displacements averaged over the control

segment grew with increasing tolerance (Fig 3.9), becoming significantly different when tolerance was larger than 30% (Table 3.6). The percentage change in nodal displacement (ΔU_n) relative to the baseline model also increased with greater tolerance. The mean ΔU_n was greater than 5% when tolerance levels greater than 20% were employed (Fig 3.9), becoming significantly different when the tolerance was larger than 30% (Table 3.6). Considering the three different ways of analyzing displacement, a tolerance of less than 16% should be applied in order for nodal displacements to be accurate. In the tibia, all three displacement metrics converged to baseline model values at approximately 16% tolerance. These results were also not displayed as they were similar to those of the femur model.

For the specific case examined in this study, taking into account all three convergence indicators (i.e. stress, strain energy density and nodal displacement), the FE solution for the femur model would be considered accurate if the material properties were grouped using a tolerance level (α) of at most 16% to 20%. The FE tibia model was accurate when material properties were grouped with a slightly lower tolerance level of 16%. These tolerance values represent an objective level of heterogeneity that is most appropriate for the models of the particular subject.

3.3.3.4 Homogeneous and Isotropic Models

The FE femur model with homogeneous bone produced significantly different von Mises stresses, SED and nodal displacements compared to the fully heterogeneous baseline model (Table 3.7). Similarly, the incorporation of fully isotropic material properties resulted in significantly different von Mises stress, SED, and displacement differences from the baseline levels (Table 3.7).

3.3.4 Verification of grouping results

Two major bone groups were visible after applying the grouping procedure (with a tolerance level of 20%) to a CT slice of the femur. One group (containing bone

between 456 and 1138 HU) had two wing-like sections centered about the intercondylar notch. The corresponding CT image, thresholded with a 456 to 1138 HU attenuation window, produced an area of highlighted bone with similar shape (Fig 3.10). The second group was notable because of its hollow patch in the center; in its corresponding CT image thresholded with a 195 to 737 HU window, the cancellous bone in the center was also absent (Fig 3.11). This uncaptured region in the center is similar in shape to the hollow region of the merged bone.

Grouping of bone in a proximal tibia slice produced a meso-region with a large gap down the center (Fig 3.12). In the corresponding thresholded CT image, highlighted bone appeared on the medial and lateral regions with none appearing in the center.

3.4 Discussion

In subject-specific FE models, an appropriate representation of a subject's unique bone tissue properties is critical to accurate stress predictions. Bone density distribution in a subject's knee is heterogeneous and must be modeled in some fashion. The modeling of heterogeneous bone is typically simplified in FE models by grouping bone of similar density together. The conventional technique is to group solely on the density (or attenuation) of the bone without considering the anatomical location of the bone. Whereas this may be suitable for computational purposes, it gives no insight into the condition of the bone. A new technique is presented which performs a spatial analysis of the bone condition before grouping. As a result, bone groups that are formed not only have similar density but are spatially distinct from other groups; in essence, patches of bone with similar physiological condition are identified.

Such grouping is unique to this technique because it allows for regions with overlapping attenuations unlike the conventional method where bone is grouped in regions with distinct non-intersecting attenuation ranges (Peng et al., 2006;

Lengsfeld et al., 1998; Keyak et al., 1993). A comparison of the two merging techniques can be provided using a bone slice from the distal tibia. Using the technique presented in this study, the merged bone contained three regions with overlapping attenuation ranges (Fig 3.13). Regions 1 and 3 contained very similar attenuation ranges compared to the much lower range of Region 2. Using the conventional method described in Taddei et al. (2006), the tibial bone was divided into 381 groups, each with a range of approximately 4 HU. Even with such a narrow range, each group generally contained bone throughout the tibia because of the heterogeneous nature of bone. For example, the group that captured anterior bone similar to Region 1 also captured some posterior cancellous bone (Fig 3.13b). These two regions are physically removed from each other, and therefore our technique considers them as distinct groups despite their similar attenuations. This method provides much more flexibility in distinguishing regions of similar bone to accommodate the extremely heterogeneous nature of bone.

The development of a methodology to detect localized regions of similar bone density within extremely heterogeneous bone tissue can have exciting clinical applications. For example, the technique can be used as a tool for detecting early failure of total knee replacement (TKR) surgery. Post-operative CT images of TKR recipients can be analyzed to identify and, more importantly, quantify regions of relatively weaker bone in the knee. The potential shrinkage of these regions of interest due to osteoporosis can be tracked over time and the change in the actual bone density values of such regions can be calculated. Using such information, the clinician can recommend treatment programs to improve the outcome of the TKR surgery for the patient.

The difficulty in distinguishing cortical from cancellous bone geometry in subject-specific modeling techniques has led to the use of bone grouping to assist in segmentation (Taddei et al., 2004). The method to date cannot clearly distinguish between cortical and cancellous bone, as can be seen in Figs 3.10 to

3.12, where groups meant to exclusively group cancellous bone inadvertently captured cortical bone as well. This is a consequence of the physiological nature of bone whereby density is not always associated with its location. Thus, using the conventional material properties modeling technique to perform segmentation is not likely to be successful. Even with the inherent spatial analysis in the technique presented here, some cancellous bone meso-regions would merge with cortical bone meso-regions if the two bones were not considered separately.

The consequences of an inability to distinguish cortical from cancellous bone should not be underestimated. The empirical relationships used to estimate the stiffness of the cortical bone are different from those used for the cancellous bone (Rho et al., 1995). If a bone group contains a mixture of cortical and cancellous bone and its stiffness is interpreted with a relationship intended exclusively for cortical bone, the stiffness of the group will generally be overestimated. As an alternative, many studies have used the relationship reported in Carter and Hayes (1977), which is supposedly applicable across the range of cortical and cancellous bone densities. However, it has been shown that mechanical properties of cortical and cancellous bones are too different to be described by a single relationship (Rice et al., 1988; Rho et al., 1995). Since neither the conventional technique nor the technique presented in this study can adequately separate cortical from cancellous bone, a geometry-based technique such as the one presented in Chapter 2 must be relied upon to distinguish the two bones before their material properties can be interpreted from the CT data.

3.4.1 Verification of grouping results

It is difficult to experimentally verify the results of the present technique because regions with small density ranges cannot easily be identified *in vitro* and is even more difficult *in vivo*. A method of verifying the appropriateness of the groups generated by the technique presented in this study was through visual comparison with groups generated by a commonly used method. Thresholding is essentially a method of identifying a single group of bone of similar density within a CT

image, with a similarity criterion defined by the attenuation window. The region split and merge technique identifies groups of similar bone under a different similarity criterion defined by a tolerance parameter (α). For an identical attenuation range, the bone group generated using the thresholding technique should contain relatively the same bone as the group generated using the region split and merge technique, although the split and merge procedure may have sub-divided the thresholded bone into several groups if they were not physically connected.

Bone grouped at demonstrated slices in the femur and tibia produced meso-regions with very unique shapes that were also distinguishable in the thresholded groups. For example, adjusting the attenuation window to a range of 456 to 1138 HU produced a wing-shaped group in the thresholded image that was also generated by the region split and merge technique. Several other irregularly shaped groups containing large holes or gaps were verified against the thresholding technique for a number of different attenuation windows. However, the regions formed in split and merge technique did not include the small isolated groups of bone scattered throughout the thresholded image. This demonstrated the unique ability of this technique to identify bone that is anatomically representative, i.e. the groups formed are spatially similar in addition to having similar attenuation.

The clear similarity between the groups produced with the region split and merge technique and the threshold technique provides strong evidence toward the appropriateness of the former technique in identifying naturally observed patterns in bone density. It should be emphasized that the group produced in the region split and merge was not obtained by adjusting an attenuation window but was arrived at objectively as a consequence of grouping based on a non-attenuation based parameter (α).

The grouping procedure used 2 different constraints to identify bone of similar attenuation, rather than using the same constraint for both stages of the procedure as is normally recommended (Gonzalez and Woods, 2008). This was necessary to avoid biasing the results towards the order in which the regions were merged. With a spread-based constraint (equation (2)), grouping results were insensitive to the merging order. The appropriateness of applying two different constraints was confirmed from the results of the verification.

3.4.2 Convergence Tolerance

The merging technique was applied to FE models of the femur and tibia to objectively determine a level of heterogeneity that provided both computational savings and an accurate solution. Modeling full heterogeneity is computationally expensive and can be eased by collecting bone into groups with similar densities. Within a certain tolerance level, the stress, SED and displacement results of these simplified models still converged toward the results of the fully heterogeneous model. Accurate solutions (i.e. within 5% of baseline values) were achieved when tolerance levels of less than 20% were used in the grouping procedure (Fig 3.14). In the FE femur model, this degree of heterogeneity required 19,454 unique material property sets.

The number of material property sets needed to generate accurate solutions in other FE femur models was much lower than the number suggested in this study. At least 15 different material properties needed to be assigned to a proximal femur model to generate maximum von Mises stresses and displacements within 5% of baseline levels (Peng et al., 2006). In a distal femur, at least 23 materials were needed to yield a maximum SED error below 10% of baseline (Zannoni et al., 1998). However, a greater level of heterogeneity seems to be associated with better accuracy: a proximal femur model containing 82 groups achieved good accuracy (r^2=0.77; Keyak et al., 1993) while a model containing 381 groups achieved an even better accuracy (r^2=0.91; Taddei et al., 2006).

However, the above comparison must be tempered by the fact that the above models were mainly proximal femora. Also, the grouping technique developed in this study was based on completely different principals. The conventional technique groups bone based on an adjustable attenuation window whereas this technique groups bone based on a combination of spatial and attenuation criteria. This technique presented here uses a greater amount of distinction in its grouping analysis, resulting in smaller and more numerous groups. As illustrated by Fig 3.13, larger groups in the other models would likely be broken down into smaller groups with the present technique. Most importantly, the number of material property groups employed in the above models varied greatly, a consequence of the subjective nature of the conventional material properties modeling technique. The studies offered no explanation for the particular selection of bone groups, suggesting that the level of heterogeneity modeled was purely arbitrary. Thus, it is difficult to establish what is considered an appropriate level of heterogeneity when the conventional technique is applied. This can be established by the present technique based on an objective parameter, i.e. tolerance level. Incorporating such a technique would allow better comparison across various subjects to gain a general sense of how much heterogeneity needs to be modeled.

3.4.3 Homogeneous and Isotropic Bone Properties

Increasing the tolerance level reduces the number of groups by assuming that bone which can be quite different is rather similar. With a large enough tolerance, all bone would be assumed similar, i.e. homogeneous. Previous studies have demonstrated that homogeneity affects the results of stress, displacement, and strain energy density distribution (Zannoni et al., 1998; Peng et al., 2006; Taddei et al., 2006). Stresses and displacements in a FE proximal femur model were quite different when homogeneity was assumed (Peng et al., 2006). Similarly, a distal femur model assuming homogeneous bone produced a maximum strain energy density 170% greater than when 614 different material properties were used (Zannoni et al., 1998).

In this study, it was found that homogeneity affected stress, SED, and displacement results in the distal femur (Table 3.7). The results were quite similar to those seen when a 50% tolerance was used in the grouping procedure, and therefore were not considered accurate relative to the baseline model. Hence, merging with a 50% tolerance is rather impractical since computational effort is required to generate over 1000 different bone groups yet the stress solution is practically identical to a homogeneous model. The Young's moduli of cortical and cancellous bones in the homogeneous model was considerably different than that assumed in another subject-specific homogeneous model, e.g. 19.3 GPa (cortex) and 590 MPa (cancellous) (Taddei et al., 2006). It is unclear how the two bone types were delineated in that model but, in this study, cortical and cancellous bones were carefully distinguished using the technique described in Chapter 2. Therefore, cortical and cancellous bones were interpreted using different equations (Rho et al., 1995) whereas the other study employed one single equation to interpret both bone types.

A parametric comparison of isotropic and orthotropic bone properties showed they only had small differences on stresses and displacements in the proximal femur (Peng et al., 2006). However, in this study, significant stress, SED, and displacement differences were seen in the distal femur (Table 3.7), even under axial loading for which the assumption of isotropic bone is most applicable (Huiskes et al., 1983). The results of this study suggest that material property simplifications such as homogeneity and isotropy that are appropriate for the proximal femur cannot automatically be assumed to be appropriate for the distal femur. The greater sensitivity to these two particular characteristics may originate from the large differences in anatomical geometries and material properties between the proximal and distal femora (Rho, 1992), and would suggest that their biomechanical responses to axial loading are likely different.

3.4.4 Computational Effort

The main necessity of employing a grouping procedure is to reduce computational time while maintaining the integrity of the results. In the baseline model, where each element is assigned a unique material property, the computational time required to assign the material properties was greater than the time needed to calculate the actual solution. The grouping operation adds additional time to the modeling process but is ultimately beneficial through reduced material property assignment time. However, a computationally-reduced model must at minimum generate an accurate solution. The baseline model took 444 minutes of CPU time to produce a solution. However, similarly acceptable stress predictions (i.e. within 5% of baseline levels) can be generated in half the time by modeling heterogeneity with a tolerance level of 20%.

In the subject-specific FE models of this study, stresses, strain energy densities, and displacements in the control region exhibited instabilities at tolerances larger than 30%, as seen in the peaks and valleys of the trends displayed in Figs 3.6 to 3.8. The idea of the grouping technique is to replace the true attenuation of the bone with a slightly less accurate but representative attenuation. A slight deviation in attenuation will produce a slightly different but acceptable result in the finite element model. However, for the case studied, the deviation became unacceptable at tolerances above 30%, since a majority of the pixels were grouped into mid-range attenuation levels (Fig 3.5). The grouping was not always predictable because of the complex bone density distributions present in physiological systems. As a result, some unrepresentative low- to mid-range attenuation groups dominated, thus reducing the general stress level and underestimating the true stresses. In contrast, the 20% tolerance level generated an even distribution of groups in low-, mid- and upper-range attenuation levels. As such, a more accurate reflection of the true stress state was generated.

3.4.5 Mapping Strategy

Techniques used to map CT data to finite elements can influence the stress distribution (Taddei et al., 2004). In this study, element attenuations were calculated by averaging the attenuations of voxels intersecting the element. A simpler and faster approach to mapping the groups was to assign each finite element the attenuation of its nearest CT voxel (Merz et al., 1996; Peng et al., 2006). This approach reduced the number of unique property sets in the FE model to amounts that were similar to other FE studies (Keyak et al., 1993; Taddei et al., 2006) (Table 3.8). The smaller number of groups reduced computational time used in finite element analysis, but the models generated stresses that were noticeably different from their counterparts (Table 3.9). Such stresses are likely less representative of the physiological situation. Although averaging the CT data to estimate the element attenuation substantially increased the CPU time, it likely produced a better representation of bone heterogeneity, and has been shown to produce accurate stress predictions (Taddei et al., 2006).

3.5 Summary and Conclusions

In this study, subject-specific models of the distal femur and proximal tibia with accurately defined cortical bone thicknesses were used to examine the modeling of bone heterogeneity. An innovative application of an image processing technique in the context of material properties modeling was introduced to facilitate a new grouping strategy, which gathered together bone based not only on density but also on location. The technique emphasized the need for an objective methodology to model an appropriate level of heterogeneity that captures the natural variation of bone density seen in CT images. The subsequent FE models would lend themselves to better FE analyses.

A comparison with thresholded CT images verified that bone groups generated from the new technique were anatomically realistic. The verified technique was used to examine the minimal level of heterogeneity needed in a FE model to generate an accurate solution with minimal computational effort. A fully

heterogeneous model containing unique material properties for each finite element was not necessary to generate an appropriate solution. Von Mises stress, strain energy density, and nodal displacements could still be predicted within 5% accuracy using a simplified FE femur model containing approximately 20,000 (rather than 47,000) bone groups, each with attenuations varying less than 20% from the group mean. In the FE tibia model, a maximum attenuation variability of 16% was needed to achieve an accurate solution. For both models, a substantial computational time savings of 60% was gained with the simplified bone properties. An oversimplified representation of bone properties, such as homogeneity and isotropy, produced significantly different stress levels from the more representative heterogeneous models.

Table 3.1: Specifications of CT images obtained in vivo *from a 37-year-old human female.*

Slice Orientation	Field of View (mm)	Thickness (mm)	Separation (mm)	Overlap (mm)	Resolution (mm/pixel)
Transverse	300	1.25	1.0	0.25	0.5859
Sagittal	300	2.00	2.9	0	0.5859

Table 3.2: Number of groups generated from grouping operation for each tolerance. The groups include cortical and cancellous bone.

Tolerance (%)	Femur	Tibia
0	47,159	40,605
10	35,944	26,092
20	19,454	14,652
30	4,973	2,341
40	2,959	1,183
50	1,210	261

Table 3.3: Computational times needed to group bone into similar regions using MATLAB. Times to assign material properties to the model and solution generation times are also compared for different tolerance levels.

Tolerance (%)	Grouping time (minutes)	Material properties assignment time (minutes)	Solution time (minutes)	Total time (minutes)
0	N/A	440	4	444
10	186	345	4	535
20	50	117	4	171
30	17	29	4	50
40	8	20	4	32
50	4	7	4	15

Table 3.4: Mean and standard deviation of von Mises stress in elements of control segment at various tolerance levels. Also included are the mean and standard deviation of relative stress difference ($\Delta\sigma_e^{VM}$, calculated from equation (3)) for each tolerance level. The mean $\Delta\sigma_e^{VM}$ is not calculated from the mean stress values in the second column from the left hand side of the Table. (*) indicates a significant difference from the baseline (0% tolerance) stress.

Tolerance (%)	Von Mises Stress		Stress Difference from Baseline ($\Delta\sigma_e^{VM}$)	
	Mean (MPa)	SD (MPa)	Mean	SD
0	4.34	2.82	--	--
10	4.29	2.81	2%	2%
20	4.33	2.87	4%	3%
30	4.31	2.53	11%	10%
40	3.87*	2.32	16%*	11%
50	3.67*	2.29	19%*	12%

Table 3.5: Mean and standard deviation of strain energy density (SED) in elements of control segment at various tolerance levels. Also included are the mean and standard deviation of relative SED difference (ΔSED_e) for each tolerance level. The mean ΔSED_e is not calculated from the mean SED the second column from the left hand side of Table. (*) indicates a significant difference from the baseline (0% tolerance) SED.

Tolerance (%)	Strain Energy Density		SED Difference from Baseline (ΔSED_e)	
	Mean (J/mm^3)	SD (J/mm^3)	Mean	SD
0	$1.84x10^{-3}$	$2.57x10^{-3}$	--	--
10	$1.83x10^{-3}$	$2.59x10^{-3}$	3%	2%
20	$1.83x10^{-3}$	$2.56x10^{-3}$	4%	3%
30	$2.18x10^{-3}$*	$2.97x10^{-3}$	23%*	16%
40	$2.07x10^{-3}$*	$2.96x10^{-3}$	18%*	16%
50	$2.14x10^{-3}$*	$3.17x10^{-3}$	19%*	16%

Table 3.6: Mean and standard deviation of nodal displacements in control region at various tolerance levels. Also included are the mean and standard deviation of relative displacement difference (ΔU_n) for each tolerance level. The mean ΔU_n is not calculated from the mean displacement in the second column from the left hand side of Table. (*) indicates a significant difference from the baseline (0% tolerance) displacement.

Tolerance (%)	Nodal Displacement		Displacement Difference from Baseline (ΔU_n)	
	Mean (mm)	SD (mm)	Mean	SD
0	2.44×10^{-2}	1.85×10^{-2}	--	--
10	2.46×10^{-2}	1.85×10^{-2}	1%	1%
20	2.53×10^{-2}	1.85×10^{-2}	5%	3%
30	2.89×10^{-2}*	2.14×10^{-2}	18%*	6%
40	3.13×10^{-2}*	2.20×10^{-2}	32%*	9%
50	3.38×10^{-2}*	2.35×10^{-2}	43%*	11%

Table 3.7: Means and standard deviations of von Mises stress, strain energy density, and nodal displacement in control segment with homogeneous and isotropic bones. Data for the baseline model and at 50% tolerance are included for comparison. Also included are the means and standard deviations of relative displacement differences. (*) indicates a significant difference from the baseline (0% tolerance) value.

Tolerance (%)	Von Mises Stress		Stress Difference ($\Delta\sigma_e^{VM}$)		Strain Energy Density		SED Difference (ΔSED_e)		Nodal Displacement		Displacement Difference (ΔU_n)	
	Mean (MPa)	SD (MPa)	Mean	SD	Mean (J/mm^3)	SD (J/mm^3)	Mean	SD	Mean (mm)	SD (mm)	Mean	SD
0	4.34	2.82	--	--	$1.84x10^{-3}$	$2.57x10^{-3}$	--	--	$2.44x10^{-2}$	$1.85x10^{-2}$	--	--
50	3.67*	2.29	19%*	12%	$2.14x10^{-3}$*	$3.17x10^{-3}$	19%*	16%	$3.38x10^{-2}$*	$2.35x10^{-2}$	43%*	11%
Homogeneous	3.64*	2.31	19%*	12%	$2.16x10^{-3}$*	$3.24x10^{-3}$	19%*	15%	$3.41x10^{-2}$*	$2.38x10^{-2}$	44%*	11%
Isotropic	3.85*	2.60	15%*	12%	$1.31x10^{-3}$*	1.78E-03	31%*	18%	$1.94x10^{-2}$*	$1.54x10^{-2}$	23%*	9%

Table 3.8: A comparison of the number of groups generated using two different mapping strategies. The first strategy averaged the pixel attenuations intersecting an element (AVERAGED); the second assigned an element the attenuation value of the nearest pixel (UNAVERAGED). Results are compared for both cortical and cancellous bone.

	Number of Groups			
Tolerance	Cortical Bone		Cancellous Bone	
(%)	Averaged	Unaveraged	Averaged	Unaveraged
0	12,420	1,206	34,739	892
10	10,294	67	25,650	62
20	5,976	29	13,478	28
30	3,134	8	1,839	7
40	1,298	8	1,661	6
50	358	5	852	5

Table 3.9: A comparison of the von Mises stresses in control segment of FE femur model with elements mapped using two strategies. The first strategy averaged the pixel attenuations intersecting an element (AVERAGED); the second assigned an element the attenuation value of the nearest pixel (UNAVERAGED).

	Von Mises Stress (MPa)			
Tolerance	Averaged		Unaveraged	
(%)	Mean	SD	Mean	SD
0	4.34	2.82	4.58	2.89
10	4.29	2.81	4.53	2.87
20	4.33	2.87	4.58	2.94
30	4.31	2.53	4.57	2.54
40	3.87	2.32	3.96	2.30
50	3.67	2.29	3.68	2.29

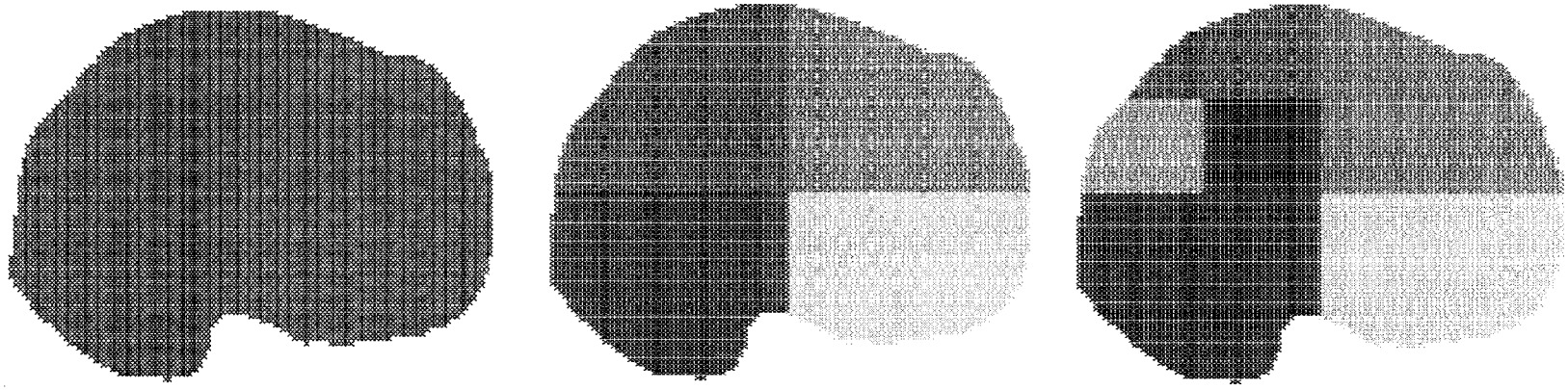

Figure 3.1: An example of the splitting procedure. (a) A region of tibial cancellous bone under analysis (before the splitting procedure). (b) Since the region did not meet the similarity criterion, it was divided into 4 sub-regions. (c) The top-left sub-region did not meet the similarity criterion and was further sub-divided into 4 smaller regions.

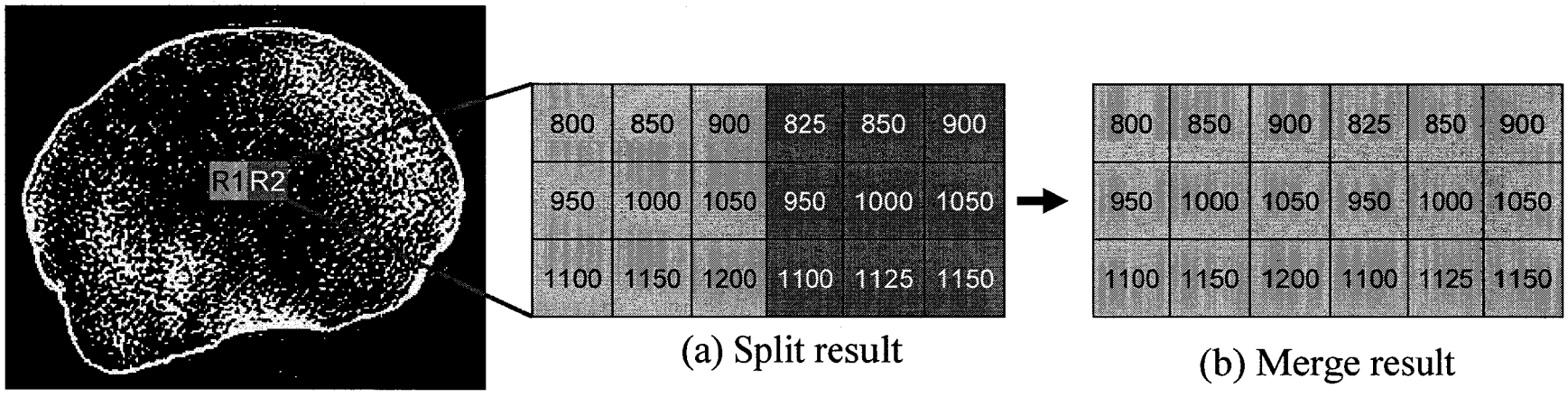

Figure 3.2: Sub-regions R1 and R2 are two groups of bone taken from the cancellous bone of the tibia approximately 20 mm from the joint line. Each box represents a pixel and its associated attenuation value is given. (a) Region splitting results in two groups of pixels, R1 (light gray) and R2 (dark gray). The attenuation spread of R1 is 800 - 1200 HU; the spread of R2 is 825 - 1150 HU. The attenuations in R1 have a greater spread, therefore merging begins with R1. The attenuations of all the pixels in R2 are within the spread of R1 therefore it is merged with R1. The result is a meso-region containing the pixels of R1 and R2, as shown in (b). The spread of the meso-region is 800 - 1200 HU, the same as it was for R1 before the merge.

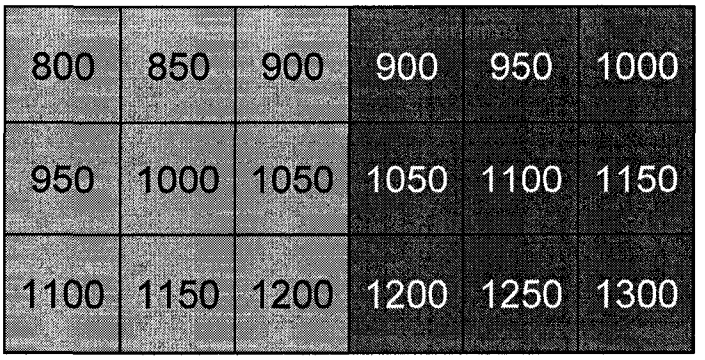

Merge result without enhanced procedure
(a)

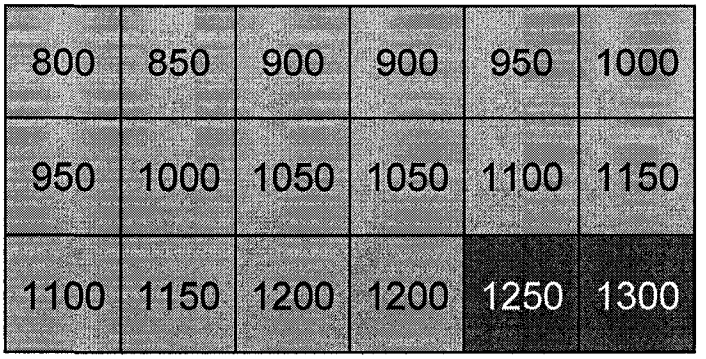

Merge result with enhanced procedure
(b)

Figure 3.3: An example of the enhanced merge procedure, which allows smaller parts of a whole region to be merged. The attenuation spread of R1 is 800 - 1200 HU; the spread of R2 is 900 - 1300 HU. If only whole regions are allowed to merge, regions R1 and R2 would remain separate with a straight border between them, as shown in (a). With the enhanced procedure, which allows for curved borders between neighbouring regions, a sub-region of R2 would merge with R1 resulting in a curved border between the regions, as shown in (b) (note that the dark boxes (pixels) will form part of the curve). The spread of R1 would remain 800 - 1200 HU while the spread of R2 becomes 1250 - 1300 HU.

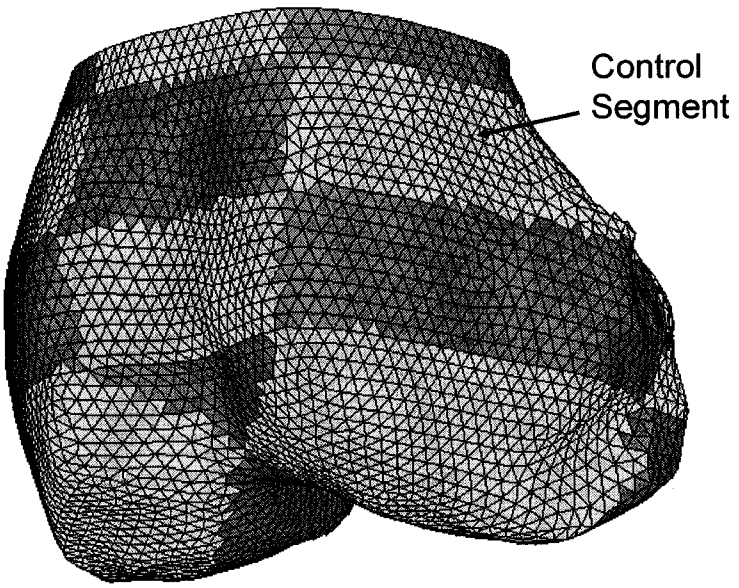

Figure 3.4: The 16 divided segments of the femur cortex with control segment used for convergence analysis identified.

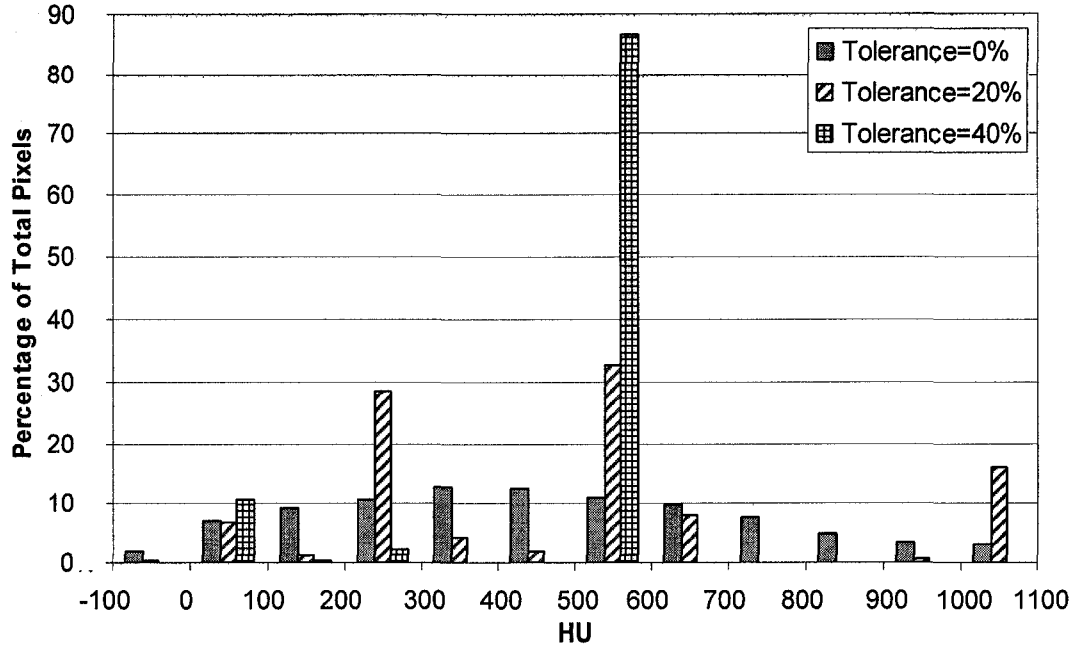

(a)

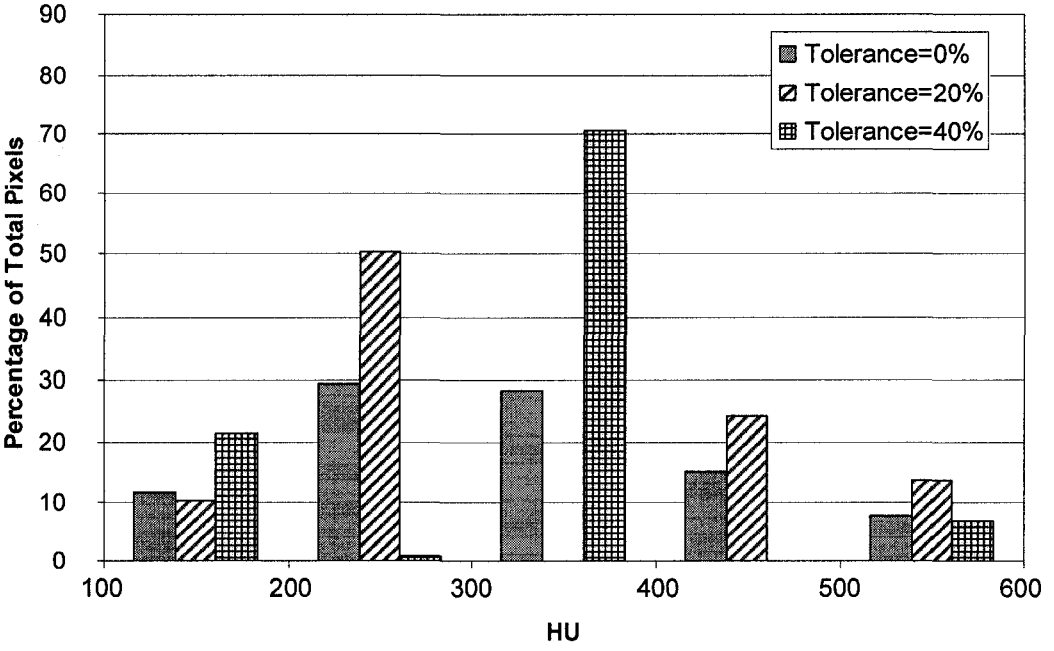

(b)

Figure 3.5: Distribution of attenuation values for femur (a) cortical bone and (b) cancellous bone grouped using three different tolerance levels.

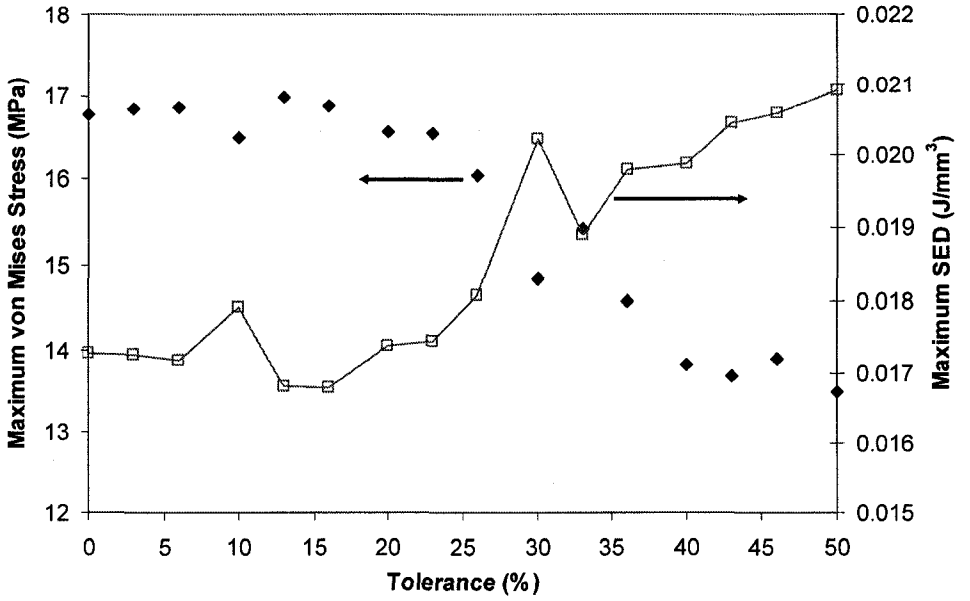

(a)

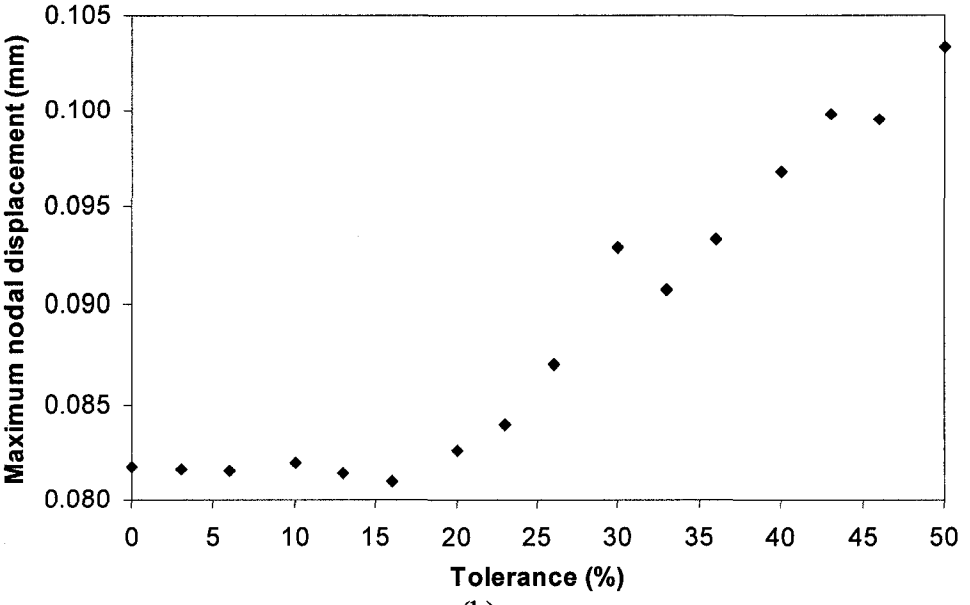

(b)

Figure 3.6: The maximum von Mises stress, strain energy density and nodal displacements as a function of tolerance level. For FE femur model: (a) Comparison of maximum von Mises stress and strain energy density with tolerance levels in control segment (the line is to guide the eyes); (b) comparison of maximum nodal displacement with tolerance levels in control segment. Stresses data should be read from left axis; strain energy density should be read from right axis.

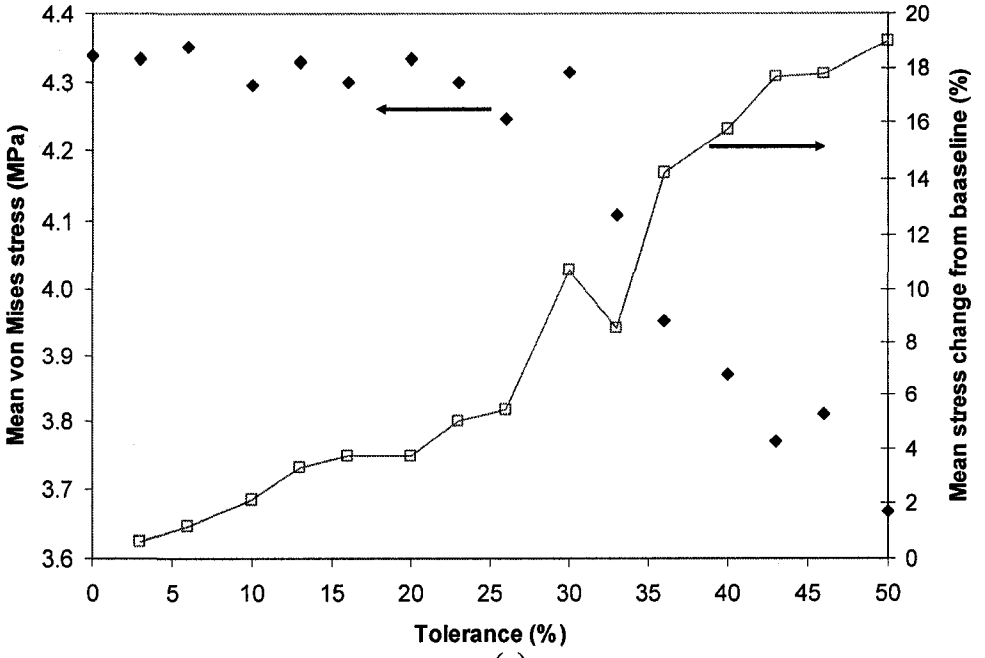

(a)

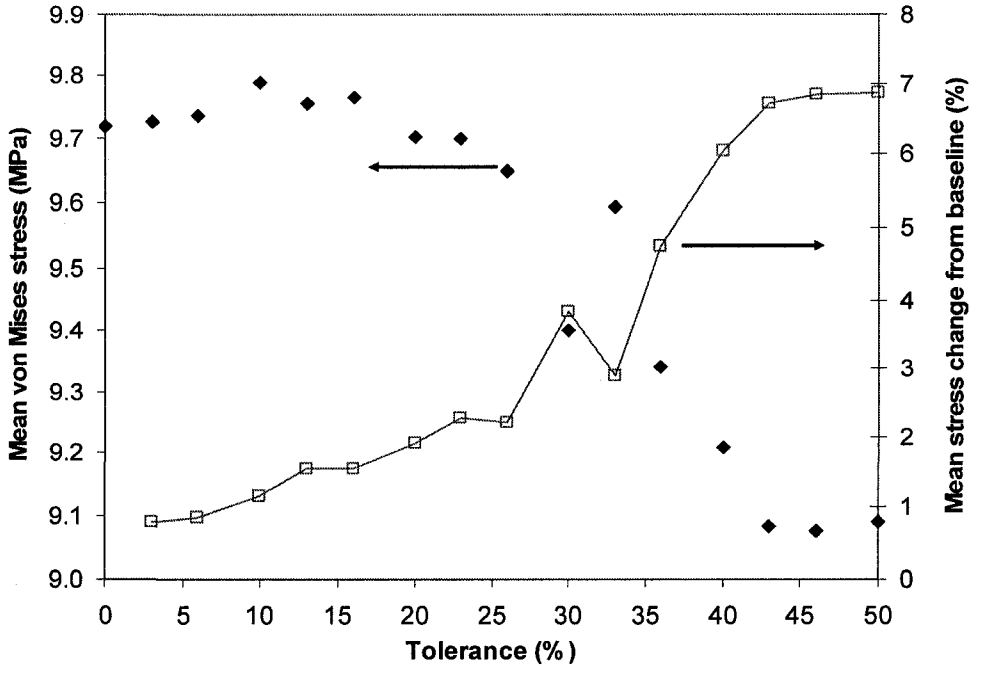

(b)

Figure 3.7: Comparison of mean von Mises stresses with tolerance level (left axis). The mean stress change in each element from baseline levels are also compared for various tolerance levels (right axis). The results for the FE femur and tibia models are displayed in (a) and (b), respectively. The lines are to guide the eyes.

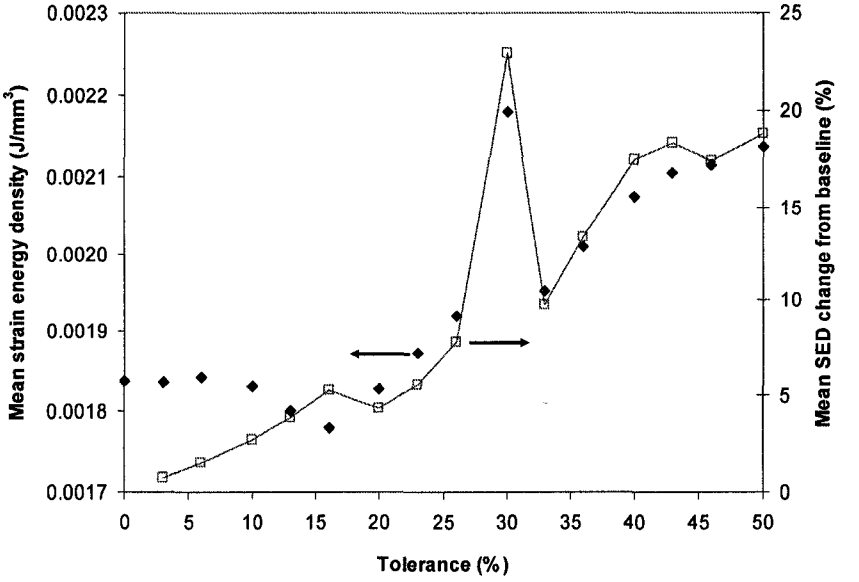

Figure 3.8: Comparison of mean strain energy density with tolerance level (left axis) for the FE femur model. The mean strain energy density change in each element from baseline levels are also compared for various tolerance levels (right axis). The line is to guide the eyes.

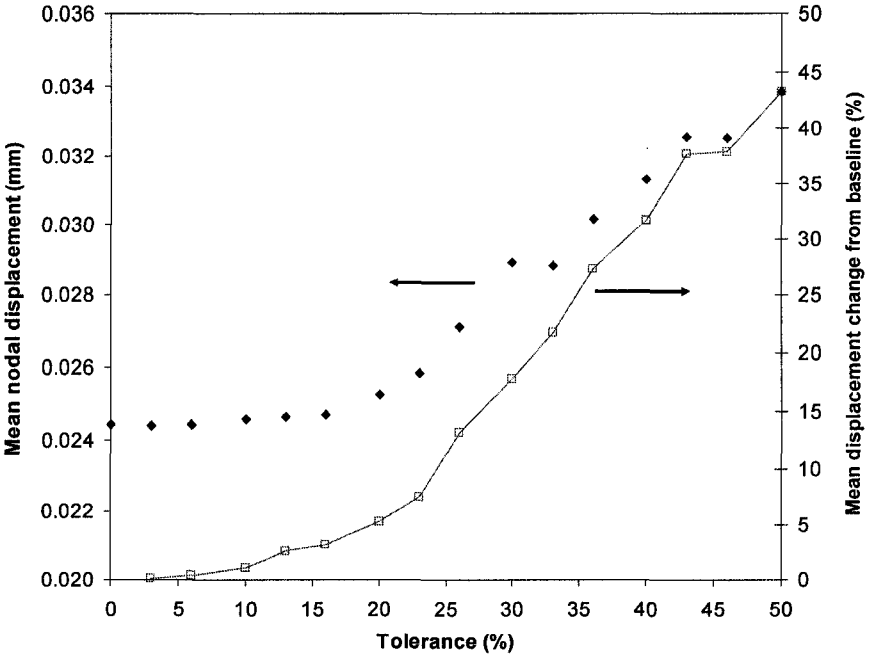

Figure 3.9: Comparison of mean nodal displacement with tolerance level (left axis) for the FE femur model. The mean displacement change in each node from baseline levels are also compared for various tolerance levels (right axis). The line is to guide the eyes.

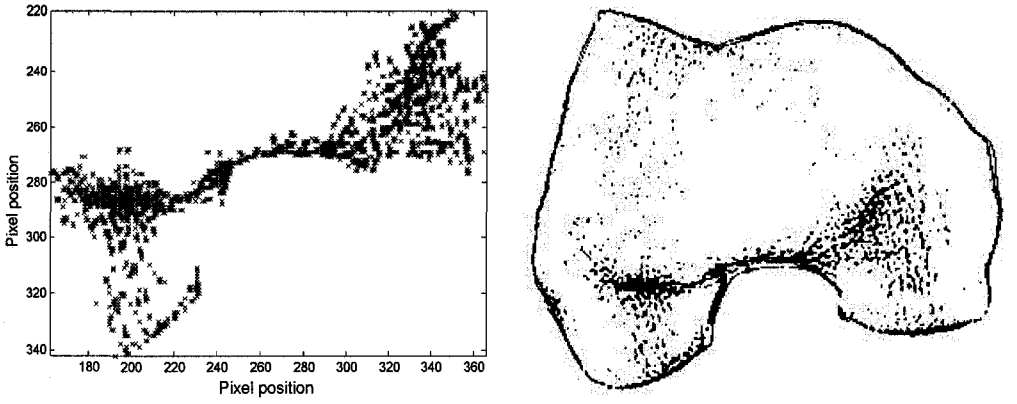

(a) (b)

Figure 3.10: The cancellous bone of a CT slice of the femur located approximately 28 mm from the joint line merged using a tolerance level of 20%. A region containing attenuations between 456 and 1138 HU emerged, shown in (a). The CT image was thresholded using this range resulting in the image shown in (b), where the highlighted bone anterior to the intercondylar notch is very similar in shape to the merged region. Note that (a) is a zoomed view of area shown in (b).

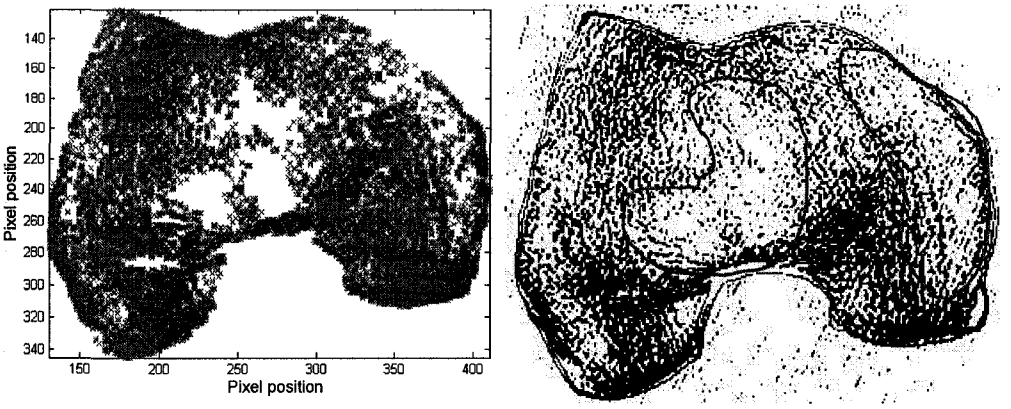

(a) (b)

Figure 3.11: The cancellous bone of a CT slice of the femur located approximately 28 mm from the joint line merged using a tolerance level of 20%. A region containing attenuations between 195 and 737 HU emerged, shown in (a). The CT image was thresholded using this range resulting in the image shown in (b), where the highlighted bone is very similar in shape to the merged region, including the softer cancellous bone in the regions enclosed by the red border.

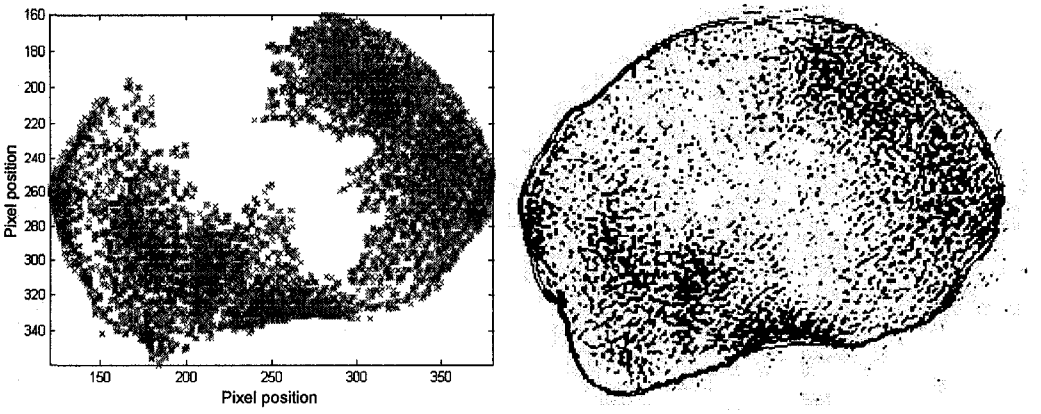

(a) (b)

Figure 3.12: The cancellous bone of a CT slice of the tibia located approximately 20 mm from the joint line merged using a tolerance level of 20%. A region containing attenuations between 243 and 848 HU emerged, shown in (a). The CT image was thresholded using this range resulting in the image shown in (b), where the highlighted bone is very similar in shape to the merged region, including the softer cancellous bone in the center.

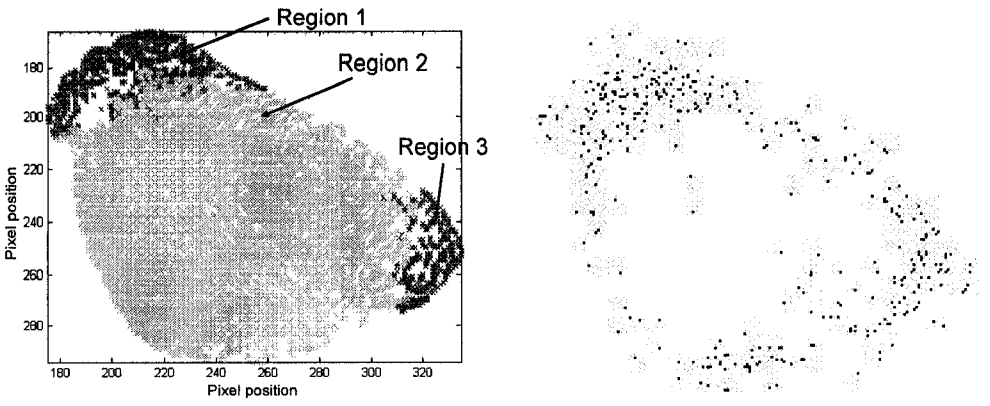

(a) (b)

Figure 3.13: The cancellous bone of a CT slice of the tibia located approximately 55 mm from the joint line merged using a tolerance level of 20%. Regions with three separate attenuations ranges emerged, shown in (a). Region 1 contains attenuations from 358 to 1017 HU; region 2 contains attenuations from -102 to 339 HU; region 3 contains attenuations from 337 to 1000 HU. The bone was also grouped with a conventional method. A resulting region containing attenuations from 356 to 360 HU is shown in (b). Using this method, outer fringes of cortical bone were also captured with the cancellous bone. Note that this is a result of the methods used to date.

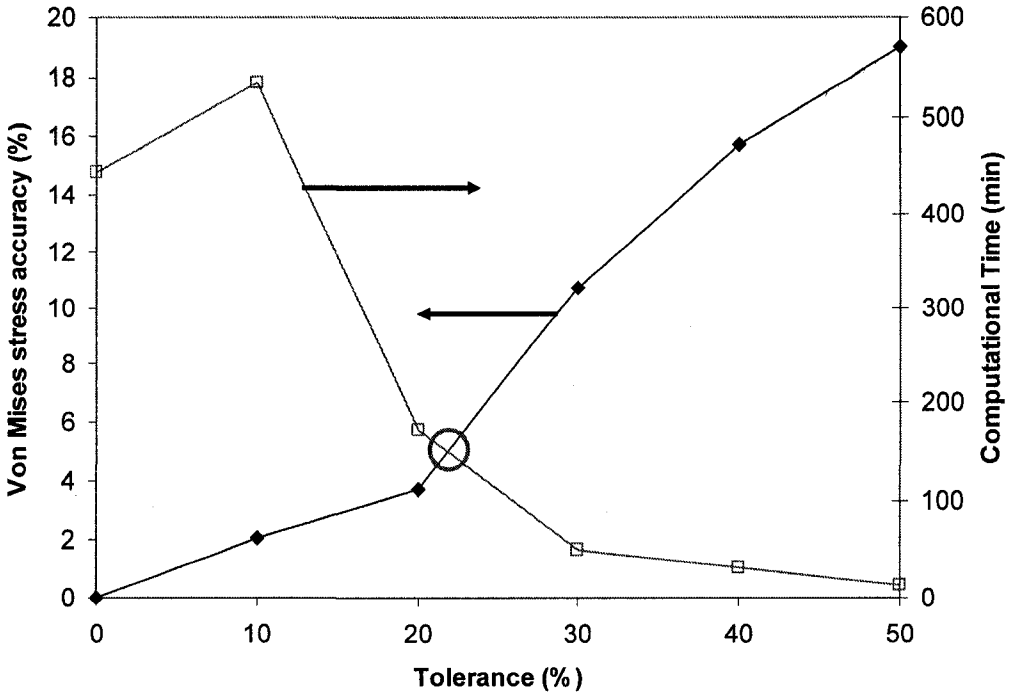

Figure 3.14: A comparison of von Mises stress accuracy and computational time required to generate solutions for each tolerance level in the FE femur model. A tolerance level of 20% can provide a balance between an accurate solution (i.e. error < 5%) and minimal computational time.

References

Askew, M. J., Lewis, J. L., 1981. Analysis of model variables and fixation post length effects on stresses around a prosthesis in the proximal tibia. Transactions of ASME, Journal of Biomechanical Engineering 103, 239-245.

Ashman, R. B., Rho, J. Y., Turner, C. H., 1989. Anatomical variation of orthotropic elastic moduli of the proximal human tibia. Journal of Biomechanics 22, 895-900.

Au, A. G., Liggins, A. B., Raso, V. J., Amirfazli, A., 2005. A parametric analysis of fixation post shape in tibial knee prostheses. Medical Engineering and Physics 27, 123-134.

Au, A. G., Palathinkal, D., Liggins, A. B., Raso, V. J., Carey, J., Lambert, R. G., Amirfazli, A., 2008. A NURBS-based technique for subject-specific construction of knee bone geometry. Computer Methods and Programs in Biomedicine 92, 20-34.

Ciarelli, M.J., Goldstein, S.A., Kuhn, J.L., Cody, D.D., Brown, M.B., 1991. Evaluation of orthogonal mechanical properties and density of human trabecular bone from the major metaphyseal regions with materials testing and computed tomography. Journal of Orthopaedic Research 9, 674-682.

Gonzalez, R.C., Woods, R. E., 2008. Digital Image Processing, 3rd ed. Pearson Prentice Hall, Upper Saddle River, NJ.

Huiskes, R., Janssen, J. D., Slooff, T. J., 1981. A detailed comparison of experimental and theoretical stress-analyses of a human femur. Proceedings of the joint ASME-ASCE applied mechanics, fluids engineering and bioengineering conference AMD, 211-234.

Keyak, J.H., Fourkas, M.G., Meagher, J.M., Skinner, H.B., 1993. Validation of an automated method of three-dimensional finite element modelling of bone. Journal of Biomedical Engineering 15, 505-509.

Lengsfeld, M., Schmitt, J., Alter, P., Kaminsky, J., Leppek, R., 1998. Comparison of geometry-based and CT voxel-based finite element modelling and experimental validation, Medical Engineering and Physics 20, 512-522.

Merz, B., Niederer, P., Muller, R., Ruegsegger, P., 1996. Automated finite element analysis of excised human femora based on precision-QCT. Transactions of the ASME: Journal of Biomechanical Engineering 118, 387-390.

Peng, L., Bai, J., Zeng, X., Zhou, Y., 2006. Comparison of isotropic and orthotropic material property assignments on femoral finite element models under two loading conditions. Medical Engineering and Physics 28, 227-233.

Rice, J. C., Cowin, S. C., Bowman, J. A., 1988. On the dependence of the elasticity and strength of cancellous bone on apparent density. Journal of Biomechanics 21, 155-168.

Rho, J. Y., 1992. Mechanical properties of cortical and cancellous bone. Ph.D. Dissertation, University of Texas Southwestern Medical Center, Dallas, TX, USA.

Rho, J.Y., Hobatho, M.C., Ashman, R.B., 1995. Relations of mechanical properties to density and CT numbers in human bone. Medical Engineering and Physics 17, 347-355.

Snyder, S.M., Schneider, E., 1991. Estimation of mechanical properties of cortical bone by computed tomography. Journal of Orthopaedic Research 9, 422-431.

Taylor, W.E., Roland, E., Ploeg, H., Hertig, D., Klabunder, R., Warner, M.D., Hobatho, M.C., Rakotamanana, L., Clift, S.E., 2002. Determination of orthotropic bone elastic constants using FEA and modal analysis. Journal of Biomechanics 35, 767-773.

Taddei, F., Pancanti, A., Viceconti, M., 2004. An improved method for the automatic mapping of computed tomography numbers onto finite element models. Medical Engineering and Physics 26, 61-69.

Taddei, F., Cristofolini, L., Martelli, S., Gill, H.S., Viceconti, M., 2006. Subject-specific finite element models of long bones: an in vitro evaluation of the overall accuracy, Journal of Biomechanics 39, 2457-2467.

Taddei, F., Schileo, E., Helgason, B., Cristofolini, L., Viceconti, M., 2007. The material mapping strategy influences the accuracy of CT-based finite element models of bones: An evaluation against experimental measurements. Medical Engineering and Physics 29, 973-979.

Viceconti, M., Bellingeri, L., Cristofolini, L., Toni, A., 1998. A comparative study on different methods of automatic mesh generation of human femurs. Medical Engineering and Physics 20, 1-10.

Williams, J. L., Lewis, J. L., 1982. Properties and an anisotropic model of cancellous bone from the proximal tibial epiphysis. Transactions of ASME, Journal of Biomechanical Engineering 104, 50-56.

Zannoni, C., Mantovani, R., Viceconti, M., 1998. Material properties assignment to finite element models of bone structures: a new method. Medical Engineering and Physics 20, 735-740.

Chapter 4: A numerical stress analysis of the distal femur: the effect of soft tissue loading

4.1 Introduction

The human knee is one of the most frequently analyzed structures in the human body (Huiskes and Chao, 1983). The knee is subjected to significant muscle loads during movement; if the load is excessive, its bones may even face damage (Viceconti et al., 2006). However, many of the finite element (FE) knee bone models have not included the muscles and ligaments that stabilize and move the joint, ostensibly in order to provide simpler and more computationally efficient models (Polgar et al., 2003). In such cases, stresses in the knee are frequently assumed to be caused by a simple tibiofemoral compression of 3 times body weight at full knee flexion, representative of peak forces occurring during gait (Morrison, 1970). A large majority of these models have been developed to study the design and performance of total knee replacement prostheses (Lewis et al., 1982; Murase et al., 1983; Vasu et al., 1986; Lewis et al., 1998; Hashemi and Shirazi-Adl, 2000; Au et al., 2005a; Sarathi Kopparti and Lewis, 2007). Such design studies are parametric and therefore the exclusion of soft tissue forces may be considered acceptable.

The necessity of predicting stresses that are physiologically representative is clearly case-specific. Ostensibly, FE models attempting to understand the aetiology of clinical pathologies should incorporate more physiological boundary conditions. However, the few FE models of the distal femur that have been used to understand clinical occurrences such as bone loss (Tissakht et al., 1996; van Lenthe et al., 1997), implant migration (Taylor et al., 1998), disease aetiology (Nambu et al., 1991), articular cartilage damage (Pena et al., 2008), posterior cruciate ligament reconstruction (Kim et al., 2005), and anterior cruciate ligament reconstruction (Au et al., 2005b) have not collectively included muscle and ligament forces. It can be envisaged that the inclusion of soft tissue forces into some of these models may improve comparisons with clinical data.

Although muscle forces are clearly involved in the rigid body displacement of the knee bones, their effect on the internal bone stresses is unclear. It has been found that including muscle forces produced during gait substantially changes the internal forces, strains and stresses of the proximal femur (Duda et al., 1997, 1998). However, a similar investigation has not been performed for the distal femur or proximal tibia. Thus, it should be clarified if muscle and ligament forces will influence stresses in knee bone models, a particularly important consequence if such models are intended to simulate physiological situations.

Of the few FE knee models that have included soft tissue loading, the majority are mainly concerned strictly with the ligaments (Kim et al., 2005) or the tibiofemoral joint surface (Haut Donahue et al., 2002; Pena et al., 2008), rather than the internal bone stresses. The FE models that explored internal bone stresses assumed single point muscle attachments (Vichnin et al., 1979; Sarrathi Kopparti and Lewis, 2007). A recent study has criticized this point loading approach and has suggested that it may be a significant source of error (Polgar et al., 2003). However, there are no studies documenting whether incorporating soft tissue forces over closed areas rather than at single points is more appropriate.

The purpose of this study was to investigate the general influence of soft tissue forces on distal femur FE models. Specifically, it was of interest to observe the sensitivity of the stress distribution to the presence of soft tissue loading. The appropriateness of representing soft tissues attachments as points rather than closed areas was also investigated. The analysis was restricted to stresses produced during the stance phase of gait. Stresses were observed for a FE representation of a surgically-repaired femur, where the addition of soft tissue forces could be potentially important in drawing proper conclusions. An elaborate discussion of the model development was provided to give the reader a collection of references that can be used to obtain information about soft tissue forces and attachments in the femur and tibia.

4.2 Materials and Methods

A three-dimensional FE model of the distal femur was used to predict stress distribution. This model was previously used to examine stress distribution from tunnel placement and button compression in anterior cruciate ligament (ACL) reconstructions under a relatively simple load condition (i.e. a tibiofemoral compression of 3 times body weight at full extension without the influence of soft tissue forces) (Au et al., 2005b). However, it was of interest to know if a more complete representation of the musculoskeletal forces would influence the behaviour of the model.

The geometry was constructed from a composite femur (Greer, 1999) and is available on the Internet at the International Society of Biomechanics Finite Element Repository (ISB, 2001). Cortical and cancellous bones were divided into 25 volumes and assigned orthotropic and heterogeneous material properties mapped from experimental data (Rho, 1992) and subchondral bone was assumed to be isotropic and homogeneous. The model was meshed with 2 mm 10-node tetrahedral elements, resulting in 147,543 elements and 211,037 nodes. A convergence analysis was used to validate mesh adequacy. For computational efficiency, the femur was sectioned 110 mm proximal to the most distal condylar location; a sensitivity analysis showed that longer femoral lengths did not affect stress distribution.

4.2.1 Applied Loads and Boundary Conditions

A loading case modeling the knee during the stance phase of gait from heelstrike to toe-off was studied. The stance phase was chosen because, compared to the swing phase, the soft tissue and joint compression forces were more prominent. Therefore, resulting stress levels will be higher and provide better insight regarding the influence of soft tissue loading and its implementation strategy. Stress distributions were analyzed at 10% intervals of the gait cycle, with heelstrike and toe-off assumed as 0% and 50% of the gait cycle, respectively. At

each interval, tibiofemoral compression, patellofemoral compression, and soft tissue (i.e. muscle and ligament) loading were incorporated into the model (Table 4.1). These forces were all obtained from a single musculoskeletal model in which equilibrium forces were calculated for each gait cycle interval (Anderson and Pandy, 2001). In all simulations, the proximal end of the femur was fixed in all directions.

4.2.1.1 Tibiofemoral Compression

One of the underlying objectives of this study was to develop a model which incorporated the most physiologically representative loading possible. A point load representation of the tibiofemoral compression was avoided because, physiologically, tibiofemoral compression is non-uniformly distributed over the femoral condylar surface (Brown and Shaw, 1984). Representations of this compression on the femoral surface are limited in the literature, therefore a technique translating the available tibial pressure information was applied to approximate the loading on the femoral condyles. Experimentally determined contact pressure distribution schematics (Fukubayashi and Kurosawa, 1980) for the tibia were digitized and the pressure contours mapped onto a tibia FE model. These contours were then mapped to the femur by translating the tibial distribution in an equal and opposite manner. A similar technique has also been used in Au et al. (2005b).

Compression will occur at different contact points on the condyles depending on the flexion angle of the knee, and therefore will change during the gait cycle. The contact points on the femoral condyles during the gait cycle have not been quantified, therefore they were estimated using a CAD assembly of the knee bones created with Pro/Engineer® (Parametric Technology Corp., Waltham, MA). Contact points at full extension were determined by mapping experimentally observed tibia contact points (Scarvell et al., 2004); points at increasing flexion angles were assumed to lie along common medial and lateral centerlines and placed using the arc lengths reported by Brown and Shaw (1984). At each

interval of the gait cycle, the translated pressure contour was centered at the appropriate contact point.

Pressure contours are dependent on the compression force and therefore the contours were different for each gait interval. Pressure contours were only available for select compression forces; for forces where contour maps were not available, contact areas were estimated for the desired compression (Fukubayashi and Kurosawa, 1980). The force was then uniformly distributed over the contact area. While this method involves combining data from various sources (Anderson and Pandy, 2001; Brown and Shaw (1984); Fukubayashi and Kurosawa, 1980), it was felt that this provided the best representation of physiological tibiofemoral loading on the femur since comprehensive data were not available.

4.2.1.2 Patellofemoral Compression

The approach used in representing patellofemoral compression was similar to that used for tibiofemoral compression. The model incorporated the contact patterns reported by Ahmed et al. (1983). These patterns were representative of the contact at the retropatellar surface, but due to the scarcity of suitable patterns, the femoral forces were assumed to be equal and opposite to those of the patella. Patellofemoral compression forces were not available from the musculoskeletal model, therefore they were estimated from the flexion angle and quadriceps force (Van Eijden et al., 1986).

4.2.1.3 Soft Tissue Representation

The tensile forces, insertion sites and lines of action for each muscle and ligament were characterized for each interval of the gait cycle. The PCL was assumed to have anterolateral (aPCL) and posteromedial (pPCL) bands, with each band sustaining different forces at different flexion angles. At full extension, the aPCL and pPCL sustained 40% and 60% of the total PCL force, respectively (Fox et al., 1998). The PCL force distribution was only available for 0 and 30 degrees flexion (Fox et al., 1998); therefore, as a first order approximation, linear

interpolation was used to determine the distribution of force at the various flexion angles. The MCL was assumed to have 4 bands (Fig 4.1b), with forces distributed proportionally to the relative cross-sectional area of each bands as suggested by Crowninshield et al. (1976). The anterior portion of the superficial band (aMCL) was assumed to sustain 40% of the MCL force while the remaining 60% was evenly divided among the posterior (pMCL), deep (dMCL), and oblique (oMCL) portions. The LCL was assumed to be a single band (Fig 4.1c). Forces were uniformly distributed over the ligament attachments.

Muscles represented in the femur model included the gastrocnemius (medial and lateral heads), the adductor magnus, and the popliteus (Fig 4.1). Forces were uniformly distributed over each muscle attachment area. For the gastrocnemius, the force was evenly divided over the medial and lateral heads. Quadriceps and hamstrings muscles were not included in the model as they do not attach at the distal femur.

4.2.1.4 Soft Tissue Insertion Sites

In this model, ligament and muscle attachment sites were considered to be enclosed areas rather than single points. Whenever possible, the attachment sites were located using quantitative descriptions based on anatomical landmarks. These attachment sites can be assumed as identical throughout the gait cycle. In terms of the ligaments, only the posterior cruciate ligament (PCL), medial collateral ligament (MCL), and lateral collateral ligament (LCL) needed to be modeled in the ACL reconstruction model. The shape of the PCL insertion (i.e. footprint) was modeled using the description provided by Harner et al. (1999) (Fig 4.1a). Its attachment in the femur is complex as it sits partly on the intercondylar notch and partly on the condyle. It was placed using the clock positions of Mejia et al. (2002); the ligament had an attachment width of approximately 32 mm, similar to the observations of Van Dommelen and Fowler (1989). No quantitative information was available regarding the insertion location of the MCL therefore it was modeled using the illustrations of Mains et

al. (1977). The insertion site of the LCL was determined using the borders of the femoral condyle (Meister et al., 2000); it was attached to the lateral epicondyle as described in Gray's Anatomy (1973). The footprints and attachment locations of the 3 muscles were modeled using information from the muscle standardized femur (Viceconti et al., 2003) and anatomy texts (Netter, 2002; Gray's Anatomy, 1973).

The accuracy of the soft tissue attachments was confirmed by comparing the centroids of the insertion areas with the National Institutes of Health's Terry dataset (Kepple et al., 1998) and a musculoskeletal model (Delp, 1990). The centroids of the modeled muscles and ligaments were assumed to be the centers of the attachment areas. The comparison was performed with the assistance of the CAD model. Coordinates from the Terry and Delp datasets were translated to the most representative locations on the CAD model. To minimize error in the comparison, the coordinate systems of the three datasets were aligned and the data normalized to the length of the CAD femur. To align the coordinate axes of the datasets with the CAD coordinate system, the Terry dataset points were rotated 4 degrees varus, and the Delp dataset points by 7 degrees valgus and 1 degree flexion.

4.2.1.5 Soft Tissue Lines of Action

Muscle and ligament lines of action were uniquely defined for each interval of the gait cycle. The lines of action were determined using the CAD knee assembly. The centroids of the ligament and muscle attachment sites were defined on the CAD femur and tibia as described above; the lines of actions were assumed to be straight lines connecting corresponding centroids.

4.2.2 Methodology to Study the Effect of Loading Conditions

To investigate the sensitivity of stress distribution in the distal femur to the presence of soft tissue loading, two FE models were created. In the first model, tibiofemoral, patellofemoral, and soft tissue forces were assigned; in the second,

the soft tissue forces were removed. Stresses in the models were compared at 0%, 10%, 40%, and 50% of the gait cycle. These intervals were chosen as they presented different combinations of tibiofemoral compression and soft tissue force levels. For example, at 0%, tibiofemoral compression, LCL, gastrocnemius and adductor magnus forces were all at the same order of magnitude whereas, at 50%, these forces were all at different orders of magnitude (Table 4.1). Identical material properties and boundary conditions were used for the two models.

To investigate the effects of point and area loading on stress distribution, two FE models were used. The first model distributed muscle and ligament forces over the closed areas seen in Fig 4.1, whereas the second model placed the muscle and ligament forces at their respective centroids. The magnitudes and lines of action of the soft tissue forces were identical in both models. Identical material properties and boundary conditions were applied to the two models.

The effects of point loading were only investigated at heelstrike to avoid the tibiofemoral compression forces from masking the stress effects of the soft tissue forces. At heelstrike, LCL, gastrocnemius, adductor magnus, and tibiofemoral compression forces all shared the same order of magnitude (Table 4.1); at the other gait intervals, tibiofemoral compression was an order of magnitude greater and would likely mask the stress effects from the soft tissues. While high tibiofemoral compression forces may only mask stresses in the more distal bone, to reduce any potential masking, it was more prudent to perform the sensitivity analysis under heelstrike conditions.

4.2.3 Cortical Stress from Button-Type Fixation

In practice, ACL reconstruction is performed by drilling tunnels into the femur and tibia, placing the graft within these tunnels, and anchoring the graft to a button placed on the femoral cortex. The graft is looped around a polyester band which passes through holes of the button to secure the graft. In the model, coaxial guide and enlarged tunnels were created (Fig 4.1a). An enlarged tunnel of 8 mm

diameter was inserted at the intercondylar notch, and rotated 15 degrees relative to the midsagittal plane and 35 degrees relative to the midcoronal plane (Fu et al., 2000).

Graft fixation was modeled using a device similar to the EndoButton® (Smith & Nephew Endoscopy, Andover, MA) (Fig 4.2). The device was used for illustrative purposes only and this study is not meant to examine its performance in any manner. The button was placed just above the guide tunnel aperture at the lateral cortex of the femur. To model the tension from the polyester band, a single force was placed at the center of the outer surface of the button and directed along the axis of the tunnel (in this way it is not necessary to model the graft as only its representative force is needed). The magnitude of this force was assumed to be identical to that of the physiological ACL (Table 4.1). Contact elements were used to model the interface between the button and the cortex. The button was meshed with 0.5 mm tetrahedral elements.

4.3. Results

4.3.1 Insertion Sites

The centroid locations of the ligament attachments were compared with the attachment points of the Terry dataset (Table 4.2). As the PCL was divided into two bands, two centroids were compared with a single attachment point from the Terry dataset. A similar comparison was used for the MCL. The ligaments had a mean difference of 10.2 mm. The largest difference was in the placement of the aPCL. The muscle centroids were compared with both the Terry and Delp datasets. Their placements were similar to those estimated by Delp (1990), with a mean difference of 9.9 mm. Slightly larger differences were observed when compared to the Terry dataset (mean = 16.4 mm), with the largest discrepancy in the placement of the popliteus. The acceptability of the ligament and muscle placement was strengthened by the fact that the corresponding lines of action were similar to those observed experimentally (Herzog and Read, 1993 (Table 4.3).

4.3.2 Influence of Soft Tissue Loading on Stress Distribution

The sensitivity of stress levels in the surgically-altered femur to the presence of soft tissue loading was examined by comparing a model incorporating muscle and ligament forces with one neglecting these forces. Von Mises stress distributions were compared at 5 transverse and sagittal slices through the bone. The LCL, gastrocnemius and adductor magnus were of particular interest since they exhibited large forces and would likely have the most influence on the stress distribution. The influence of each was examined at the interval of the gait cycle where it exerted its largest force.

The LCL pulled with the most force at the 10% interval of the gait cycle. Observing a transverse slice taken near the LCL insertion (25 mm from the joint line), stresses in a 10 mm radius around the insertion site appeared to be particularly influenced. The stress concentration caused levels to increase from near-zero to over 6 MPa (Figs 4.3a and 4.4a). The adductor magnus muscle pulled with most force at heelstrike. It produced a stress concentration nearly 7 mm in radius around its insertion site 58 mm from the joint line, which nearly quadrupled local stresses (Fig 4.4b). Although the gastrocnemius muscle pulled with nearly 1000 N of force at the 50% interval of the gait cycle, stress concentrations were not as apparent around its attachment site (Figs 4.4c and 4.4d). This is mainly due to the distribution of its force over a large attachment area. Its presence altered the general stress levels over a large radius.

The stress alterations caused by the muscle and ligaments were not localized to the bone near the insertion sites, as can be seen in the contour plots (Fig 4.3). The entire set of muscle and ligament forces produced during gait can cause a collective change in the general stress levels throughout the gait cycle, as evidenced by changes at heelstrike (Fig 4.3a), 10% gait (Fig 4.3b), and toe-off (Fig 4.3c). Stress levels would rise or fall depending on which muscles were activated, with the cortical stresses appearing particular sensitive to the presence

of soft tissues (Fig 4.3). Of importance for ACL reconstruction, cancellous bone around the tunnel sustained a much different stress pattern with the introduction of soft tissue forces (Fig 4.3c and 4.4f).

4.3.3 Point Loading versus Closed Area Loading

To investigate the effects of point and area loading, stress levels were observed during heelstrike. As mentioned in Section 4.2.2, stresses were only observed at heelstrike to avoid masking effects from the tibiofemoral compression. Stresses were observed at transverse slices taken at the insertion sites of selected muscles and ligaments. The LCL was observed 25 mm from the joint line; the adductor magnus at 58 mm; the lateral gastrocnemius at 44 mm; and the medial gastrocnemius at 47 mm. Contour plots showed that point loading produced substantial stress concentrations at attachment locations (Fig 4.5). A closer investigation of stress levels along selected paths confirmed this observation. Using a point load increased the local stress of the LCL attachment by sevenfold compared to a distributed load (Fig 4.6a). The effects were localized to about a 2 mm radius. Assuming the insertion of the adductor magnus as a point load increased surface stress by 25 times (Fig 4.6b). Stresses around a 6 mm radius were affected. In the gastrocnemius muscle insertions, a point load assumption increased local stresses by 208% and 100% in the medial (Fig 4.6c) and lateral attachment sites (Fig 4.6d), respectively. Stress concentrations affected an area of about 12 mm around the gastrocnemius insertion. Higher stress concentrations were observed at locations with higher soft tissue forces. The stress distributions revealed that the region of bone affected by localized stress concentrations was generally larger for point loading compared to area loading (compare Fig 4.4 with Fig 4.6).

4.3.4 Cortical Bone Stress from the Button Device

Cortical bone stress *patterns* at the proximal tunnel aperture resulting from button compression were similar throughout the stance phase of the gait cycle, with the highest stress consistently located on the distal edge of the aperture (Fig 4.7). The

highest aperture stress occurred at 20% of the gait cycle while stresses were the lowest at heelstrike (Table 4.4). This trend corresponded directly with the force pulling on the bottom, which was assumed to be the ACL force (Fig 4.8). However, the presence of the soft tissues did not greatly affect the stress levels, which was clearly dominated by the tension from the polyester band (Table 4.4).

4.4 Discussion

The majority of distal femur and proximal tibia FE models have been developed to study total knee replacement prosthesis design. The designs are frequently analyzed based on peak forces produced during the gait cycle. This peak force of approximately 3 times body weight occurs during toe-off (Anderson and Pandy, 2001). At this gait interval, muscles forces are also active which can influence the stress distribution in the knee bones (Table 4.1). Such forces are almost always ignored in FE models as they have been generally assumed to be of minor importance (Duda et al., 1997). Modeling muscles and ligaments is time consuming (Polgar et al., 2003) and thus they would not likely be included in FE models unless there is clear evidence that their inclusion will alter study conclusions. It has been shown that muscle forces influence the strains and stresses in the upper region of the femur (Duda et al., 1997, 1998), but evidence is still required regarding their influence in the distal femur and proximal tibia. Such information can be helpful in determining if FE models simulating gait require the inclusion of muscles and ligaments to fully characterize the stress state.

4.4.1 Insertion Sites

The model obtained from the ISB Finite Element Repository (ISB, 2001) was constructed from a composite femur that did not include muscles or ligaments. Therefore, soft tissue information had to be approximated from external sources such as anatomy texts and published studies, resulting in placement errors potentially as high as 2.4 cm. The method used in this study was similar to that

used for the muscle standardized femur, which had similar levels of error (Viceconti et al., 1998).

Some of the placement error can be attributed to the fact that muscles have large attachment sites, and it is difficult (or perhaps not very representative) to select a single attachment point. The attachment points of the Terry and Delp datasets were gathered using a palpation procedure and the reported points could lie anywhere within an attachment site. There are also very appreciable differences in muscle origins and insertions between specimens of very different size (Brand et al., 1982). Inter-individual variations in attachment centroids reported by Duda et al. (1996) were the same order of magnitude as the placement errors in the distal femur model. Thus, the technique presented in this study can be used to model a reasonable representation of physiological gait conditions. This study also demonstrates that a basic representation of physiological loading conditions can still be achieved for distal femur and proximal tibia models. For the more common case where geometries do not have pre-defined soft tissue attachment locations, such locations can be estimated using information available in literature. Muscle and ligament data can be synthesized using the techniques demonstrated in this study to create a more sophisticated model, with the understanding that the model is meant to represent a typical situation.

4.4.2 Point Loading versus Closed Area Loading

In the model presented here, soft tissue attachment sites were assumed to be closed areas rather than single points. Muscles such as the gastrocnemius and adductor magnus physiologically distribute their large forces over a broad area; concentrating such forces at a single point would unrealistically increase the stress levels at the insertion point. This was confirmed from stress concentrations observed around point-loaded insertion sites, where point loading increased stress levels by as much as 25 times.

During heelstrike, this stress concentration affected bone within a radius as large as 12 mm. This radius of influence will grow with the larger forces associated with other intervals of the gait cycle. Thus, if regions of interest are near attachment sites (e.g. the lateral epicondyle, the posterior condyles, and the posteromedial shaft), assuming soft tissue forces as point loads is not recommended. This may have consequences in bone remodeling simulations where an overestimation of stress may lead to sites of potential bone resorption being overlooked.

4.4.3 Influence of Soft Tissue Loading on Stress Distribution

One of the major objectives of this study was to examine the stress sensitivity to muscle and ligament forces in a distal femur FE model. For loading representative of the stance phase of gait, it was found that muscle and ligament forces altered stress distribution throughout the distal femur. Expectedly, the soft tissues caused stress concentrations in the cortical bone near the insertion areas, mainly at the lateral epicondyle, medial shaft, and posterior condyles, where the strongest muscles and ligaments attached. Such stress concentrations could elevate stress levels by more than 6 MPa during gait, a substantial amount considering the cortical stresses were generally around 5 MPa without soft tissues. Bone as far as 10 mm were influenced by these stress concentrations, thus cancellous bone near the attachment sites can also be affected.

Of greater significance, the influence of soft tissue forces was not localized to the attachment sites. Cortical stresses away from the attachment sites generally increased throughout the gait cycle with the presence of soft tissues (Fig 4.3b). In particular, at toe-off, the collective set of muscle and ligament forces created a net moment which bent the femur posteriorly, increasing stresses in the posterior half while decreasing those in the anterior half (Fig 4.3c). This occurrence is particularly important because FE models have often oversimplified loading produced at toe-off. Distal femur FE models have been used to explain clinically observed bone loss from stress shielding after total knee replacement surgery, in

which regions of particular interest were located in condyles (Van Lenthe et al., 1997). The study simulated gait at toe-off but only applied tibiofemoral and patellofemoral compression. Nearly all FE knee bone models incorporate some form of physiological loading. However, models which assist in understanding clinical phenomena should incorporate loading representative of functional activities such as walking or running, as the pathology may be caused by mechanical stresses occurring in daily living. More physiologically representative loading of the distal femur must include soft tissue forces as this study has shown that it has a definite influence on stress levels. Stress levels in the cancellous bone were influenced by as much as 2 MPa, which can substantially change study conclusions considering nominal cancellous bone stresses are in the same order of magnitude (Tissakht et al., 1996; Au et al., 2007; Sarathi Kopparti et al., 2007).

Since stress differences appeared to be more prominent at toe-off compared to the other gait cycle intervals, it can be speculated that the gastrocnemius muscle played a major role in altering the stress distribution. However, the full extent of its influence may have been underestimated due to masking from tibiofemoral and patellofemoral compression. The effects from the LCL and adductor magnus were examined at gait intervals where compression was generally lower but not entirely absent. If a strict sensitivity analysis of each soft tissue was to be performed, all forces other than the one of interest would be removed from the model. However, the method used in this study provided a sense of the importance of including soft tissue forces in the context of a physiological activity. The result showed that, in cases where soft tissue forces are expected to be influential such as walking, it is important to account for these forces as they will alter the stress distribution.

4.4.4 Stress Distribution in ACL-reconstructed femur

As a demonstrative example to examine the effects of soft tissue incorporation, stress levels occurring from button-type fixation in an ACL reconstruction were observed. During the early post-operative time period, the button must

adequately anchor the graft and assist in minimizing graft movement in the tunnel. Therefore, the cortex must be able to sustain early post-operative stresses during rehabilitation exercises such as walking.

A similar case was previously examined but did not include physiologically representative soft tissue forces (Au et al., 2005a). In this study, it was found that the cortical stress at the tunnel aperture was fairly insensitive to the presence of soft tissue forces; however, the influence of the soft tissues may have been masked by the large local stresses generated from the button compression. Thus, it is not necessary to include soft tissue forces to the previously developed ACL-reconstruction model when it is being used to study button compression. The conclusions presented in the previous study still remain relevant. In this study, those conclusions are strengthened by observing stresses across the entire gait cycle. A maximum stress of 112 MPa was predicted to occur during gait, which is clearly below the ultimate strength of cortical bone, approximately 193 MPa (Reilly and Burstein, 1975), so the bone will not fracture in the short term. However, this level of stress may cause fatigue failure in the cortical bone if applied over a 10-year period. Due to the fact that stresses will decrease as the graft gradually incorporates into the bone and that bone microdamage is constantly being repaired by the body, stress levels from button-type fixation are not expected to compromise button-type fixation when considering gait-type forces.

The results generated using this FE model regarding ACL reconstruction stresses are for demonstrative purposes and should not be assumed as being clinically accurate. However, experimental validation of this distal femur FE model is difficult to perform since the model was created from a variety of data sources and experimental strain data for the distal femur are not available in literature. We have previously validated the corresponding tibia FE model (Au et al., 2005a); as the presented model here was constructed in the same manner as the tibia model we expect its solutions to be similarly representative.

This study was conducted as a parametric analysis to understand the influence of muscle and ligament forces on stress distribution, therefore the results of the models are still relevant.

4.5 Summary and Conclusions

In this study, a distal femur FE model was used to study the sensitivity of stresses to muscle and ligament forces produced during gait. Stresses in both cortical and cancellous bone were particularly affected at toe-off, where the soft tissue forces altered the stresses in nearly the entire femur. To date, the ability of soft tissue forces to influence stresses outside of their attachment sites has not been explicitly demonstrated for the distal femur.

A method of implementing soft tissue forces to distal femur FE models was demonstrated by synthesizing data from publicly available sources such as anatomical atlases and published literature. Such sources show that soft tissues attach to the bone over large areas and this should be reflected in the model. Distributing the muscle and ligament forces over an area reduces stress concentration in the bone around the attachment sites, but does not completely eliminate it. If a point load representation is used, stress concentrations will be greatly exaggerated and affect an even larger area of bone. Thus, careful attention must be paid when interpreting stresses in bone near the lateral epicondyle, medial shaft, or posterior condyles.

Table 4.1: Summary of the tibiofemoral, patellofemoral, muscle and ligament loading forces, and corresponding knee flexion angle applied at each interval of the gait cycle.

Gait Cycle (%)	0	10	20	30	40	50
Knee Flexion Angle (°)	0	10	20	10	5	10
Tibiofemoral Compression (N)	343	343	1373	687	1373	2060
Patellofemoral Compression (N)	15	217	468	137	63	107
ACL (N)	80	180	300	130	150	100
PCL (N)	5	5	5	5	5	5
MCL (N)	25	5	5	10	5	5
LCL (N)	130	175	5	25	130	5
Gastrocnemius (N)	114	20	20	25	35	956
Adductor Magnus (N)	390	46	46	46	46	46
Popliteus (N)	5	5	5	5	5	5

Table 4.2: Difference in attachment point locations measured by root mean squared error (RMSE) between this study and the studies of Kepple et al. (1998) (Terry dataset) and Delp (1990).

Soft Tissue Structure	**Terry dataset RMSE (mm)**	**Delp dataset RMSE (mm)**
aPCL	15.9	--
pPCL	6.8	--
aMCL	11.2	--
pMCL	9.7	--
oMCL	9.7	--
dMCL	7.7	--
Adductor Magnus	4.8	4.9
Medial Gastrocnemius	16.9	12.0
Lateral Gastrocnemius	19.5	12.9
Popliteus	24.4	--

Table 4.3: A comparison of line of action angles in the vertical plane with experimental values of Herzog and Read (1993). Angles are clockwise positive with 0 degrees pointing anteriorly. Lines of action were compared for a knee in full extension.

Structure	This study	Experimental
Semitendinosus	259°	255°-270°
Semimembranosus	262°	255°-265°
ACL	aACL: 223° pACL: 215°	215°-223°
PCL	aPCL: -47° pPCL: -60°	-40° – -70°
LCL	-87°	-70° – -80°
MCL	aMCL: 249° pMCL: 250° oMCL: 249° dMCL: 258°	257° – 262°

Table 4.4: Summary of the maximum von Mises stress from button compression on the tunnel aperture with and without the inclusion of muscle and ligament forces. Stresses without muscle and ligament forces were only observed for 0%, 10%, 40%, and 50% intervals of the gait cycle. All maximum stresses occurred at the distal edge of the tunnel aperture.

Gait Cycle (%)	0	10	20	30	40	50
Maximum stress with soft tissue forces (MPa)	32	67	112	49	60	61
Maximum stress without soft tissue forces (MPa)	31	64	--	--	58	40

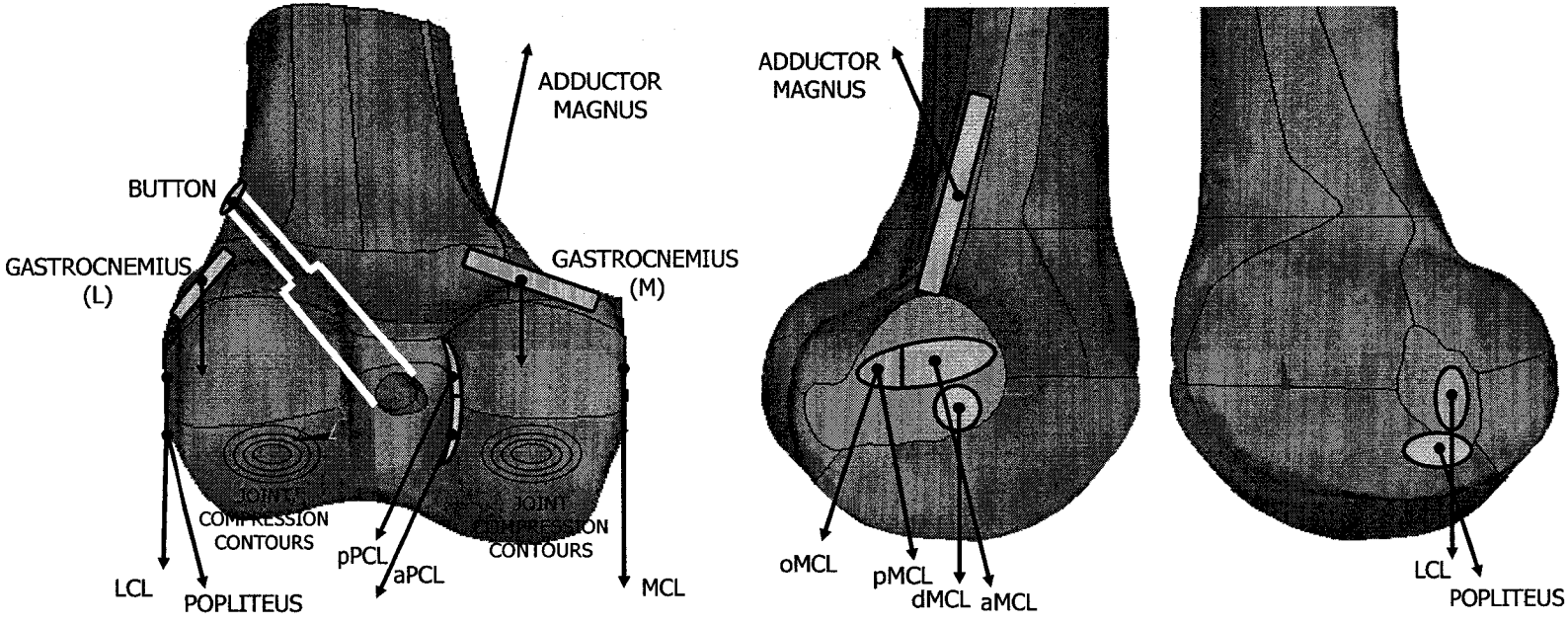

Figure 4.1: Schematic of loading condition for FE distal femur model. The solid white line depicts the bone tunnel used in ACL reconstruction; the button (BUTTON) is placed over the tunnel aperture. Attachment areas are approximations of those used in model. Arrows show approximate line of action at full extension. The PCL contains anterolateral (aPCL) and posteromedial (pPCL) bands, and the MCL contains anterior (aMCL), posterior (pMCL), oblique (oMCL), and deep (dMCL) bands. Three muscles were represented (gastrocnemius, adductor magnus, and popliteus). The ellipses represent the joint pressure contour borders used to model non-uniform distributed tibiofemoral loading (note the perspective used to show the bone).

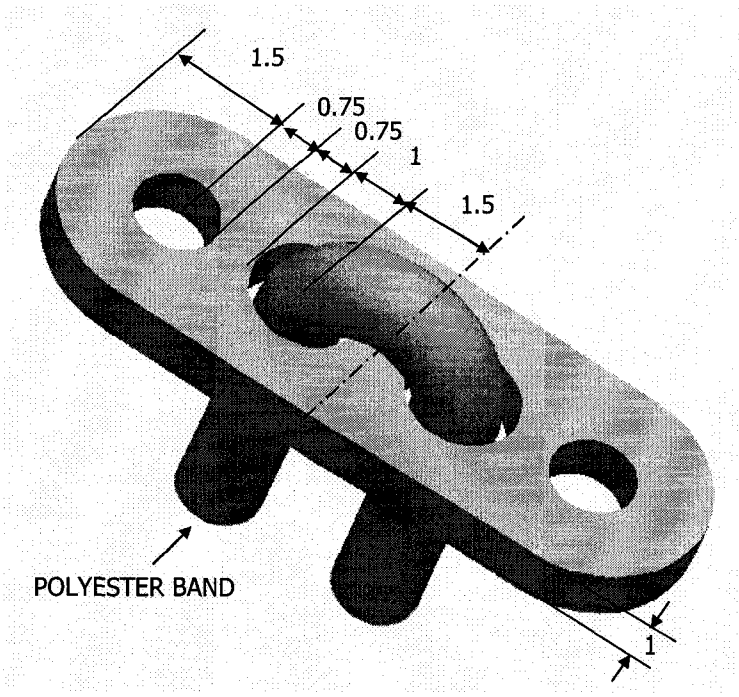

Figure 4.2: Schematic diagram showing button with polyester band looped through the two central holes. All dimensions in mm.

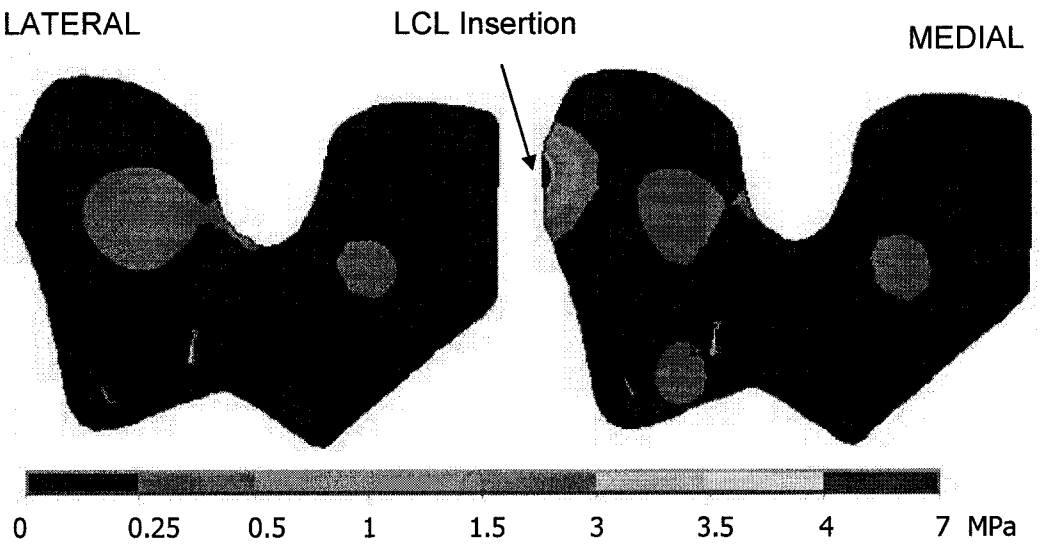
LATERAL
LCL Insertion
MEDIAL
0
0.25
0.5
1
1.5
3
3.5
4
7 MPa

(a)

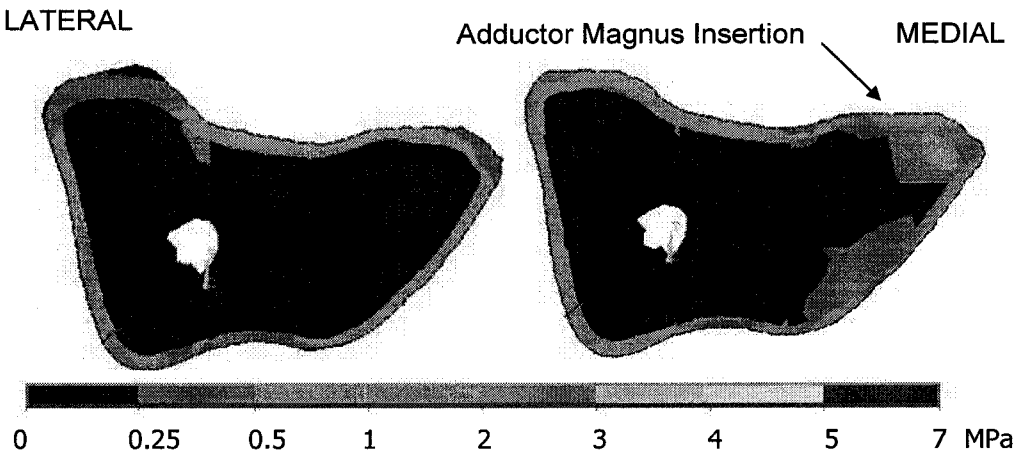
LATERAL
Adductor Magnus Insertion
MEDIAL
0
0.25
0.5
1
2
3
4
5
7 MPa

(b)

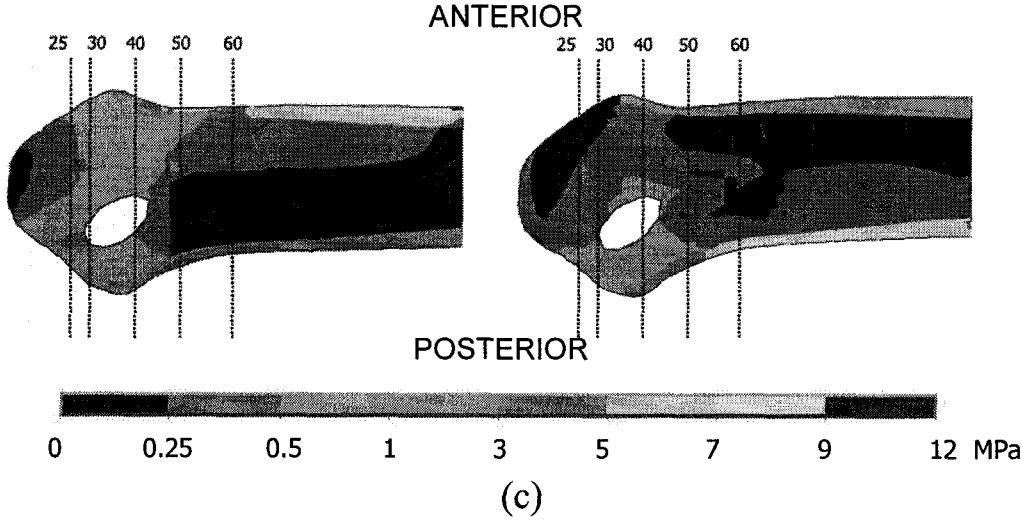

Figure 4.3: Von Mises stress contour plots of the femur. The left and right columns show plots of the model without and with muscle and ligament loading, respectively. Transverse slices were taken at the insertion areas of the LCL and adductor magnus. (a) A slice was cut through the LCL insertion 25 mm proximal to the joint line at 10% interval of gait cycle; (b) a slice was cut through the adductor magnus insertion 50 mm proximal to the joint line at 0% interval of gait cycle. The relative position of the transverse slices in the femur is shown by the dotted lines in (c), a midsagittal slice taken at 50% interval of gait cycle in (c). White enclosed areas are the bone tunnels representative of ACL reconstruction.

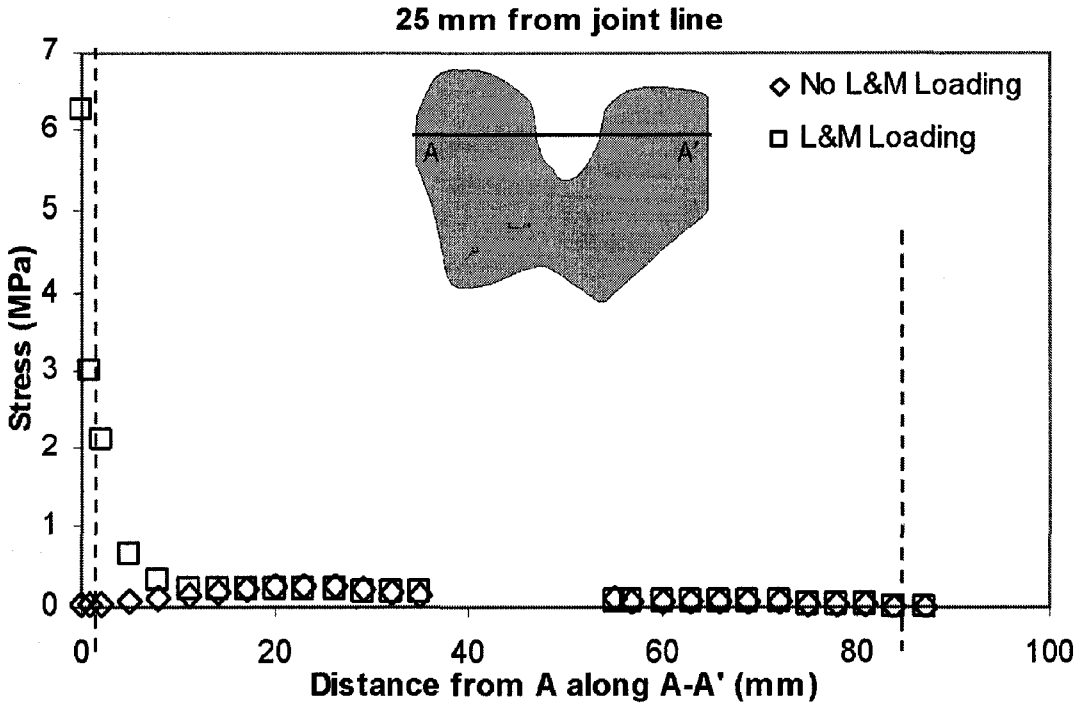
25 mm from joint line
Stress (MPa)
Distance from A along A-A' (mm)
No L&M Loading
L&M Loading
A
A'
0
1
2
3
4
5
6
7
0
20
40
60
80
100

(a)

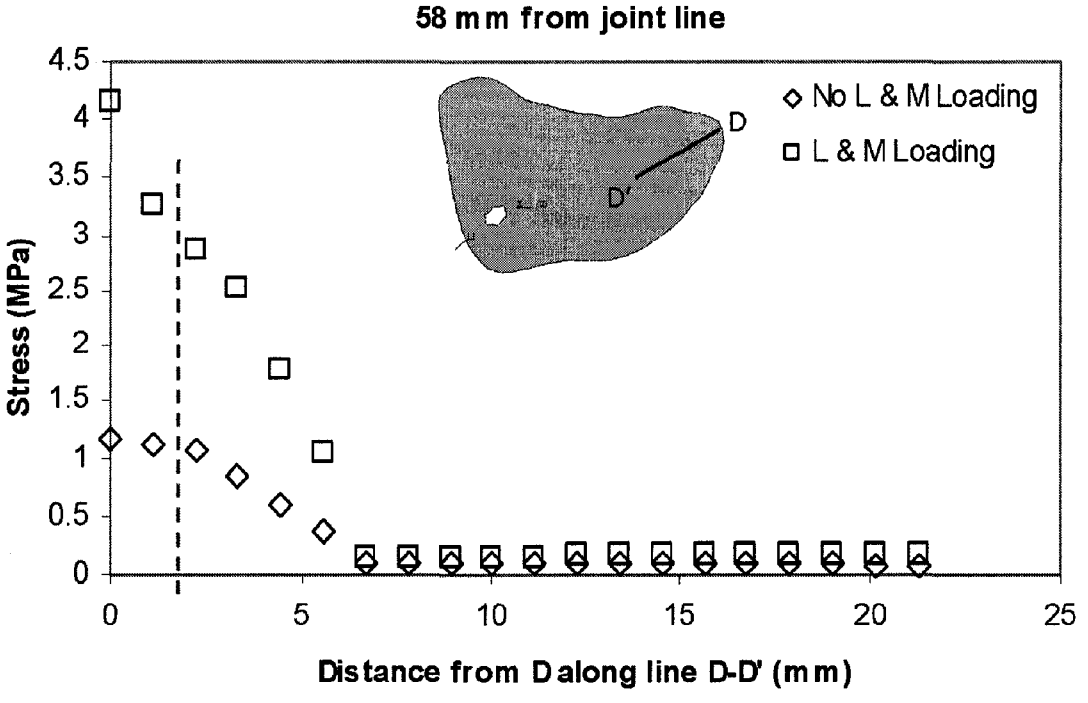
58 mm from joint line
Stress (MPa)
Distance from D along line D-D' (mm)
No L & M Loading
L & M Loading
D
D'
0
0.5
1
1.5
2
2.5
3
3.5
4
4.5
0
5
10
15
20
25

(b)

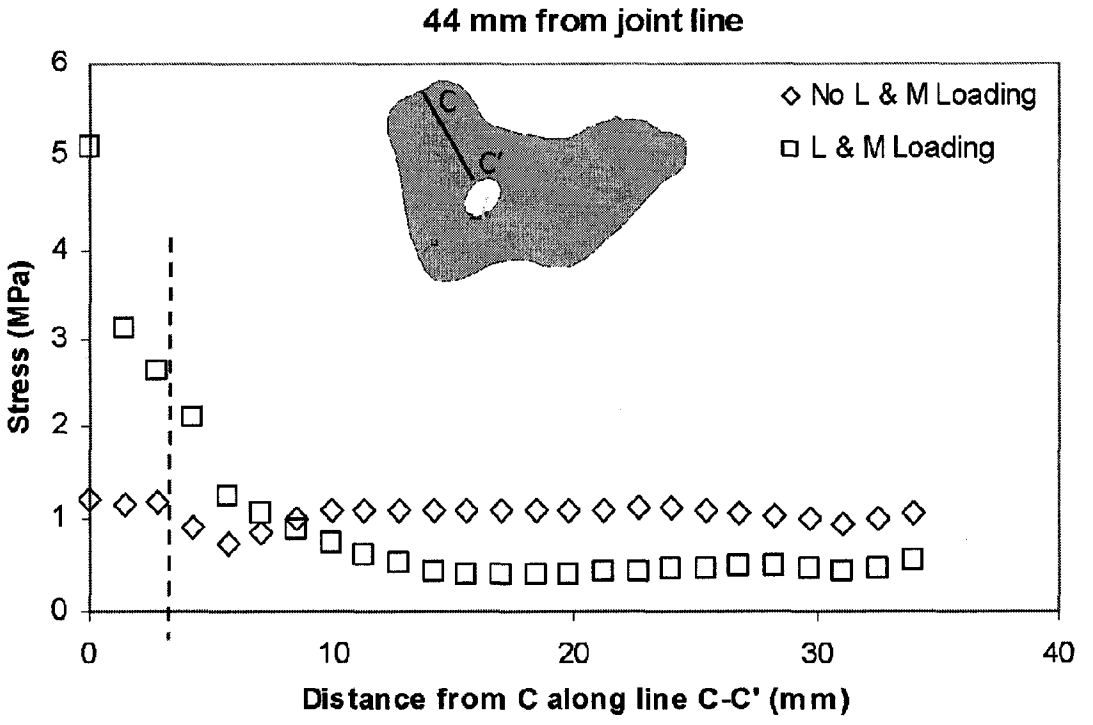
44 mm from joint line
Stress (MPa)
Distance from C along line C-C' (mm)
No L & M Loading
L & M Loading
C
C'
0
1
2
3
4
5
6
0
10
20
30
40

(c)

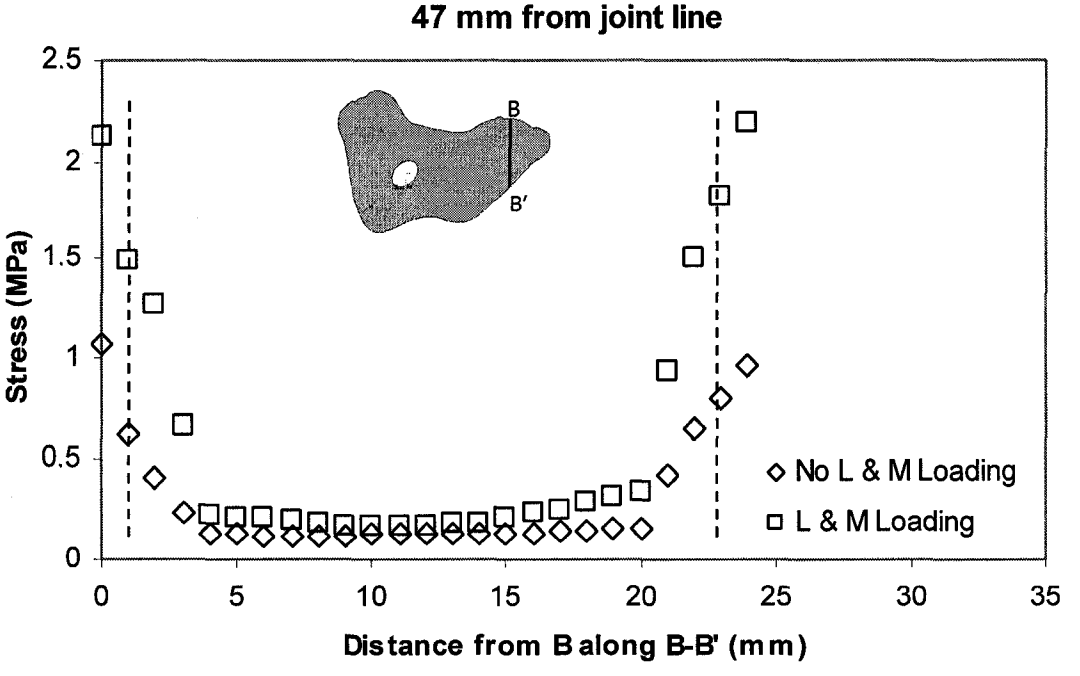
47 mm from joint line
Stress (MPa)
Distance from B along B-B' (mm)
No L & M Loading
L & M Loading
B
B'
0
0.5
1
1.5
2
2.5
0
5
10
15
20
25
30
35

(d)

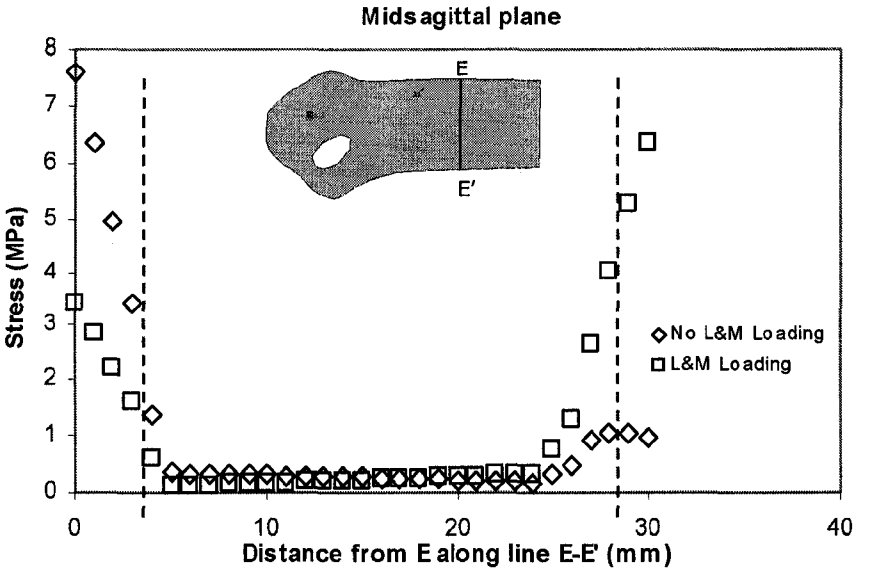

(e)

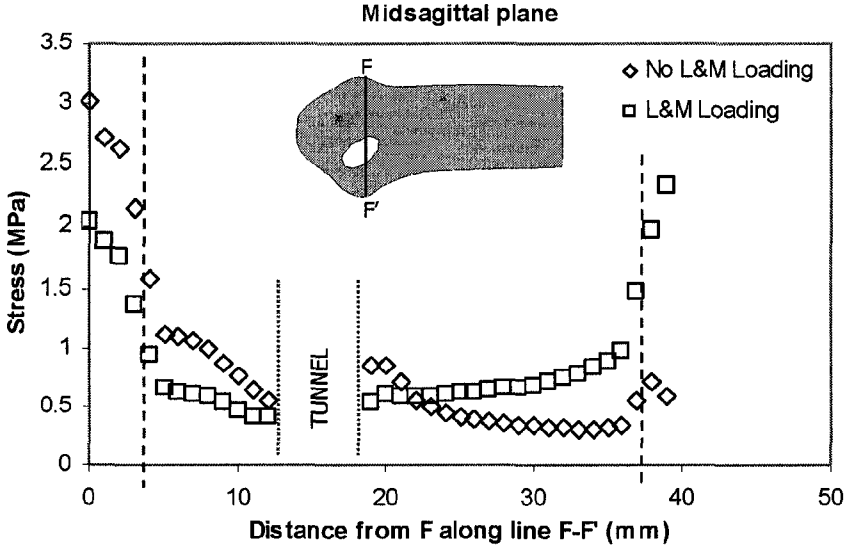

(f)

Figure 4.4: Von Mises stress paths traced across the attachment of (a) the LCL (at 10% interval of gait cycle); (b) the adductor magnus (at 0% interval); (c) the lateral gastrocnemius (at 50% interval); (d) the medial gastrocnemius (at 50% interval). Sagittal stress paths were traced across (e) the femoral shaft (at 50% interval), and (f) the intercondylar bone (at 50% interval). The gap in the points occurs because of the bone tunnel. The dashed lines delineate the approximate interface of cortical and cancellous bone. "L & M" stands for ligaments and muscles.

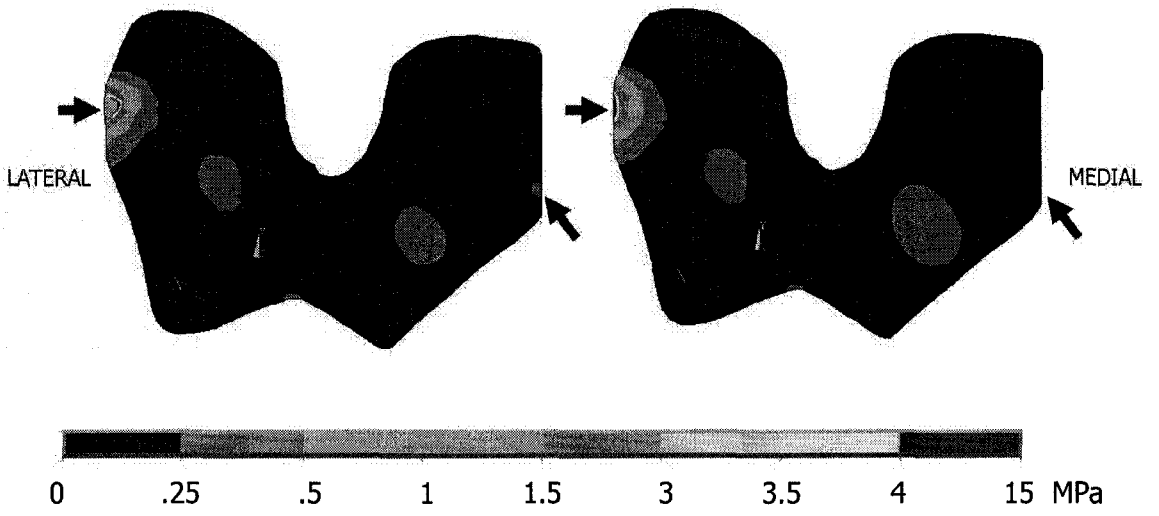

Figure 4.5: Von Mises stress contour plots of femur with point loading (left) and with area loading (right). Transverse section is located 25 mm proximal to the joint line. Load conditions at 0% of gait cycle were used. Arrows highlight notable stress changes occurring in the bone at the LCL and MCL attachment sites.

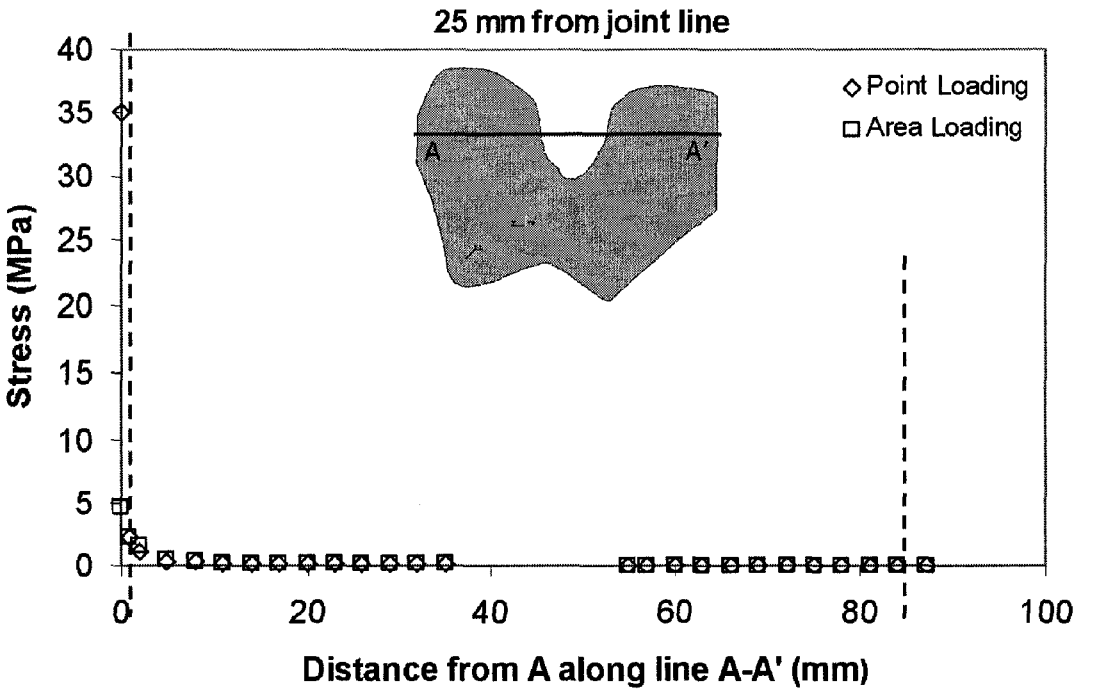
25 mm from joint line
Point Loading
Area Loading
A
A'
Stress (MPa)
0
5
10
15
20
25
30
35
40
0
20
40
60
80
100
Distance from A along line A-A' (mm)

(a)

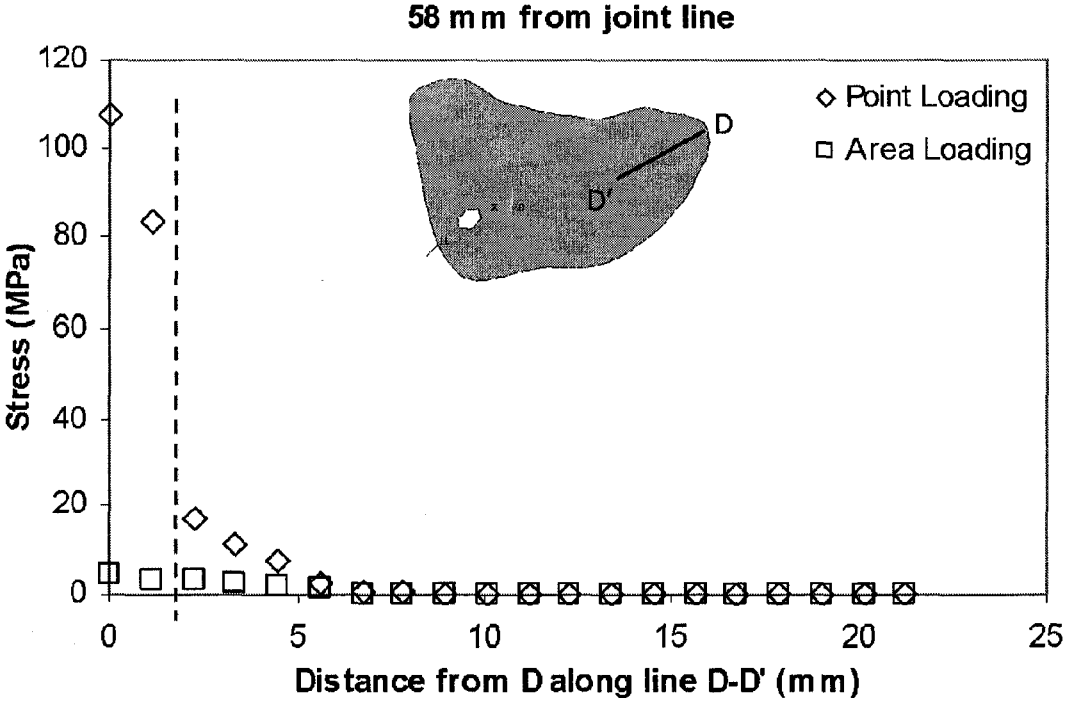
58 mm from joint line
Point Loading
Area Loading
D
D'
Stress (MPa)
0
20
40
60
80
100
120
0
5
10
15
20
25
Distance from D along line D-D' (mm)

(b)

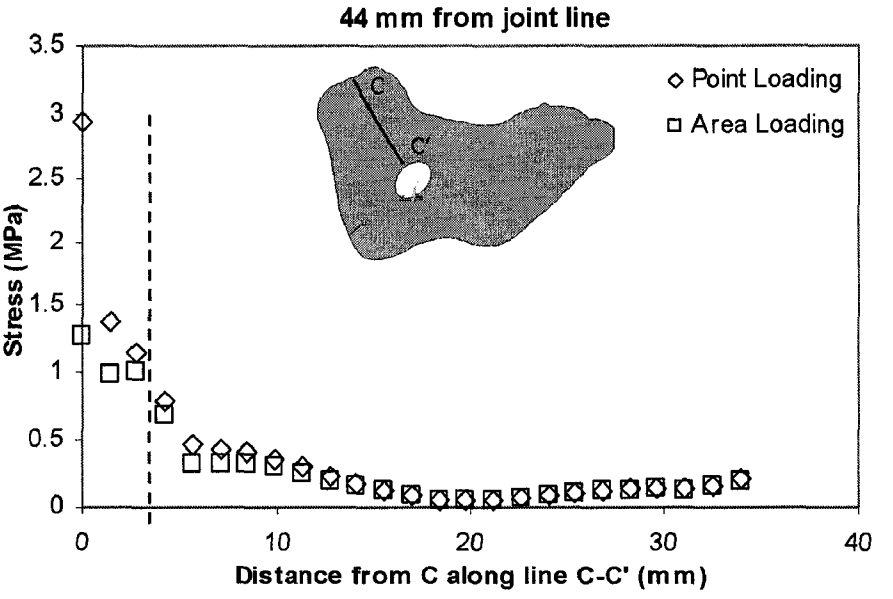

(c)

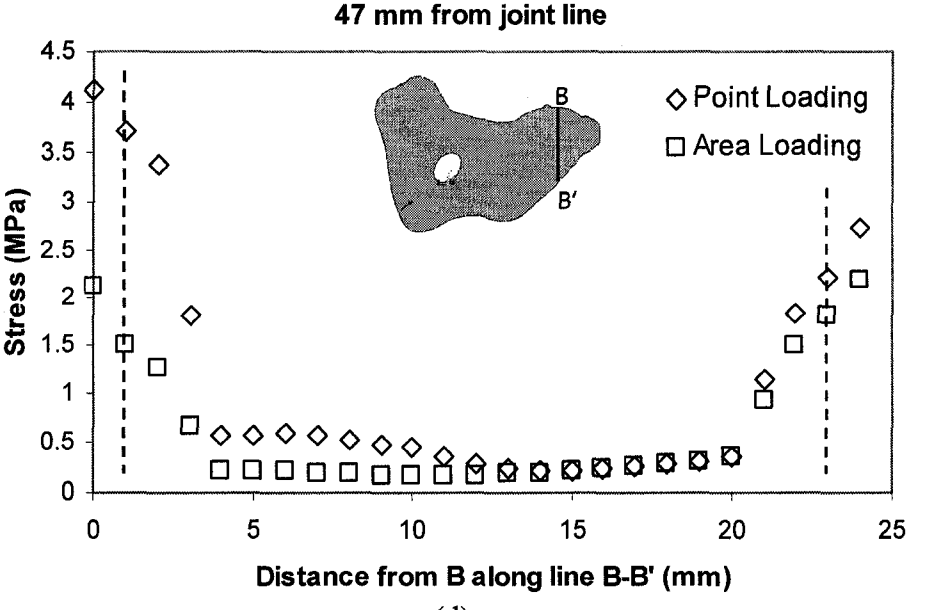

(d)

Figure 4.6: Von Mises stress paths traced across transverse sections of the femur at 0% interval of gait cycle. Slices were taken at the insertion areas of the LCL, gastrocnemius and adductor magnus. Stresses were observed at paths traced across the attachment of: (a) the LCL (the gap in the points occurs because of the intercondylar space); (b) the adductor magnus; (c) the medial gastrocnemius; (d) the lateral gastrocnemius. Dashed lines delineate the approximate interface of cortical and cancellous bone.

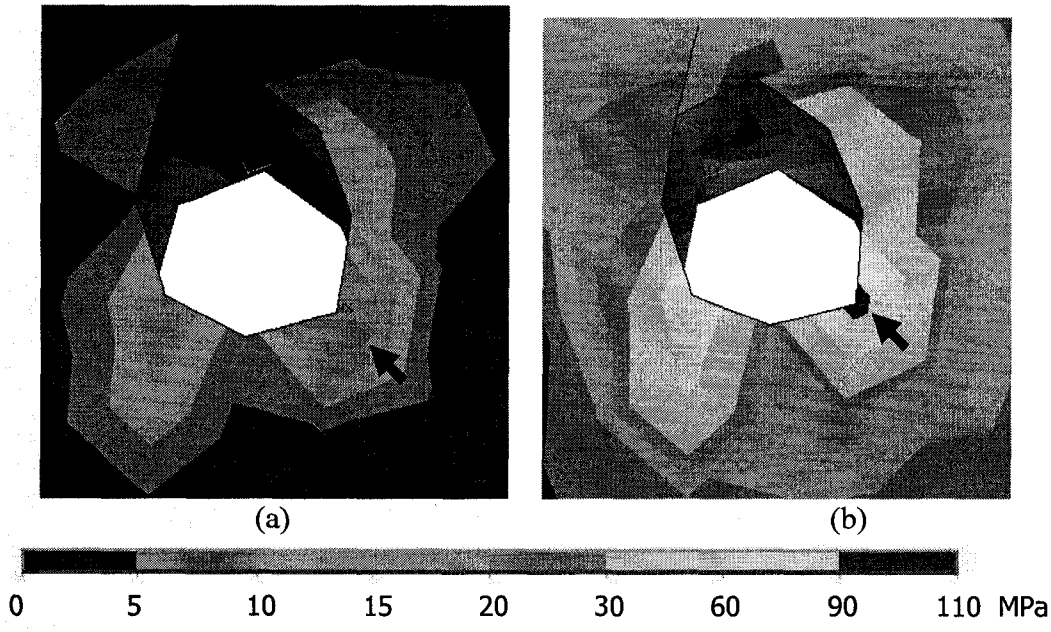

Figure 4.7: Von Mises stress contour plots of cortical bone stress at the tunnel aperture caused by button compression. Stresses are shown for (a) 0% of gait cycle and (b) 20% of gait cycle. The highest stresses were located on the distal edge of the aperture (arrow).

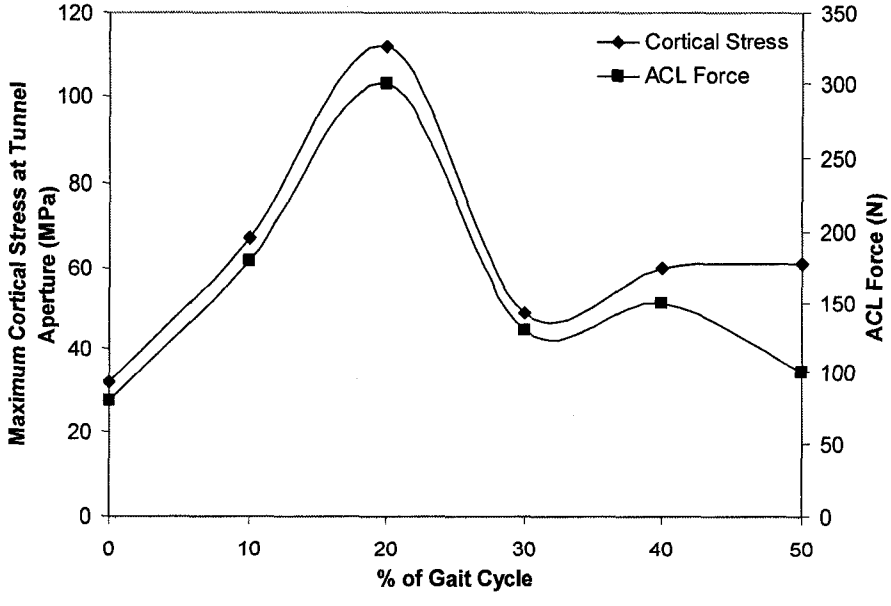

Figure 4.8: The relationship of maximum cortical stress at the tunnel aperture to the ACL force over the stance phase of the gait cycle, with curves to guide the eyes. The stress is read off the left axis; the force read off the right axis.

References

Ahmed, A. M., Burke, D. L., Yu, A., 1983. In-vitro measurement of static pressure distribution in synovial joints – Part II: Retropatellar surface. Transactions of the ASME: Journal of Biomechanical Engineering 105, 226-236.

Anderson, F. C., Pandy, M. G., 2001. Static and dynamic optimization solutions for gait are practically equivalent. Journal of Biomechanics 34, 153-161.

Au, A. G., Liggins, A. B., Raso, V. J., Amirfazli, A., 2005a. A parametric analysis of fixation post shape in tibial knee prostheses. Medical Engineering and Physics 27, 123-134.

Au, A. G., Raso, V. J., Liggins, A. B., Otto, D. D., Amirfazli, A., 2005b. A three-dimensional finite element stress analysis for tunnel placement and buttons in anterior cruciate ligament reconstructions. Journal of Biomechanics 38, 827-832.

Au, A. G., Raso, V. J., Liggins, A. B., Amirfazli, A., 2007. Contribution of loading conditions and material properties to stress shielding near the tibial component of total knee replacements. Journal of Biomechanics 40, 1410-1416.

Benjaballah, M. Z., Shirazi-Adl, A., Zukor, D. J., 1995. Biomechanics of the human knee joint in compression: Reconstruction, mesh generation and finite element analysis. The Knee 2, 69-79.

Beynnon, B., Yu, J., Huston, D., Fleming, B., Johnson, R., Haugh, L., Pope, M.H., 1996. A sagittal plane model of the knee and cruciate ligaments with application of a sensitivity analysis. Transactions of the ASME: Journal of Biomechanical Engineering 118, 227-239.

Brand, R. A., Crowninshield, R. D., Wittstock, C. E., Pedersen, D. R., Clark, C. R., Van Krieken, F. M., 1982. A model of lower extremity muscular anatomy. Transactions of the ASME: Journal of Biomechanical Engineering 104, 304-310.

Brown, T. D., Shaw, D. T., 1984. In vitro contact stress distribution on the femoral condyles. Journal of Orthopaedic Research 2, 190-199.

Crowninshield, R., Pope, M. H., Johnson, R. J., 1976. An analytical model of the knee. Journal of Biomechanics 9, 397-405.

Delp, S. L., 1990. A computer-graphics system to analyze and design musculoskeletal reconstructions of the lower limb. Ph.D. thesis, Stanford University, Stanford, CA, USA.

Duda, G. N., Brand, D., Freitag, S., Lierse, W., Schneider, E., 1996. Variability of femoral muscle attachments. Journal of Biomechanics 29, 1185-1190.

Duda, G. N., Schneider, E., Chao, E. Y. S., 1997. Internal forces and moments in the femur during walking. Journal of Biomechanics 30, 933-941.

Duda, G. N., Heller, M., Albinger, J., Schulz, O., Schneider, E., Claes, L., 1998. Influence of muscle forces on femoral strain distribution. Journal of Biomechanics 31, 841-846.

Eibeck, P. A., Swenson, L. W., Schurman, D. J., Piziali, R. L., 1979. Finite element stress analysis of hinged tibial component total joint replacements. Transactions of the 25th ORS Meeting, 298.

Fox, R. J., Harner, C. D., Sakane, M., Carlin, G. J., Woo, S. L.-Y., 1998. Determination of the in situ forces in the human posterior cruciate ligament using robotic technology. American Journal of Sports Medicine 26, 395-401.

Fu, F. H., Bennett, C. H., Ma, C. B., Menetrey, J., Lattermann, C., 2000. Current trends in anterior cruciate ligament reconstruction. Part II: Operative procedures and clinical correlations. American Journal of Sports Medicine 28, 124-130.

Fukubayashi, T., Kurosawa, H., 1980. The contact area and pressure distribution pattern of the knee. Acta Orthopaedica Scandinavica 51, 871-879.

Gray's Anatomy, 1973, 29th American ed., edited by Goss, C.M. Lea and Febiger, Philadelphia, PA.

Harner, C. D., Baek, G. H., Vogrin, T. M., Carlin, G. J., Kashiwaguchi, S., Woo, S. L.-Y., 1999. Quantitative analysis of human cruciate ligament insertions. Arthroscopy 15, 741-749.

Hashemi, A., Shirazi-Adl, A., 2000. Finite element analysis of tibial implants - effect of fixation design and friction model. Computer Methods in Biomechanics and Biomedical Engineering 3, 183-201.

Haut Donahue, T. L., Hull, M. L., Rashid, M. M., Jacobs, C. R., 2002. A finite element model of the human knee joint for the study of tibio-femoral contact. Transactions of the ASME: Journal of Biomechanical Engineering 124, 273-280.

Herzog, W., Read, L. J., 1993. Lines of action and moment arms of the major force-carrying structures crossing the human knee joint. Journal of Anatomy 182, 213-230.

Huiskes, R., Chao, E.Y.S., 1983. A survey of finite element analysis in orthopaedic biomechanics: the first decade. Journal of Biomechanics 16, 385-409.

Kim, S.-J., Shin, J. W., Lee, C. H., Shin, H. J., Kim, S.-H., Jeong, J.-H., Lee, J. W., 2005. Biomechanical comparisons of three different tibial tunnel directions in posterior cruciate ligament reconstruction. Arthroscopy 21, 286-293.

Kepple, T. M., Sommer, H. J., Lohmann Siegel, K., Stanhope, S. J., 1998. A three-dimensional musculoskeletal database for the lower extremities. Journal of Biomechanics 31, 77-80.

Lewis, J. L., Askew, M. J., Jaycox, D. P., 1982. A comparative evaluation of tibial component designs of total knee prostheses. Journal of Bone and Joint Surgery [Am] 64-A, 129-135.

Lewis, G., Jonathan, V., Kambhampati, S., 1998. Effect of material property representation on stresses in endoprostheses. Bio-Medical Materials and Engineering 8, 11-23.

Liu, W., Maitland, M. E., 2000. The effect of hamstring muscle compensation for anterior laxity in the ACL-deficient knee during gait. Journal of Biomechanics 33, 871-879.

Mains, D. B., Andrews, J. G., Stonecipher, T., 1977. Medial and anterior-posterior ligament stability of the human knee, measured with a stress apparatus. American Journal of Sports Medicine 5, 144-153.

Meister, B. R., Michael, S. P., Moyer, R. A., Kelly, J. D., Schneck, C. D., 2000. Anatomy and kinematics of the lateral collateral ligament of the knee. American Journal of Sports Medicine 28, 869-877.

Mejia, E. A., Noyes, F. R., Grood, E. S., 2002. Posterior cruciate ligament femoral insertion site characteristics. American Journal of Sports Medicine 30, 643-651.

Morrison, J. B., 1970. The mechanics of the knee joint in relation to normal walking. Journal of Biomechanics 3, 51-61.

Murase, K., Crowninshield, R. D., Pedersen, D. R., Chang, T.-S., 1983. An analysis of tibial component design in total knee arthroplasty. Journal of Biomechanics 16, 13-22.

Nambu, T., Gasser, B., Schneider, E., Bandi, W., Perren, S. M., 1991. Deformation of the distal femur: a contribution towards the pathogenesis of osteochondrosis dissecans in the knee joint. Journal of Biomechanics 24, 421-433.

Netter, F. H., 2002. Atlas of Human Anatomy, 3rd ed., ICON Learning Systems, Teterboro, NJ.

Pena, E., Calvo, B., Martinez, M. A., Doblare, M., 2008. Computer simulation of damage on distal femoral articular cartilage after meniscectomies. Computers in Biology and Medicine 38, 69-81.

Polgar, K., Gill, H. S., Viceconti, M., Murray, D. W., O'Connor, J. J., 2003. Development and numerical valildation of a finite element model of the muscle standardized femur. Proceedings of the Institution of Mechanical Engineers (Part H) 217, 165-172.

Rakotomanana, R. L., Levyraz, P. F., Curnier, A., Heegaard, J. H., Rubin, P. J., 1992. A finite element model for evaluation of tibial prosthesis-bone interface in total knee replacement. Journal of Biomechanics 25, 1413-1424.

Reilly, D. T., Burstein, A. H., 1975. The elastic and ultimate properties of compact bone tissue. Journal of Biomechanics 8, 393-405.

Rho, J. Y., 1992. Mechanical properties of cortical and cancellous bone. Ph.D. thesis, University of Texas Southwestern Medical Center, Dallas, TX, USA.

Sarathi Kopparti, P., Lewis, G., 2007. Influence of three variables on the stresses in a three-dimensional model of a proximal tibia-total knee implant construct. Bio-Medical Materials and Engineering 17, 19-28.

Scarvell, J. M., Smith, P. N., Refshauge, K. M., Galloway, H. R., Woods, K. R., 2004. Evaluation of a method to map tibiofemoral contact points in the normal knee using MRI. Journal of Orthopaedic Research 22, 788-793.

Song, Y., Debski, R. E., Musahl, V., Thomas, M., Woo, S. L.-Y., 2004. A three-dimensional finite element model of the human anterior cruciate ligament: a computational analysis with experimental validation. Journal of Biomechanics 37, 383-390.

Taylor, M., Tanner, K. E., Freeman, M. A. R., 1998. Finite element analysis of the implanted proximal tibia: a relationship between the initial cancellous bone stresses and implant migration. Journal of Biomechanics 31, 303-310.

Tissakht, M., Ahmed, A. M., Chan, K. C., 1996. Calculated stress-shielding in the distal femur after total knee replacement corresponds to the reported location of bone loss. Journal of Orthopaedic Research 14, 778-785.

Van Dommelen, B. A., Fowler, P. J., 1989. Anatomy of the posterior cruciate ligament. American Journal of Sports Medicine 17, 24-29.

Van Eijden, T. M. G. J., Kouwenhoven, E., Verburg, J., Weijs, W. A., 1986. A mathematical model of the patellofemoral joint. Journal of Biomechanics 19, 219-229.

Van Lenthe, G. H., De Waal Malefijt, M. C., Huiskes, R., 1997. Stress shielding after total knee replacement may cause bone resorption in the distal femur. Journal of Bone and Joint Surgery [Br] 79, 117-122.

Vasu, R., Carter, D. R., Schurman, D. J., Beaupre, G. S., 1986. Epiphyseal-based designs for tibial plateau components - I. Stress analysis in the frontal plane. Journal of Biomechanics 19, 647-662.

Viceconti, M., Ansaloni, M., Baleani, M., Toni, A., 2003. The muscle standardized femur: a step forward in the replication of numerical studies in biomechanics. Proceedings of the Institution of Mechanical Engineers [Part H] 217, 105-110.

Viceconti, M., Testi, D., Taddei, F., Martelli, S., Clapworthy, G. J., Van Sint Jan, S., 2006. Biomechanics modeling of the musculoskeletal apparatus: status and key issues. Proceedings of the IEEE 94, 725-739.

Vichnin, H. H., Hayes, W. C., Lotke, P. A., 1979. Parametric finite element studies of tibial component fixation in the total condylar knee prosthesis. Proceedings of the 25th Annual ORS Meeting, 99.

Wismans, J., Veldpaus, F., Janssen, J., 1980. A three-dimensional mathematical model of the knee joint. Journal of Biomechanics 13, 677-685.

Zavatsky, A. B., O'Connor, J. J., 1993. Ligament forces at the knee during isometric quadriceps contractions. Proceedings of the Institution of Mechanical Engineers 207, 7-18.

Chapter 5: Experimental verification of finite element models of a composite femur and tibia

5.1 Introduction

Determining mechanical stresses in human bones is important for clinical and research purposes. This knowledge can be beneficial in planning rehabilitation after limb-salvage procedures (Taddei et al., 2003), identifying failure scenarios in biomedical applications (Completo et al., 2007a), identifying the appropriate load regime after skeletal surgery (Viceconti et al., 2004), and support in pre-operative planning (Viceconti et al., 2004). It can be used to provide deeper understanding of mechano-biological phenomenon (Taddei et al., 2006) and to evaluate the risk of femoral fracture (Viceconti et al., 2004). These mechanical stresses are difficult to measure and study *in vitro* and often employ finite element (FE) models, which have the ability to simulate strains and stresses internally within the bone and at bone-implant interfaces (Gray et al., 2007). Such models can be used to predict strains and stresses for variety of conditions, thus they are frequently employed in the design and evaluation of joint prostheses and fixation devices. However, a high level of confidence in predictions can only be associated with accurate and valid FE models.

FE models must be constructed using elements that provide a converged solution to ensure accuracy. Additionally, FE models should represent the physical situation they are simulating, i.e. the geometry, mechanical behaviour and boundary conditions of the bones. The validity of FE models should be tested through experimental verification.

Composite and animal bones are often used as surrogates for cadaveric specimens in experimental studies as they are easier to handle and more readily available. Composite femora and tibia have been used to suitably predict the performance of intact bones under axial and bending loads (Cristofolini et al., 1996; Cristofolini and Viceconti, 2000). Whereas they cannot represent the biological response of

natural femurs, composite bones can adequately simulate the geometry of cadaveric specimens (Cristofolini et al., 1996; Cristofolini and Viceconti, 2000). On the other hand, bovine bone has similar mechanical properties to human bone (Carter and Hayes, 1977; Ashman and Rho, 1988; Hodgskinson and Currey, 1992) but cannot represent their geometry. Several studies have experimentally verified FE models of the femur and tibia using composite bones (Gray et al., 2007; Completo et al., 2007b; Completo et al., 2007c; Stolk et al., 2002; Waide et al., 2004). The few FE animal bone models have generally been limited to equine bone (Hinterhofer et al., 2000; Merritt et al., 2006).

The aim of the current study was to provide preliminary validation of a comprehensive framework for constructing subject-specific FE models, specifically the geometry and material properties construction aspects. The efficacy of the technique was analyzed through a comparison of surface strain data gathered from physical and FE models of composite and bovine bones. A proper validation of these models will provide a level of confidence for using the framework in constructing accurate subject-specific FE models of human knee bones. A side focus of the study was to highlight factors that may affect a proper comparison of experimental and simulated results.

5.2 Materials and Methods

A composite left femur and tibia (third generation, model numbers 3303 and 3301, respectively) from Sawbones (Pacific Research Labs, Vashon Island, WA) and a right bovine tibia (hind limb) were used in this study. Their surface strains were measured under axial loading using a materials testing machine. Three FE models were created from computed tomography (CT) images of these three bones. The mechanical tests were simulated on the FE models and the predicted strains were compared with those measured from the experiments.

5.2.1 Experiments

Thirteen tri-axial stacked strain gauge rosettes (Omega Engineering Inc., Stamford, CT) were placed on each bone (Fig 5.1). The gauges were placed at different levels on the anterior, posterior, medial and lateral faces of the composite and bovine tibia to gain a sense of the strain distribution throughout the entire bone. Gauges were similarly placed on the femur and included the condyles and intercondylar notch. Each strain gauge was aligned with either the horizontal or vertical axis of the bones. All strain gauges were connected to a 40-channel data acquisition system (National Instruments, Austin, TX) which was connected to a PC installed with LabView (National Instruments, Austin, TX) for data recording at 0.5 Hz. The positions of the gauges were measured using a 3D coordinate measuring machine (CMM; Microval, Brown and Sharpe, North Kingstown, RI).

An electromechanical actuator (IDC Motion EC3-B, Danaher Motion, Wood Dale, IL) was used to apply the load on the medial and lateral condyles (Fig 5.2). Forces were applied directly on the condyles and were controlled using feedback from a 6 degree-of-freedom load cell (model MC6-6-200, AMTI, Watertown, MA) and a Kollmorgen Servostar S306 controller (Danaher Motion, Wood Dale, IL). A custom-made loading jig was used to transmit forces to the medial and lateral condyles simultaneously. The jig consisted of two adjustable aluminum rods attached to a slotted aluminum plate to control the load placement on the condyles. The rods were adjusted to contact the approximate center of the medial and lateral tibial condyles. Nylon balls were attached to the end of each rod to reduce stress concentration on the bone. The rod lengths were individually adjusted to contact the condylar surfaces simultaneously.

Four uniaxial strain gauges (CEA 13062UW350, Vishay Intertechnology, Inc., Malvern, PA) were placed on each rod and connected together in a full bridge to observe the force distributed through each rod. The gauges were balanced using a

conditioner before each test. The observed voltages were used to proportion the load placed on each condyle in the FE models.

The proximal femur and the distal tibia were removed and the extremities of the remaining bone were potted using polymethylmethacrylate (PMMA). Each pot was rigidly secured in the testing machine to prevent it from rotating. The load was manually increased to 150 lb (667 N) for the composite bones and 300 lb (1,334 N) for the bovine bone at a rate of 1 mm/min and held for 10 seconds. To ensure the repeatability of the results, each bone was tested five times. The experimental results are presented as the average of the five repetitions.

The maximum and minimum principal strains within the plane of the gauge were calculated at all gauge locations. Also, the in-plane angle between the maximum principal strain and the horizontal axis was calculated. Von Mises strains were also calculated at all gauge locations as it was not influenced by strain direction and provided a general idea of the 3-D strain distribution. The differences between measured and predicted strains were compared and outliers were detected using Chauvenet's criterion (Stolk et al., 2002). This is a commonly accepted statistical test that checks whether a data point belongs to the same statistical distribution as all the others. If it does not, it should be considered an outlier and removed during further analyses.

5.2.2 Finite Element Analyses

To construct the FE models, the bones were CT scanned (Somatom Sensation 64, Siemens AG, Munich, Germany) prior to any mechanical testing. Images were obtained with a slice thickness of 0.6 mm with a 512 x 512 pixel resolution using a 160 mm and 240 mm field of view for the composite and bovine bone, respectively. The CT images were segmented and used to construct a 3-D geometry using the semi-automated subject-specific (SASS) technique described in Chapter 2. The material properties used in the composite models were provided by the manufacturer ($E_{cortical}$ = 12.4 GPa; $E_{cancellous}$ = 104 MPa) and

assumed to be homogeneous. The mechanical properties of the bovine bone were interpreted from the CT image data using an empirical relationship which covered the density range of cortical and cancellous bone (Carter and Hayes, 1977):

$$E=3790\rho^3 \quad (1)$$

The materials were assumed to be isotropic and linearly elastic. The geometries were meshed with 2 mm 10-node tetrahedrons using HyperMesh (Altair Inc., Troy, MI) (Fig 5.3). The number of elements and nodes were chosen based on previous convergence studies (Au et al., 2005). The resulting composite femur FE model contained 102,460 elements and 174,582 nodes; the composite tibia FE model consisted of 161,725 elements and 230,195 nodes; and the bovine tibia had 182,062 elements and 267,767 nodes. Finite element analysis was performed using ANSYS (Swanson Inc., Houston, PA).

The boundary conditions in the FE models were defined to reproduce the experimental setup. The contact points on the physical bone surface were marked with ink and measured with the CMM. The coordinates were transformed to the FE coordinate system using the method described below. The nodes matching closest to the transformed contact points were assigned forces matching the experiment. The minimum and maximum principal strains on the planes of the rosettes were observed at the locations matching those in the experiment. The predicted strains were averaged over a 2.5x2.5 mm region, the approximate size of the strain gauges, centered on the node closest to the rosette center.

Ball bearings were placed on the surface of the bones prior to CT scanning to assist in aligning the physical and FE coordinate systems. Alignment was performed by matching the positions of 3 ball bearings in the physical coordinate system (measured using the CMM) with the same 3 ball bearings in the FE coordinate system. The transformation matrix was determined by minimizing the total distance between the ball bearings points measured using the CMM and the corresponding points from the FE model using a custom routine written in MATLAB (Math Works, Natick, MA) (see Chapter 2). This allowed the

transformation of strain gauge rosette and load placement locations from the physical coordinate system to the FE model.

Maximum and minimum principal strains acting in the gauge planes were recorded for locations corresponding to the experimental strain measurement sites. These were compared to the principal strains calculated from the strain gauge measurements. Linear regression analyses were performed to determine the correspondence between measured and predicted strains. Experimental strains were treated as independent variables and FE strains as dependent ones. A slope and r^2 close to 1, in combination with a small intercept, would indicate good agreement between FE and experimental strains. A Bland-Altman plot (Bland and Altman, 1986) was also used to compare the experimental and finite element methods of strain measurement by plotting the difference between the two scores against the mean for each specimen. Such plots have become a standard accessory in validity or method-comparison studies; they can be used to provide greater insight into linear regression results by highlighting substantial differences in the two measures across their range of values (Hopkins, 2004).

5.2.3 Sensitivity Analysis

A number of sensitivity tests were performed using the FE composite bone models to better understand how modeling errors may affect the correspondence between measured and predicted strains. Two major modeling aspects were of particular interest: material properties and loading conditions. To estimate the effect inaccurate material properties may have on strains, two FE models for each composite bone were created with varying material properties. One model contained a 20% increase in Young's moduli for both cortical and cancellous bone; the other assumed a 20% decrease in Young's moduli.

Errors associated with modeling loading conditions were categorized into two main groups: (1) inaccurate load placement and (2) inaccurate replication of forces. Load placement was based on an approximate translation of the two

contact points on the physical model to their location on the FE model (as described in Section 5.2.2). The sensitivity of predicted strains to an error in placement was analyzed by shifting the two point loads into five different configurations. Locations were shifted 2 mm (i.e. approximately one element length) anteriorly, posteriorly, medially, laterally, and outward.

Inaccurate replication of forces may occur from assuming point loading in the FE models even though contact between the rods and the joint surface was in fact occurring over a small area. The sensitivity of strains to the point load assumption was explored by replacing point loads with a uniformly distributed load of identical magnitude. The contact area on the joint surfaces of the physical bones was not measured and therefore loading on each condyle of the FE models was assumed to be uniformly distributed over 11 nodes, centered on the point-contact node.

Purely axial loading assumes that the long axis of the bone is aligned with the vertical axis of the testing apparatus. A correct replication of such loading also requires that the long axis be aligned with the vertical axis of the FE coordinate system. If any of these two are misaligned, then the force direction will not be correctly replicated. Therefore, the inaccurate replication of force direction is essentially a consequence of misalignment between the experimental and FE coordinate systems. To estimate the sensitivity of strain results to such misalignment, two FE models were compared. The long axis of the bone was aligned with the vertical axis of the global coordinate system in one model; in the second model, the bone was rotated 5 degrees valgus relative to the global coordinate system. In both models, the compression was applied along the vertical axis of the global coordinate system.

Strains were observed from identical locations for all the models used in the sensitivity analysis. Strains were reported as an average of the nodal strains corresponding to the strain gauge sensing area. If was of interest to explore if this

technique would produce different results than if the strain was only recorded from the node closest to the rosette center.

Strains were analyzed locally by observing the changes at each individual rosette location. They were also analyzed globally by observing the change in the goodness of prediction of the model, i.e. the linear regression statistics. This was of particular importance since the underlying objective of the FE model was to mimic the entire physical bone. To gauge how much influence each modeling aspect had on the goodness of prediction of the model, a linear regression was used analyze the strains of each model constructed for the sensitivity analysis. The experimental strains were treated as independent variables and therefore remained consistent throughout each linear regression analysis. The numerical strains changed with each new model and therefore were assumed as dependent variables. Von Mises strains were employed in the sensitivity analysis because they characterized the general 3-D strain state with a single value, which allowed for simpler interpretation of the effects caused by the sensitivity parameters.

5.3 Results

5.3.1 Experiments

The loads placed on the bones over the five tests were very consistent (Table 5.1), and resulted in experimental strain measurements that were highly repeatable. The average standard deviation of the von Mises strains over five loading tests was 2.5, 2.9, and 6.5 microstrain in the composite femur, composite tibia, and bovine tibia, respectively. The largest standard deviations were on the anterior surface of the bovine tibia (Table 5.2).

An outlier analysis was performed on the difference in measured and predicted strain values. The strains determined from strain gauge rosette T1 of the composite tibia were found to be outliers using Chauvenet's criterion and were omitted in subsequent analyses. Strains measured from rosettes F10 of the

composite femur and B2 of the bovine tibia were also determined to be outliers and were omitted in subsequent analyses (see Fig 5.1).

5.3.2 Experiment and FE Model Comparison

5.3.2.1 Composite Tibia

The voltages from the loading rods showed that the medial and lateral condyles sustained 55% and 45% of the load, respectively. A comparison of measured and predicted principal and von Mises strains showed good agreement (Table 5.3 and Figs 5.4a and 5.4b). The average errors (calculated as root mean squared error, RMSE) of the principal and von Mises strains were 47.0 microstrain and 26.4 microstrain, respectively. The predicted principal directions were all within 20 degrees of measured directions, with an RMSE of 10 degrees. Linear regression analysis of the principal strain data indicated a good correlation between the measurements and predictions ($r^2 = 0.91$), with slope of 0.90 and an intercept of -3 microstrain (Fig 5.4c); the regression line for the von Mises strains had an r^2 of 0.95, a slope of 0.89, and an intercept of 16 microstrain (Fig 5.4e). A Bland-Altman plot showed small differences between measured and predicted strains consistently across the range of strain values (Fig 5.4f). The largest strains were seen on the posterior surface suggesting that the axial compression loading resulted in posterior bending of the tibia. Relatively large errors were observed in this region, particularly on the more curved surfaces (i.e. T2-T4 in Fig 5.2a).

5.3.2.2 Composite Femur

In the composite femur, the load was divided 30% to the medial condyle and 70% to the lateral condyle. The majority of Von Mises strains predicted from the femur FE model were within an order of magnitude of the experimental strains (Table 5.4). The RMSE of the principal and von Mises strains were 191.5 microstrain and 144.5 microstrain, respectively. The predicted principal directions had an average error (RMSE) of 35 degrees compared to measured directions. Linear regression analysis of the principal strain data revealed an r^2 of 0.75, with a slope of 1.33, and an intercept of -14 microstrain (Fig 5.5c). Linear

regression analysis of von Mises strains produced an r^2 of 0.45, with a slope of 1.15, and an intercept of 63 microstrain (Fig 5.5e). Regions of the femur with complex curvatures such as the intercondylar notch (F11) had larger errors. Errors on the order of several hundred microstrain were observed on the lateral surface of the femur (F12 and F13 in Fig 5.2b). A Bland-Altman plot showed increased error with higher levels of strain (Fig 5.4f).

5.3.2.3 Bovine Tibia

In the bovine tibia, the load was divided 34% to the medial condyle and 66% to the lateral condyle. The RMSE of the principal and von Mises strains were 43.4 microstrain and 46.8 microstrain, respectively. The average error (RMSE) of the principal directions was 20 degrees. Linear regression analysis of the principal strain data indicated a good correlation between the measurements and predictions ($r^2 = 0.82$), with slope of 1.03, and an intercept of -22 microstrain (Fig 5.6c). The regression line for von Mises strains had an r^2 of 0.74, a slope of 0.86, and an intercept of -15 microstrain (Fig 5.6e). The Bland-Altman plot showed that differences between measured and predicted strains were fairly consistent across the range of strain values (Fig 5.6f).

5.3.3 Sensitivity Analysis of Material Properties

To estimate the effect inaccurate material properties may have had on strains, two composite femur FE models were created: one with a 20% increase and the other with a 20% decrease in the manufacturer-provided Young's modulus. The largest changes in strain values occurred at F11-F13, with a peak change of 177 microstrain (Table 5.6). The composite tibia FE model had a slightly lower sensitivity to the changes in mechanical properties, with a peak difference of 99 microstrain (Table 5.6).

Varying the material properties of the cortical and cancellous bone had only minor effects on the regression analysis results. The coefficient of determination r^2 was insensitive to the material properties for both the composite femur and tibia

FE models (Table 5.7). Varying the material properties changed the regression line slope at most by 0.28 and intercept by a maximum of 16 microstrain in the composite femur model. The goodness of prediction of the composite tibia model was even less sensitive to the changes in material properties.

5.3.4 Sensitivity Analysis of Loading Conditions

Among the five different load configurations used to gauge the sensitivity of strains to load placement, a maximum change of 70.6 microstrain from the center configuration was observed (Table 5.8). Similar results were seen in the composite tibia model. Regression analysis revealed that the predictive power of the model was slightly more sensitive to load placement changes compared to material properties changes. In the composite femur, shifting the loads anteriorly produced the largest change in the regression analysis parameters (Table 5.7). In this configuration, r^2, slope, and intercept changed by 0.08, 0.13, and 10.22 microstrain, respectively. Shifting the load anteriorly also produced the greatest change in predictive power in the composite tibia model, but this change was small. The r^2 changed by a maximum of 0.07; slope by a maximum of 0.21; and intercept by a maximum of 33.16 microstrain.

Very little change was observed throughout the strain gauge locations in the composite femur FE model whether point-loading or uniformly-distributed loading was used, therefore the results are not reported here. Strains similarly displayed minimal variability in the composite tibia FE model.

In the femur FE model, a 5 degree valgus rotation produced a peak change of 160 microstrain (Table 5.9). The changes were largest at the lateral surface of the femur (F12, F13 in Fig 5.1b). Load alignment appeared to have the greatest effect on the goodness of prediction of the model compared to material properties and load placement (Table 5.7). Rotating the model by 5 degrees valgus particularly affected the slope and intercept of the regression line; the slope changed by 0.19 and the intercept changed by 32.67 microstrain. The strain changes from a 5

degree valgus rotation in the tibia FE model were as large as 144 microstrain (Table 5.9). Notably, the overall correspondence between the measured and predicted strains worsened dramatically (Table 5.7). The r^2 decreased by 0.23, the slope decreased by 0.16, and the intercept increased by 25.17 microstrain.

5.3.5 Variability of Predicted Strains in Gauge Region

The standard deviation and range of von Mises strain values can be used to gain a sense of the variability beneath each strain gauge. In the composite tibia FE model, standard deviations were all an order of magnitude lower than the mean strains. However, the difference between maximum and minimum strains in a single rosette area was as large as 122 microstrain (Table 5.10). In the composite femur, standard deviations were clearly greater. In one rosette (F11), von Mises strains varied by as much as 700 microstrain (Table 5.10). For both the composite femur and tibia, the goodness of prediction improved if von Mises strains were averaged over the gauge area rather than using the node closest to the rosette center.

5.4 Discussion

5.4.1 Goodness of Prediction of FE Models

FE models of the composite femur and tibia and bovine tibia were verified with experiments in which axial compression was applied. The linear regression results of the composite tibia compared well with the data from other studies performing axial compression on composite tibiae (Gray et al., 2007; Completo et al., 2007c). In those studies, the slopes of the regression lines ranged from 0.90 to 1.28, the intercepts ranged from -22.02 to 21.36, and the r^2 ranged from 0.91 to 0.97. In this study, relatively larger errors were observed on the upper posterior surface, particularly on the more curved surfaces (i.e. T2-T4 in Fig 5.2). The strains in the proximal posterior tibia have similarly been difficult to predict in other composite tibia FE models (Gray et al., 2007; Completo et al., 2007c).

The femur FE model generally overpredicted experimental strains, resulting in a higher linear regression slope and lower correlation than those seen in other composite femur validation studies (Viceconti et al., 1998; Completo et al., 2007b). To gain a sense of the strain distribution over the entire bone, strains in geometrically complex regions such as the condyles and intercondylar notch (F9 and F11 in Fig 5.2) were observed in addition to strains at simpler regions such as the shaft. This is in contrast to the other studies, which only compared strains measured in regions of simple geometry. Strains measured at geometrically complex regions may not be accurate because a proper placement of strain gauges may not occur and they are also susceptible to local bone stiffness abnormalities.

A bovine bone was used in this study to validate the geometry and material properties modeling aspects of the subject-specific FE modeling framework. Animal bones are not commonly used for validation purposes since cadaveric bones are preferred. Generally, the biological system used to assess the usefulness and predictive power of a model is not important. The bovine tibia was suitable in this preliminary phase as it allowed for the development of an experimental protocol before cadaveric bones are used. Since no bovine model validation studies were found in literature, a comparison was made with studies using cadavers. The linear regression results of the bovine tibia compared well with studies modeling the proximal femur (Keyak et al., 1993; Taddei et al., 2006; Taddei et al., 2007). In those studies, the slopes of the regression lines ranged from 0.63 to 1.03, the intercepts ranged from 0 to 84, and the r^2 ranged from 0.63 to 0.92. Differences between measured and predicted strains may have partly resulted from interpreting stiffness properties using an empirical relationship that was not strictly meant for bovine bone (Carter and Hayes, 1977). Relationships between density and Young's modulus specifically for bovine bone have been reported (Hodgskinson and Currey, 1992; Hodgskinson et al., 1997), but are only suitable for a narrow cancellous bone density range. The relationship reported by Carter and Hayes (1977) was based on a larger range of densities, including bovine cortical bone, and therefore it was felt to be more suitable for this study

since the range of bone densities in the bovine tibia specimen was quite large. The use of the above relationship required an assumption of isotropic bone properties, which may not be strictly physiological and may have introduced some error in the predictions.

5.4.2 Sensitivity Analysis

In this study, several important assumptions were made with respect to the construction of the FE model and the replication of experimental conditions, both of which may have affected the correspondence between measured and predicted strains in all 3 specimens. It was of interest to quantify the impact of these assumptions on the goodness of prediction of the models, and was best accomplished using a sensitivity analysis of the composite bone FE models. Although many other validation studies have incorporated similar assumptions, this level of analysis has not been attempted by those studies.

5.4.2.1 Sensitivity of Strains to Material Properties

The cortical and cancellous bones of FE models are often characterized using material properties provided by the manufacturer. However, the manufacturer-provided value for the cortical bone may not be entirely correct, as it does not take into account the local density abnormalities and the layer of pure epoxy coating the cortex. The cortical bone contains a coat of pure epoxy (Gray et al., 2007), which may lower the overall elastic modulus of the cortex (Stolk et al., 2002). Stolk et al. (2002) have estimated that the actual Young's modulus of the cortical bone is 19% lower than manufacturer-provided value. Therefore, incorporating an incorrect material property into the FE model may have an impact on the results of the validation. This impact was quantified using a sensitivity analysis in which the manufacturer-provided Young's moduli of the cortical and cancellous bones were varied by 20%. These material properties changes were found to have very little impact on the overall goodness of prediction of the FE models. This was highlighted by the fact that the r^2 value was completely insensitive to the varying material properties. Thus, incorporating manufacturer-provided material

properties will not likely affect the outcomes of a validation. However, local strain changes should not be overlooked since they changed by as much as 177 microstrain in the femur and up to 100 microstrain in the tibia. This may be indicative of the local abnormalities which exist in composite bones. Such abnormalities are more common in the regions containing complex geometry (e.g. the intercondylar notch), where there is relatively less glass-fiber (Cristofolini et al., 1996; Completo et al., 2007c). These abnormalities should be taken into consideration if strains (or stresses) in a particular area of the composite bone are of interest.

5.4.2.2 Sensitivity of Strains to Load Placement

Proper validation requires an appropriate replication of the loads applied by the materials testing machine. However, the location in the FE model where the load is applied may not always be representative of the physical location. In validation studies of femur and tibia FE models, the methodology used to identify the load placement location was rarely detailed. The nodes selected in the FE models for load application appeared somewhat arbitrary and therefore the model might not have replicated the experimental loading accurately. In this study, a sensitivity analysis was performed to quantify how much load placement inaccuracy would affect the goodness of prediction of the FE model.

Load placement location of the two compression forces on the physical bone was translated to the FE models using the method described in Section 5.2.2, which required alignment of the CMM and FE model coordinate systems. The error in the translation was estimated from the alignment error, and was 2.1 mm for the composite femur, and 2.8 mm for the composite tibia. Therefore, by varying load placement by an amount similar to the translation error, and observing the strain changes, one can gain a sense of the impact inaccurate load placement can have on validation results. Because the load can potentially be misplaced in any direction along the joint surface, many different load configurations could have been tested. However, the loads were shifted in 5 basic directions to see if strains

were more sensitive to offset in any particular direction. In this study, it was found that the goodness of prediction was slightly more sensitive to an anterior offset. Local strains were not as sensitive to changes in load placement compared to changes in material properties. In contrast, though, the collective change in strains had a bigger impact on the goodness of prediction. The observed changes in regression results were large enough that an effort should be made to replicate the load placement position as accurately as possible in the FE model. Since contact points may shift due to bone deflecting mid-loading (Gray et al., 2007), an effort should be made to record the load placement location when the bone is fully deflected.

5.4.2.3 Sensitivity of Strains to Load Direction and Misalignment

Validation studies of the distal femur and proximal tibia often compare strains generated in the bones from purely compressive loading. Such loading is used because it is relatively easy to apply in a materials testing machine and also in the FE environment. However, pure compression will be applied to the bone only when the long axis of the physical specimen is aligned with the vertical axis of the testing machine.

It is important to align the vertical axis of the specimen with that of the testing apparatus, as even a small misalignment can cause large bending moments and overshadow the deflection from a pure axial load (Cristofolini and Viceconti, 2000). It has been suggested that this can be accomplished by aligning reference axes defined using bone landmarks with the machine axis (Ruff and Hayes, 1983; Stolk et al., 2002; Gray et al., 2007). However, such a method is subjective and may still introduce some error in the alignment. The amount of error that a misalignment may cause in validation results has never been quantified. This was explored by comparing a perfectly aligned model with one that was rotated by 5 degrees valgus, an amount representative of the tibiofemoral angle when a person is standing upright (Williams, 1999). The results showed that the goodness of prediction was noticeably affected by misalignment in the femur and, in

particular, the tibia, where r^2 changed by more than 0.2. The misalignment also had an effect at the local level as individual strains changed by over 160 microstrain. Thus, great care should be taken to ensure that the long axis of the bone is correctly aligned with the loading axis in the testing apparatus and vertical axis in the FE simulation.

In this study, the tibia was potted with 0 degrees adduction. However, since the bones were used in a separate experiment where accurate replication of the physiological tibiofemoral axis was necessary, the femur was potted with an angular offset of about 3 degrees valgus and 4 degrees flexion. Thus, the vertical loads were better aligned with the tibia than the femur. The results of the sensitivity analysis may provide a partial explanation for the difference in the goodness of prediction between the two models. However, the goodness of prediction is also affected by the number of observations that are being compared. In this study, a much smaller number of strains were observed compared to other validation studies (Taddei et al., 2007; Gray et al., 2007). It can be envisioned that an increased number of observations obtained from different loading scenarios would improve the goodness of prediction of the FE models.

5.4.2.4 Sensitivity of Strains to Point Contact Assumption

Point forces were applied to all the FE models in this study, as is commonly done in similar validation studies (Gray et al., 2007; Completo et al., 2007b; Completo et al., 2007c). However, in the experiment, contact was observed to occur over a small area due to flattening of the nylon ball at the bone interface. A recent validation study suggested that point loading may affect strains within 25 mm of the load origin (Gray et al., 2007). In this study, all strain gauges were placed more than 25 mm from the loads. The comparison of point loading with area loading further showed that the rosette locations were far enough away from the load origin that the contact condition had negligible effect on the strain, thus the assumption of point loading was acceptable in this study.

5.4.3 Replication of Experimental Loading Conditions

In this study, an axial loading condition was chosen because it was representative of the natural loading condition of the lower limb. Although loading in the testing machine was intended to be purely compressive through the vertical displacement of the actuator, load cell data showed that transverse forces and bending moments were also experienced by the bones during the experiment (Table 5.1). Transverse forces, and their associated bending moments, should not have been present if pure compression was applied to the bones. Contact with a curved joint surface may have caused bending of the rods, as evidenced by their strain gauge output. This bending was caused by the inability of the rods to freely translate since they were locked into position in the slotted plate. Consequently, they pushed transversely on the bone. Although the transverse forces were at least an order of magnitude lower than the axial forces, they should be minimized since they can cause relatively large bending moments in bones. A feature allowing the rods to move freely along the horizontal plane with the use of a horizontal cross-rail attached to the testing apparatus is therefore necessary. However, even this may not completely obviate horizontal forces due to friction forces in the rails (Gray et al., 2007). A number of different setups including metallic spheres (Completo et al., 2007b) and hinges (Cristofolini and Viceconti, 2000) have been employed in an attempt to apply purely compressive loading on the bones but it is not known if this was actually achieved since no load cell data were reported.

Both condyles in the femur and tibia were simultaneously loaded in the experiments, with different forces placed on each condyle (as seen in the natural condition). Previous studies have suggested that this may cause large reproducibility errors and have employed unicondylar loading (Completo et al., 2007c; Gray et al., 2007); such loading is not physiologically representative and therefore was not employed in this study. Strain gauges on the rods provided an estimate of the proportion of the total load sustained by each condyle. However, the total could not be differentiated into its transverse and axial components. Therefore, in the FE simulation, both transverse and axial forces were divided

between each condyle according to the same proportion. The proportions for each model were reported in Section 5.3.2.

Although it may not be possible to completely eliminate the presence of transverse forces in cases of vertical compression, they should at least be accurately measured to allow better replication of loading conditions in the FE models.

5.4.4 Improving Finite Element Strain Representation

Typically, strain gauge locations in the physical bone are mapped to the FE model by registering measurements acquired with a digitizing arm or a coordinate measuring machine (Completo et al., 2007b; Gray et al., 2007; Taddei et al., 2006, 2007). In this study, rosette centers were digitized using CMM and translated to their closest nodes in the FE model using the same alignment technique for load placement. Translation errors of approximately 0.6 mm and 1.1 mm were present for the composite femur and tibia, respectively; similar registration error was reported by Taddei et al. (2007).

In some studies, numerical strains were only observed at the nodes closest to the rosette center (Completo et al., 1997b; Keyak et al., 1993). Validation results may be sensitive to the nodal locations used to observe strains, especially in locations of high strain gradient. The large variability in strains occurring within the small strain gauge area suggests that large strain gradients were occurring in the composite bones, particularly in the femur (Table 5.10). To account for such gradients, strains in the nodes corresponding to the gauge's sensing area should be averaged (Taddei et al., 2007). In this study, if only a single node was used to represent the gauge location, the goodness of prediction of the model was worse (Table 5.7). Thus, a more correct comparison is facilitated by averaging nodal strains; this may also help compensate for the registration error associated with mapping the strain gauge location.

5.4.5 Improving Principal Strain Comparison

Principal strains are commonly used to assess validity of FE models (Keyak et al., 1993; Stolk et al., 2002; Waide et al., 2004; Completo et al., 2007b, 2007c; Gray et al., 2007; Taddei et al., 2007). They are compared with experimental strains measured from strain gauges, which are the gold standard for measuring strains on bone surfaces. Most studies try to align the vertical strain gauges with the long axis of the bone, ostensibly by visual inspection (Completo et al., 2007b; Gray et al., 2007). However, this may not be accomplished accurately and therefore measured axial strains should not be directly compared with predicted ones, and it is better to compare principal strains. However, a careful methodology must be followed to correctly compare principal strains. Generally, experimental and FE strains cannot be directly compared because bone surfaces are generally not aligned with any of the major planes of the FE model. Commercial finite element software may not output surface strains for 3-D elements. However, the predicted and measured principal strains must be in the same plane for proper comparison. This may not occur when the model surface is not smooth, but an effort must be made to ensure that the computed principal strains being used for comparison are parallel to the model surface (Keyak et al., 1993). In this study, it was verified that 2 of the 3 principal strains were parallel to the surface and therefore they could be properly compared with the measured strains. In situations where FE strains are not aligned with the surface, they would need to be transformed to the surface plane. It should always be explicitly mentioned in validation studies that in-plane strains are being compared, as poor communication may lead to confusion regarding whether a proper comparison is being performed.

Principal strains are vectors therefore the directions of the principal strains should be reported with their magnitudes. A comparison of principal directions was provided in this study to provide bring greater strength to the validation (Tables 5.3 to 5.5). However, such a comparison has not been performed in some validation studies (Gray et al., 2007; Completo et al., 2007b) or only discussed in brief (Completo et al., 2007c). Bone is anisotropic and, therefore, its failure

strength is direction-dependent. The ability to accurately predict strain direction is necessary if, for example, the FE models are being used to assess potential bone fracture. A predicted strain magnitude that compares well with a measured one does not imply that they will also have similar directions. For example, the measured and predicted magnitudes at location B12 in the bovine tibia are similar but the directions of the strains are much different (Table 5.5). Thus, an explicit comparison of principal directions should be provided in validation studies to ensure a complete assessment of a model's predictive capabilities.

5.5 Summary and Conclusions

The objective of this study was to provide preliminary validation of the geometry and material properties construction techniques developed for subject-specific FE models. FE models of a composite tibia and a bovine tibia constructed with these techniques simulated the physical models with good accuracy. The FE model of a composite femur was also fairly accurate but requires a larger set of observations to ensure that the modeling techniques are effective.

An aspect of the experimental loading was not accurately replicated in the FE model, which may have resulted in underestimation of the validity of the FE models. Unintended transverse loading occurred at the joint surface and could not be measured accurately during the experiment. Therefore, some assumptions were necessary when attempting to simulate the transverse and axial forces in the FE models.

This study also highlighted some assumptions frequently made in validation studies and analyzed the effects they may have on reported results. The global and local effects were examined using a sensitivity analysis, and quantified using linear regression analyses and traditional error analysis. Improper simplification of composite bone material properties by using manufacturer-provided data was not seen to greatly affect the validation results. A greater impact was observed when experimental loading conditions were not accurately replicated in the FE

simulations. The goodness of prediction in FE models was affected if the forces in the experiment were not placed at the same location in the simulation. In this study, the validation results were most affected when the directions of the loads were not correctly implemented due to a slight misalignment between the loading axis of the test apparatus and the vertical axis in the FE environment.

Predicted strain values should be averaged over the gauge sensing area to facilitate a more realistic comparison of strain values. This improved representation of strain values resulted in a better correlation between measured and predicted strains. A careful methodology must be followed to ensure that principal strains are correctly compared in validation studies. Principal strains from the FE model must be confirmed to be parallel to the bone surface before comparison with measured strains. Additionally, the directions of principal strains must be compared and reported since matching strain magnitudes do not necessarily imply identical strain vectors. A full characterization of principal strains is necessary to accurately gauge the validity of a FE model.

The issues presented in this study should be kept in mind when one is reviewing validation literature or conducting a validation experiment themselves.

Table 5.1: Mean and standard deviation of five sets of load cell readings for composite tibia, composite femur, and bovine tibia.

	Composite Tibia		Composite Femur		Bovine Tibia	
	Mean	SD	Mean	SD	Mean	SD
Fx (lb)	-11.21	0.09	-3.04	0.11	-12.09	0.23
Fy (lb)	-9.38	0.08	3.25	0.23	-36.85	0.39
Fz (lb)	158.04	1.01	154.96	1.98	294.99	3.26
Mx (lb-in)	-76.74	0.00	34.83	1.42	-12.72	7.02
My (lb-in)	64.34	0.86	11.80	0.00	-83.40	4.09
Mz (lb-in)	3.94	0.41	-2.81	0.50	5.93	1.03

Table 5.2: Mean and standard deviation (in microstrain) of five sets of von Mises strains in the composite tibia, composite femur, and bovine tibia. For strain gauge locations, see Fig 5.1.

Composite Tibia			Composite Femur			Bovine Tibia		
Strain Gauge	Mean	SD	Strain Gauge	Mean	SD	Strain Gauge	Mean	SD
T1	449.2	7.9	F1	153.0	4.6	B1	95.5	1.8
T2	286.4	5.6	F2	177.3	2.2	B2	195.8	4.1
T3	296.0	4.0	F3	5.7	0.5	B3	92.5	4.4
T4	305.7	3.8	F4	21.4	0.4	B4	263.4	6.0
T5	325.6	4.7	F5	8.5	1.0	B5	96.9	3.8
T6	129.8	2.0	F6	125.2	1.3	B6	149.9	2.0
T7	186.0	3.6	F7	433.3	4.8	B7	214.2	3.4
T8	28.5	0.8	F8	332.3	3.1	B8	59.1	11.4
T9	159.1	9.3	F9	214.3	2.6	B9	67.3	28.0
T10	102.7	2.0	F10	308.2	3.0	B10	42.0	2.1
T11	126.8	1.9	F11	297.5	3.1	B11	44.2	6.0
T12	145.1	3.2	F12	243.9	2.8	B12	20.0	2.4
T13	6.1	0.8	F13	298.7	3.6	B13	127.5	8.8

Table 5.3: Measured and predicted principal and von Mises strains (in microstrain), with corresponding error, for composite tibia. Principal directions (in degrees) were measured clockwise from the horizontal axis.

	Minimum principal strain			Maximum principal strain			Principal direction			Von Mises strain		
Strain Gauge	Measured	Predicted	Error	Measured	Predicted	Error	Measured	Predicted	Error	Measured	Predicted	Error
T2	-290.1	-246.5	43.6	-15.4	-27.5	12.1	5.2	2.1	3.1	286.4	239.1	47.3
T3	-278.0	-269.0	9.0	94.3	31.2	63.2	3.9	3.1	0.8	296.0	262.0	34.0
T4	-155.9	-155.9	0.0	345.9	264.2	81.7	-19.7	-6.4	13.4	305.7	297.9	7.8
T5	-389.1	-408.6	19.5	51.2	151.2	100.0	-17.2	-0.8	16.4	325.6	394.2	68.6
T6	-135.0	-152.5	17.5	-24.3	-11.4	13.0	-1.5	-4.4	3.0	129.8	147.0	17.1
T7	-183.4	-204.8	21.4	28.1	16.3	11.7	8.5	9.2	0.7	186.0	198.5	12.5
T8	-19.7	-11.6	8.1	21.9	1.0	20.9	-5.9	5.7	11.7	28.5	13.3	15.3
T9	-21.4	-0.9	20.5	198.2	170.5	27.7	10.9	-0.4	11.3	159.1	168.5	9.4
T10	-4.4	-46.7	42.3	115.2	146.3	31.1	13.3	25.6	12.4	102.7	147.2	44.5
T11	-124.2	-113.6	10.6	22.3	14.7	7.6	7.2	-2.1	9.3	126.8	110.7	16.1
T12	-147.7	-135.6	12.1	29.7	15.8	13.9	-5.6	-7.2	1.6	145.1	131.7	13.4
T13	2.0	-39.7	41.7	6.4	18.6	12.2	-32.8	-14.8	18.0	6.1	42.6	36.4

Table 5.4: Measured and predicted principal and von Mises strains (in microstrain), with corresponding error, for composite femur. Principal directions (in degrees) were measured clockwise from the horizontal axis.

	Minimum principal strain			Maximum principal strain			Principal direction			Von Mises strain		
Strain Gauge	Measured	Predicted	Error	Measured	Predicted	Error	Measured	Predicted	Error	Measured	Predicted	Error
F1	-52.1	-131.1	78.9	145.1	50.9	94.2	10.8	-4.9	15.7	153.0	136.3	16.7
F2	-49.3	-62.4	13.1	173.4	185.4	12.0	-3.4	-28.2	24.8	177.3	189.6	12.2
F3	-11.7	-1.7	10.0	1.4	55.7	54.3	35.5	-61.0	96.5	5.7	67.1	61.4
F4	-35.4	-9.0	26.5	0.0	49.7	49.7	-33.5	-35.0	1.5	21.4	51.0	29.6
F5	-8.7	-62.5	53.8	1.5	60.2	58.8	18.1	42.5	24.4	8.5	84.7	76.2
F6	-141.3	-154.4	13.1	12.2	49.1	36.9	-12.9	-2.0	10.9	125.2	153.0	27.9
F7	-405.8	-166.4	239.4	145.5	59.8	85.7	1.1	-11.3	12.4	433.3	171.5	261.8
F8	-352.0	-460.4	108.4	120.1	83.1	37.0	-13.1	-12.7	0.3	332.3	453.5	121.2
F9	-224.6	-292.7	68.1	59.9	111.7	51.8	22.1	79.6	57.5	214.3	292.4	78.1
F11	-102.4	-320.7	218.3	307.5	618.2	310.7	-0.8	6.0	6.8	297.5	676.8	379.2
F12	-245.1	-506.1	261.0	31.2	6.2	25.0	-0.7	-3.5	2.9	243.9	490.0	246.1
F13	-312.5	-726.6	414.0	-58.0	-101.8	43.7	-2.7	-2.2	0.4	298.7	707.2	408.5

Table 5.5: Measured and predicted principal and von Mises strains (in microstrain), with corresponding error, for bovine tibia. Principal directions (in degrees) were measured clockwise from the horizontal axis.

	Minimum principal strain			Maximum principal strain			Principal direction			Von Mises strain		
Strain Gauge	Measured	Predicted	Error	Measured	Predicted	Error	Measured	Predicted	Error	Measured	Predicted	Error
B1	-96.1	-101.0	4.9	-25.9	38.8	64.7	12.0	-0.2	12.2	95.5	103.0	7.5
B3	-95.5	-137.4	41.9	8.2	99.4	91.2	-3.1	-6.7	3.6	92.5	162.0	69.5
B4	-270.6	-220.3	50.3	34.4	77.5	43.1	2.5	-3.6	6.1	263.4	222.7	40.7
B5	-100.1	-44.6	55.5	8.0	5.2	2.8	18.9	29.4	10.5	96.9	43.6	53.3
B6	-109.1	-60.4	48.7	109.0	70.3	38.6	24.9	28.4	3.5	149.9	87.7	62.2
B7	-142.9	-82.0	60.9	167.8	133.5	34.3	20.7	12.6	8.1	214.2	148.4	65.9
B8	-52.4	-3.4	49.0	30.8	16.2	14.6	-19.0	-23.0	4.0	59.1	16.1	43.0
B9	-63.4	-4.9	58.5	-30.5	4.3	34.8	12.2	15.7	3.5	67.3	6.2	61.2
B10	-16.6	-0.5	16.1	40.0	10.3	29.7	1.2	-3.6	4.8	42.0	10.2	31.8
B11	-39.8	0.7	40.5	22.1	7.8	14.3	14.2	-37.6	51.8	44.2	7.7	36.5
B12	-20.6	-8.7	11.9	2.3	9.6	7.3	-3.2	33.6	36.8	20.0	12.4	7.6
B13	-132.3	-95.4	36.8	-6.7	47.4	54.1	2.7	-21.1	23.8	127.5	101.1	26.4

Table 5.6: Von Mises strains (in microstrain) observed in FE composite femur and tibia models with different Young's moduli. Young's moduli of cortical and cancellous bones were increased and decreased by 20% of the manufacturer-provided values, E=12.4 GPa (cortex) and E=104 MPa (cancellous). The difference in strain values between the altered E and manufacturer-provided E are provided.

Composite Femur						Composite Tibia					
Strain Gauge	E	E+20%	E-20%	Difference (E+20%)	Difference (E-20%)	Strain Gauge	E	E+20%	E-20%	Difference (E+20%)	Difference (E-20%)
F1	136.3	113.6	170.3	22.7	34.1	T2	239.1	199.3	298.9	39.9	59.8
F2	189.6	158.0	237.0	31.6	47.4	T3	262.0	218.3	327.5	43.7	65.5
F3	67.1	55.9	83.9	11.2	16.8	T4	297.9	248.2	372.3	49.6	74.5
F4	51.0	42.5	63.8	8.5	12.8	T5	394.2	328.5	492.8	65.7	98.6
F5	84.7	70.6	105.9	14.1	21.2	T6	147.0	122.5	183.7	24.5	36.7
F6	153.0	127.5	191.3	25.5	38.3	T7	198.5	165.5	248.2	33.1	49.6
F7	171.5	142.9	214.3	28.6	42.9	T8	13.3	11.1	16.6	2.2	3.3
F8	453.5	377.9	566.9	75.6	113.4	T9	168.5	140.4	210.6	28.1	42.1
F9	292.4	243.7	365.5	48.7	73.1	T10	147.2	122.7	184.0	24.5	36.8
F11	676.8	1058.1	846.0	112.8	169.2	T11	110.7	92.3	138.4	18.5	27.7
F12	490.0	564.0	612.5	81.7	122.5	T12	131.7	109.8	164.7	22.0	32.9
F13	707.2	408.3	884.0	117.9	176.8	T13	42.6	35.5	53.2	7.1	10.6

Table 5.7: Results of the regression analyses comparing measured and predicted von Mises strains in the models used to examine three sensitivity parameters. To analyze the influence of the material properties, Young's moduli of cortical and cancellous bones were increased and decreased by 20% of the manufacturer-provided values, E=12.4 GPa (cortex) and E=104 MPa (cancellous). To analyze the influence of load placement, six different load configurations were compared. To analyze the influence of load alignment, a perfectly aligned model was compared with one rotated by 5 degrees valgus. To analyze the influence of strain observation technique, strains averaged over the gauge area were compared with strains measured only from the gauge center.

Parameter	Model	Composite Femur			Composite Tibia		
		r^2	Slope	Intercept	r^2	Slope	Intercept
Material Properties	E	0.45	1.15	62.69	0.95	0.89	15.69
	E+20%	0.45	0.95	52.24	0.95	0.74	13.08
	E-20%	0.45	1.43	78.36	0.95	1.12	19.62
Load Placement	Center	0.45	1.15	62.69	0.95	0.89	15.69
	Anterior	0.37	1.02	72.91	0.88	0.70	48.85
	Posterior	0.50	1.24	65.75	0.94	1.10	11.04
	Medial	0.46	1.13	64.27	0.91	0.75	38.63
	Lateral	0.41	1.15	69.30	0.89	1.02	2.35
	Outward	0.43	1.12	68.51	0.91	0.84	23.28
Load Alignment	0 degrees valgus	0.45	1.15	62.69	0.95	0.89	15.69
	5 degrees valgus	0.41	0.96	95.36	0.72	0.73	40.86
Strain Observation	Averaged strains	0.45	1.15	62.69	0.95	0.89	15.69
	Closest strains	0.32	1.12	188.60	0.90	0.81	24.41

Table 5.8: Von Mises strains (in microstrain) predicted in FE composite femur and tibia models implementing different load configurations. The maximum difference in strain between the five altered configurations and the original configuration (Center) is shown for each strain gauge location.

Strain Gauge	Center	Anterior	Posterior	Medial	Lateral	Outward	Maximum difference
F1	136.3	203.0	65.6	143.6	128.0	133.2	70.6
F2	189.6	194.7	201.7	166.4	212.6	192.4	23.2
F3	67.1	53.5	97.4	71.2	64.0	62.5	30.2
F4	51.0	36.4	86.2	45.4	67.2	50.6	35.2
F5	84.7	90.6	81.2	92.4	105.1	84.0	20.4
F6	153.0	131.9	191.5	193.2	114.7	164.8	40.2
F7	171.5	113.3	237.7	175.2	170.4	170.3	66.3
F8	453.5	397.2	511.8	471.9	445.8	419.9	58.3
F9	292.4	251.5	347.8	301.9	281.6	313.9	55.5
F11	676.8	657.6	702.0	725.2	660.4	638.0	48.5
F12	490.0	479.6	501.7	426.5	551.0	522.7	63.5
F13	707.2	690.9	722.3	653.6	759.2	737.1	53.6
T2	239.1	210.9	275.8	224.8	255.5	217.1	36.7
T3	262.0	225.1	316.4	259.7	269.4	250.1	54.4
T4	297.9	267.5	334.3	294.0	307.2	268.1	36.4
T5	394.2	349.2	457.8	328.2	441.2	406.3	66.0
T6	147.0	151.1	146.5	115.7	173.4	157.4	31.3
T7	198.5	187.6	219.0	143.4	244.2	191.5	55.2
T8	13.3	18.9	40.2	10.1	17.4	18.5	26.9
T9	168.5	200.7	140.6	181.2	163.8	162.9	32.2
T10	147.2	177.6	115.8	132.6	151.2	140.1	31.4
T11	110.7	126.3	85.3	149.6	78.0	123.6	38.9
T12	131.7	129.8	128.5	191.3	84.8	140.1	59.6
T13	42.6	74.7	19.8	75.1	19.0	46.8	32.6

Table 5.9: Variability of von Mises strains (in microstrain) caused by a 5 degree valgus rotation in the FE composite femur and tibia models.

Composite Femur				Composite Tibia			
Strain Gauge	0 degrees valgus	5 degrees valgus	Difference	Strain Gauge	0 degrees valgus	5 degrees valgus	Difference
F1	136.3	179.7	43.5	T2	239.1	280.5	41.3
F2	189.6	95.8	93.8	T3	262.0	251.0	11.0
F3	67.1	79.5	12.3	T4	297.9	295.2	2.7
F4	51.0	40.4	10.6	T5	394.2	464.4	70.2
F5	84.7	169.4	84.7	T6	147.0	176.5	29.6
F6	153.0	274.2	121.1	T7	198.5	342.4	143.8
F7	171.5	204.6	33.1	T8	13.3	24.6	11.3
F8	453.5	410.2	43.3	T9	168.5	173.5	5.0
F9	292.4	348.1	55.8	T10	147.2	139.5	7.7
F11	676.8	706.0	29.2	T11	110.7	62.3	48.4
F12	490.0	329.0	161.0	T12	131.7	47.1	84.6
F13	707.2	583.6	123.7	T13	42.6	75.8	33.3

Table 5.10: Variability of von Mises strains (in microstrain) inside each strain gauge region in the FE composite femur and tibia models.

Composite Femur					Composite Tibia				
Strain Gauge	Mean	SD	Minimum	Maximum	Strain Gauge	Mean	SD	Minimum	Maximum
F1	136.3	33.7	86.9	183.1	T2	239.1	8.3	225.8	251.3
F2	189.6	44.6	141.1	263.1	T3	262.0	15.5	245.0	288.8
F3	67.1	19.8	49.7	107.8	T4	297.9	34.3	245.4	354.7
F4	51.0	25.1	9.7	97.5	T5	394.2	44.9	342.0	464.4
F5	84.7	16.9	63.8	109.2	T6	147.0	14.9	128.7	175.9
F6	153.0	38.4	95.8	202.9	T7	198.5	15.0	179.0	219.6
F7	171.5	19.6	145.0	200.4	T8	13.3	7.0	5.1	25.7
F8	453.5	42.3	385.2	511.1	T9	168.5	18.9	134.9	197.8
F9	292.4	74.8	167.0	404.3	T10	147.2	29.1	105.4	178.4
F11	676.8	246.8	272.2	1068.8	T11	110.7	13.4	89.5	132.6
F12	490.0	22.7	450.6	515.9	T12	131.7	9.7	118.4	144.3
F13	707.2	90.2	579.4	871.1	T13	42.6	6.9	31.3	53.5

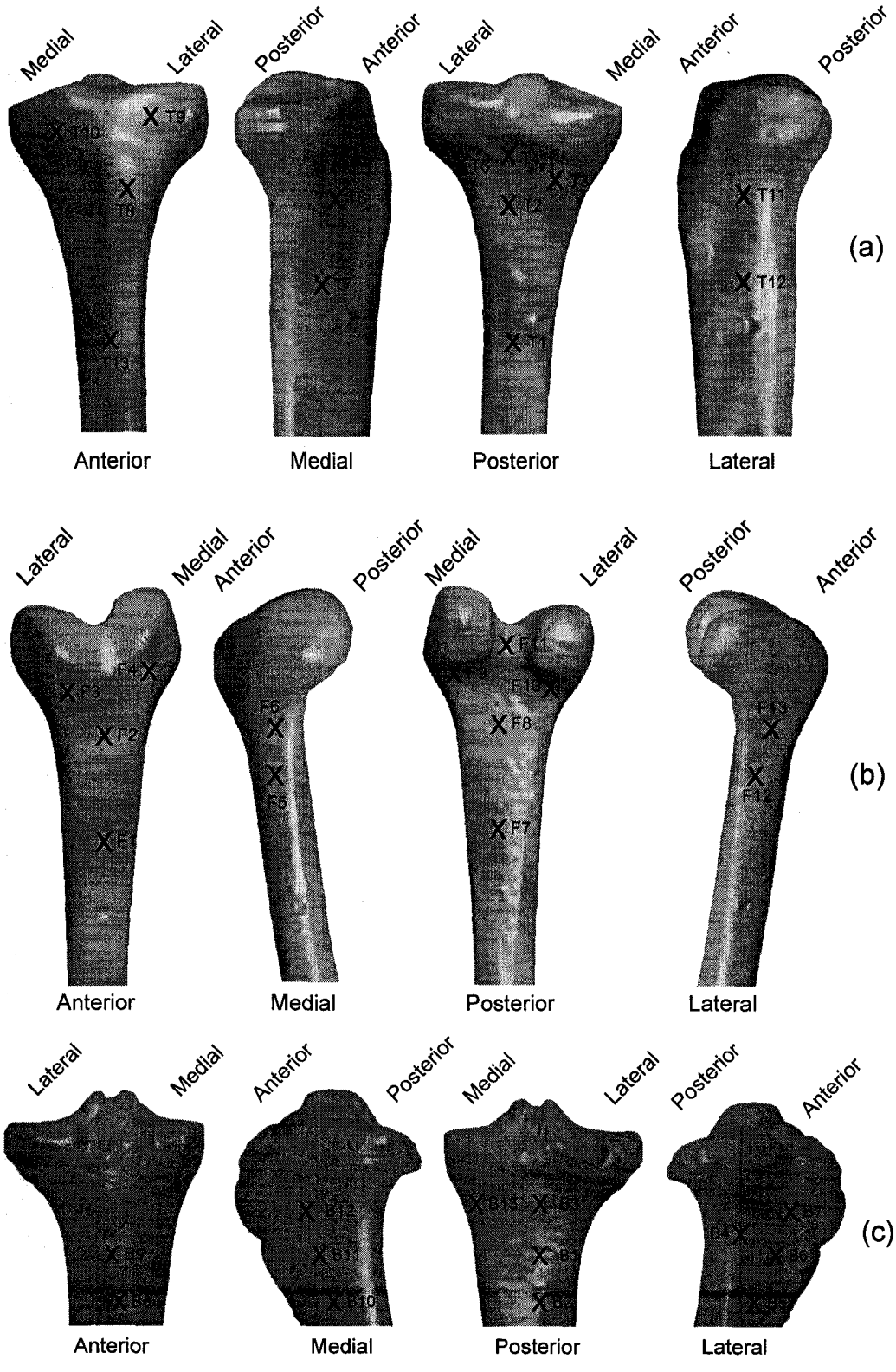

Figure 5.1: Schematic of strain gauge rosette placement in the composite tibia (a), composite femur (b), and bovine tibia (c).

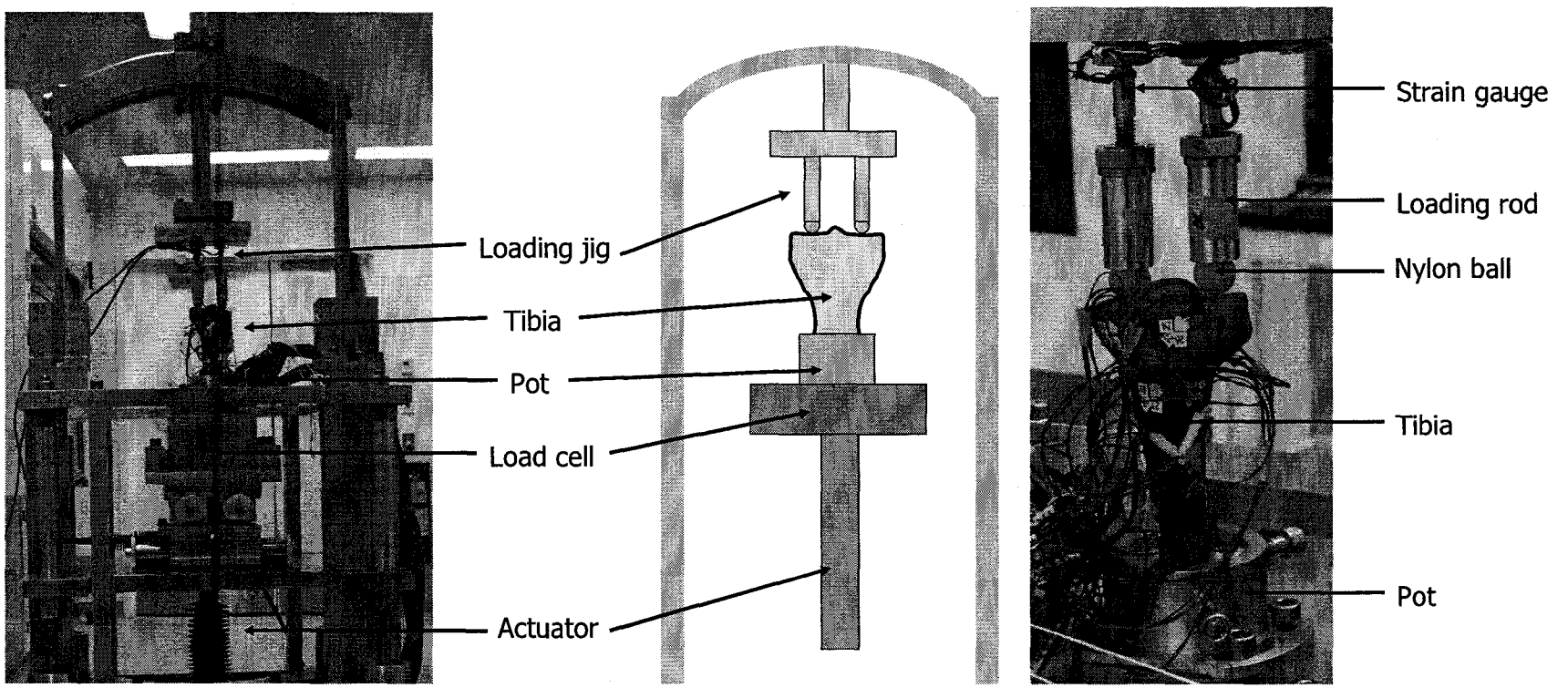

Figure 5.2: (a) The mechanical testing apparatus with strain gauged composite tibia. A schematic of the apparatus is shown in (b). A more detailed view of the loading jig is shown in (c).

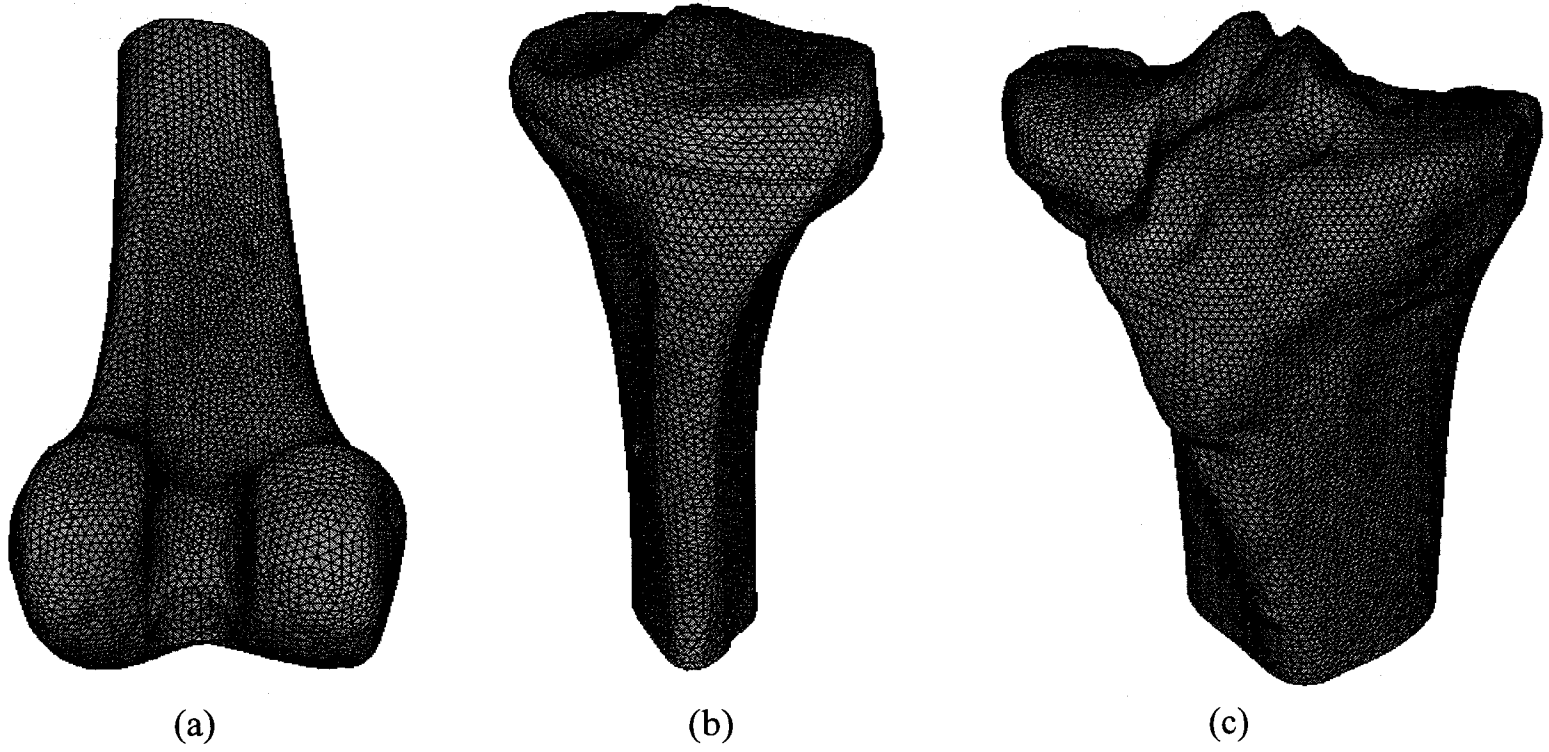

Figure 5.3: FE models of the composite femur (a), composite tibia (b), and bovine tibia (c).

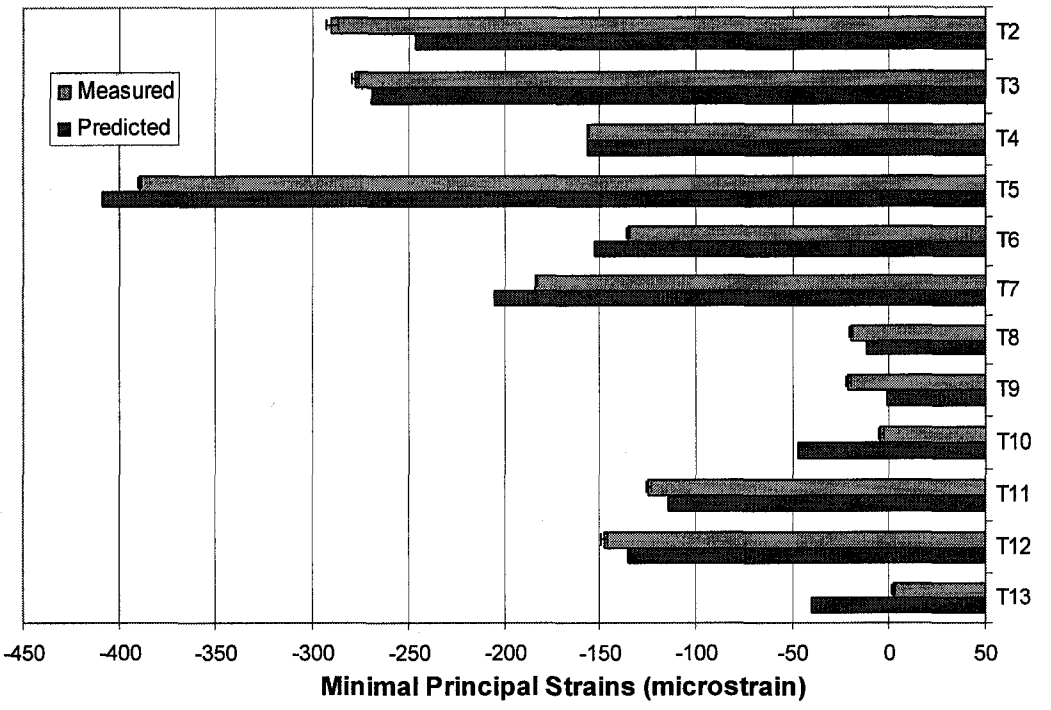
Measured
Predicted
T2
T3
T4
T5
T6
T7
T8
T9
T10
T11
T12
T13
-450
-400
-350
-300
-250
-200
-150
-100
-50
0
50
Minimal Principal Strains (microstrain)

(a)

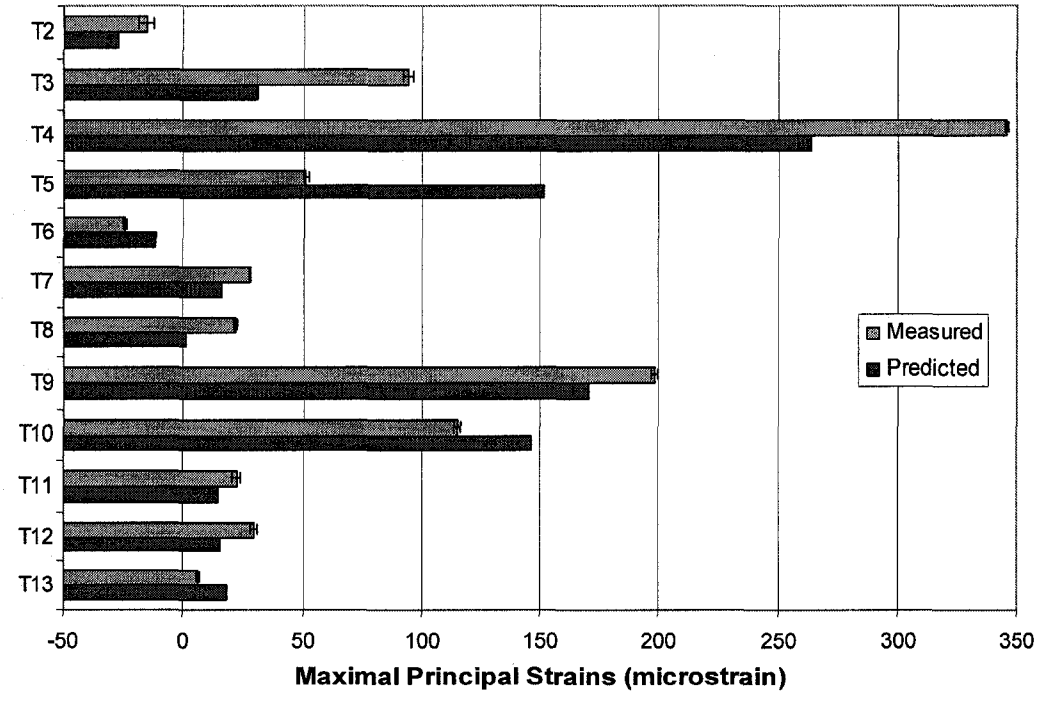
T2
T3
T4
T5
T6
T7
T8
T9
T10
T11
T12
T13
Measured
Predicted
-50
0
50
100
150
200
250
300
350
Maximal Principal Strains (microstrain)

(b)

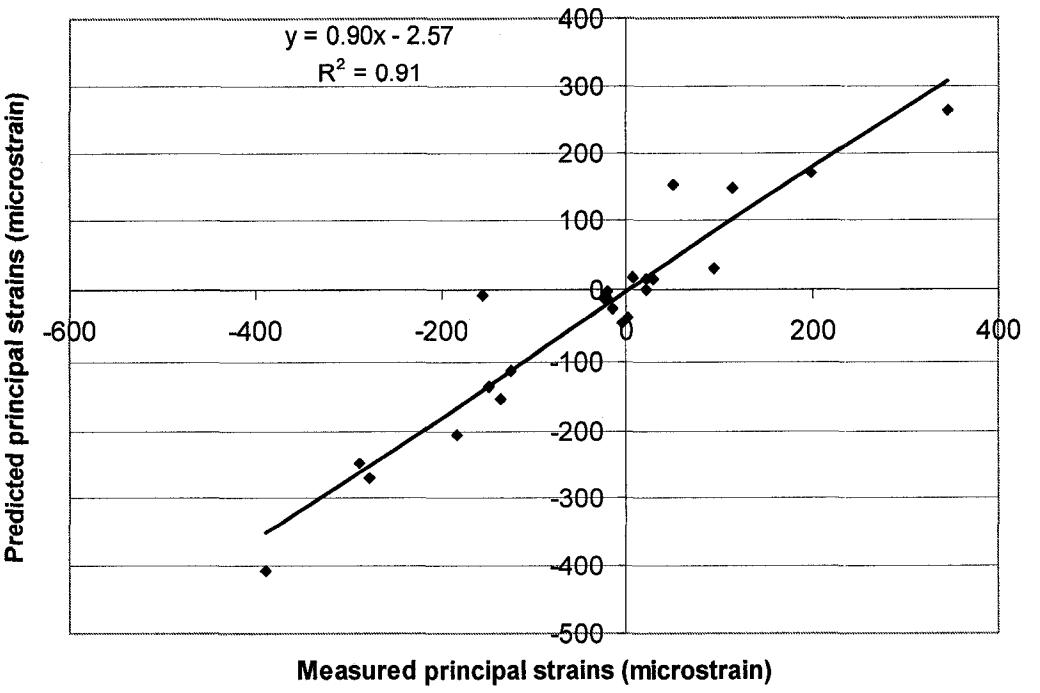
y = 0.90x - 2.57
R^2 = 0.91
Predicted principal strains (microstrain)
Measured principal strains (microstrain)
400
300
200
100
0
-100
-200
-300
-400
-500
-600
-400
-200
0
200
400

(c)

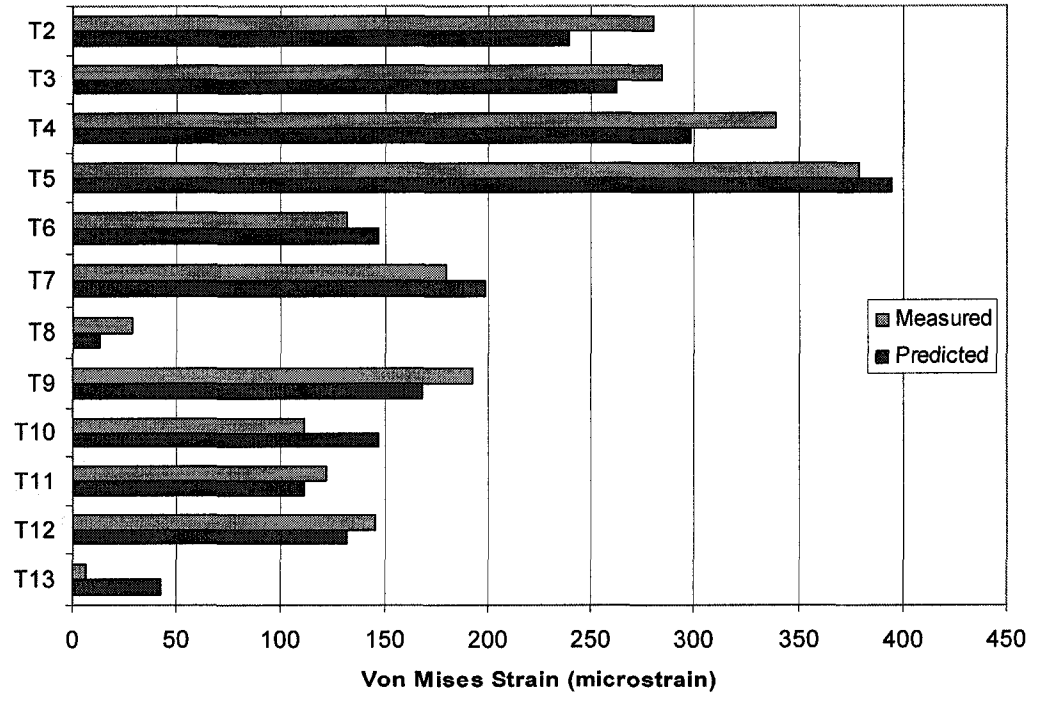
T2
T3
T4
T5
T6
T7
T8
T9
T10
T11
T12
T13
Measured
Predicted
0
50
100
150
200
250
300
350
400
450
Von Mises Strain (microstrain)

(d)

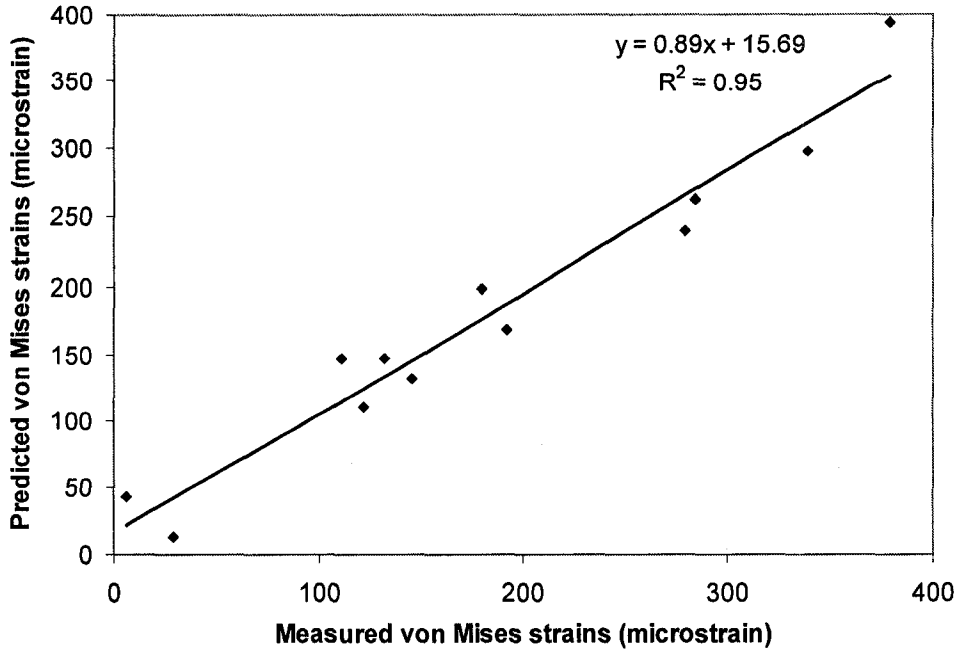

(e)

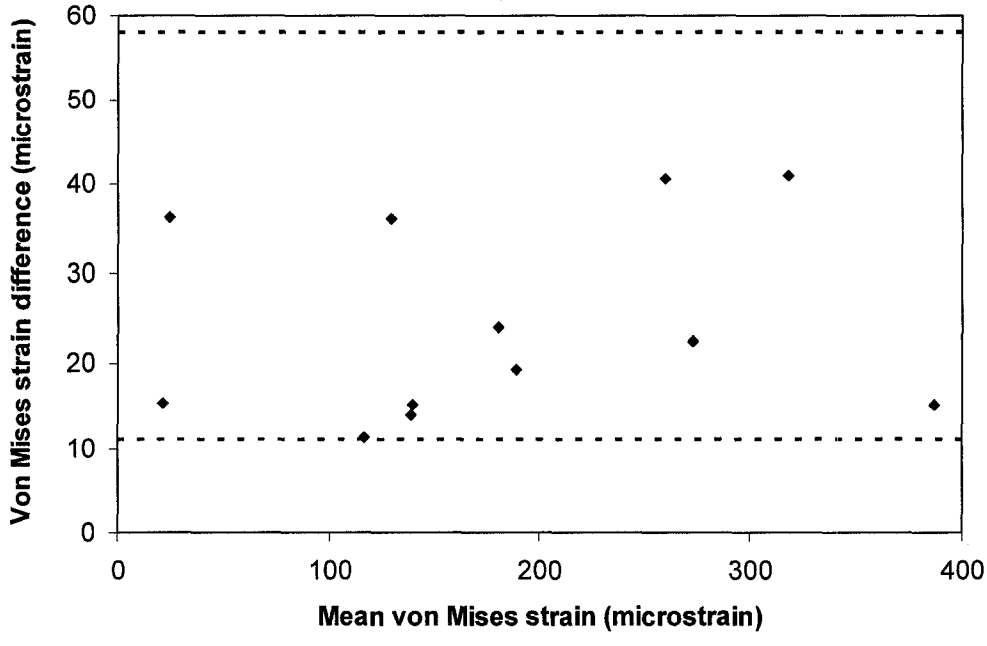

(f)

Figure 5.4: A comparison of measured and predicted (a) minimum and (b) maximum principal strains, with corresponding linear regression results shown in (c) for the composite tibia. A comparison of von Mises strains and the corresponding linear regression results is shown in (d) and (e), respectively. In (f), a Bland-Altman plot of mean versus difference in von Mises strains is shown, with dotted lines showing 95% confidence intervals.

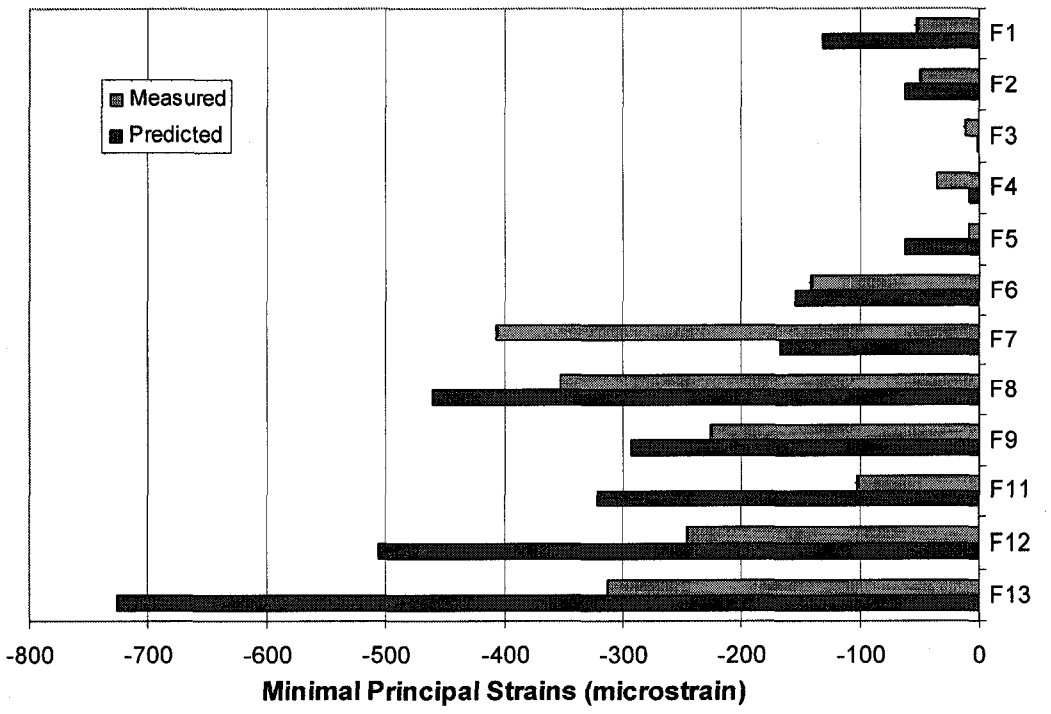
Measured
Predicted
F1
F2
F3
F4
F5
F6
F7
F8
F9
F11
F12
F13
-800
-700
-600
-500
-400
-300
-200
-100
0
Minimal Principal Strains (microstrain)

(a)

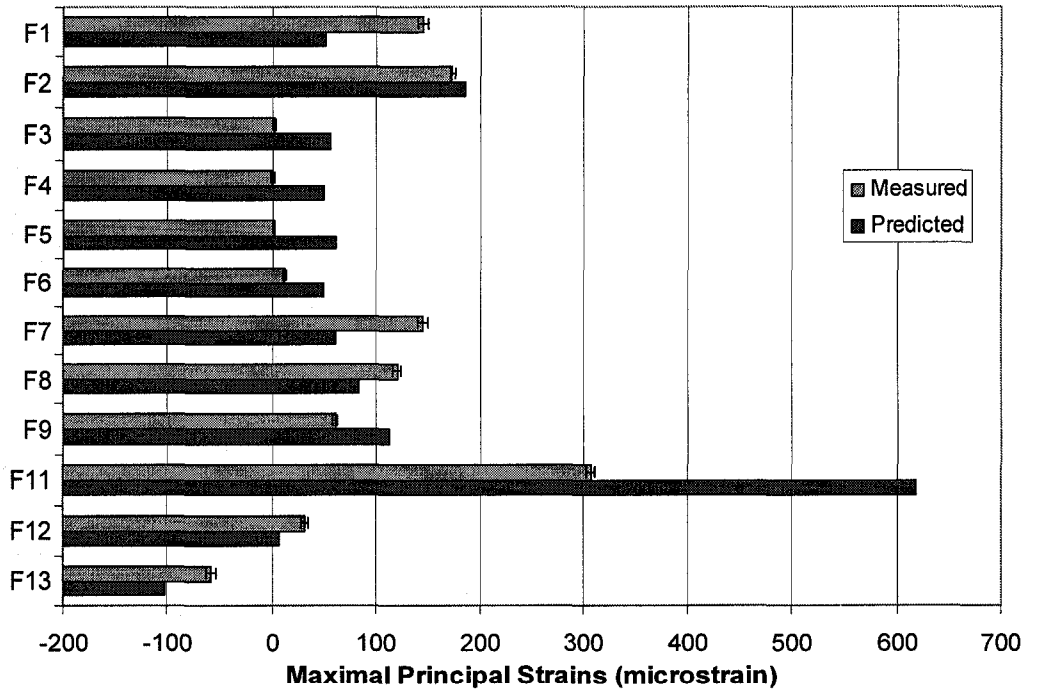
F1
F2
F3
F4
F5
F6
F7
F8
F9
F11
F12
F13
Measured
Predicted
-200
-100
0
100
200
300
400
500
600
700
Maximal Principal Strains (microstrain)

(b)

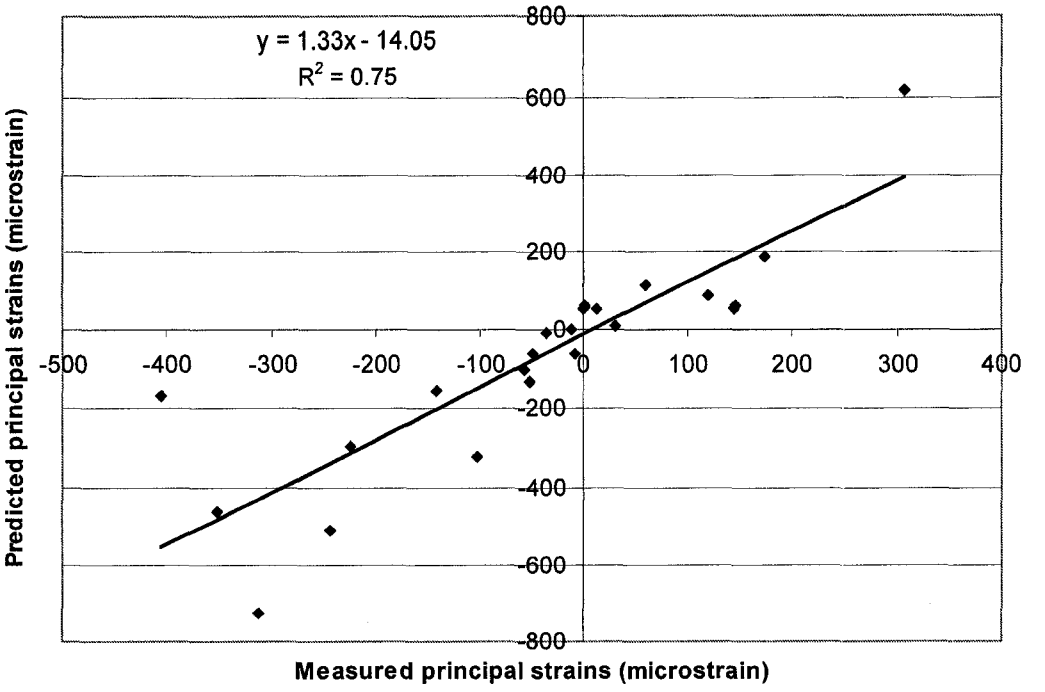
y = 1.33x - 14.05
R^2 = 0.75
Predicted principal strains (microstrain)
Measured principal strains (microstrain)
800
600
400
200
0
-200
-400
-600
-800
-500
-400
-300
-200
-100
0
100
200
300
400

(c)

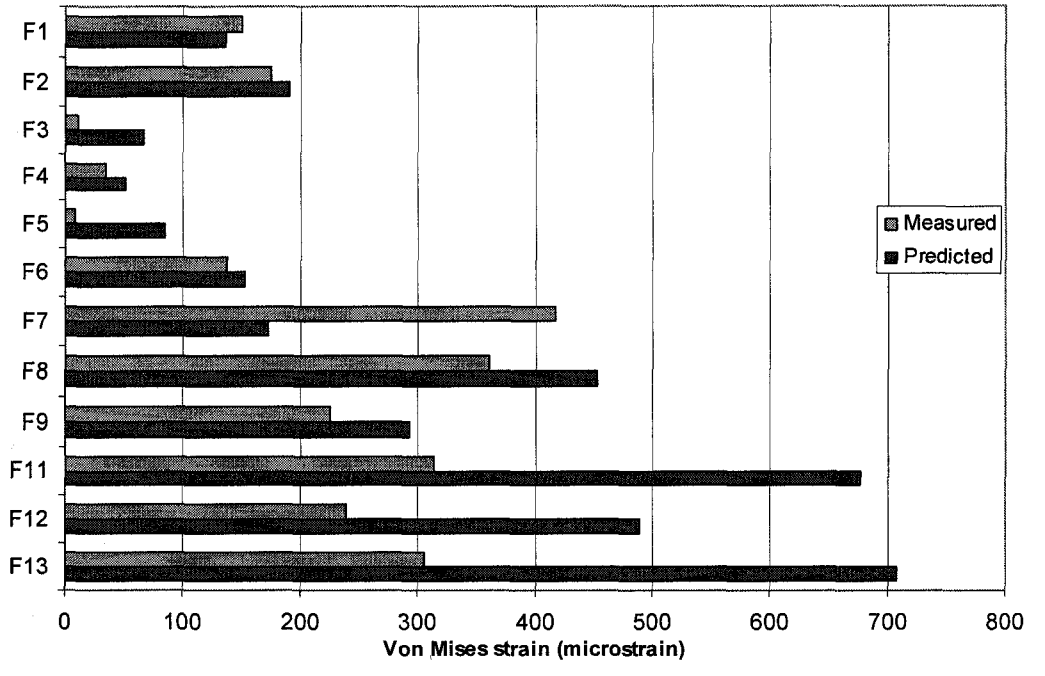
F1
F2
F3
F4
F5
F6
F7
F8
F9
F11
F12
F13
Measured
Predicted
0
100
200
300
400
500
600
700
800
Von Mises strain (microstrain)

(d)

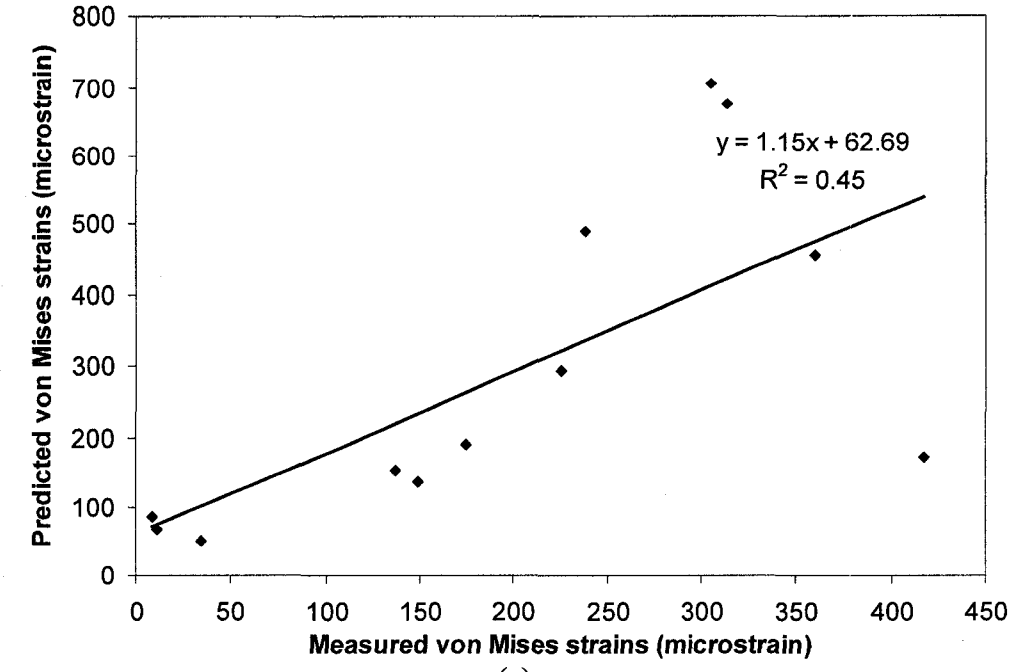

(e)

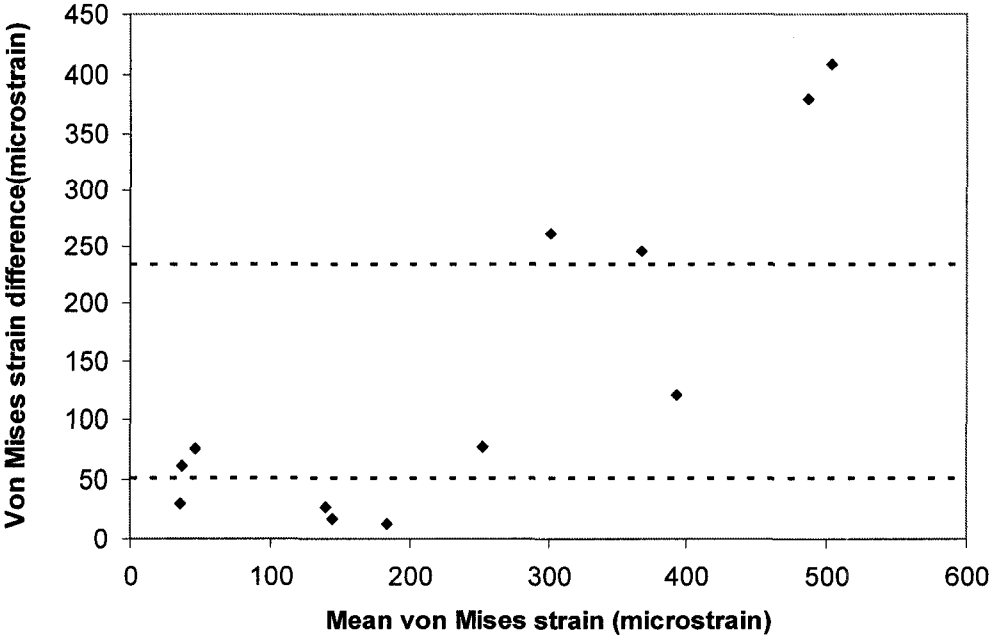

(f)

Figure 5.5: A comparison of measured and predicted (a) minimum and (b) maximum principal strains, with corresponding linear regression results shown in (c) for the composite femur. A comparison of von Mises strains and the corresponding linear regression results is shown in (d) and (e), respectively. In (f), a Bland-Altman plot of mean versus difference in von Mises strains is shown, with dotted lines showing 95% confidence intervals.

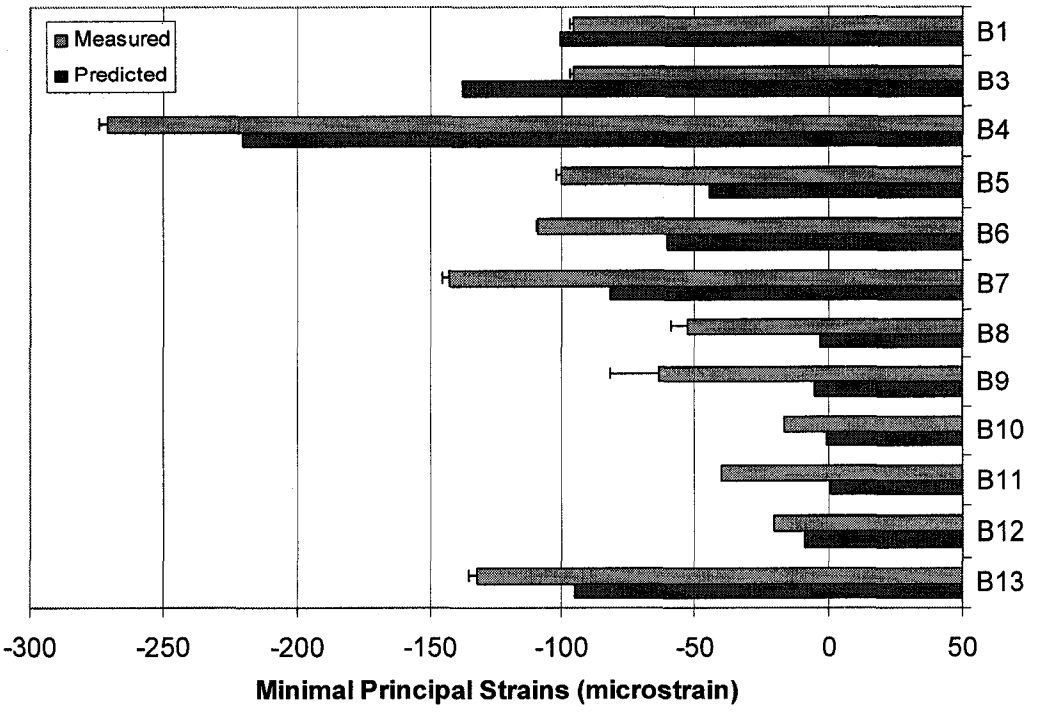
Measured
Predicted
B1
B3
B4
B5
B6
B7
B8
B9
B10
B11
B12
B13
-300
-250
-200
-150
-100
-50
0
50
Minimal Principal Strains (microstrain)

(a)

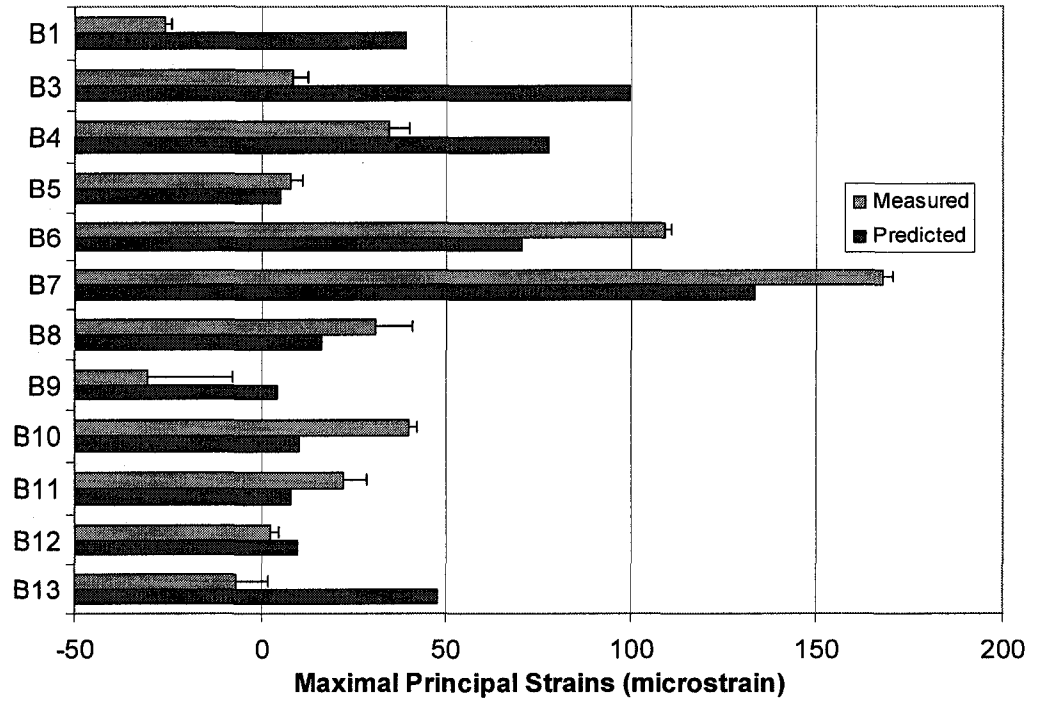
B1
B3
B4
B5
B6
B7
B8
B9
B10
B11
B12
B13
Measured
Predicted
-50
0
50
100
150
200
Maximal Principal Strains (microstrain)

(b)

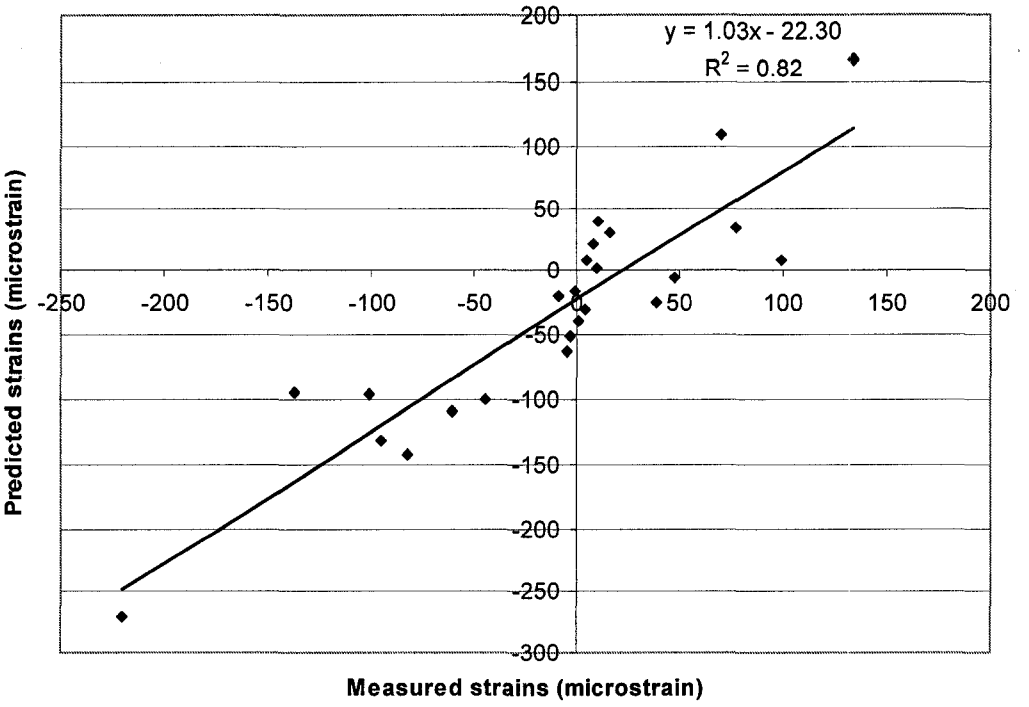
y = 1.03x - 22.30
R^2 = 0.82
Predicted strains (microstrain)
Measured strains (microstrain)
200
150
100
50
0
-50
-100
-150
-200
-250
-300
-250
-200
-150
-100
-50
50
100
150
200

(c)

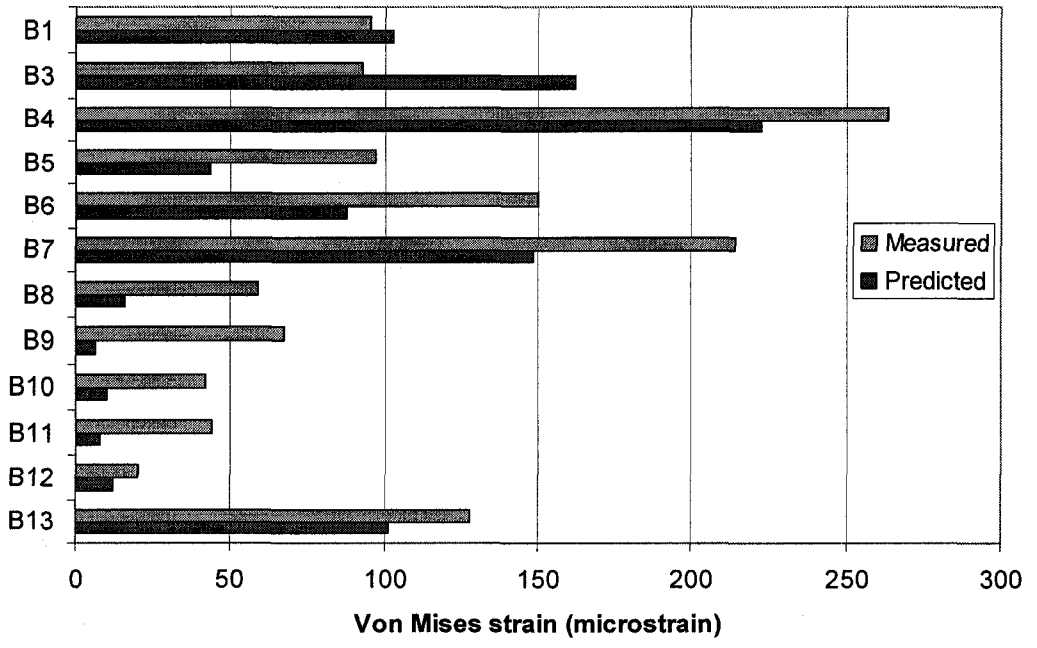
B1
B3
B4
B5
B6
B7
B8
B9
B10
B11
B12
B13
Measured
Predicted
0
50
100
150
200
250
300
Von Mises strain (microstrain)

(d)

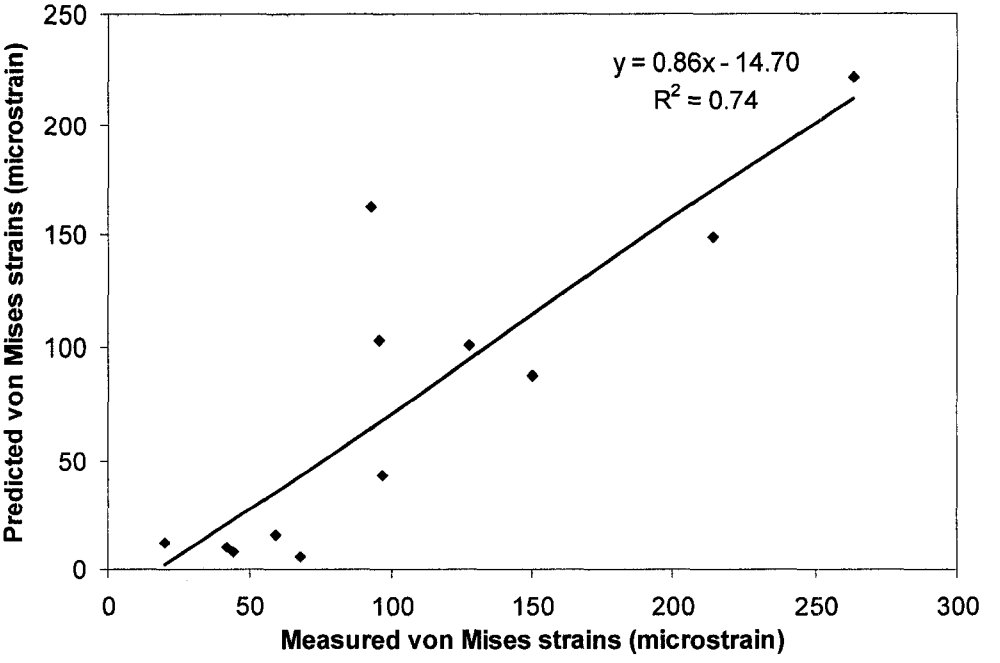

(e)

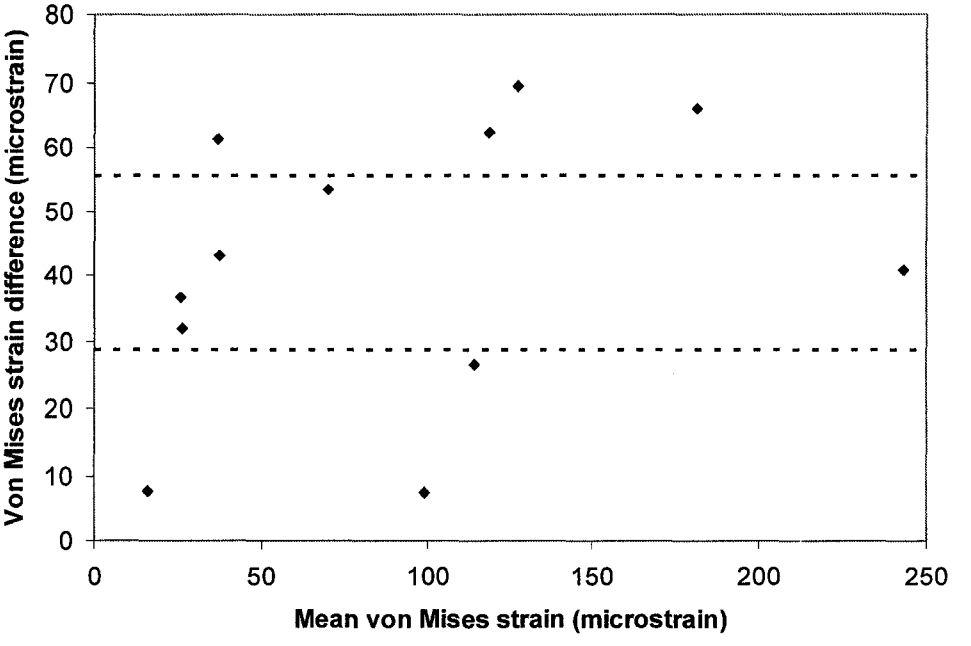

(f)

Figure 5.6: A comparison of measured and predicted (a) minimum and (b) maximum principal strains, with corresponding linear regression results shown in (c) for the bovine tibia. A comparison of von Mises strains and the corresponding linear regression results is shown in (d) and (e), respectively. In (f), a Bland-Altman plot of mean versus difference in von Mises strains is shown, with dotted lines showing 95% confidence intervals.

References

Ashman, R. B., Rho, J. Y., 1988. Elastic modulus of trabecular bone material. Journal of Biomechanics 21, 177-181.

Au, A. G., Liggins, A. B., Raso, V. J., Amirfazli, A., 2005. A parametric analysis of fixation post shape in tibial knee prostheses. Medical Engineering and Physics 27, 123-34.

Bland, J. M, Altman, D. G., 1986. Statistical methods for assessing agreement between two methods of clinical measurement. Lancet i, 307-310

Carter, D. R., Hayes, W. C., 1977. The compressive behavior of bone as a two-phase porous structure. Journal of Bone and Joint Surgery [Am] 59-A, 954-962.

Completo, A., Simoes, J. A., Fonseca, F., 2007a. Experimental evaluation of strain shielding in distal femur in revision TKA. Experimental Mechanics doi 10.1007/s11340-007-9101-5.

Completo, A., Fonseca, F., Simoes, J. A., 2007b. Experimental validation of intact and implanted distal femur finite element models. Journal of Biomechanics 40, 2467-2476.

Completo, A., Fonseca, F., Simoes, J. A., 2007c. Finite element and experimental cortex strains of the intact and implanted tibia, Transactions of the ASME: Journal of Biomechanical Engineering 129, 791-797.

Cristofolini, L., Viceconti, M., Cappello, A., Toni, A., 1996. Mechanical validation of whole bone composite femur models. Journal of Biomechanics 29, 525-535.

Cristofoloni, L., Viceconti, M., 2000. Mechanical validation of whole bone composite tibia models. Journal of Biomechanics 2000, 279-288.

Gray, H. A., Zavatsky, A. B., Taddei, F., Cristofolini, L., Gill, H. S., 2007. Experimental validation of a finite element model of a composite tibia. Proceedings of the Institution of Mechanical Engineers (Part H) 221, 315-324.

Heiner, A. D., Brown, T. D., 2001. Structural properties of new design of composite replicate femurs and tibias. Journal of Biomechanics 34, 773-781.

Hinterhofer, C., Stanek, C., Haider, H., 2000. The effect of flat horseshoes, raised heels and lowered heels on the biomechanics of the equine hoff assessed by finite element analysis (FEA). Journal of veterinary medicine. A, Physiology, pathology, clinical medicine 47, 73-82.

Hodgskinson, R., Currey, J. D., 1992. Young's modulus, density and material properties in cancellous bone over a large density range. Journal of materials science. Materials in medicine 3, 377-381.

Hodgskinson, R., Njeh, C. F., Currey, J. D., Langton, C. M., 1997. The ability of ultrasound velocity to predict the stiffness of cancellous bone in vitro. Bone 21, 183-190.

Hopkins, W. G., 2004. Bias in Bland-Altman but not Regression Validity Analyses. Sportscience 8, 42-46.

Keyak, J.H., Fourkas, M.G., Meagher, J.M., Skinner, H.B., 1993. Validation of an automated method of three-dimensional finite element modelling of bone. Journal of Biomedical Engineering 15, 505-509.

Merritt, J. S., Burvill, C. R., Pandy, M. G., Davies, H. M., 2006. Determination of mechanical loading components of the equine metacarpus from measurements of strain during walking. Equine veterinary journal. Supplement 36, 440-444.

Ruff, C. B., Hayes, W. C., 1983. Cross-sectional geometry of Pecos Pueblo femora and tibiae - a biomechanical investigation: I. Method and general patterns of variation. American Journal of Physical Anthropology 60, 359-381.

Stolk, J., Verdonschot, N., Cristofolini, L., Toni, A., Huiskes, R., 2002. Finite element and experimental models of cemented hip joint reconstructions can produce similar bone and cement strains in pre-clinical tests. Journal of Biomechanics 35, 499-510.

Taddei, F., Viceconti, M., Manfrini, M., Toni, A., 2003. Mechanical strength of paediatric oncology: a finite element study. Proceedings of the Institution of Mechanical Engineers (Part H) 217, 111-119.

Taddei, F., Cristofolini, L., Martelli, S., Gill, H. S., Viceconti, M., 2006. Subject-specific finite element models of long bones: an in vitro evaluation of the overall accuracy. Journal of Biomechanics 39, 2457-2467.

Viceconti, M., Bellingeri, L., Cristofolini, L., Toni, A., 1998. A comparative study on different methods of automatic mesh generation of human femurs. Medical Engineering and Physics 20, 1-10.

Viceconti, M., Davinelli, M., Taddei, F., Cappello, A., 2004. Automatic generation of accurate subject-specific bone finite element models to be used in clinical studies. Journal of Biomechanics 37, 1597-1605.

Waide, V., Cristofolini, L., Stolk, J., Verdonschot, N., Boogaard, G. J., Toni, A., 2004. Modelling the fibrous tissue layer in cemented hip replacements: experimental and finite element methods. Journal of Biomechanics 37, 13-26.

Williams, J. J., 1999. Disorders of the lower extremity in children. In: Baratz, M., Watson, A. D., Imbriglia, J. E. (Eds), Orthopaedic Surgery: The Essentials, 1st ed. Thieme, New York, NY, pp. 675-692.

Chapter 6: Contribution of loading conditions and material properties to stress shielding near the tibial component of total knee replacements*

6.1 Introduction

Aseptic loosening is a major failure mechanism of total knee replacement (TKR) and is partly attributed to stress shielding of the bone by the prosthesis (Van Loon et al., 1999). To date, the large difference in the Young's modulus between implant material and the surrounding bone has been considered the main contributing factor to stress shielding (Bureau, 2005). Current methods to improve TKR design include better tibiofemoral articulation (McEwen et al., 2005; Greenwald and Heim, 2005) as well as improving the bone-implant interface via novel materials (Bureau, 2005). Stress shielding in the bone for select TKR implant materials and post geometries have been examined via finite element (FE) studies (Au et al., 2005; Askew and Lewis, 1981). Implant wear studies have shown that prosthetic joint surface congruency, and therefore the loading condition, is crucial in reducing implant wear (McEwen et al., 2005; Currier et al., 2005). The loading conditions at the tibiofemoral joint interface may also affect stress shielding but this relationship has not been well examined.

Loading conditions can be characterized by a combination of load pattern, load placement on the condylar surface, and bone or implant condylar surface geometry. This investigation examines the effects of material properties and the above three characteristics of loading conditions on the bone stress state for a prosthesis similar to a commercially available model. Models of a surgically altered tibia with various implant materials, load patterns, and load placements were compared to a model of the natural pre-TKR tibia.

---

* A version of this chapter has been published in Au et al., 2007. Journal of Biomechanics 40: 1410-1416.

6.2 Materials and Methods

A three dimensional finite element model of the proximal tibia was used to predict the stress state. Details of the basic model are given in Au et al. (2005), so only a brief description is provided here. Geometrical reconstruction of a composite tibia was used to model the anatomy. Cortical and cancellous bone were assigned orthotropic and heterogeneous material properties mapped from experimental data (Rho, 1992). The model was meshed with 2 mm 10-node tetrahedral elements, resulting in 212,694 elements and 300,277 nodes. A convergence analysis was used to validate mesh adequacy. For computational efficiency, the tibia was sectioned 90 mm distal to the most proximal location; a sensitivity analysis showed that a longer bone length has a negligible effect on stress distribution. The distal end of the tibia was fixed in all directions.

6.2.1 Loading Conditions

Stress distributions were analyzed at the 15% interval of the gait cycle. This position presented a combination of high soft tissue forces and tibiofemoral compression, both of which were incorporated into the model (Table 6.1). Experimentally determined contact pressure distribution schematics (Fukubayashi and Kurosawa, 1980) for the tibia were digitized and the pressure contours mapped onto the tibia FE model (Au et al., 2005). The pressure contours were placed on the tibial condyles corresponding to experimentally determined data for the flexion angle at the 15% interval of the gait cycle (Scarvell et al., 2004; Wretenberg et al., 2002). An identical loading pattern was used when the implant was present to allow for comparative study. Two load patterns representative of two different implants were also applied to examine the load pattern characteristic of loading condition (Morra and Greenwald, 2004). The selected implant contour patterns represent the pressures observed at approximately the 15% interval of the gait cycle.

Soft tissue loading in the model incorporated both muscle and ligament forces (Table 6.1). The ACL and PCL were assumed to have anterior and posterior

bands, the MCL was assumed to have deep and superficial bands; loading was distributed proportionally to the relative cross-sectional area of the bands (Crowninshield et al., 1976). The lines of action of the soft tissues were determined using an assembled CAD femur and tibia containing pre-defined soft tissue attachment locations. The knee was flexed according to physiological conditions and the lines of actions were assumed to be straight lines connecting corresponding attachment sites. A comparison with experimentally determined data (Herzog and Read, 1993) showed the lines of action calculated from the CAD model for the knee at full extension were well within physiological limits (Table 6.2).

In this model, ligament and muscle attachments were considered to be enclosed areas, rather than the usual single points, for better physiological representation and to avoid stress concentration artifacts. The insertion shapes reflected those illustrated in the literature (Harner et al., 1999; Mains et al., 1977; Netter, 2002; Gray's Anatomy, 1973). To compare the accuracy of our soft tissue attachments, the centroids of each attachment area were compared with the National Institutes of Health's Terry dataset (Kepple et al., 1998) and the musculoskeletal model of Delp (1990) using the CAD knee assembly. Coordinates from the Terry and Delp datasets were translated to the most representative locations on the CAD model and compared with the attachment centroids of the FE model. All attachments were located reasonably close considering the natural physiological variation of the bones.

6.2.2 Tibial Knee Prosthesis Model

The tibial component of the knee prosthesis was created and assembled to the tibia in Pro/Engineer® (PTC, Needham, MA) and the entire assembly was exported to ANSYS® (Swanson Inc., Houston, PA) for analysis. The prosthesis was a representation of the Osteonics Scorpio™ model (Stryker Howmedica Osteonics, Kalamazoo, MI); however, its use is for illustrative purposes only and this study is not meant to examine its performance in any manner. A 2 mm layer

of polymethylmethacrylate (PMMA) was modeled beneath the tray and a 1 mm layer of PMMA around the post and flanges (Fig 6.1b). All interfaces in the models were assumed to be perfectly bonded.

Four FE models were created, varying the presence and material properties of the prosthesis (Fig 6.1). Ti6Al4V was assigned a Young's modulus (E) of 117 GPa and a Poisson's ratio (ν) of 0.3 (Senepati and Pal, 2002). A hypothesized low modulus material (E = 837 MPa; ν = 0.3) was used to investigate the influence of implant modulus on stress shielding; the modulus value was determined from a volume-weighted average of the cancellous bone sections in the model. It should be noted that stiffness is a function of material and geometry. However, as the geometries of the models are identical, stiffness in this case only varies with material property and thus the term is used interchangeably with Young's modulus as is commonly done.

To study the effects of loading condition, a model (called "Second Control") was created where the tray, post and flanges were removed and the shape of the superior bone replicated the implant geometry and was assigned bone properties comparable to the natural tibia location (i.e. the mechanical properties of subchondral bone) (Fig 6.1c). The Second Control retained an identical load pattern and load placement to the natural tibia while varying the articulating geometry, thereby isolating the stress shielding effect of the implant geometry. In addition, it controlled for the influence of the implant post and flanges and the bone-implant interface.

Two additional FE models containing prostheses were created; each was loaded with a different implant load pattern (see Section 6.2.1).

6.3 Results and Discussion

All stresses were normalized to those determined from a model of an intact tibia, Fig 6.1a (a pre-operative stress state which should be obtained by an ideal TKR

prosthesis). Stresses were observed along 12 paths placed parallel to the long axis of the bone (Fig 6.2). The paths were 1 or 6 mm from the cement-bone interface, where stress shielding is generally observed.

6.3.1 Material property influence on stress distribution

The introduction of the prosthesis reduced stress in nearly all regions of tibial bone. The Ti6Al4V implant greatly reduced stress levels in the bone up to approximately 25 mm beneath the tray and then generally increased stresses until the bottom of the implant (37 mm) (Fig 6.3). This post-operative stress shielding effect has previously been attributed to the difference in Young's modulus between implant material and bone. It is argued that high modulus metals currently used (e.g. Ti6Al4V) take over much of the mechanical bone stresses thereby underloading the bone compared to its natural non-implant state. To reduce stress shielding, it has been suggested that orthopaedic fixations should be manufactured with elastic properties identical to those of natural bone (Gefen, 2002). To this end, the stress effect of implant modulus was examined by comparing Ti6Al4V with one whose modulus is in the order of cancellous bone (Fig 6.3). The Low Modulus material increased stress levels 25 mm beneath the tray but reduced stresses in the distal regions compared to Ti6Al4V (Figs 6.3a and b). Thus, an implant with modulus in the order of magnitude of the surrounding cancellous bone can be potentially beneficial in the region directly beneath the tray. However, it is quite evident that stress shielding still remains, so other causes should be investigated.

6.3.2 Loading condition influence on stress distribution

A particularly important finding from this investigation is that the tibiofemoral loading condition (i.e. loading pattern, load placement on the condylar surface, and bone or implant condylar surface geometry) greatly contributes to stress shielding. The alteration of joint articulation geometry due to TKR surgery is at least as important as material property in observed stress shielding immediately post-operation. For example, in the anterior bone 15 mm distal to the tray, the

altered geometry caused 50% of the stress shielding whereas the Ti6Al4V contributed the other 30% (Fig 6.3a). This stress shielding effect from the altered condylar surface geometry is seen throughout the proximal tibia (Figs 6.3b and c). In general, the altered condylar surface geometry aspect of the tibiofemoral loading condition from the TKR implant can itself cause stress shielding (cf. Second Control vs. Natural Tibia, Fig 6.3) by changing the bending moments exerted at the articulating surface and thereby altering the stress distribution within the bone. The use of a high modulus implant material such as Ti6Al4V further accentuates this stress shielding in bone directly beneath the tray (Fig 6.3).

The load placement on the condylar surface aspect of the tibiofemoral loading condition, examined by shifting a single load pattern around the condyles, is also an important contributor to stress shielding. Shifting the tibiofemoral loading 5 mm towards the midline notably reduces the stress shielding (Fig 6.4). So examining Figs 6.3 and 6.4 shows that careful load placement on the condylar surface and material selection can achieve a better stress shielding performance.

This study assumed identical loading conditions for the natural tibia and implant to more clearly identify differences in stress levels caused by the load placement on the condylar surface and bone or implant condylar surface geometry aspects of the loading condition. However, pressure contours for the natural tibia and the implant are physiologically different (cf. Fukubayashi and Kurosawa (1980) and Morra and Greenwald (2004)). A deeper investigation into this aspect has shown that, even with the adoption of two different representative implant pressure contours (Morra and Greenwald, 2004), the stress trends observed in each of the 12 paths of the implant model are very similar to those seen when using a less representative contour. The stress magnitudes, however, differed depending on the pressure contour used (Fig 6.5). Thus, adopting a more representative implant pressure contour would change the relative stress levels between implant and natural tibia but not the characteristic stress trends caused by the introduction of the implant as described above. It therefore remains that loading conditions (an

aspect of which is the load pattern) are an important factor in stress shielding of the tibial bone, particularly in the region 25 mm beneath the subchondral bone.

Distinctly different patterns can be seen in the bone 25 mm beneath the subchondral bone from those which appear more distally. The 25 mm region corresponds to a region of bone directly beneath the implant which has been clinically observed to undergo significant bone loss regardless of the type of prosthesis (Petersen et al., 1995; Levitz et al., 1995), with loss occurring in both the short term (3 months: Li and Nilsson, 2000) and long term (7 years: Lonner et al., 2001). Thus, to restore pre-operative stress levels in the tibia and minimize bone resorption requires careful consideration of the effects of both loading conditions (i.e. load placement on the condylar surface, contact patterns, bone or implant condylar surface geometry) and material properties (e.g. a stiff implant can be beneficial in more distal regions of bone) in the design of TKR prostheses.

Table 6.1: Summary of loads placed on the tibia. Loads were obtained from Anderson and Pandy (2001) and Shelburne et al. (2004). ACL, PCL, deep MCL and oblique MCL loads were removed in all models where a prosthesis was present.

Tibiofemoral compression	1030 N
Anterior ACL	106 N
Posterior ACL	119 N
Anterior PCL	2 N
Posterior PCL	3 N
Anterior MCL	2 N
Posterior MCL	1 N
Deep MCL	1 N
Oblique MCL	1 N
Gracilis	5 N
Iliotibial tract	44 N
Sartorius	5 N
Semimembranosus	90 N
Semitendinosus	28 N
Popliteus	5 N
Patellar tendon	254 N

Table 6.2: A comparison of line of action angles in the vertical plane with experimental values of Herzog and Read (1993). Angles are clockwise positive with 0 degrees pointing anteriorly.

Structure	This study	Herzog and Read
Semitendinosus	259°	255°-270°
Semimembranosus	262°	255°-265°
ACL	aACL: 223°	215°-223°
	pACL: 215°	
PCL	aPCL: -47°	-40° – -70°
	pPCL: -60°	
LCL	-87°	-70° – -80°
MCL	aMCL: 249°	257° – 262°
	pMCL: 250°	
	oMCL: 249°	
	dMCL: 258°	

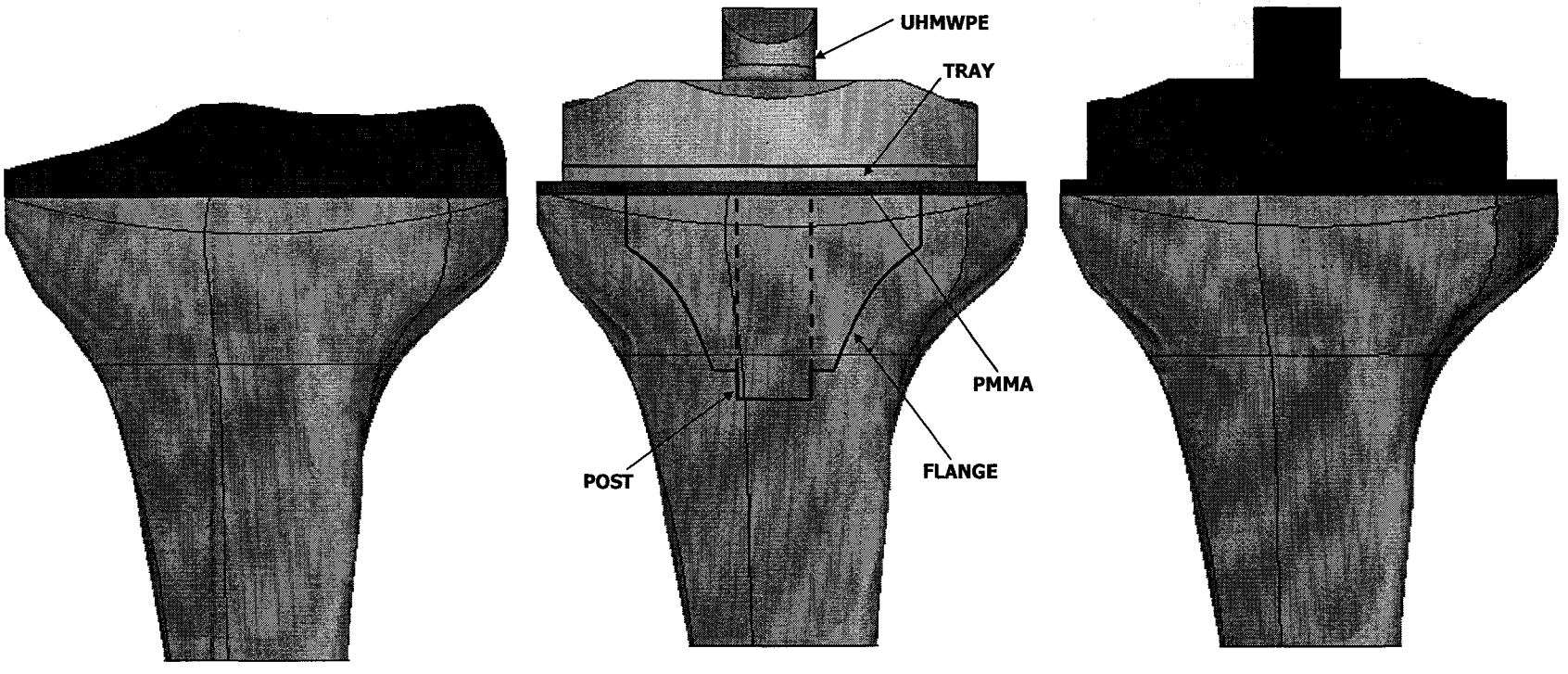

Figure 6.1: A schematic of the FE models used in this investigation. (a) A model of the natural pre-TKR tibia was used as the baseline of comparison (First Control) for (b) models with a Ti6Al4V and a Low Modulus prosthesis and (c) a model with the shape of the superior bone replicating the implant geometry (Second Control); the material property is that of bone similarly colour coded in (a).

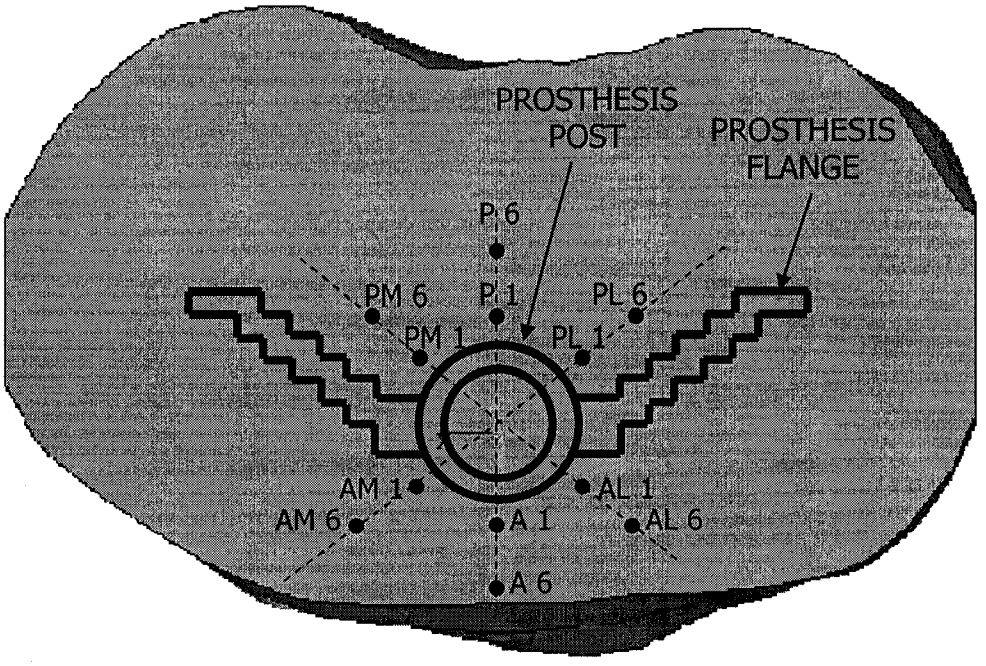

Figure 6.2: A schematic of the 12 stress path locations as viewed from a transverse section of the tibia. The paths extended from the bottom of the PMMA layer beneath the implant tray to the distal end of the tibia. A: anterior, P: posterior, M: medial, L: lateral, 1: one mm radially from cement-bone interface, 6: six mm radially from cement-bone interface. The outline in black is a superior view of the implant cross-section.

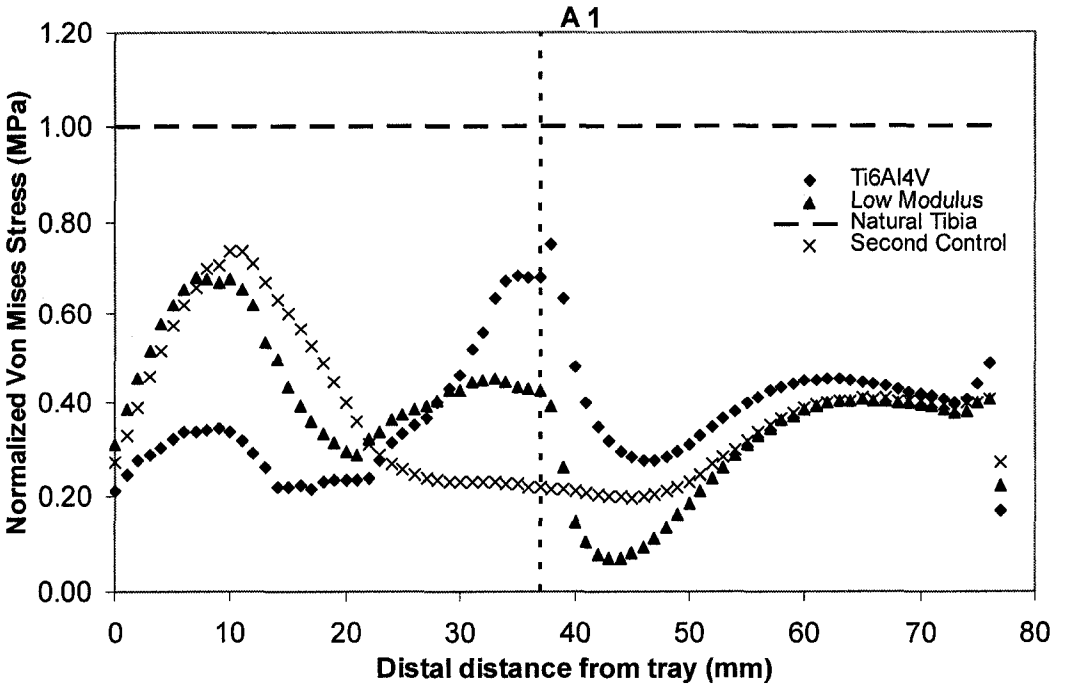
A 1
Normalized Von Mises Stress (MPa)
1.20
1.00
0.80
0.60
0.40
0.20
0.00
0
10
20
30
40
50
60
70
80
Distal distance from tray (mm)
Ti6Al4V
Low Modulus
Natural Tibia
Second Control

(a)

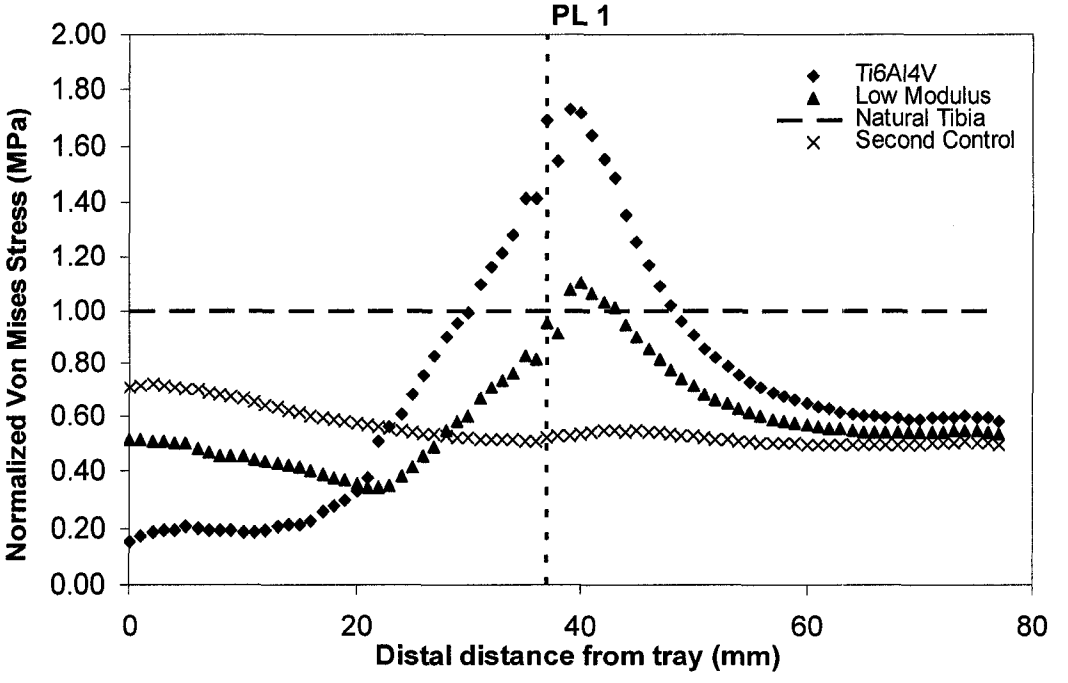
PL 1
Normalized Von Mises Stress (MPa)
2.00
1.80
1.60
1.40
1.20
1.00
0.80
0.60
0.40
0.20
0.00
0
20
40
60
80
Distal distance from tray (mm)
Ti6Al4V
Low Modulus
Natural Tibia
Second Control

(b)

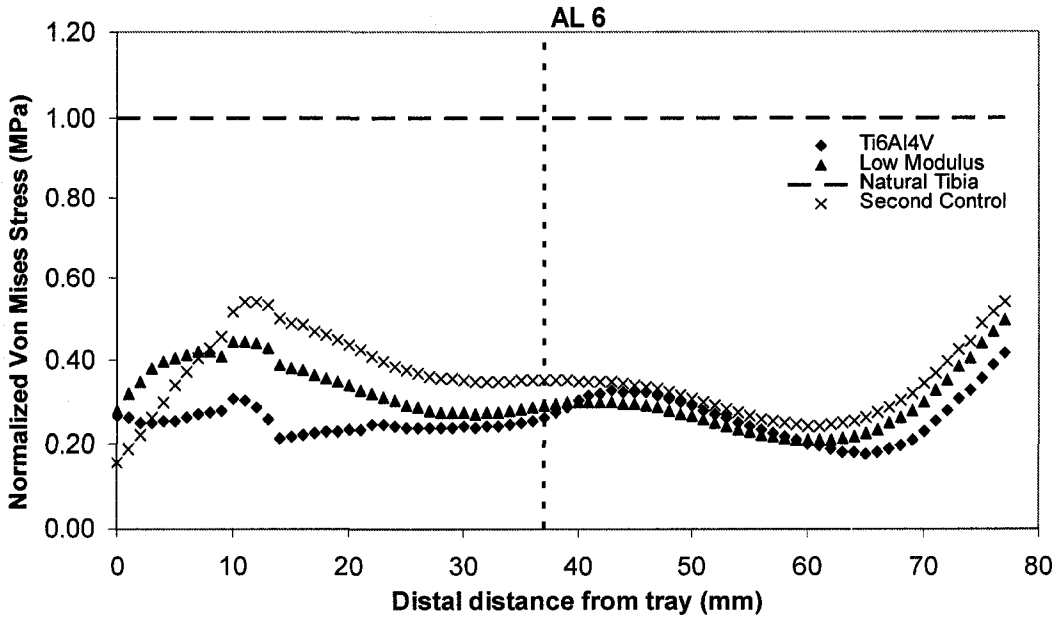

(c)

Figure 6.3: A comparison of the normalized von Mises bone stresses resulting from changes in the material properties and loading conditions of the implant. Stresses are shown for a high modulus implant (Ti6Al4V) as compared with a much lower modulus implant (Low Modulus) in cancellous bone (a) 1 mm anterior to the post, (b) 1 mm postero-lateral to the post and (c) 6 mm antero-lateral to the post. Stresses are also shown for the FE model with altered loading conditions (Second Control). All stresses are normalized to those observed in the natural tibia (- symbol). The vertical dotted line demarcates the bottom edge of the post.

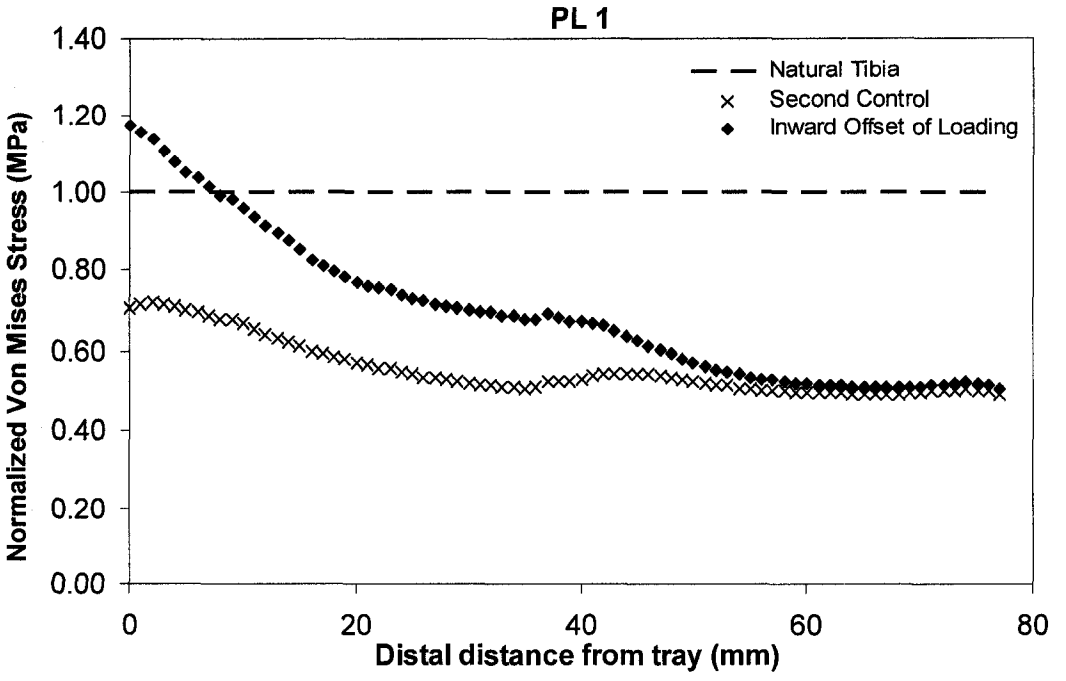

Figure 6.4: A comparison of the normalized von Mises bone stresses resulting from changes in the loading conditions of the implant. Stresses are shown for the FE model with the shape of the superior bone replicating the implant geometry under normal physiological loading (Second Control) and with the medial and lateral tibial condylar loads offset 5 mm toward the midsagittal plane (Inward Offset of Loading). All stresses are normalized to those observed in the natural tibia (- symbol).

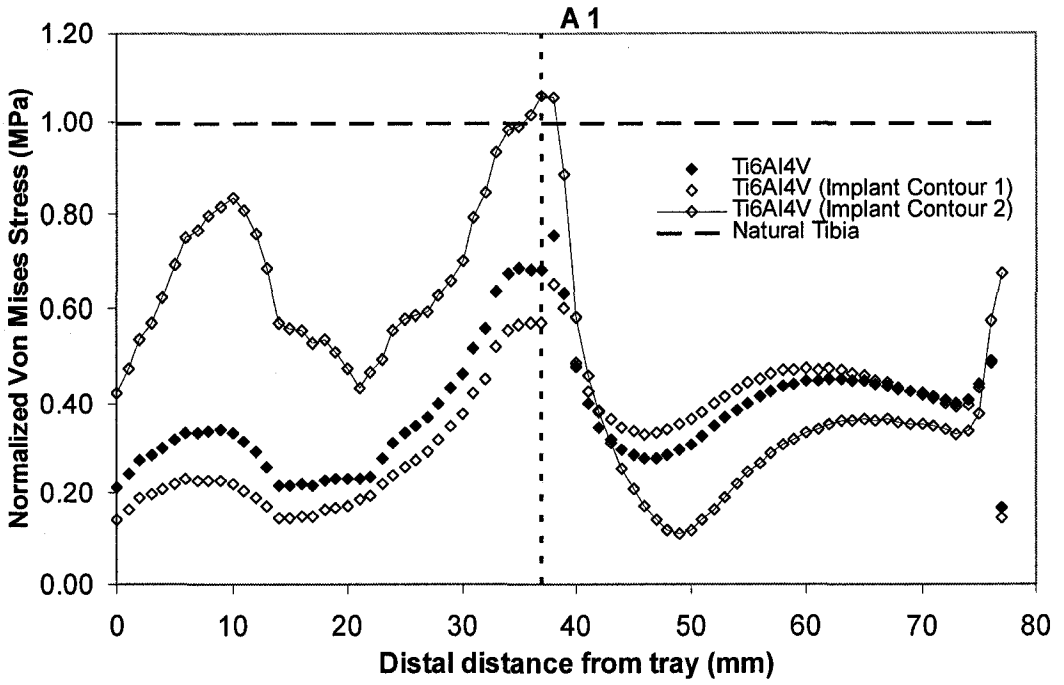

Figure 6.5: A comparison of the normalized von Mises bone stresses resulting from changes in the load patterns of the implant. Stresses are shown for the FE model containing a Ti6Al4V implant loaded with a pattern identical to the natural tibia (Ti6Al4V). Stresses are also shown for the same FE model loaded with two separate patterns similar to those observed in two different commercially available implants (Ti6Al4V Implant Contour 1 and Ti6Al4V Implant Contour 2). All stresses are normalized to those observed in the natural tibia (- symbol).

References

Anderson, F. C., Pandy, M. G., 2001. Static and dynamic optimization solutions for gait are practically equivalent. Journal of Biomechanics 34, 153-161.

Au, A. G., Liggins, A. B., Raso, V. J., Amirfazli, A., 2005. A parametric analysis of fixation post shape in tibial knee prostheses. Medical Engineering and Physics 27, 123-134.

Au, A. G,, Liggins, A. B,, Raso, V. J., Amirfazli, A,, 2007. Contribution of loading conditions and material properties to stress shielding near the tibial component of total knee replacements. Journal of Biomechanics 40, 1410-1416.

Bureau, M. N., 2005. Biomimetic polymer composites for orthopedic implants. Proceedings of the 3rd International Symposium on Advanced Biomaterials/Biomechanics, 142.

Choi, K., Kuhn, J. L., Ciarelli, M. J., Goldstein, S. A., 1990. The elastic moduli of human subchondral, trabecular, and cortical bone tissue and the size-dependency of cortical bone modulus. Journal of Biomechanics 23, 1103-1113.

Crowninshield, R., Pope, M. H., Johnson, R. J., 1976. An analytical model of the knee. Journal of Biomechanics 9, 397-405.

Currier, J. H., Bill, M. A., Mayor, M. B., 2005. Analysis of wear symmetry in a series of 94 retrieved polyethylene tibial bearings. Journal of Biomechanics 38, 367-375.

Delp, S. L., 1990. A computer-graphics system to analyze and design musculoskeletal reconstructions of the lower limb. Ph.D. thesis, Stanford University, Stanford, CA, USA.

Fukubayashi, T., Kurosawa, H., 1980. The contact area and pressure distribution pattern of the knee. Acta Orthopaedica Scandinavica 51, 871-879.

Gefen, A., 2002. Computational simulations of stress shielding and bone resorption around existing and computer-designed orthopaedic screws. Medical and Biological Engineering and Computing 40, 311-322.

Gray's Anatomy, 1973, 29th American ed., edited by Goss, C.M. Lea and Febiger, Philadelphia, PA.

Greenwald, A. S., Heim, C. S., 2005. Mobile-bearing knee systems: ultra-high molecular weight polyethylene wear and design issues. AAOS Instructional Course Lectures 54, 195-205.

Harner, C. D., Baek, G. H., Vogrin, T. M., Carlin, G. J., Kashiwaguchi, S., Woo, S. L.-Y., 1999. Quantitative analysis of human cruciate ligament insertions. Arthroscopy 15, 741-749.

Herzog, W., Read, L. J., 1993. Lines of action and moment arms of the major force-carrying structures crossing the human knee joint. Journal of Anatomy 182, 213-230.

Kepple, T. M., Sommer, H. J., Lohmann Siegel, K., Stanhope, S. J., 1998. A three-dimensional musculoskeletal database for the lower extremities. Journal of Biomechanics 31, 77-80.

Levitz, C. L., Lotke, P. A., Karp, J. S., 1995. Long-term changes in bone mineral density following total knee replacement. Clinical Orthopaedics and Related Research 321, 68-72.

Li, M. G., Nilsson, K. G., 2000. Changes in bone mineral density at the proximal tibia after total knee arthroplasty: a 2-year follow-up of 28 knees using dual energy x-ray absorptiometry. Journal of Orthopaedic Research 18, 40-47.

Lonner, J. H., Klotz, M., Levitz, C. Lotke, P. A., 2001. Changes in bone density after cemented total knee arthroplasty. Journal of Arthroplasty 16, 107-111.

Mains, D. B., Andrews, J. G., Stonecipher, T., 1977. Medial and anterior-posterior ligament stability of the human knee, measured with a stress apparatus. American Journal of Sports Medicine 5, 144-153.

McEwen, H. M. J., Barnett, P. I., Bell, C. J., Farrar, R., Auger, D. D., Stone, M. H., Fisher, J., 2005. The influence of design, materials and kinematics on the in vitro wear of total knee replacements. Journal of Biomechanics 38, 357-365.

Morra, E. A., Greenwald, A. S., 2004. Tibial plateau abrasion in mobile bearing knee systems during walking gait III: a finite element study [cited 2005 February 24]. Available from: http://www.orl-inc.com/knee_publications/2004/FEA%20MBK%20Walking%202004.pdf.

Netter, F. H., 2002. Atlas of Human Anatomy, 3rd ed., ICON Learning Systems, Teterboro, NJ.

Petersen, M. M., Nielsen P. T., Lauritzen J. B., Lund, B., 1995. Changes in bone mineral density of the proximal tibia after uncemented total knee arthroplasty. Acta Orthopaedica Scandinavica 66, 513-516.

Rho, J. Y., 1992. Mechanical properties of cortical and cancellous bone. Ph.D. Dissertation, University of Texas Southwestern Medical Center, Dallas, TX, USA.

Scarvell, J. M., Smith, P. N., Refshauge, K. M., Galloway, H. R., Woods, K. R., 2004. Evaluation of a method to map tibiofemoral contact points in the normal knee using MRI. Journal of Orthopaedic Research 22: 788-793.

Senepati, S. K., Pal, S., 2002. UHMWPE-Alumina ceramic composite, an improved prosthesis materials for an artificial cemented hip joint. Trends in Biomaterials and Artificial Organs 16, 5-7.

Shelburne, K. B., Pandy, M. G., Anderson, F. C., Torry, M. R., 2004. Pattern of anterior cruciate ligament force in normal walking. Journal of Biomechanics 37, 797-805.

Staubli, H.-U., Rauschning, W. (1994) Tibial attachment area of the anterior cruciate ligament in the extended knee position. Knee Surgery, Sports Traumatology, Arthoscopy 2: 138-146.

Van Loon, C. J. M., De Waal Malefijt, M. C., Buma, P., Verdonschot, N., Veth, R. P. H., 1999. Femoral bone loss in total knee arthroplasty: a review. Acta Orthopaedica Belgica 65, 154-163.

Wrentenberg, P., Ramsey, D. K., Nemeth, G., 2002. Tibiofemoral contact points relative to flexion angle measured with MRI. Clinical Biomechanics 17, 477-485.

Chapter 7: Summary, Conclusions, and Future Directions

This thesis introduced, for the first time, a single comprehensive framework that can be used to construct subject-specific finite element models of the femur and tibia from CT images. The framework interlinked several new modeling innovations to improve upon the weaknesses of current methods in representing geometry, materials properties and loading conditions.

The first major part of the framework focused on constructing personalized 3-D representations of a knee bone anatomy from *in vivo* CT images. Specifically, the need to correctly capture the cortical bone is crucial to the overall validity of the model. Previous techniques have identified the cortex from CT using attenuation- or intensity-based thresholding techniques, and have mistakenly overrepresented its thickness due to the similarity of cortical and cancellous bone density. The technique introduced in this thesis introduced a new and innovative approach by focusing on attenuation gradients at the cortical interfaces, rather than the gradients themselves, allowing for a more accurate representation of cortical thickness. The general methods of constructing long bones such the femur and tibia employ images from a single plane of view, typically transverse CT images. Such methods have great difficulty accurately constructing the intercondylar notch and condyles in the distal femur because of its bifurcating geometry. The strategy presented in this thesis suggests the use of CT data from both transverse and sagittal planes to accurately define these two complex structures in the femur; this strategy also allows proper definition of the intercondylar spine of the tibia. Voxel meshing is the most commonly used technique in the clinical community for constructing subject-specific models because of its ease of use. However, it suffers from both of the above weaknesses. In addition, the models frequently contain jagged surfaces in areas of high curvature such as the condyles and intercondylar notch. The subject-specific geometries constructed in this thesis use smooth NURBS-based surfaces to avoid the potential stress concentrations associated with such jagged surfaces. The techniques introduced in this thesis addressed 3 of the major weaknesses

observed in current bone geometry construction techniques but still have several limitations. The technique is not automated and requires a fair amount of user interaction and judgement, particularly in the extraction of cortical interfaces and the generation and merging of the 3-D transverse and sagittal surfaces. It is therefore not as user-friendly and cannot construct models as rapidly as commercial software. Complex 3-D curvatures such as the intercondylar notch and epicondyles were not captured with high accuracy in the models presented in this study.

The second major aspect of the framework dealt with material properties modeling of the bone tissue. In all subject-specific models, the mechanical properties of the bone have been interpreted directly from the CT attenuation data. Previous studies have shown that conventional techniques of modeling bone properties, in combination with accurate representations of the geometry, can be used to construct accurate subject-specific FE models of the femur. However, they are limited by two major simplifications: assuming isotropic bone stiffness and merging cortical with cancellous bone. Such assumptions could compromise their accuracy for more complicated loading conditions such as torsion, for which they were not tested. The material properties modeling technique introduced in this thesis countered the first assumption by emphasizing the use of orthotropic bone. Orthotropic properties were incorporated by calculating 9 separate constants from the CT attenuation data using empirical relationships. Cortical and cancellous bones were separated from each other as a consequence of accurately defining the cortical thickness using the above geometry technique. A crucial part of tailoring a FE model to an individual is modeling their unique and heterogeneous bone density distribution. The degree to which this heterogeneity is represented is quite subjective, depending on the amount of computational ease. The innovative application of an image processing technique was presented in this thesis to eliminate this subjectivity. The segmentation of the bone into groups of similar density (i.e. the representation of heterogeneity) was automated using a computer algorithm, effectively removing the subjectivity. The algorithm

implemented an image processing technique which analyzed each CT image and extracted regions of bone with similar density and location within the knee. The material properties modeling technique requires less user intervention than the geometry modeling stage as the image analysis is automated using MATLAB algorithms. Nevertheless, there are several limitations to this technique. First, for the appropriate tolerance levels suggested in Chapter 3, the algorithm can take a substantial amount of time to group the bone. The number of groups generated can also result in longer processing times from the finite element software; it can be assumed that the conventional techniques would require less time since a much smaller number of groups were consistently reported in the literature. Secondly, the interpretation of material properties relies on the use of empirical equations. It has been shown that cortical bone (in particular in the tibia) is poorly correlated with bone density. Accurately estimating the stiffness of the cortical bone for a particular individual may require information other than CT.

It must be noted that the material properties simplifications used in other studies are not always inappropriate. Modeling any situation using finite element methods will always require certain simplifications; the appropriateness of the simplifications depends on the question being answered. While the use of orthotropic and heterogeneous bone is emphasized in this thesis in the interest of generating models with better predictive capability, its implementation can require a substantial amount of user time. If a lower level of accuracy is acceptable and can be used to draw proper conclusions, incorporating simplified material properties is advisable in order to reduce user and computer effort.

The third aspect of the framework concerned the application of loading conditions to the subject-specific FE models, with specific emphasis on the incorporation of muscle and ligament forces. The notable absence of any muscle and ligament forces in nearly all distal femur and proximal tibia FE models in the literature, justified by the contention that these more computationally efficient models would not greatly influence conclusions, prompted an examination of the

necessity of incorporating the soft tissues. A technique was introduced to incorporate the forces produced by the various muscles and ligaments surrounding the knee. By synthesizing information from anatomy texts, musculoskeletal and CAD models, a full set of loading conditions representing gait in the knee was modeled, i.e. tibiofemoral compression, patellofemoral compression, and muscle and ligament forces. Such a technique was used to gain a sense of the internal stresses that may be produced in a natural femur or tibia during walking. In Chapter 5, it was revealed that the muscle and ligament forces produced during gait did have an effect on stress distribution in the distal femur. Stresses were substantially affected directly around the attachment sites (from stress concentrations) while more subtle changes were seen throughout the cancellous bone. Whether such changes in the stress levels will impact the conclusions of a study obviously depends on the question of interest. Again, the balance between the substantial amount of time required to model the soft tissue forces and the accuracy of the results must be considered. Also, despite the fact that geometry and material properties were representative of a particular individual, the loading conditions implemented in the models were not subject-specific. The implementation of subject-specific loading conditions is a tremendous undertaking and was outside the scope of this thesis.

Experimental verification of predictions from the subject-specific models is necessary to show that the framework is acceptable. As the framework is meant to produce representative models of the human knee, ideally it should be compared with data from a cadaveric knee. However, *in vitro* experimental data was not obtained from a human knee in this thesis and weakens the conclusions that can be drawn regarding the acceptability of the framework. Nevertheless, a sense of the validity was gained through a series of preliminary experiments using composite and bovine bones. Geometries constructed using this technique were found to be representative of the physiological anatomy through a comparison with digital and physical surface measurements. Also, a comparison of surface strains produced in composite and bovine bones from mechanical loading

produced promising results. This provided some confidence regarding the ability of the technique to properly model a combination of subject-specific geometry and material properties. However, as shown in Chapter 6, the predicted strains did not fully match with measured strains and therefore improvements in the experimental protocol are needed to (1) produce more deterministic loading such as pure compression and (2) to correctly align the long axis of the bones with the vertical axis of the testing machine.

A variety of techniques were introduced in this thesis to address weakness in the modeling of geometry, material properties and loading conditions. The models constructed using this technique were not meant to answer any specific clinical or research question, but rather to demonstrate how such techniques could be implemented. Depending on the question that the FE model is being used to answer, it may not be necessary to implement all of the techniques into the particular model. Although the techniques were presented under a framework umbrella, most of the techniques can be used in isolation to improve a particular aspect of a FE model. It is hoped that the ideas presented in this thesis will be used to improve the general subject-specific modeling process so that FE models will become more helpful tools for both the research and clinical communities.

7.1 Future Directions

In the immediate future, the technique needs to be validated using cadaveric bone. The preliminary validation presented in this thesis employed composite and bovine bones which are not completely representative of human bone. Validation with cadaveric bone will ensure that the geometry and material property modeling techniques presented in this thesis can be used to construct FE models that are representative of human knee bones. The accuracy of the subject-specific cadaver model can be assessed using the procedure described in Chapter 5.

In the longer term, the incorporation of subject-specific loading conditions will be necessary. The current technique loads the subject-specific model with generic

loading conditions that are still physiologically relevant. MRI-based images of the subject's knee can be used to estimate the insertions of muscles and ligaments. Lines of action and soft tissue forces can be obtained using musculoskeletal models constructed from geometry and force data specific to the individual. Tibiofemoral and patellofemoral compression can be approximated using contact elements in the finite element simulation, with even better predictions generated if menisci are modeled in the knee.

One of the potential research applications of the subject-specific FE models is improving the design of TKR implants. The models in their current state can be used to examine stress shielding in the immediate post-operative time period. However, with the implementation of bone adaptation algorithms, this model can be used to examine the stress condition in a subject's knee 5 or 10 years post-operatively.

Appendix A: Geometry Construction Details

Spline fitting

The SASS technique incorporated an automated spline fitting process in which a series of interconnected cubic splines was fitted to periosteal and endosteal interface points to produce a single smooth curve. The process began by fitting interface points with a spline of pre-defined length ("startlength"). The goodness-of-fit of the spline was measured using a correlation coefficient (r^2). If the fit was acceptable (i.e. $r^2>0.9$) then the spline was extended to fit more points (added in multiples of "startlength") and the r^2 was measured and compared with its previous value. The process was repeated until a maximum r^2 was obtained, producing a single spline. A second spline was fit to the remaining points by repeating the above process, starting where the first spline ended. Spline fitting was completed when all points were fitted by the series of splines. The spline fitting operation was automated by a module written in MATLAB 6.1.

Each contour was defined as a series of interconnected splines (Fig A.1) and its smoothness was quantified principally by the mean r^2 of the splines. However, additional information about the smoothness was gained by observing the mean deviation of the curve from the original non-fitted interface points. Two important parameters potentially influenced the smoothness of the curve: (1) the origin of the curve, i.e. the location along the interface where spline fitting begins and (2) the "startlength". The automated spline fitting process of the SASS technique was used to investigate both parameters using transverse periosteal interface points at three levels of the composite femur (i.e. diaphysis, metaphysis and epiphysis). To investigate the sensitivity of smoothness to the curve origin (parameter 1), a curve was initiated at all points along the interface. A cubic spline was initially fitted to 12 interface points (i.e. "startlength"=12). The process continued until all interface points were fitted, resulting in a smooth curve. The absolute deviation of the curve from each interface point was measured and averaged; the r^2 of the splines defining the curve were also averaged.

The "startlength" of 12 for the above investigation was chosen arbitrarily. To investigate the sensitivity of smoothness to "startlength" (parameter 2), interfaces were fitted with splines of fixed length from a fixed origin. For example, one curve would consist of splines only 8 points long; another curve would consist only of 9-point splines. Interfaces were fitted with a minimum spline length of 8 points to a maximum length in which one spline fitted the entire set of points. The collective mean r^2 and deviation of the splines were observed.

The results in Table A.1 showed that smoothness of the curve remained relatively insensitive to its origin. Considering all three levels, the splines represented the interface points with an average error of about 0.2 mm and a maximum error of about 0.6 mm. The splines therefore represented the interface points with sub-pixel accuracy as the CT image resolution was 0.3125 mm/pixel. In all cases, r^2 was acceptable. Therefore, the location where spline fitting began was not overly important.

Table A.1: Comparison of curve smoothness by varying curve origin.

Level	Number of Interface Points	r^2			Deviation (mm)		
		Mean (SD)	Max	Min	Mean (SD)	Max	Min
Diaphysis	271	0.996 (0.001)	0.998	0.994	0.116 (0.022)	0.251	0.082
Metaphysis	564	0.990 (0.002)	0.993	0.983	0.220 (0.098)	0.591	0.111
Epiphysis	774	0.996 (0.001)	0.997	0.992	0.186 (0.038)	0.386	0.103

The choice of a "startlength" of 12 was therefore acceptable for investigating parameter 1. However, using a startlength between 8 and 80 points would have been equally acceptable. The mean r^2 for this range of "startlength" were all

above 0.97 and the mean deviations were all below 1 pixel (0.3125 mm) for all 3 levels. Therefore, a spline fit process with startlength between 8 and 80 points could generate smooth curves which appropriately represent periosteal and endosteal interfaces. It should be noted that fitting interface points with splines less than 5 points long produced jagged curves and therefore should be avoided.

The automated spline fitting process of the SASS technique is robust, generating smooth curves which are relatively insensitive to both the origin of the spline fit and the length of its underlying splines. The sub-pixel deviation means that it contributes very little error to surface construction, therefore the majority of the error lies in the CAD surface generation process, which has been shown to be accurate.

Endosteal interface interpolation

Osteopenic or osteoporotic bone is frequently present in TKR surgery candidates. Consequently, CT images obtained *in vivo* from such patients will result in poor contrast at certain locations. In the SASS technique, a gradient operator was applied to such images and often revealed the location of the endosteal interface, allowing for successful construction of the endosteal surface. However, several areas of weak bone yielded extremely weak gradients which could not be detected using Path Analysis. Subsequently, gaps were present in the endosteal edge extraction (Fig A.2a). Closed curves were necessary for CAD surface generation therefore the gaps in the edge extraction needed to be filled. Spline fitting did not consistently interpolate representative interface points for large gaps. A more effective method was to estimate the interface points using data from the surrounding region where Path Analysis extraction was successful.

Interpolation was performed automatically using a module written with MATLAB 6.1. During Path Analysis, endosteum regions which could not be identified due to weak gradients were recorded. The cortical thickness of the successfully extracted endosteal interface points were concurrently recorded.

After completing the Path Analysis, the cortical thicknesses of the gaps were estimated using the thickness information of the surrounding cortex. The thicknesses for each point in the gap were linearly interpolated using data before and after the gap. Using the thickness information, the endosteum coordinates could be estimated by revisiting the Path Analysis in the gaps. This provides a smooth closure of the gap through reasonable estimation of the cortical thickness (Fig A.2b). Although physiologically no interface may actually exist in regions of weak bone, the interpolation is a necessary step since a closed endosteal curve is needed for surface generation. A careful and reasonable estimate of the endosteal interface is provided by the SASS technique.

CT Scanner Capabilities and Slice Separation

A side benefit of using larger slice separation to construct SASS models is the reduction of radiation exposure to the patient. For single-detector CT (SDCT) machines, scanning at a higher slice thickness will reduce additional radiation exposure to the patient, but the algorithm used to reconstruct to smaller thickness post-CT will reduce the fidelity of the data. Thus, with the SASS technique, patients can benefit from reduced radiation exposure and accurate geometry models. Recent advances in CT scanner technology have allowed for improved imaging capabilities while simultaneously reducing radiation exposure to the patient. In particular, multi-detector CT (MDCT) scanners can scan at higher slice thickness and reconstruct to smaller thickness post-CT without additional radiation exposure while maintaining data fidelity. However, the greatest impact of using a 3 mm slice separation in constructing SASS models is the ability to reduce computational time while still accurately capturing the geometry. Thus, sub-3 mm data, whether obtained from SDCT or MDCT, is not entirely necessary in constructing an accurate model.

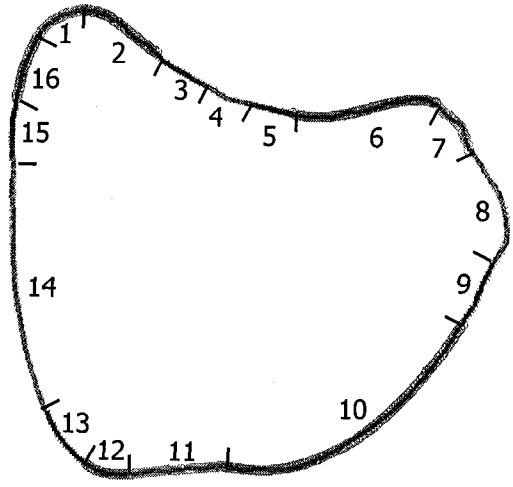

Figure A.1: A series of 16 interconnected splines defining a periosteal contour located in the human distal femur.

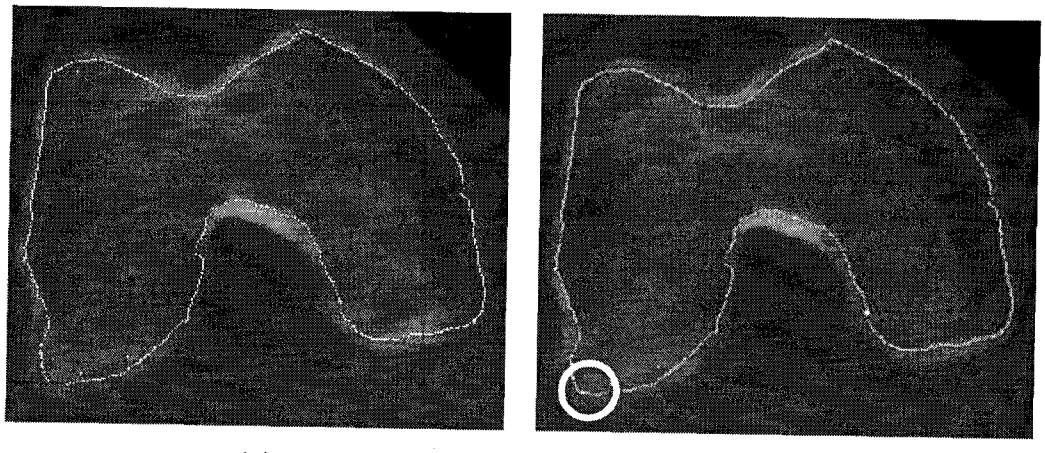

(a) (b)

Figure A.2: A transverse CT image of the human distal femur, located 12 mm from the joint line, showing the endosteal interface points extracted using Path Analysis. The gap in the lower left quadrant seen in (a) was filled in by interpolating the cortical thickness based on the surrounding cortex (b).

Appendix B: Empirical Relationships for Modeling Cortical and Cancellous Bone

Empirical relationships from several sources were used to determine the elastic constants from the apparent density.

Femoral cortical bone

Cortical bone in the femur was defined using a cylindrical coordinate system, where direction r is radial, direction c is circumferential, and direction z is axial for equations (B1) to (B9). Young's modulus was calculated using relationships from Rho et al. (1995):

$$E_r = -6.087 + 0.010\rho \quad \text{(B1)}$$

$$E_c = -4.007 + 0.009\rho \quad \text{(B2)}$$

$$E_z = -6.142 + 0.014\rho \quad \text{(B3)}$$

where E is Young's modulus (GPa) and ρ is apparent density (kg/m^3). Relationships between shear modulus and apparent density for cortical bone were not available in literature. Using the data available in Rho (1992), the following relationships were generated to calculate the shear modulus:

$$G_{rc} = 0.0030\rho - 1.4132 \quad \text{(B4)}$$

$$G_{rz} = 0.0032\rho - 0.8067 \quad \text{(B5)}$$

$$G_{cz} = 0.0035\rho - 0.9874 \quad \text{(B6)}$$

where G is shear modulus (MPa) and ρ is apparent density (kg/m^3). Orthotropic Poisson's ratios were obtained from Rho (1992):

$$\nu_{rc} = 0.417 \quad \text{(B7)}$$

$$\nu_{rz} = 0.232 \quad \text{(B8)}$$

$$\nu_{cz} = 0.225 \quad \text{(B9)}$$

Femoral cancellous bone

Cancellous bone in the femur was defined using a Cartesian coordinate system, where direction *AP* is anterior-posterior; direction *ML* is medial-lateral; direction *SI* is superior-inferior for equations (B10) to (B18). Young's modulus was calculated using relationships from Rho et al. (1995):

$$E_{AP} = 0.01\rho^{1.79} \tag{B10}$$

$$E_{ML} = 0.01\rho^{1.82} \tag{B11}$$

$$E_{SI} = 0.82\rho^{1.27} \tag{B12}$$

where E is Young's modulus (MPa) and ρ is apparent density (kg/m^3). Relationships between shear modulus and apparent density in the cancellous bone of the femur could not be found in literature. Therefore empirical relationships for the cancellous bone of the tibia were used (Ashman et al., 1989):

$$G_{AP-ML} = 0.48\rho - 27.74 \tag{B13}$$

$$G_{AP-SI} = 0.53\rho - 13.19 \tag{B14}$$

$$G_{ML-SI} = 0.66\rho - 8.93 \tag{B15}$$

where G is shear modulus (MPa) and ρ is apparent density (kg/m^3). Although cancellous bone is known to be orthotropic, only transversely isotropic Poisson's ratios could be found (Williams and Lewis, 1982):

$$\nu_{AP-ML} = 0.52 \tag{B16}$$

$$\nu_{AP-SI} = -0.07 \tag{B17}$$

$$\nu_{ML-SI} = -0.02 \tag{B18}$$

Tibial cortical bone

Cortical bone in the tibia was defined using a cylindrical coordinate system, where direction r is radial, direction c is circumferential, and direction z is axial for equations (B19) to (B24). Young's modulus was calculated using relationships from Rho (1992):

$$E_r = 4.055 + 0.004\rho \quad \text{(B19)}$$

$$E_c = 4.291 + 0.004\rho \quad \text{(B20)}$$

$$E_z = -3.842 + 0.013\rho \quad \text{(B21)}$$

where E is Young's modulus (GPa) and ρ is apparent density (kg/m^3). Relationships between shear modulus and apparent density for cortical bone were not available in literature. Using the data available in Rho (1992), the following relationships were generated to calculate the shear modulus:

$$G_{rc} = 0.0012\rho - 1.7903 \quad \text{(B22)}$$

$$G_{rz} = 0.0021\rho - 1.2237 \quad \text{(B23)}$$

$$G_{cz} = 0.0024\rho - 1.3603 \quad \text{(B24)}$$

where G is shear modulus (GPa) and ρ is apparent density (kg/m^3). The same orthotropic Poisson's ratios were used for the femoral and tibial cortical bone (equations (B7) to (B9)).

Tibial cancellous bone

Cancellous bone in the femur was defined using a Cartesian coordinate system, where direction *AP* is anterior-posterior; direction *ML* is medial-lateral; direction *SI* is superior-inferior for equations (B25) to (B27). Young's modulus was calculated using relationships from Rho et al. (1995):

$$E_{AP} = 0.06\rho^{1.51} \quad \text{(B25)}$$

$$E_{ML} = 0.06\rho^{1.55} \quad \text{(B26)}$$

$$E_{SI} = 0.51\rho^{1.37} \quad \text{(B27)}$$

where E is Young's modulus (MPa) and ρ is apparent density (kg/m^3). The same empirical relationships between shear modulus and apparent density were used for the femoral and tibial cancellous bone (equations (B13) to (B15)). The same Poisson's ratios were also used (equations (B16) to (B18)).